Stellar Streams, Dwarf Galaxy Pairs, and the Halos in which they Reside

Sarah Pearson

Submitted in partial fulfillment of the
requirements for the degree
of Doctor of Philosophy
in the Graduate School of Arts and Sciences

COLUMBIA UNIVERSITY

2018

ABSTRACT

Stellar Streams, Dwarf Galaxy Pairs, and the Halos in which they Reside

Sarah Pearson

In this Dissertation we explore how the nature of tidal interactions tear gravitationally bound systems apart into distinct morphological and kinematic structures. We use the properties of these structures, persisting for billions of years, to investigate the potential of the Milky Way Galaxy and to disentangle the baryonic evolution of gas in dwarf galaxy interactions. We approach these problems through a combination of observations, and simulations, as well as comparisons between the two.

In particular, we use the properties of the thin, curved stellar stream emerging from the old, Milky Way globular cluster, Palomar 5 (Pal 5) to show that its mere existence can rule out a moderately triaxial potential model of our Galaxy. Pal 5-like streams on appropriate orbits diffuse much further in space from the orbital path (dubbed "stream-fanning") in this triaxial potential than in the oblate case. We further show that torques from the Milky Way's Galactic bar, can create ever-widening gaps in stellar streams. The fact that the bar can create such under densities, demonstrates that we should be careful when interpreting gaps in stellar streams as indirect evidence of the existence of dark matter subhalos in our Galaxy.

We carry out a systematic study of resolved neutral hydrogen (HI) synthesis maps of 10 interacting dwarf galaxy pairs. The pairs are located in a range of environments and captured at various interaction stages. We find that the neutral gas is extended in the

interacting pairs when compared to non-paired analogs, indicating that gas is tidally pre-processed. Additionally, we find that dwarf-dwarf interactions enable the "parking" of gas at large distances to serve as a continual gas supply channel to the dwarfs until accretion by a more massive host.

We model a specific dwarf pair in our sample, NGC 4490/85, which is an isolated analog of the Magellanic Clouds and is surrounded by a $\sim$50 kpc extended HI envelope. We use hybrid N-body and test-particle simulations along with a visualization interface to simultaneously reproduce the observed present-day morphology and kinematics. Our numerical results confirm that encounters between two dwarf galaxies can "park" baryons at very large distances, without the aid of environmental effects. The extended tidal features will continue to evolve over several billion years which will affect the efficiency of gas stripping if such dwarf pairs are accreted by a massive host. In contrast, in isolated environments dwarf-dwarf interactions can create a long-lived supply mode of gas to the merger remnant potentially explaining the population of dwarfs in the field with large gas envelopes, but limited star formation. All of these topics share the common theme of utilizing morphological and kinematic structures left behind from ongoing gravitational interactions on various scales.

Contents

List of Figures

List of Tables

(This page left intentionally blank.)

ACKNOWLEDGMENTS

More than anything, I want to thank my three PhD advisors Kathryn V. Johnston, Mary E. Putman and Gurtina Besla. Kathryn, for always conveying your extreme excitement in all projects we have worked on, for always making me feel like I could do whatever I put my mind to and for actively telling me I am doing great. It really made a difference throughout the years. Mary, for your mentorship, encouragement, your positive reinforcements, and for teaching me everything I know about HI observations. Gurtina, for your enormous drive, which is highly contagious, for your career advise and for caring as much as you do. To all of you, for being incredible role models and for supporting my outreach efforts.

Thank you George C. Privon and Andreas H. W. Küpper for everything you taught me. Thank you both for putting up with me when my eagerness translated into impatience. Andreas, thank you for encouraging me to give my first conference talk and for your genuine excitement for "stream-fanning". Thank you George, for being such a wonderful host in Chile and for tolerating my frustration when I could not find a dynamical match for, let's say, a number of months (see Chapter 5).

Thank you to my fellow Columbia U. graduate students, especially Susan, Andrew, Adrian, Dan, Lauren, Andrea, Alejandro, David, Tomer, Steven and Munier for your friendship, support and inspiration. Things that come to mind are binging on sushi while doing late night homework sets, pool at the Ding-Dong Lounge, guitar playing and singing, walks to McGolrick Park, Little King, an attempt at starting a math philosophy club, switching off our brains with movie nights and nail polish. Thanks to the NYC astronomy community Kelle, Matt, Jacqueline, Zoltan, Jules, Greg, and thank you my friends in NYC: Stefanie, Josephine. Thank you Nicole. To all my Danish friends for visiting me throughout the years: Lea, Benedikte, AK, Amalie, Madeline, Celine and Malene.

I am grateful to Malene Vested and Per Andersen. The three of us did our very first problem set together in undergrad, and who would have known how much we would teach each other those three years. For being my mental buddies through each and every exam. "W other".

Thank you to Johnny Karl White (1980-2017) and Brett Van Deusen for helping me realize my dream of creating the outreach program: Space with Sarah. I cannot begin to describe the joy this project has brought me, especially at times when the PhD got a little too nitty gritty.

Thank you Enrico Ramirez-Ruiz, Laura A. Lopez and Daniel Castro for giving me scientific confidence and making me believe I could be accepted to graduate school in the US. Sometimes a single conversation can change your entire life: for me that was in Saint Emilion when Enrico suggested I did a research project at UC Santa Cruz.

To Jens Hjorth and Anja C. Andersen for welcoming me into the world of Danish astronomy. You have been and continue to be fantastic mentors and inspirations to me.

To my siblings: Christopher who's fascination with astrophysics rubbed off on me at an early age. Emily, for being exactly who you are. Your pure kindness continues to baffle me and I cannot imagine ever seeing your face without smiling. To Jonathan for listening to my story on Betelgeause in Sri Lanka, and for your wonderful character. Martin for taking such an interest my field. You are all very special to me, and I find comfort knowing that I have a home wherever you are.

Thank you to my mother, Seija Pearson, for laughing at my elementary school math teacher when he said I was too much of a perfectionist. For your love and complete devotion. For your support of my pursuits and for your full and utter interest in any minor project I ever take on. I am thankful to my father, Claus Hyldahl, who made me love math from the age of 5 and who sparked my curiosity for the world around me through stargazing and

discussions of nature's puzzles. Your logical way of thinking and constant questioning of the world around you has made me a better scientist.

Finally, I am grateful to my dearest friend, Anna L. Poulsen, who has been my family throughout the years in NYC and my friend since you were born. While we do not spend a lot of time discussing science, it was indeed you who suggested that I should apply to DARK, who always encouraged me to do more, believed in me, taught me how to negotiate and beyond everything always gave me your undevoted attention, love and advise whenever I needed it. I am proud that I can call you a constant in my life.

2018, New York City

Chapter 1

Introduction

> *It is far more natural and conceivable to regard them as being not such enormous single stars but systems of many, whose distance presents them in such a narrow space that the light, which is individually imperceptible from each of them, reaches us on account of their immense multitude in a uniform pale glimmer . . . all this is in perfect harmony with the view that these elliptical figures are just universes and, so to speak, Milky Ways, like those whose constitution we have just unfolded.*
>
> – Immanuel Kant, 1755

Galaxies are enormous collections of stars and gas connected in a web of dark matter that spans our entire Universe. Reaching this level of understanding has not been simple. In fact astronomers have only been certain of the existence of "galaxies" for about one hundred years, as Hubble confirmed that the distances to Andromeda's Cepheid stars were indeed much larger than the distance to the stars we can see with our naked eye in the Milky Way (Hubble 1929). Since then, our understanding of the Universe and our place within it has grown immensely. We know now that the Milky Way contains hundreds of billions of stars, while the observable Universe contains at least as many galaxies. However, when attempting to study these galaxies a problem presents itself: the timescale available

for human exploration is puny when compared to the timescales involved in galactic growth and evolution. Even if we stared at a galaxy for the next thousand years, not much would change on galactic scales. So by what means do we disentangle how the galaxies around us came into existence and took their current form?

To our great advantage, light travels at a finite speed, permitting us to study the Universe at different epochs by looking farther away. When astronomers do this, they indeed see an evolution in galactic properties: in the past galaxies formed stars more violently (the formation of stars peaked when the Universe was ~ 3.5 Gyr old corresponding to $z \sim 1.9$: e.g. Madau & Dickinson 2014) and galaxies were more compact at earlier times (e.g. van Dokkum et al. 2015). Thus, we get a sense of growth and evolution by looking back in time and this can give us hints as to how a galaxy like our own Milky Way "ended up" taking its present form. However, it is a difficult exercise to trace back and match which type of galaxy might correspond to a certain other galaxy at later times (see e.g. van Dokkum et al. 2010, van Dokkum et al. 2013).

We can also look at the question from a theoretical perspective. Within our current paradigm of cosmology, simulations of large scale structure formation (e.g. *The Millennium Simulation*: Springel et al. 2005, *The Illustris Simulation*: Vogelsberger et al. 2014), suggest that galaxies go through a phase of accretion of gas and dark matter from the cosmic web, and subsequently grow in size and mass by merging with other galaxies and hierarchically accreting smaller systems. The dark matter mass function is nearly self-similar (e.g. Gao et al. 2004, van den Bosch et al. 2014) and at early times the Universe should be filled with small fragmented halos of dark matter, colliding with each other, acting as building blocks for the more massive galaxies we see today.

These hints from simulations suggest another observational approach as the process of hierarchical accretion should still occur at present day, and a Milky Way type galaxy should

be surrounded by 100-1000s of satellites (Klypin et al. 1999, Diemand et al. 2008), some of which should be hosts of galaxies and some of which should be completely dark. According to Wetzel et al. (2015), a large fraction (30-60%) of these satellite systems will fall in as groups, potentially pre-processed through tides prior to infall (see e.g. Besla et al. 2012). The accretion of these smaller satellite systems will not happen instantaneously, but tidal forces from the host galaxy will tear the satellites apart into distinct morphological and kinematic structures persisting for billions of years (e.g. Allen & Richstone 1988, Johnston et al. 1995, Johnston 1998). This process will occur at various mass scales and mass ratios, and the disruption mechanism will depend sensitively on the internal structure of the objects involved. Through our understanding of gravity, we can therefore turn a single snapshot of a galaxy into a detailed map of its assembly history by examining the tidal features surrounding it. We refer to the process of reconstructing the past from signatures in the present as "galactic archeology" (see e.g. Bullock & Johnston 2005). By studying galactic interactions on various scales, we can build an intuition for how galaxies evolved into their current form and how their mass might be distributed at present day. Aided by hidden symmetries, governed by the laws of gravity, we can thus unravel the dynamical history of a galaxy.

One of the first steps towards utilizing these structures for galactic exploration was made by Arp (1966). They discovered that many galaxies appear "peculiar" in their morphologies (see *The Atlas of Peculiar Galaxies*). The galaxies came in odd shapes and different sizes hinting at a morphological transition. But what made these galaxies look peculiar? It was not obvious at the time that these were mergers of galaxies with various mass ratios, inclinations, viewing angles and separations which Toomre & Toomre (1972) systematically convinced us was the case. Indeed mergers were key drivers of morphological transformations of spirals. Using clues from these tidal features astronomers could now start to make qualified

estimates of: what did the system look like a few billion years ago, and what will it look like in the future?

Due to the difficulties involved when looking through the overwhelming field of stars in our Milky Way, only much later did we discover signatures of past interaction events and hierarchical assembly for our own and close neighboring galaxies. Ibata et al. (1994) discovered the Sagittarius dwarf spheroidal galaxy (Sgr) as an elongated group of co-moving stars, and Mateo et al. (1996) found Sgr members more than 10° from the dwarf, which has now been detected to wrap around our entire Galaxy (e.g. Majewski et al. 2003). We have since developed clever techniques to contrast the stars (e.g. matched filtering: Rockosi et al. 2002), and can detect stellar streams in our own and external galaxies. At present day we know of ~ 40 stellar streams in our own Galaxy (e.g. Grillmair & Carlin 2016, Shipp et al. 2018, Malhan et al. 2018) from both disrupting dwarf galaxies and globular clusters and we know of 4 stellar streams in Andromeda (e.g. McConnachie et al. 2009)[1]. Additionally, by studying nearby interactions of dwarf galaxies, we see galaxy assembly in our backyard (also known as "near-field cosmology"). We can detect the mutual interaction between dwarfs (e.g. Tully et al. 2006, Stierwalt et al. 2015, Pearson et al. 2016, Carlin et al. 2016), and even detect the predicted assembly of these dwarfs as we have discovered groups of dwarfs (Stierwalt et al. 2017) and streams around dwarfs (Martínez-Delgado et al. 2012a).

The above discussion gives a broad overview of the origin of debris structures created by tidal interactions on various mass scales and mass ratios. The morphology and kinematics of all these features give us clues of billions of years of dynamical evolution. In what follows, the focus lies on two distinct stripping mechanisms for which we can wind time either backwards or forwards: 1) Tidal stripping of stars from gravitationally bound stellar satellite systems orbiting larger galaxies, creating what we will refer to as "stellar streams" (Section 1.1) and

[1]When we first hypothesized that the fuzzy object, Andromeda, was another galaxy, who would have thought we would be able to disentangle its accretion and dynamical history?

2) Quasi resonant stripping governing disk galaxy interactions creating what we will refer to as "tidal tails" (Section 1.2). In this Dissertation the goal is to build upon the hundreds of years of work that enabled the exploration of galactic properties from dynamical structures. In particular, we will use the knowledge to develop new techniques and uncover the yet hidden clues the Universe provides of galaxies' pasts and futures. We outline the structure of the Dissertation in Section 1.3.

1.1 Satellite disruption and debris evolution

Stellar streams from disrupting dwarf galaxies or globular clusters orbiting a host potential can stretch over several kiloparsecs (kpc), which is one of the many ways in which we witness gravity manifesting itself on large scales. We can observe these streams as over-dense, coherent kinematic and morphological structures in both our own (e.g. GD1: Grillmair & Dionatos 2006, Sgr: Majewski et al. 2003, Pal 5: Odenkirchen et al. 2003) and external galaxies (e.g. Martínez-Delgado et al. 2015a, McConnachie et al. 2009). As the stripped stars were once closely tied together in energy and angular momentum space, we can use their distribution in phase space to retrace where they were once located, and what affected them along their paths. In this Subsection we discuss what sets the escape conditions for stars eventually becoming stream members, and how the phase space distribution evolves after stars are stripped from their respective gravitationally bound systems (Section 1.1.1). Additionally, we discuss how streams can be used to indirectly probe the underlying potentials of their host galaxies (Section 1.1.2).

1.1.1 Tidal radius and stripping

For a star orbiting within a progenitor system, which simultaneously orbits a host galaxy, there is a certain point at which the internal gravitational forces acting on the star from its progenitor are roughly equal to the tidal forces from the entire host galaxy's potential. We call this point "the tidal radius", r_t. If we assume a point mass host potential, a point mass progenitor and a circular orbit for the progenitor's orbit within the host potential, we can calculate the radius at which a test particle should experience the same gravitational force from the progenitor as the entire host potential (the restricted three-body problem):

$$r_t = R \left(\frac{m_{\rm prog}}{3M_{\rm host}(R)} \right)^{(1/3)} \tag{1.1}$$

where $m_{\rm prog}$ is the mass of the progenitor, $M_{\rm host}$ is the mass of the host potential and R is the distance from the progenitor to the host, which is assumed to be much larger than the tidal radius, r_t. Hence, at a distance larger than r_t from the center of the progenitor system a test particle would be located at a saddle point (Lagrange point) in the effective potential (at the last "zero velocity surface") and should escape through the Lagrange points (see e.g. Binney & Tremaine 2008). In reality, this is a more complex process as neither the host nor the progenitor are point masses and the progenitor orbit is often eccentric. Although naively, if we know the mass of the progenitor and the approximate mass enclosed within its orbit we can predict whether the progenitor should have stellar streams emerging from its tidal radius. This will be the case if the radius of the cluster is larger than the tidal radius. In contrast, if we see a stream but not its progenitor (e.g. Orphan: Belokurov et al. 2006, GD1: Grillmair & Dionatos 2006), hidden in the streams' widths alone, as determined by their tidal radius, we can guess the initial properties of what was once a gravitationally bound system now stretched into long streams due to the external tidal field of its host potential.

While the equation for the tidal radius is based on many assumptions, as we shall see at several points in this Dissertation the approximation is quite adequate.

For non-circular orbits, the enclosed mass will vary over the course of the motion through the host galaxy. We therefore need to take into account the change in the host galaxy potential due to the position along the orbit. In this framework the tidal radius can be expressed as:

$$r_t = \left(\frac{G m_{prog}}{\Omega^2 - \partial^2 \phi / \partial R^2} \right)^{(1/3)} \tag{1.2}$$

where Ω is the angular velocity of the cluster on its orbit about the galactic centre, G is the gravitational constant, ϕ is the galactic potential and R is the current radius of the orbit (see e.g. Küpper et al. 2012).

As the progenitor orbiting the host galaxy is not a point mass either, the escape conditions will also be affected by the internal motion within the progenitor. Read et al. (2006) showed that stars on prograde orbits within a progenitor with respect to the orbit around the galaxy, will preferentially be stripped, and that there are different stripping radii for stars on prograde, radial vs. retrograde orbits, due to their slight energy differences. The progenitors are themselves fascinating laboratories for many dynamical processes and after the progenitor is stripped of stars beyond its tidal radius (which evolves with its changing mass), stars will continue to escape the progenitor through the Lagrange points due to internal heating of the progenitor members (e.g. through two-body relaxation: Heggie & Hut 2003). The progenitor eventually evaporates through this process or likely gets destroyed by a pass through the disk of the galaxy as hypothesized for the Milky Way globular cluster, Palomar 5 (Dehnen et al. 2004).

We can understand the subsequent evolution of stars escaping through the Lagrange points as evolving on orbits with slightly higher and lower energies than their progenitor, due to their $\pm r_t$ offsets from the progenitor's center. The stars with higher energy with

respect to the progenitor move to larger radii orbits forming the trailing arm, and the stars with lower energies with respect to the progenitor move to orbits with smaller radii and form the leading arm. We can estimate the spread in energy of the debris as the change in the potential at the debris location set by the tidal radius (following Johnston 1998, Johnston et al. 2001):

$$\Delta E = r_t \left(\frac{d\phi}{dR} \right) \tag{1.3}$$

This energy change is large as compared to the internal energy of the cluster, but small compared to the orbital energy (if $m_{\rm prog} << M_{\rm host}$). To understand how the debris spreads due to the energy offset, ΔE, we can investigate how much the orbital period of the leaked stars changes as compared to the cluster's orbital period ($\Delta T/T$). The angular spread of debris per orbital period can be expressed as $\Delta w = 2\pi \frac{\Delta T_\psi}{T_\psi}$. Johnston (1998) showed that the azimuthal periods depend sensitively on energy, but that almost no effect is seen when changing the angular momentum, L (see also Hendel & Johnston 2015). Assuming the progenitor is orbiting in the outskirts of a logarithmic potential where the rotation curve is flat and the circular velocity, v_c, therefore constant (which is often the case for the progenitors forming stellar streams), the energy can be expressed as:

$$E = \frac{1}{2} v_c^2 + v_c^2 \log(r/r_0) \tag{1.4}$$

The azimuthal orbital period in this region of the potential is $T_\psi = 2\pi r_c / v_c$, such that

$$E = \frac{1}{2} v_c^2 + v_c^2 \log(T_\psi) + v_c^2 \log\left(\frac{v_c}{2\pi r_0} \right) \tag{1.5}$$

and we can thereby express the change in energy over time as:

$$\frac{\partial E}{\partial t} = v_c^2 \frac{\partial T_\psi}{\partial t} \frac{1}{T_\psi} \tag{1.6}$$

Hence the angular spread in debris per orbital time can be expressed as:

$$\Delta w = 2\pi \frac{\Delta T_\psi}{T_\psi} = 2\pi \frac{\Delta E}{v_c^2} \tag{1.7}$$

and we can thereby quite simply estimate the spread of debris per orbital period set by the scale of the tidal radius.

Similarly, the density along the stream can be estimated depending on the change in energy (and mass loss rate). The self-gravity in the stream should have very little effect on the stream evolution, as the density in streams does not exceed the critical density required for the external and internal forces to balance (Johnston 1998). On the other hand, including the mass of the cluster has proven to be very important in reproducing especially the length of the streams when modeling their disruption (e.g. Gibbons et al. 2014, Amorisco 2015), as this affects the scale of the change in energy.

For progenitors which might have started off as rotating disks (see e.g. Gibbons et al. 2016, and Section 1.2), the orientation of the disk with its orbital angular momentum spin vector will not remain constant throughout the disruption, leading to precession which is in literature often attributed to the asphericity of the host potential. For satellite disruption in this Dissertation we focus on globular cluster streams, where the mass ratio of the progenitor (cluster) to the host (the Milky Way) is $< 10^{-6}$ and we do not expect rotation to play a role.

To summarize, stellar stream members have slight deviations in orbital energy from their initial progenitors systems (and large energy deviations compared to the internal energy of their progenitor) explaining why they stay close and coherent in phase space, if they are evolving on regular orbits in the potential (see Pearson et al. 2015, Price-Whelan et al.

2016a). As we shall see, this make them powerful probes of their underlying potentials dominating their future evolution.

1.1.2 Streams as potential measures

With the framework described above, several methods have been developed to use stellar streams as potential measures. Due to a spread in energy and angular momentum between each stream star and the progenitor, the stream stars do not simply follow the orbit of the cluster, and careful techniques have been developed to avoid making this assumption (e.g. Küpper et al. 2015). Throughout this Dissertation we use different techniques to reproduce stream observations (see Chapter 2, 3), using over-densities along streams and radial velocities, as it is possible to fit one without the other[2]. Several "streak-line"-methods (e.g. Varghese et al. 2011, Lane et al. 2012, Küpper et al. 2012, Bonaca et al. 2014, Fardal et al. 2015a, Amorisco 2015, Gibbons et al. 2014, Bovy 2014) have been developed and exploit the quite simplistic evolution of stream debris. These methods have in common that they treat each star as a massless particle escaping uniformly in time through the Lagrange points (tidal radius), where their future motion only depends on the mass distribution of the underlying potential and in some cases the mass of the progenitor. Despite the fact that the stripping should be dominated by bursts around pericenter for eccentric orbits, Bovy (2014) showed that approximating the mass loss as constant is a viable assumption as the debris spreads and overlaps rapidly due to phase mixing. However, the density along the stream might not be accurately represented[3]. Several groups implement scatter around various parameters (velocity dispersion, dispersion in escape position etc.) to more realistically capture the details of the stream evolution. In this Dissertation we use a variety of these

[2]See Küpper et al. (2015) Table 5 for a comparison between recovering parameters using over-densities, weighted over-densities, or an interpolated centerline analysis approach when simulating Pal 5.

[3]It is however also unclear how well the density from a direct N-body simulation compares to reality.

methods, and we compare to direct N-body simulations. Below we describe a few examples of how the dark matter shape and mass distribution have been probed using stellar streams (1.1.2.1), we discuss the promise of indirectly detecting dark matter substructure using stellar streams (1.1.2.2), and we briefly discuss stellar streams in the context of the Galactic bar (Section 1.1.2.3).

1.1.2.1 Dark matter shape and mass distribution

Within the Λ *Cold Dark Matter* (ΛCDM) description of our Universe, our Galaxy is thought to consist of $\sim$80% dark matter. From large scale structure simulations of dark matter alone, we know that dark matter in a galaxy can be distributed in shapes which are oblate, prolate or triaxial and even have a transition from one to the other at various radii (Jing & Suto 2002). Adding baryons to these large scale structure simulations, we further know that the central parts of the dark matter profiles become more "cored" and more spherical in the presence of baryons (Garrison-Kimmel et al. 2014, Wetzel et al. 2016).

Following the first detection of stellar streams in our Galaxy, the field has grown immensely. Streams have become extremely popular, because of their promise to uncover the yet to be detected dark matter within our Galaxy which dominates the underlying galactic potential. Several clever utilizations of streams have been proposed and exploited in literature. Price-Whelan et al. (2014) demonstrated how knowing the phase space information of a few stream member stars very precisely, can in principle reveal the underlying Galactic potential, as given the correct potential, the stars should all end up in the same progenitor after "re-winding" their orbits. Küpper et al. (2015) demonstrated that forward-modeling fast streakline-models and comparing the generated stream properties to observations through continuous likelihood functions, one could infer MW properties, as well as the solar motion and progenitor properties. Methods fitting only apocentric distances as well as orbital plane

precession have also been suggested as efficient methods to recover the potential (Gibbons et al. 2014). Bovy et al. (2016) used multiple thin streams, GD1 & Pal 5, to constrain potential parameters, and recently Bonaca & Hogg (2018) demonstrated that streams in the galaxy carry different information content depending on their location, length and orbital properties[4]. To date, several streams have been modeled in an attempt to uncover both the shape and mass distribution of dark matter enclosed within their orbits (GD1: Koposov et al. 2010, Sgr: Law & Majewski 2010, Pal5: Küpper et al. 2015, Orphan: Newberg et al. 2010).

In principle all streams should be able to be reproduced within the same halo (see Chapter 2), but we live in a complex galaxy which might be transitioning in shape (e.g. Jing & Suto 2002, Vera-Ciro & Helmi 2013), and which most likely is sensitive to accretion events (e.g. the Magellanic Clouds: Gómez et al. 2015 and the Sgr: Laporte et al. 2018). For example Law & Majewski (2010) successfully reproduced the angular position, radial velocity and distances to Sgr stream members in a triaxial dark matter halo, although a potential which transitions in shape due to the interaction with the LMC (Vera-Ciro & Helmi 2013), and a spherical dark matter halo in which the density decreases non-monotonically with radius can also fit the Sgr data (Ibata et al. 2013). Streams have additionally been explored in time-dependent potentials with live dark matter halos (e.g. Sandford et al. 2017, Bonaca et al. 2014). Thus, we are far from done, and the true mass distribution of the Milky Way has yet to be uncovered.

1.1.2.2 Dark matter substructure

One example of a complex structure and time-dependence within ΛCDM is the prediction that dark matter should "clump" into dark matter subhalos which should be orbiting their

[4]Interestingly, they found that the sum of the constituents is larger than the information in the individual streams.

respective host galaxies' center of mass (e.g. Klypin et al. 1999, Moore et al. 1999, Diemand et al. 2008). Streams have received much attention in this area as density distortions along their arms could indicate an impact with a dark matter subhalo. As a subhalo passes by a stream the gravitational influence of the subhalo on certain affected stream members, should form gaps, growing in time simply due to the energy offset induced by the perturbation (see Section 1.1.1). These energy offsets should further depend on the encounter geometry (Erkal et al. 2016), the mass of the subhalo, the velocity of encounter and the impact parameter (see e.g. Yoon et al. 2011). Our Galaxy should be filled with dark matter subhalos not hosting stars, and there should be a non-negligible chance of these interacting with the stellar streams (Yoon et al. 2011, Carlberg et al. 2012, Sanders et al. 2016, Bovy et al. 2017). This field is particularly exciting, as competing descriptions of the nature of dark matter (e.g. warm, fuzzy: Hui et al. 2016) predict that the mass distribution of subhalos should be different than the mass distribution of subhalos within the cold dark matter paradigm. Bovy et al. (2017) makes clear predictions within the framework of ΛCDM of how many gaps we should expect to find in a given stream. Hence, using density distortions in streams we could potentially see signatures of dark matter and get closer to an understanding of the nature of dark matter.

1.1.2.3 The Galactic Bar

Another source of time-dependent impulses that can sculpt streams is the Milky Way's Galactic bar (Pearson et al. 2017). Bars are visible in ∼50% of the observed spiral galaxies at redshift, $z = 0$ (Binney & Tremaine 2008), and their "straight" (rather than trailing) nature indicates that bars are rigid structures confined by a subset of stars moving on certain orbits, all co-rotating with the same pattern speed. There is a wealth of direct and indirect evidence pointing towards the existence of a Galactic bar in the Milky Way, however due to

our placement within the disk of the Galaxy, Galactic bar parameters (e.g. its pattern speed, mass, length) are difficult to disentangle and are still subject to much debate. In Chapter 3 we demonstrate how the Milky Way's Galactic bar exerts a torque if the bar "sweeps by" the Pal 5 stream in a prograde interaction as streams members reach pericenter. This can create gaps that look similar to those from subhalos and we caution that not all stream gaps should be interpreted as due to dark matter subhalo interactions. We further argue that streams might be useful for constraining parameters of the Galactic bar, and that the kinematic influence of the Galactic bar on the Pal 5 stream indicates a rapidly spinning bar with a co-rotation radius at $\sim$4 kpc.

Observationally, it has long been argued that the Milky Way has a Galactic bar from gas kinematics, the surface brightness of the near-side of the bar, star counts and the bar's affect on stellar kinematic such as Lindblad resonances in the disk (see e.g. Kuijken 1996). Recently, WISE data (Ness & Lang 2016) revealed that the inner part of our Galaxy appeared boxy-/peanut ("X") shaped which has often been tied to the presence of a bar (Combes & Sanders 1981, Combes et al. 1990). While some argue that the Milky Way's bar has formed in situ through buckling instabilities (e.g. O'Neill & Dubinski 2003) others favor a scenario in which the bar is formed due to an interaction with a satellite (e.g. Mihos et al. 1997). Recently N-body simulations of in-situ bar formation in a galaxy like our Milky Way (e.g. Debattista et al. 2017) and bars formed in self-consistent hydrodynamical cosmological simulations (e.g. Buck et al. 2017) have successfully reproduced some of the key observational features observed for the inner parts of our Galaxy (e.g. that the "X"-shape is stronger in relatively younger (dynamically colder and metal-rich) stars than in the older (dynamically hotter and metal-poor) stars which is also seen observationally in e.g. Ness et al. 2012). In the simulations, the bar is "long" (the bar half length $\sim$ 5 kpc, which is also consistent with red clump giant star observations: Wegg et al. 2015) and therefore relatively slow (Portail

et al. 2017), with typical pattern speeds of $\Omega_b \sim$ 40 km s^{-1} kpc^{-1} and co-rotation radius, $R_{\rm CR} > 5$ kpc (typically bars extend to $\sim 0.8 \times R_{\rm CR}$).

However, some kinematic signatures in the disk of co-moving stars suggest that the Milky Way has a fast, short bar. Hunt et al. (2018a) show that the Hercules stream of co-moving stars have a distinct line-of-sight velocity distribution as seen in the APOGEE-2s data, consistent with being an effect of the outer Lindblad resonance of a fast bar. They show that if the group of stars were instead co-moving as an effect of orbiting the Lagrange points of a long slower-rotating Galactic bar, the v_{los} distribution is not well reproduced. A fast bar is somewhat at odds with it being old (and formed in situ), as the bar should have slowed down during its history due to its exchange of angular momentum with the central part of the dark matter potential (Debattista & Sellwood 1998, Debattista & Sellwood 2000). However, bars can also form through encounters (one example could be the recent Sgr/MW-disk interaction: Laporte et al. 2018), and it is possible that the Milky Way hosts a younger bar. Interestingly, most bars in external galaxies appear to be "fast" bars, where co-rotation is close to the semi-major axis of the bar (Binney & Tremaine 2008). Hunt et al. (2018b) later showed that a longer bar, can also reproduce the Hercules co-moving group of stars, if higher order Fourier terms are included in the analytic long-bar model, and Gaia should be able to disentangle the kinematic signatures.

Thus, currently there is only consensus on the direction of the rotational spin of the bar in the Milky Way (prograde with the disk: Gerhard 2011), that the angular offset from the Galactic x-axis in the direction of rotation is $\sim 27°$, and that its mass is estimated to be $\sim 10^{10}$ M$_\odot$ (Portail et al. 2016). However, there is no consensus on pattern speed and in Chapter 3 we demonstrate how streams might help answer some of the outstanding questions about our Galactic bar.

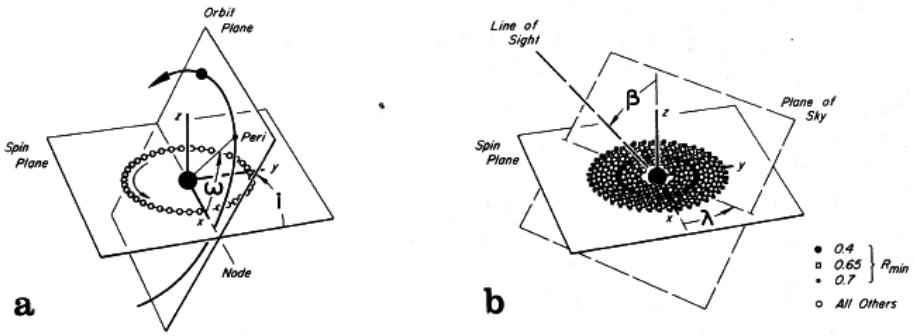

FIG. 6.—(*a*) Orbit geometry. (*b*) Viewing geometry.

Figure 1.1: Figure from Toomre & Toomre (1972) geometry: Without taking into account the internal structures of the galaxies, 16 parameters are required to define a galactic encounter between two disk galaxies and compare it to observations: the mass ratio (μ), disk orientations (i_1, ω_1) and (i_2, ω_2), the eccentricity of the orbit (e), the pericentric separation (r_{peri}), the length scale (L), the velocity scale (V), the center of mass position on the plane of the sky (X_m, Y_m), the center of mass velocity (V_c), the viewing angles ($\theta_x, \theta_y, \theta_z$) and the time of viewing (t).

1.2 Tidal stripping from rotating disk galaxy interactions

In Section 1.1, we discussed tidal stripping from progenitors which were low mass compared to their hosts and which were dominated by random internal motion. In contrast, in this Section we investigate tidal stripping for interacting *rotating* disk galaxies of comparable masses: we focus on disk interactions between dwarf galaxies ($10^8 < M_* < 7 \times 10^9$ $M_\odot$) with mass ratios lower than $\mu = 20:1$ (Chapter 4 and 5). Below we outline some of the background and theory to dynamically disentangle disk galaxy interactions. In particular, in Section 1.2.1, we discuss how the coincidence of disk motion within the interacting objects and their orbital properties can extend the tidal effects for interactions with similar mass ratios. This is quite unlike globular clusters where the orbital periods of central stars in the

progenitors (e.g. Pal 5) are much shorter ($\sim$ 1 Myr) than the orbital period of the progenitor about the host galaxy ($\sim$ 300 Myr for Pal 5). Additionally, we discuss similarities between these encounters and the suppressed stripping of stars on retrograde orbits from clusters (as mentioned in 1.1.1), as well as similarities between the encounters and the suppressed effect of the Galactic bar interacting with a stream on a retrograde as opposed to prograde orbit (as discussed in Section 1.1.2.3). We briefly discuss the dark matter potentials' affects on tidal tails stripped in disk galaxy interactions in Section 1.2.2, and we discuss degeneracies and gas in tidal interactions in Sections 1.2.3 and 1.2.4.

1.2.1 Effects of encounter geometry

To zeroth order you can describe galaxy interactions between two bodies as an impulsive kick occurring at their closest approach (pericenter, r_p) using the impulse approximation (Binney & Tremaine 1987), where the stars in the perturbed system remain strictly stationary during the encounter. However, the impulse approximation can not capture the orientation of the encounter or coupling between stars' orbital, interaction or encounter timescales, and misses the effect of having the perturber "co-orbit" with certain regions of the victim's disk, leading to a resonant behavior[5].

Toomre & Toomre (1972) demonstrated that many of the peculiar galaxies observed at the time could be understood as interacting disk galaxies at various orientations and stages of their interaction. Using massless rings of test particles surrounding a point mass galaxy, they showed that a perturber flying by at a certain distance (r_p), would distort a disk of test particles, particularly if the orbit of the perturber was prograde with respect to the disk spin. Through this mechanism, a plausible explanation was in place for forming

[5]Notice the similarity between this description and to the Galactic bar "sweeping" by certain parts of the Pal 5 stream described in Section 1.1.2.3.

bridges, leading and trailing tidal tails which provided techniques for observers to recognize signs hinting that a certain type of interaction had unfolded. Subsequent to the Toomre & Toomre (1972) work much intuition was built by modeling colliding galaxies self-consistently (e.g. Barnes 1988, Hernquist & Ostriker 1992) and through numerical experiments (Barnes & Hibbard 2009). D'Onghia et al. (2010) developed an analytical framework with various approximations to understand the scalings of tail-making, and interpret the response of rotating disks to gravitational tidal perturbations. They show that the "victim" disk galaxy is most distorted by an external perturber, if the orbital motion of the perturber is similar to the rotational disk spin of the victim. They define the parameter α to describe this:

$$\alpha = \frac{|\Omega|}{\Omega_{\rm orb}(b)} \tag{1.8}$$

where Ω is the internal angular frequency of the victim, $\Omega_{\rm orb}$ is the orbital angular frequency at the closest approach (e.g. impact parameter, b, for a straight line or pericentric separation, r_p, for a given encounter). As galactic encounters typically do not occur on circular orbits, this is a "quasi"-resonant effect as the orbital motion of the perturber changes as it moves past the victim and has the largest impact at pericenter. It is thus the similarity of the orbital spin of the perturber at pericenter as compared to the "victim" disk's spin that is the most important for determining magnitude of the perturbation in the interaction (D'Onghia et al. 2010). If the perturber is itself a disk, it too will be perturbed by the victim and the mass ratios (e.g. the tidal forces in place) will affect the magnitude of the distortions. The "quasi-resonant stripping" is a modification to the impulse approximation including the response of the stars orbiting within the "victim disk". The greatest effect is seen when $\alpha \sim 1$ (see Eq. 1.8) and the orientation of the encounter is prograde ($\Omega > 0$). For $\alpha \to 0$, this corresponds to a rapid flyby and the impulse approximation solution for the change in energy is recovered (D'Onghia et al. 2010). For retrograde orbits, the tidal response is suppressed as compared

to the impulse approximation. This is similar to the effect that retrograde orbits of stars are more likely to stay bound to progenitors in stellar stream stripping (Read et al. 2006 and Section 1.1.1) and to the retrograde bar having an insignificant effect on a stream if the motion with respect to the stream is retrograde (see Section 1.1.2.3). The "quasi-resonant stripping" formalism is less accurate for an encounter where the perturber is flying by slowly as more mass of the victim galaxy is captured by the perturber (see numerical experiments in D'Onghia et al. 2010). Interestingly in all cases of bound interactions, as the perturber returns to distort the "victim" further, the orbit will have decayed in both separation and velocity due to dynamical friction, and different regions of the "victim disk" can be affected at each encounter.

1.2.2 The dark matter potential

The first studies of the formation of tidal tails (e.g. Toomre & Toomre 1972) did not include the effect of the dark matter in which the stellar disks are embedded. It has since been shown that if the dark matter potential well of the "victim" is deeper, the tidal tails induced in an interaction are shorter and less prominent (Dubinski et al. 1999). This is due to the fact that the disk stars not only have a harder time escaping, but also get reabsorbed faster if the "victim" is more massive. Dubinski et al. (1999) showed that the shape (in addition to the mass ratio) of the potential has a strong effect on the kinematics and lengths of tidal tails, and that the escape velocity, v_e at the half-mass radius vs the disk circular velocity at that radius, v_c, provides a limit for tail making. Therefore, the extent of the disk within the dark matter halo plays an important role. Springel & White (1999) confirmed that the effective tidal response, $T_{\rm eff}$, defined as the fraction of disk material reaching more than 10 disk radii from the center of mass in an interaction, correlates with $\xi = \left(\frac{v_e}{v_c}\right)^2$ (a higher ξ yields lower tidal response) and that models with $\xi > 2.5$ should not be able to produce strong tails.

They could however produce long tidal tails in galaxies dominated by dark matter (their most extreme case was $\mu = 40 : 1$), granted that the halo spin parameter was large (yielding more extended disks). In Chapter 5 we address the effect of dark matter halos surrounding dwarf galaxies in their mutual interactions.

Interestingly, as the dark matter is thought to be on random orbits, roughly spherically distributed (see Chapter 2), more baryonic material than dark matter should be removed, fractionally, in a "quasi resonant" disk encounter. D'Onghia et al. (2009) described how this can explain the lack of luminous matter in e.g. dwarf spheroidals describing the morphological transition from a "disky" dwarf to a dwarf spheroidal. As "disky dwarfs" (which we investigate in Chapters 4 and 5) typically have dynamically hotter disks than more massive disk galaxies, the tidal features will be less thin than colder systems with same aspect ratios, as the stripped material will not all have the same initial velocity (e.g. Binney & Tremaine 2008).

1.2.3 Breaking degeneracies in galaxy interactions

While Toomre & Toomre (1972) already provided several demonstrations of different configurations and encounter geometries leading to various outcomes and signatures of galaxy interactions, it was clear that it would be a difficult task to translate observations into exact initial galaxy encounter parameters. Given the many free parameters of a galaxy encounter, it can seem like a hopeless procedure to disentangle their initial encounter geometry. Luckily, in a galaxy encounter, we do not need to explore all possible distribution functions, as in some sense the initial symmetry in the original galaxies are visible after the encounter (Barnes & Hibbard 2009). In Barnes & Hibbard (2009) they represent the mass of each galaxy with a spherical distribution of massive particles and embedded multiple disks of test particles in each of these spheres, only deciding which to display after running the simu-

lations of galaxy encounters (see also Chapter 5). In their work, they attempt to recover the initial parameters for 36 galaxy encounter simulations of $\mu = 1:1$ by matching their kinematics and morphology to HI data cubes simultaneously in different panels at various interaction stages, orientations and pericentric separations. Their work shows that matching both kinematics and morphology of tidal features simultaneously, can break degeneracies in the appearance of tidal features. Disks that were initially indistinguishable on the sky, but orientated differently in space (e.g. if their inclinations were rotated by 180°) will display distinguishable tidal features (Barnes & Hibbard 2009 fig 14), which we take advantage of in Chapter 5 when matching dwarf galaxy simulations to HI data of an observed encounter.

1.2.4 Gaseous and stellar tidal tails

As dwarfs and dwarf pairs have high gas to stellar ratios (e.g. Bradford et al. 2015, Stierwalt et al. 2015), studying their tidal features in gas is ideal. In this Dissertation we observationally investigate the gaseous distributions of dwarf galaxy interactions (Chapter 4). We focus on the dominant gaseous component: neutral hydrogen (HI), which emits photons at a wavelength of $\lambda \sim 21$ cm as the spin of the electron in the hydrogen atom flips from parallel to antiparallel with the proton's spin. However, we compare the observations to dissipationless simulations, where gas is not taken into account (Chapter 5). Barnes & Hernquist (1996) tested the effect of including gas (with the same density profile as the stellar components) to self-consistent galaxy merger simulations and found that the orbital decay and large scale tidal features were not much affected. Hence, as gravity acts similarly on the gas and the stars, adding gas should not have a large effect on the overall tidal features. However hydrodynamical effects such as gas lag and spiral structure will not be captured by dissipationless simulations. Additionally, an important caveat is that gaseous disks are often known to be more extended than stellar disks (Swaters et al. 2002) which would affect the fraction of

stripped gas vs stripped stars (see e.g. Bekki 2008, Besla et al. 2012).

1.3 Structure of Dissertation

In what follows we build on the understanding of dynamics described above, and explore how the morphology and kinematics of stellar streams and gaseous tidal tails can be used to investigate galactic parameters and histories of both our own Milky Way and external, interacting pairs of dwarf galaxies.

In Chapter 2 (published as Pearson et al. 2015), we use a combination of restricted three-body "streak-line" simulations and direct N-body simulations, combined with data of the Milky Way globular cluster, Pal 5, to demonstrate that with the morphology of the stream alone, we can distinguish between mildly triaxial potentials. We find that, in certain region of a triaxial potential, the stream "fans" out, providing a powerful technique of probing orbit distributions in galaxies.

In Chapter 3 (published as Pearson et al. 2017) we show how torques from the Milky Way's Galactic bar can produce gaps in the Palomar 5 stream, and equally as interesting we hypothesize a new method for constraining bar parameters as the gap size should sensitively depend on the torque exerted from the bar (e.g. its mass, pattern speed, and extent). We caution that it will be difficult to disentangle gaps produced by the bar for streams on prograde orbits (with respect to the Galactic disk spin) from gaps produced by subhalo encounters, and suggest that streams on retrograde orbits should be used for indirect detections of dark matter (see most recently: Price-Whelan & Bonaca 2018).

In Chapter 4 (published as Pearson et al. 2016) we investigate the gaseous distribution of 10 interacting dwarf galaxy pairs, attempting to understand their mutual tidal-preprocessing of gas at various interaction stages and in different environments. In particular, we investi-

gate the amount of mass in tidal features, the morphology of the features, and we conclude that a substantial amount of gas resides in tidal features and that the dwarfs appear to retain their gas (the tidal material will return to the systems) unless the dwarf pairs are accreted by a more massive galaxy.

In order to age-date, constrain encounter parameters and understand the timescales involved in cycling gas in dwarf-interactions, in Chapter 5 we present a detailed theoretical model matched to morphological and kinematic HI data of one particular dwarf pair from Chapter 4. This is the first galaxy encounter simulation match to data of an isolated interacting dwarf galaxy encounter, and we find that the gas remains extended for several billion years, which will affect the efficiency of gas stripping were the pair to be accreted by a more massive galaxy later.

We conclude in Chapter 6 and briefly discuss future work as extensions of this Dissertation.

Chapter 2

Tidal Stream Morphology as an Indicator of Dark Matter Halo Geometry: the Case of Palomar 5

2.1 Introduction

Simulations of large-scale structure formation suggest that all galaxies lie within triaxial dark matter halos (e.g., Bullock 2002). The Milky Way (MW) offers a unique perspective on this problem as it is the one galaxy not seen in projection and therefore the one galaxy where we can measure the true 3D shape and orientation of a dark matter halo. However, constraints from observations on the shape of the Milky Way's dark halo remain uncertain and inconsistent.

The distances, radial velocities, and positions of stars in the Sagittarius stream provide a rich data set to use to probe our dark matter halo. Law & Majewski (2010) (LM10) were the

This section contains text from an article published in the Astrophysical Journal (Pearson et al. 2015).

first to attempt modeling the MW including a fully triaxial dark matter halo using the data that were then available. Their best-fit halo model predicts an almost oblate dark matter configuration oriented perpendicular to the Galactic disk. However, concerns have been raised questioning the validity of the LM10 potential: i) Debattista et al. (2013) showed that the orientation of the halo in this model could not host a stable disk; ii) Ibata et al. (2013) suggested that it is possible to approximately reproduce the spatial and kinematic structure of the Sagittarius stream without introducing triaxiality to the dark matter halo component (although their paper does not include a quantitative assessment that their model fitted the data as well as the LM10 simulation); and iii) Belokurov et al. (2014) demonstrated that the LM10 model fits neither the extent nor the precession angle between successive apocenters in a newly found part of the Sagittarius stream. A solution to the first part of the problem was proposed by Vera-Ciro & Helmi (2013): by introducing a transition from an oblate halo at small radii to a triaxial LM10 halo on larger scales, a potential could be obtained that could host both the Sagittarius stream and the Galactic disk. However, there is not yet a model that successfully reproduces the full data set (i.e. including the more recent evidence for Sagittarius material extending out to Galactocentric distances of more than 100 kpc found by Belokurov et al. 2014), in its entirety. For this reason it is important to test any suggested potential form with other streams than just the Sagittarius stream.

In this Chapter, we look at the tidal stream originating from Palomar 5 (Pal 5), a globular cluster currently at the apocenter of its orbit, 23.6 kpc from the Sun (Dotter et al. 2011). Pal 5 is orbiting the MW at a much smaller radius than Sagittarius and thus serves as a probe of the shape of the MW in a different region of the Galaxy. Pal 5's tidal stream was first discovered by Odenkirchen et al. (2001) and was subsequently mapped over 22 degrees on the sky (Grillmair & Dionatos 2006) with a typical width of 0.7 degrees (Odenkirchen

See Gibbons et al. (2014) for an interesting discussion of what the distances to and angular positions of the apocenters *alone* might tell us about the radial density profile of the dark matter halo.

et al. 2003; Carlberg et al. 2012).

In what follows, we explore what the morphology of Pal 5's tidal tails can tell us about the gravitational potential of the MW by using a combination of restricted three-body models (Küpper et al. 2012) and N-body simulations. Our model streams are simulated in two different Milky-Way-like potentials consisting of a disk and bulge embedded within a dark matter halo that is either spherical or triaxial in shape. We show that in a LM10-like halo configuration, our simulated Pal5 streams cannot match the thin, "S"-shape and curved morphology of the observed stellar density: they are either too straight or exhibit a broad morphology which we dub *stream-fanning*. Thus the thin and curved morphology of Pal 5 alone has given us a fast and simple way to check if this particular potential form is realistic. The broader implication of this simple test is that the mere existence of many such thin streams at different distances and orientations around our Galaxy can rule out other classes of triaxial potentials.

In Section 2.2, we describe the methods used to simulate the morphology of Pal 5's tidal tails. In Section 2.3 we compare the streams produced in *streakline* models and N-body simulations to observed data within the two test-potentials. We first do a comparison to over-densities of Pal 5 stars from SDSS only, then include radial velocities of Pal 5 stars in the fit. In Section 2.4.1, we investigate further possible parameter variations, and we discuss possible origins of *stream-fanning* in Section 2.4.2. We conclude in Section 2.5.

2.2 Methods

In this work we compare two different trial galactic potentials having either a spherical or triaxial dark matter halo, which we introduce in Section 2.2.1. In Section 2.2.2 and 2.2.3, we describe how the most likely orbit within a given potential is found through a comparison of

streakline model streams with observational data. We then describe the N-body simulations used to illustrate our results in Section 2.2.4.

2.2.1 Form of the Galactic potential

In our *streakline* and N-body simulations, the potential of the MW is computed consisting of a disk and bulge embedded within a dark matter halo that is either spherical or triaxial in shape. We approximate the baryonic component of the MW using a Miyamoto & Nagai (1975) disk ($M_{disk} = 10^{11}\mathrm{M}_{\odot}$, $a = 6.5$ kpc, $b = 0.26$ kpc), and a Hernquist spheroid for the bulge ($M_{bulge} = 3.4 \times 10^{10}\mathrm{M}_{\odot}$ and $c = 0.7$ kpc) (Hernquist 1990). This parametrization of the Galactic disk and bulge was chosen for computational simplicity and is used widely in the literature. More realistic forms of disk and bulge have been proposed by, e.g., Dehnen & Binney (1998), however, our focus lies on the comparison of our models to the previous work of LM10. For the dark matter component we use two different halo potential forms:

1. *Triaxial dark matter halo*: following LM10, we parametrize the halo potential as

$$\Phi_{halo} = v_{halo}^2 \ln(C_1 x^2 + C_2 y^2 + C_3 xy + \frac{z^2}{q_z^2} + r_{halo}^2) \tag{2.1}$$

$$C_1 = \left(\frac{\cos^2\phi}{q_1^2} + \frac{\sin^2\phi}{q_2^2}\right) \tag{2.2}$$

$$C_2 = \left(\frac{\cos^2\phi}{q_2^2} + \frac{\sin^2\phi}{q_1^2}\right) \tag{2.3}$$

$$C_3 = 2\sin\phi\cos\phi\left(\frac{1}{q_1^2} - \frac{1}{q_2^2}\right) \tag{2.4}$$

where we use the exact same parameters for the triaxial dark matter halo as LM10. That is, the rotation angle of the x-axis around z from the Sun-Galactic center line is $\phi = 97$ deg, the ratios between where the equipotential contours intersect the x/y and z/y axes are q_1= 1.38, $q_z = 1.36$ respectively. $q_2 = 1.0$ by definition, $v_{halo} = 121.9$

km/s and $r_{halo} = 12.0$ kpc.

2. *Spherical dark matter halo*: we use the same potential form as above for the spherical halo potential (Equation 2.1), but now q_1= 1.0, q_2= 1.0 and q_z = 1.0. We set v_{halo} = 172.3 km/s and r_{halo} = 12.0 kpc to ensure v_{rot} = 220 km/s at R = 8.3 kpc.

The rotation curves of these two galactic potentials match the overall shape of observed MW rotation curves (cf. Sofue 2013; Irrgang et al. 2014). In this configuration, the Sun sits at $\vec{R}_{\odot} = (-8.3, 0, 0)$ kpc, with a velocity of $\vec{V}_{\odot} = (11.1, 258.1, 7.3)$ km/s (Gillessen et al. 2009, Schönrich 2012, Reid et al. 2014, Küpper et al. 2015).

2.2.2 The *Streakline* method

To create model streams along a given orbit in a specific potential, we use the *streakline* method outlined in Küpper et al. (2012), Lane et al. (2012), Bonaca et al. (2014) and Küpper et al. (2015), which is closely related to the methods used in Varghese et al. (2011) and Gibbons et al. (2014). Bonaca et al. (2014) demonstrated that the *streakline* method is a computationally efficient way of generating realistic streams that match the morphology of much more time-consuming full N-body models. *Streakline* models are restricted three-body models of tidal streams: the dissolution of a star cluster due to the tidal field of its host galaxy is approximated by a "star-cluster particle" orbiting within an analytic galaxy potential that releases test particles at a given time interval. The test particles are then integrated together with the cluster particle within the background potential. The test particles do not interact with each other, which makes the *streakline* method very fast. However, the gravitational attraction of the cluster particle on the released test particles is included, which was shown to be of importance for reproducing the morphology and length of streams from full N-body models (Küpper et al. 2012; Gibbons et al. 2014). For simplicity, the cluster particle is

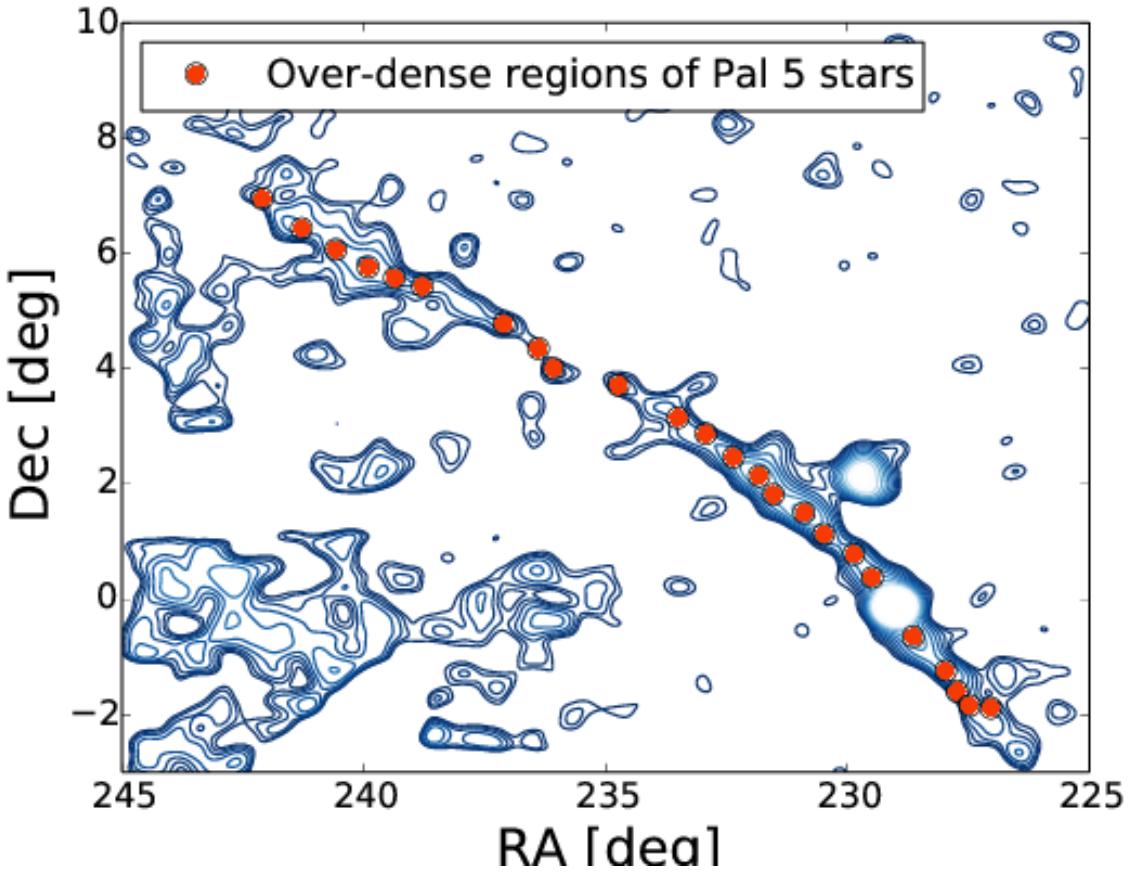

Figure 2.1: Matched-filter map of Pal 5-like stars from SDSS DR9 (blue contours). We used the over-dense regions marked as orange points to assess the likelihood of our Pal 5 *streakline* models (Balbinot et al. 2011, Küpper et al. 2015).

represented by a smoothed point mass with a smoothing length of 20 pc, which is of the order of Pal 5's half-light radius (Odenkirchen et al. 2003).

Our *streakline* model assumes that stars escape from the cluster at the tidal radius (King 1962),

$$r_t = \left(\frac{GM(t)}{\Omega^2 - \partial^2\Phi/\partial R^2} \right)^{\frac{1}{3}}, \tag{2.5}$$

at a constant rate. Here, $M(t)$ is the mass of the cluster at time t (the final, i.e. present-day, mass is $M = 15000 M_\odot$; Küpper et al. (2015)), Ω is the instantaneous angular velocity of the cluster with respect to the galactic center, Φ is the galactic potential, and R is the cluster's current galactocentric distance. To introduce some scatter into these idealized escape conditions, we apply a random Gaussian spatial offset with a width of $0.25 \times r_t$ around the Lagrangian points at the time of escape (Lane et al. 2012; Bonaca et al. 2014; Gibbons et al. 2014). The stars are given velocities matching the angular velocity of the cluster plus an additional random Gaussian velocity offset with a dispersion of 1 km/s, comparable to the velocity dispersion of the cluster. Furthermore, we assume that the cluster itself has a constant mass loss rate of 8 $M_\odot$ per Myr, which was chosen based on N-body simulations of the cluster (Küpper et al. 2015). However, we found that changing this mass loss rate has little to no effect on the results.

From the six phase-space coordinates that determine Pal 5's orbit, we fix the sky position (RA = 229.0°, Dec = -0.111°), the radial velocity (v_r = -58.7 km/s; Odenkirchen et al. 2002), and the distance (d = 23.6 kpc; Dotter et al. 2011). Hence, the only free parameters are the two proper motion components, which we vary in order to find the most likely orbit in each potential. For a given choice of phase-space coordinates, we integrate the orbit backwards for 6 Gyr and subsequently integrate it forward again while producing the *streakline* model. After releasing test particles uniformly in time from the Lagrange points and integrating

We explore the effect of varying the distance in Section 2.4.1.

them to the present day, we compare the test particle distribution to the observations and assess the likelihood of the respective model.

2.2.3 Comparison to observational data

For a given orbit within a specific potential, we compare the *streakline* models to 24 over-dense regions of color-selected Pal 5 stream stars shown in Figure 2.1 (Balbinot et al. 2011, Küpper et al. 2015). These regions were found through a *Difference-of-Gaussians* process, in which a matched-filter map of Pal 5 from SDSS data is smoothed with a small and a large Gaussian kernel, and the two maps are subtracted from each other. On the residuals map an extended-source finder algorithm like SExtractor (Bertin & Arnouts 1996) is run (see Koposov et al. 2008 and Küpper et al. 2015 for details). The locations shown in Figure 2.1 give the barycenters of extended, over-dense regions, which stood out by at least 3σ above the random fluctuations in the residuals map. These over-densities give the regions with the highest local probability of finding Pal 5 stars, and hence we require our models to go through these points.

Our comparison of the models to the observed over-densities is based on the framework developed in Hogg et al. (2010) and Hogg (2012), and applied to Pal 5 in Küpper et al. (2015). We use a likelihood of the form:

$$\mathcal{L}_{\rm OD} = \prod^{N_{OD}} \frac{1}{N_{\rm model}} \sum_{i}^{N_{\rm model}} \left(\frac{1}{\sqrt{2\pi\Delta d^2}} \exp\left[-\frac{1}{2} \left(\frac{d_{ij}^2}{\Delta d^2} \right) \right] + \Delta \right) \tag{2.6}$$

Here $N_{\rm OD}$ is the number of over-densities, d_{ij} is the distance from each model point to the j-th over-density, Δd is the uncertainties in the barycenter positions of the over-densities, determined from the extended-source finding algorithm (SExtractor) and Δ is a numerical constant set to $\Delta = 10^{-5}$. This constant allows each over-dense region to not be a part of

the stream by limiting its contribution to the likelihood to a minimum value. The maximum likelihood *streakline* model maximizes the density of model points around the observed over-densities from SDSS.

Here we do not assume or imply anything about the origin of these over-densities. However, it has been shown that over-densities in tidal tails can be produced by epicyclic motion of stars evaporating from star clusters (Küpper et al. 2010). This may indeed be the origin of some of the over-densities closer to the cluster itself; for example, Mastrobuono-Battisti et al. (2012) have shown that tidal tails of Pal 5-like clusters in fact show significant over-densities. Other possible explanations for inhomogeneities in tidal streams are variations in the mass loss rate, perturbations by dark matter subhalos, or variations in the depth of the observed data (e.g., Ngan & Carlberg 2014). However, the primary purpose of our likelihood function is to assess the alignment of our generated models with the observed streams. An alternative approach would be to instead measure the smallest distance of each point from the centroid of the stream, but this effectively assumes that the density along the stream is constant. For a detailed analysis of the differences between these two different methods see Küpper et al. (2015).

We also make use of kinematic data from the literature. Odenkirchen et al. (2009) measured 17 radial velocities of stars in Pal 5's tidal streams. When these are included in the assessment of the likelihoods, the full likelihood is:

$$\mathcal{L} = \mathcal{L}_{\mathrm{OD}} \times \mathcal{L}_{v_r} \tag{2.7}$$

$$\ln \mathcal{L} = \ln \mathcal{L}_{\mathrm{OD}} + \ln \mathcal{L}_{v_r} \tag{2.8}$$

where $\ln \mathcal{L}$ is the log-likelihood (LL) and $\mathcal{L}_{v_r}$ has the same form as Equation 2.6, but includes a comparison between the radial velocities of our models with the 17 radial velocities observed

for Pal 5.

We have fixed all potential parameters in both potentials, and can thus compare the likelihoods between the two potential forms by first using the over-densities only (Equation 2.6) and then using both over-densities and radial velocities (Equation 2.8).

2.2.4 *N*-body simulations

We construct N-body model streams of Pal 5 by using the collisional N-body code NBODY6 (Aarseth 1999, 2003). NBODY6 is GPU-enabled, which allows us to compute realistic Pal 5 model streams on a star-by-star basis over several Gyr within a day (Nitadori & Aarseth 2012).

To set up the initial cluster conditions for Pal 5, we use the publicly available code MCLUSTER (Küpper et al. 2011). The initial number of stars is set to $N = 65536$ with stellar masses of $0.4\,M_\odot$, following a Plummer density profile (Plummer 1911). We fix the radial velocity, present-day sky position and present-day distance of Pal 5 to the observationally constrained values specified in Section 2.2.2. We determine the two proper motion components of the cluster by exploring the *streakline* model streams described in Section 2.2.2 and 2.2.3. For each setup, we ran a number of N-body models with initial half-mass radii in the range 10-20 pc for 6 Gyr, and picked the model with a final cluster mass close to Pal 5's present-day mass of about $15{,}000\,M_\odot$ (Küpper et al. 2015). These models will be discussed in the following Section.

https://github.com/ahwkuepper/mcluster

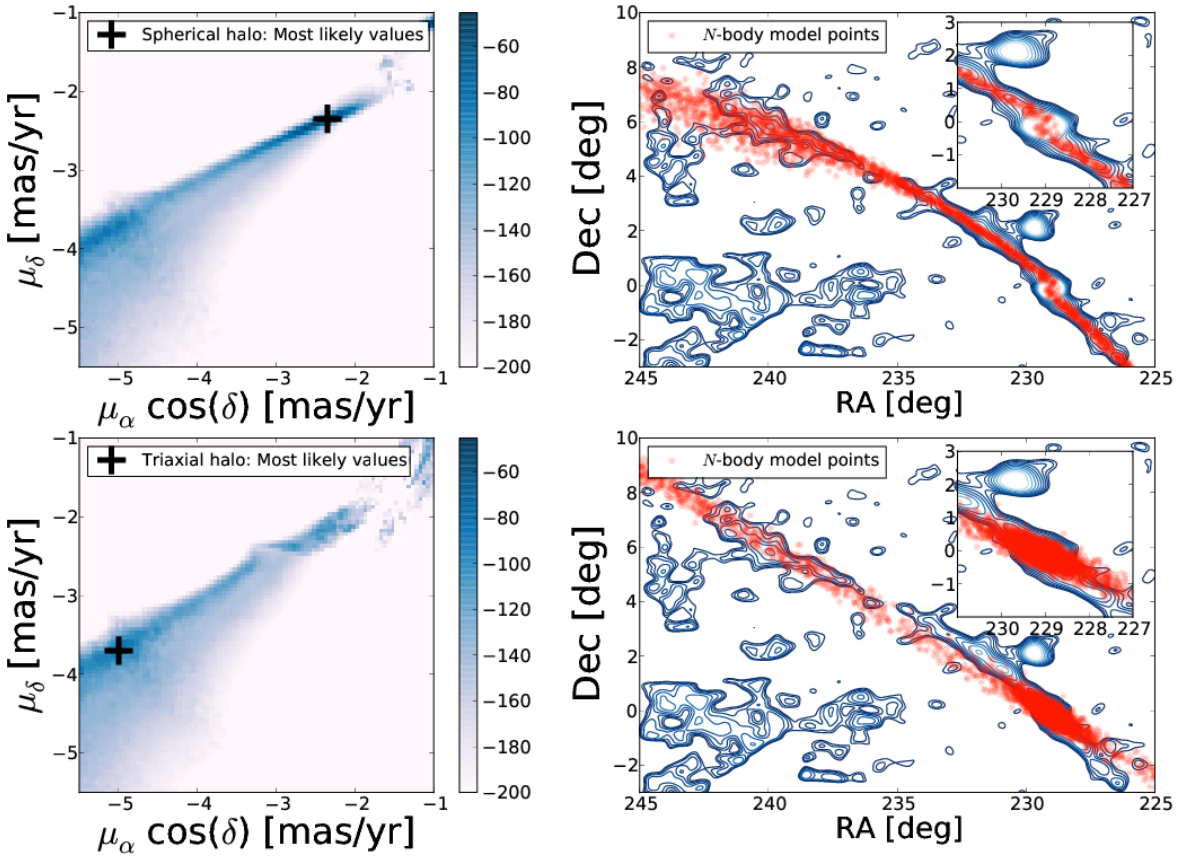

Figure 2.2: Left panels: log-likelihood value (color bar) of various proper motion configurations in the spherical potential (top) and triaxial LM10 potential (bottom) computed from *streakline* models using Equation 2.6. Right panels: NBODY6 model points (orange) of the most likely proper motion configuration in the spherical potential (top: (μ_δ, $\mu_\alpha$cos(δ)) = (-2.35, -2.35) mas yr^{-1}) and triaxial LM10 potential (bottom: (μ_δ, $\mu_\alpha$cos(δ)) = (-3.7,-5.0) mas yr^{-1}), over-plotted on SDSS density contours (blue). The *streakline* model in the triaxial LM10 potential (LL = -82) yields a much lower log-likelihood, than the spherical case (LL = -45).

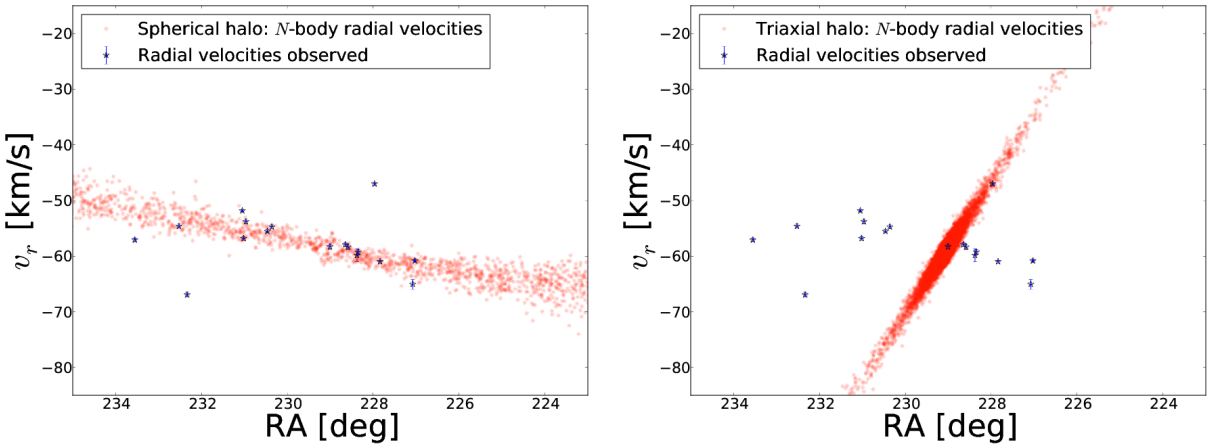

Figure 2.3: Line-of-sight velocities of NBODY6 model points (orange) along the stream from the most likely proper motion configuration in the spherical potential (left: $(\mu_\delta,\ \mu_\alpha\cos(\delta))$ = (-2.35 , -2.35) mas yr^{-1}) and the triaxial LM10 potential (right: $(\mu_\delta,\ \mu_\alpha\cos(\delta)$ = (-3.7, -5.0) mas yr^{-1}), plotted with the observed line-of-sight velocities (blue) from Odenkirchen et al. (2009).

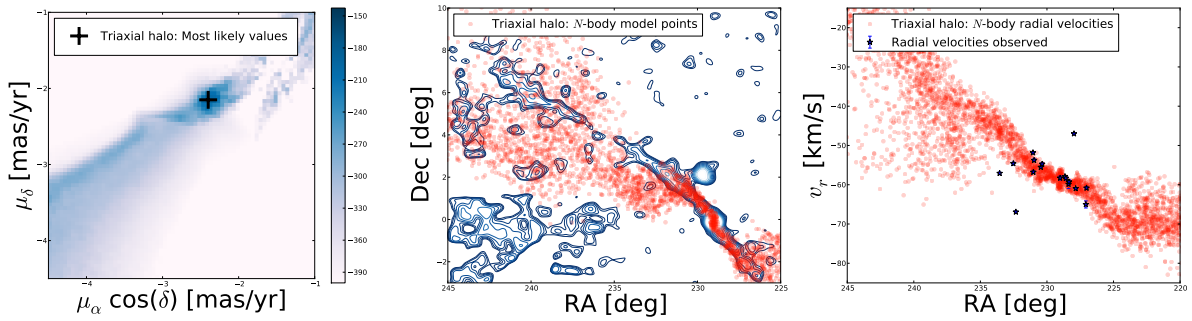

Figure 2.4: **Left panel**: log-likelihood value (color bar) of various proper motion configurations in the triaxial LM10 potential computed from *streakline* models with an integration time of 6 Gyr. Distance, radial velocity and position were fixed. The log-likelihoods are calculated using Equation 2.8. **Middle panel**: NBODY6 model points (orange) of the most likely proper motion configuration ($(\mu_\delta,\ \mu_\alpha\cos(\delta))$ = (-2.15, -2.4) mas yr^{-1}), over-plotted on SDSS density contours (blue). **Right panel**: Line-of-sight velocities of NBODY6 model points (orange), plotted with the observed line-of-sight velocities (blue) from Odenkirchen et al. 2009. The line-of-sight velocities of the N-body model points trace the observed gradient.

2.3 Results

Using the procedure outlined in Section 2.2, we examine the morphology of Pal 5 in the spherical and the triaxial LM10 halo potentials. We first run *streakline* models over a grid of reasonable proper motions in each potential for 6 Gyr, where we assess our likelihoods by comparing to over-densities in Pal 5 only (Equation 2.6). The results from this analysis are shown in the two left panels of Figure 2.2.

We find that the maximum likelihood cluster properties in the spherical and triaxial cases correspond to very different proper motions, when we calculate the likelihood from Equation 2.6: (μ_δ, $\mu_\alpha \cos(\delta)$) = (-2.35, -2.35) and (-3.7,- 5.0) mas yr^{-1}, respectively. These give transverse velocities of v_{tan} = 123 km/s (spherical) and v_{tan} = 449 km/s (triaxial) in the Galactic rest frame. Moreover, the LL for the most likely proper motions in the spherical case (LL = -45) is much more strongly peaked with a value considerably higher than in the triaxial case (LL = -82).

We visualize these results with N-body simulations evolving along the most likely orbit in the spherical and triaxial LM10 potentials shown in the right column of Figure 2.2. The N-body particles are over-plotted on the density contours of color-selected Pal 5 member stars from SDSS (blue). It is evident that the model stream in the LM10 potential does not fit the data well (bottom right). For this particular model the cluster is moving very fast, v_{tan} = 449 km/s, and is on a highly eccentric orbit. It has recently been tidally shocked and has lost a substantial amount of mass, which can be seen as a dense cloud surrounding the cluster. It clearly does not follow the observed "S"-shape (see zoom in of cluster center), nor the overall curvy morphology of the tails. Instead, the best fit model appears more like a straight line through the data points, which explains why the LL is much lower.

Figure 2.3 shows a comparison of the simulated model streams with the line-of-sight

velocities (Odenkirchen et al. 2009). The left panel shows the spherical model points, which fit the observed velocities very well even though the proper motion was chosen to match morphology alone. However, the same is not true for the triaxial LM10 case where there is a much stronger velocity gradient in opposite sense to that observed.

Motivated by the discrepancy in velocities in the triaxial case, we repeat the experiment of finding the most likely configuration of proper motions while now also comparing the *streakline* model streams to observed radial velocities from Odenkirchen et al. (2009) (Equation 2.8). In the spherical case the most likely *streakline* model yields the same values for the two proper motion components as found in Figure 2.2.

The left panel of Figure 2.4 shows the results of the parameter space search for the triaxial case. A large discrepancy is still found between the values of the LL in the spherical case (LL = -124) and triaxial case (LL= -180) when we include the radial velocities to our assessment of the likelihood (Equation 2.8). The right panel of Figure 2.4 shows that an N-body simulation of the most likely configuration of proper motions in the LM10 potential (where $(\mu_\delta, \mu_\alpha \cos(\delta)) = (-2.15, -2.4)$ mas yr^{-1}) yields a significantly better fit to the gradient of the line-of-sight velocities and $v_{tan} = 116$ km/s. However, the middle panel of Figure 2.4 demonstrates that the morphology of Pal 5's tidal tails is a poor match to the density contours of SDSS. This explains the difference in the LL between the spherical and triaxial case: the stream appears to "fan" out as the debris moves away from Pal 5. Moreover, this *stream-fanning* explains why this particular proper motion configuration was strongly disfavored when considering morphology alone.

In summary, in the spherical potential, model streams can easily be found that match the morphology of the Pal 5 stream and these coincidentally fit the observed line-of-sight velocities. In contrast, the best fit model streams to the morphology in the triaxial potential are much poorer, have a higher transverse velocity (in the following referred to as "*high-velocity*"

models), and are inconsistent with observed line-of-sight velocities. Model streams in the triaxial potential that match the line-of-sight velocities have similar proper motions to the spherical case, but have *fanned* density distributions that are inconsistent with observations (referred to as *stream-fanning* models).

However, it is important to note that even if we didn't have the 17 radial velocities along the Pal 5 stream from Odenkirchen et al. (2009), we would still have concluded (from the large discrepancy in LL) that the much simpler spherical halo yields better fits to the SDSS data.

2.4 Discussion

2.4.1 Exploring the parameter space further

In this Section we test whether any unexplored dimensions of parameter space could change the results of Section 2.3:

1. **Surface density**: we have assumed that all parts of our model streams would be observable, whereas in reality the observations could be showing us only the densest parts of the stream. For example, the *fanned* parts of the streams might not be observable in the SDSS density map due to foreground/background contamination.

2. **Integration time**: in some cases the extent of our model streams do not span over the full extent of the observations. For example, if the *fanned* parts of the streams are excluded in our model streams, the densest parts could look like thin streams, however for our original choice of a 6 Gyr integration time the model streams are too short to trace the extent of the observations. A longer integration time might lead to longer model streams.

3. **Cluster distance**: as we observe the streams in projection, the apparent curvature might change if Pal 5's present-day distance was varied. For example, the preference of the "*high-velocity*" models in the triaxial case leads to a lack of curvature in these model streams due to the proximity to perigalacticon of the stream at this point in phase space.

To address these three concerns we ran one additional grid of *streakline* models in the triaxial LM10 potential, where we explored these three dimensions in addition to allowing proper motion to vary: (1) we applied density cuts based on the surface density around each *streakline* model point, calculated using a Gaussian density kernel with a width of 1 degree, where we included 100%, 75%, 50% and 25% of the most dense regions of the streams, (2) we ran the *streakline* models for seven different integration times (4, 5, 6, 7, 8, 9 and 10 Gyr), and (3) we tested various distances (22.6, 23.1, 23.6, 24.1 and 24.6 kpc) to Pal 5 based on the observational uncertainties (Dotter et al. 2011; Dotter private communication).

For all combinations of these parameters, the highest likelihood proper motion configuration was close to the "*high-velocity*" models. However, the LL of the secondary, *stream-fanning* peak was more prominent when density cuts were applied. Figure 2.5 illustrates the success and limitation of the *stream-fanning* model by plotting the most likely model configuration ($(\mu_\delta, \mu_\alpha \cos(\delta))$ = (-2.25,-2.5) mas yr^{-1}, 50% density cut, t = 9 Gyr, d = 23.1 kpc, LL = -83) from the newly explored grid. It is evident that the dense parts of the streams provide a better fit to the SDSS density map. However, this configuration of proper motions does not yield a long, thin stream that could fit the extent of the observational coverage from the SDSS density map, even when the *fanned* parts of the streams are excluded. Hence, the *stream-fanning* peak model still fails to produce a stream that matches the observational data.

Figure 2.6 summarizes the remaining exploration over integration time and various dis-

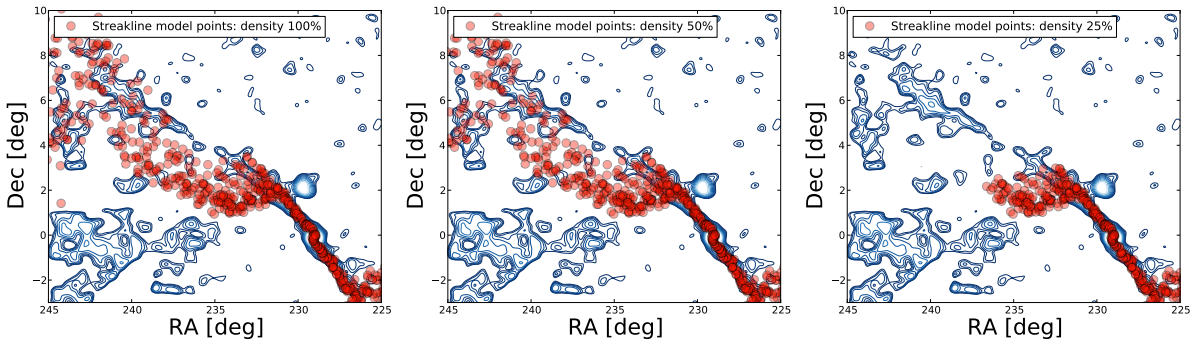

Figure 2.5: *Streakline* model points (orange) for three different surface density cuts (100%, 50% and 25%) for the most likely *stream-fanning* model over-plotted on SDSS density contours (blue). The most likely *stream-fanning* model does not yield a long, thin stream that fits the SDSS density map.

tances. The LL of the most likely *streakline* model is plotted as a function of distance for both the spherical potential and LM10 potential for various integration times. There are no significant changes in the values of the likelihoods with distance. Moreover, it is clear that the stream models in the spherical potential yield much higher values for the likelihoods.

Other parameters that remain unexplored are the assumed density profile of our cluster (we used a smoothed point-mass for the cluster particle in the *streakline* models) and exploring different velocity properties of the ejected stars. As we are mainly concerned about the morphology of the streams on large scales, where the stars' motions are dominated by the gravitational potential of the galaxy, and since we are mainly interested in the coldest part of the stream, which are given through the over-densities and produced by low-velocity escapers, we do not explore these parameters here.

Conclusively, these new explorations confirm our findings from Section 2.3: the morphology of Pal 5's tidal tails cannot be reproduced in the triaxial LM10 potential.

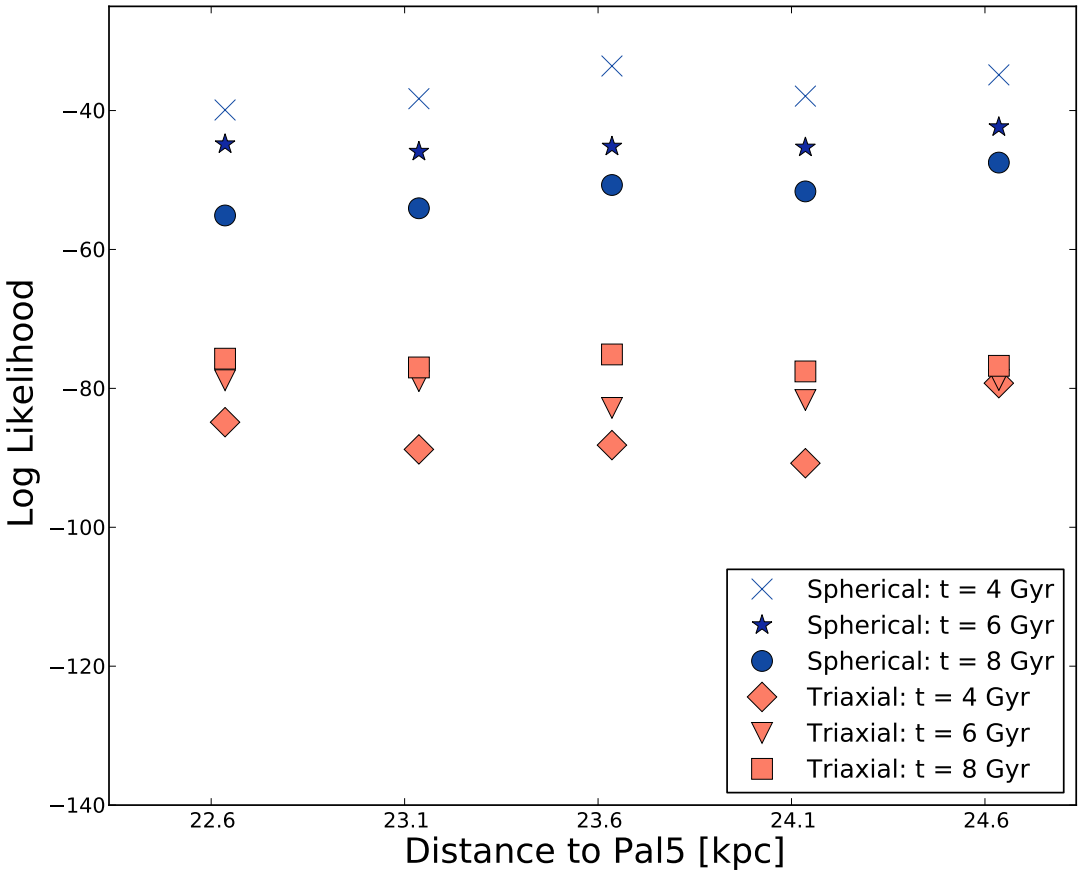

Figure 2.6: Log-likelihoods (Equation 2.6) of the most likely proper motion configurations for the spherical potential (blue) and triaxial LM10 potential (red) for various distances and integration times. The spherical potential yields much higher likelihoods in all cases.

2.4.2 Discussion of *stream-fanning*

As we have shown, it is not possible to produce a thin and curved stream like Pal 5 in a LM10 potential configuration. The streams are either too straight as the cluster is moving at a very high velocity, or, as the cluster velocity is reduced and the stream gets more curvy, it starts to *fan* out. In this Section, we discuss some tests we have done to provide more information about the process.

We first check the eccentricity of the orbit. In the triaxial case, Pal 5 could simply be on a significantly more eccentric orbit, which could make its stream appear more as a cloud than a stream (see e.g. Johnston et al. 2008). However, it is important to note that the orbital parameters such as eccentricity (e) and apocenter distance (R_{apo}) of the *stream-fanning* orbit shown in Figure 2.4 ($e = 0.34$, $R_{apo} = 18.6$ kpc) are very similar to the parameters for the spherical model stream's orbit shown in the top panel of Figure 2.2 ($e = 0.39$, $R_{apo} = 19.4$ kpc). Here eccentricity is defined as: $e = \frac{R_{apo}-R_{peri}}{R_{apo}+R_{peri}}$.

We next investigate the orbital classes of the *stream-fanning* model orbits to see whether these orbits are loop or box orbits. Regular loop orbits preserve a sense of rotation about the long or short axis of the potential, whereas box orbits may approach close to the center of the potential and have (on average) smaller pericenters, both of which would affect the disruption of the cluster and subsequent evolution of the debris.

To explore the orbits around the *stream-fanning* region in LM10, we investigate a grid from μ_δ -2.0 to $-2.3\,\mathrm{mas\,yr^{-1}}$ and $\mu_\alpha\cos(\delta)$: -2.3 to $-2.55\,\mathrm{mas\,yr^{-1}}$ (see left panel of Figure 2.4) with step sizes of 0.05 mas yr^{-1}, while fixing v_r = -58.7 km/s, d = 23.6 kpc and t = 6 Gyr. The streams from these initial conditions were all *fanned*. These orbits have v_{tan} = 100 – 137 km/s. To determine the orbital class of each orbit from the investigated grid, we check for a sign change in the angular momentum about any of the coordinate axes. We

find that all orbits in the *stream-fanning* region preserve the sign of their angular momenta which suggests they are on loop orbits. An additional test was made by integrating all the final cluster particle positions in the *fanned* tails from Figure 2.4 backwards in LM10 for 6 Gyr. All of these particles were also on loop orbits.

Another possibility is that the debris is *fanned* in LM10 due to Pal 5 and its debris being on chaotic orbits. That is, if Pal 5 was on a chaotic orbit, the orbits of debris stars could diverge significantly from the cluster's trajectory (an example of this was shown in Figure 11 of Fardal et al. (2015a)). To check if the *stream-fanning* of Pal 5 in LM10 is due to chaos, we measure the Lyapunov spectrum (e.g. Froeschlé et al. 1997; Skokos 2010) of the cluster orbit for each orbit in the *stream-fanning* grid. We use the maximum Lyapunov exponent, $\lambda_{\rm max}$, for an orbit to ask whether it is chaotic over a timescale comparable to the interaction time of the cluster with the host potential. We do this by measuring the Lyapunov time:

$$t_{\rm lyap} = \frac{1}{\lambda_{\rm max}} \tag{2.9}$$

We find that some orbits are stochastic, but have Lyapunov times $\gtrsim$ 20 Gyr (e.g., many times the integration time of any of the stream models above).

Finally, we attempt to compute the Hessian of the Hamiltonian for this potential in action-space, evaluated at the orbit of the cluster. For a thin stream to form, the Hessian should be dominated by a single eigenvalue (see, e.g., Bovy 2014; Sanders & Binney 2013), however since the fanned debris is instead spread over two dimensions, we aim to check whether the Hessian along Pal 5's orbit is instead dominated by two eigenvalues of comparable magnitude. To convert from phase-space to action-angle coordinates, we use the algorithm and code from Sanders & Binney (2014). We find that for and around the stream-fanning orbit of Pal 5, action-angle solutions cannot be found. This could be an indication

of chaos, but the long Lyapunov times indicate that perhaps a different mechanism is at play. When investigating the time variability of the "toy actions" — which, in the method of Sanders & Binney (2014) are modeled as a Fourier series expansion in a combination of the target actions, generating function, and toy angles — we find that there are many prominent "spikes" that correspond to the orbit passing through the midplane of the disk potential. The transformation to action-angle coordinates is failing due to the non-adiabatic forcing of the disk potential, however it is unclear whether this is a failure of the method or because the disk potential is destabilizing the orbit itself and making it more irregular (where actions do not exist). Thus, we are unable to compute the Hessian.

From our preliminary investigation, we conclude that the Pal 5 stream in LM10 does not appear to be *fanned* due to Pal 5 being on an orbit that takes it closer to the Galactic center either due to high eccentricity or box orbits, nor due to Pal 5 being on a chaotic orbit in LM10. We additionally note that we have tried and failed to use the machinery of Sanders & Binney (2014) to compute actions and angles for the stream-fanning orbit. Thus, the origin of *stream-fanning* remains uncertain. We are currently studying this phenomenon and postpone a more thorough exploration of its origin to our forthcoming work (Price-Whelan et al., in prep).

2.5 Conclusion

In this paper we used the thin and curved morphology of the Pal 5 stream alone (without the need for additional dimensions of information) to rule out the triaxial shape of the Galactic halo potential as suggested by Law & Majewski (2010). That the Galactic halo potential is not of the form suggested by Law & Majewski (2010) is not very surprising or new, as the LM10 potential has been pointed out to have several issues (see Section 2.1). However, we

found that models evolved along Pal 5-like orbits in this particular triaxial potential generally exhibited an unusual morphological signature - which we dubbed *stream-fanning*.

There are several examples already in the literature where morphology alone has been used to rule out certain forms of the Galactic potential. For example: the degree of alignment of the tails from Sagittarius along a single great circle was used to discuss how far from spherical the Galaxy's potential might be (Ibata et al. 2001; Johnston et al. 2005; Fellhauer et al. 2006); Lux et al. (2012) showed that the path of the 45 degree long stream associated with the globular cluster NGC 5466 was incompatible with spherical or prolate halo models of a variety of parametric forms; and (as mentioned in the introduction) the precession angle between successive apocenters traced by Sagittarius' debris has been interpreted as an indicator of the radial density profile of the dark matter halo (Belokurov et al. 2014; Gibbons et al. 2014).

The discovery of *stream-fanning* as a phenomenon sensitive to the triaxiality of the mass distribution adds a new approach to this toolkit of potential measures. We already know of many other thin streams at different radii and orbiting with different orientations throughout the Milky Way that could be investigated using this new approach (e.g., NGC 5466 (Grillmair & Johnson 2006), GD-1 (Grillmair & Dionatos 2006), Orphan (Belokurov et al. 2007, Casey et al. 2013), Acheron, Cocytos, Lethe, Styx (Grillmair 2009), Triagulum (Bonaca et al. 2012), Ophiuchus (Bernard et al. 2014)), and fainter streams are likely to be discovered in the future. Mapping these even more distant structures in velocity can only be more challenging. While the origin of *stream-fanning* is still under investigation (Price-Whelan et al., in prep), this first study of Pal 5 indicates the promise of using the *absence* of stream fanning in observed streams as a means to rule out classes of potentials. Collectively, the existence and location of these thin streams should provide broad but powerful constraints on the shape of the MW potential on large scales.

Acknowledgments

We thank the referee for a very detailed report, which helped to improve the quality of the paper significantly. KVJ thanks Hanni Lux for the initial collaborative work that led to this project. This work was supported in part by the National Science Foundation under Grant No. AST-1312196. AHWK acknowledges support from NASA through Hubble Fellowship grant HST-HF-51323.01-A awarded by the Space Telescope Institute, which is operated by the Association of Universities for Research in Astronomy, Inc., for NASA, under contract NAS 5-26555. APW is supported by a National Science Foundation Graduate Research Fellowship under Grant No. 11-44155. This research made use of Astropy, a community-developed core `Python` package for Astronomy (Astropy Collaboration et al. 2013).

Chapter 3

Gaps and length asymmetry in the stellar stream Palomar 5 as effects of Galactic bar rotation.

3.1 Introduction

The Pal 5 stream has received much attention since its initial discovery (Odenkirchen et al. 2001) in the Sloan Digital Sky Survey: SDSS (York et al. 2000). The SDSS photometric density maps of the stream, combined with subsequent kinematic measurements for both the cluster (Odenkirchen et al. 2002; Fritz & Kallivayalil 2015; Dotter et al. 2011) and stream stars (Odenkirchen et al. 2009; Kuzma et al. 2015), have enabled precise dynamical modeling of the density distribution along the Pal 5 stream to constrain the shape and radial profile of the mass distribution of the Milky Way (Küpper et al. 2015; Bovy et al. 2016).

As seen by the SDSS and other northern follow-up (Ibata et al. 2016), the trailing arm

This section contains text from an article published in Nature Astronomy (Pearson et al. 2017).

extends ≈15° before fading into the background. The density structure of the trailing arm is not smooth: apparent density fluctuations along the trailing arm could indicate recent interactions with dark matter subhalos (Yoon et al. 2011; Carlberg et al. 2012; Erkal et al. 2017; Bovy et al. 2017), but it is still debated whether they arise from observational or dynamical effects (Thomas et al. 2016).

Survey footprints have until recently limited exploration of the leading arm. Previous simulations predict leading and trailing arms with similar angular extents at Pal 5's present day position (Dehnen et al. 2004; Pearson et al. 2015; Küpper et al. 2015). In contrast, recently-released photometric catalogs from the Pan-STARRS 1 survey: PS1 (Chambers et al. 2016) which enhance the southern coverage of the stream (Bernard et al. 2016), show that the leading arm only extends ≈8° from the cluster center before abruptly ending (see matched filter density map in Figure 3.2, left panel). It is unlikely that this apparent truncation is caused by observational selection effects because the stream extension is not seen in nearer or farther distance bins (Bernard et al. 2016). What has cut off the leading arm of Pal 5?

Most previous studies have modeled the evolution of Pal 5 in an analytic, static Milky Way potential consisting of a bulge, disk, and dark matter halo. However, recent work has demonstrated that inlcuding a time-dependent, triaxial bar can greatly affect the morphologies of streams (Hattori et al. 2016; Price-Whelan et al. 2016b) and could create density differences between leading and trailing arm of Pal 5 (Erkal et al. 2017), even though Pal 5's perigalacticon (≈7–8 kpc) is far from the supposed extent of the bar (≈4 kpc; Wegg & Gerhard 2013). Motivated by these theoretical and observational findings, in this Article we further explore the effect of a rotating Galactic bar on the morphology of the Pal 5 stream.

3.2 Methods

Potential

We use a three-component mass model to represent the gravitational field of the Milky Way with disk, halo, and bar components as shown in the left panel of Figure 3.1. In detail, we use a Miyamoto-Nagai disk (Miyamoto & Nagai 1975) and a flattened Navarro-Frenk-White profile for the halo (Navarro et al. 1996). Expressed as gravitational potentials, the disk and halo models are parametrized as:

$$\Phi_{\rm disk}(R,z) = -\frac{G\,M_{\rm disk}}{\sqrt{R^2+\left(a_{\rm disk}+\sqrt{z^2+b_{\rm disk}^2}\right)^2}} \tag{3.1}$$

$$\Phi_{\rm halo}(R,z) = -\frac{G\,M_{\rm halo}}{r_{\rm halo}}\,\frac{\ln(u+1)}{u} \tag{3.2}$$

where R is the cylindrical radius, z is the standard Cartesian coordinate, and

$$u = \frac{\sqrt{R^2+z^2/q_{\rm halo}^2}}{r_{\rm halo}} \quad . \tag{3.3}$$

All other variables are parameters set to values described in Table 3.1. The bar potential is a low-order basis-function expansion (BFE) representation of a triaxial, exponential density profile (Wang et al. 2012; Price-Whelan et al. 2016b) given by

$$\rho_{\rm bar} = \rho_0\left[\exp\left(-r_1^2/2\right)+r_2^{-1.85}\,\exp(-r_2)\right] \tag{3.4}$$

$$r_1 = \left[\left((x/x_0)^2+(y/y_0)^2\right)^2+(z/z_0)^4\right]^{1/4} \tag{3.5}$$

$$r_2 = \left[\frac{q^2\,(x^2+y^2)+z^2}{z_0^2}\right]^{1/2} \tag{3.6}$$

Table 3.1: Parameters for the simulations.

name	value
$M_{\rm halo}$	5×10^{11} M$_\odot$
$r_{\rm halo}$	18 kpc
$q_{\rm halo}$	0.94
$M_{\rm disk}$	6×10^{10} M$_\odot$
$R_{\rm disk}$	3 kpc
$z_{\rm disk}$	280 pc
$M_{\rm bar}$	10^{10} M$_\odot$, Portail et al. 2015
$r_{\rm bar}$	1.1 kpc
α	27 deg
Ω_b	*varied*
Pal 5 (RA, Dec)	$(229, -0.124)^\circ$, Odenkirchen et al. 2002
v_r	-58.7 km s^{-1}, Bovy et al. 2016
d	22.9 kpc
$(\mu_\alpha cos\delta, \mu_\delta)$	(-2.296,-2.257) mas yr^{-1}, Fritz & Kallivayalil 2015

with scale-lengths fixed to $x_0 = 1.49$ kpc, $y_0 = 0.58$ kpc, $z_0 = 0.4$ kpc, and $q = 0.6$ (Dwek et al. 1995; Wang et al. 2012). Following previous work, we use the "self-consistent field" BFE formalism (SCF: Hernquist & Ostriker 1992). The physical scales of the bar are reflected in the scale-mass and scale-radius assumed in the BFE (see Table 1), with the remaining radial and angular behavior of the bar in Equation 3.4, 3.5 and 3.6 captured by including expansion terms up to n=2 and l=6. We do not include a spherically symmetric Galactic bulge because the mass in this component is likely small compared to the bar ($M_{\rm bar} = 10^{10}$ M$_\odot$ Portail et al. 2015).

The bar component rotates with frequency vector anti-aligned with the z coordinate axis $\mathbf{\Omega} = -\Omega_b\,\hat{z}$ (i.e. in the direction of Galactic rotation) and has a present day (t=0) angular offset from the Galactic x-axis in the direction of rotation, $\alpha = 27^\circ$, which is consistent with observations. We set the disk and halo potential parameters following previous studies (Bovy 2015; Bovy et al. 2016), but remove mass from the disk to include the bar component. We have checked that the cylindrically-averaged rotation curve and surface density profiles

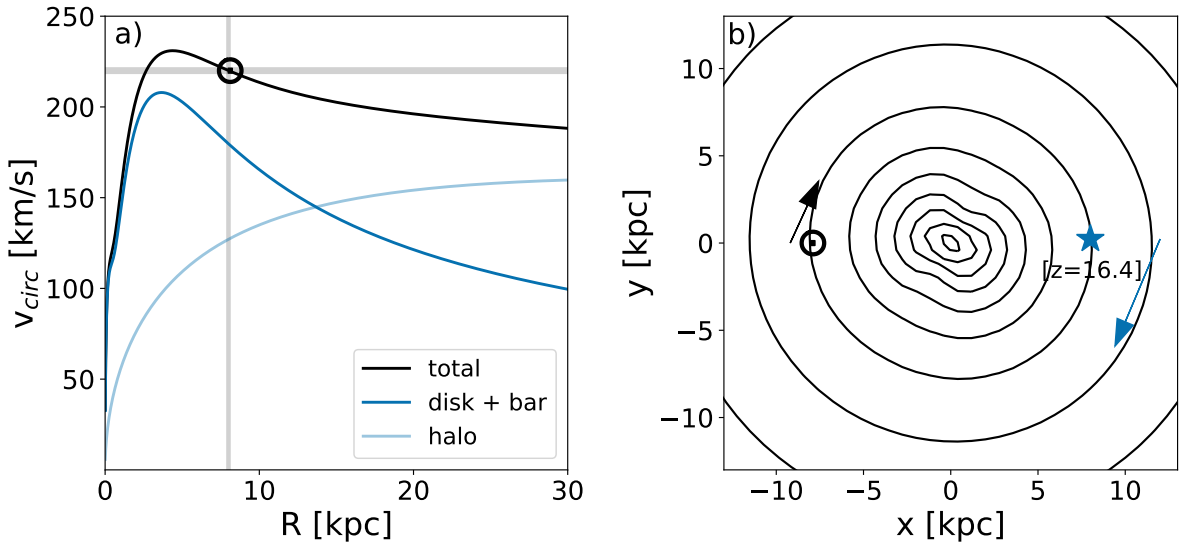

Figure 3.1: **The Galactic potential**. a: Circular velocity curves for the barred Milky Way potential model introduced in Section 3.2. The black line shows the sum of all components, the dark blue line show the sum of the disk and bar components and the light blue line shows the dark halo component. Vertical and horizontal gray lines shows the approximate position of the Sun ($\odot$) and its circular velocity. b: Contours of constant surface density in the plane for the barred Milky Way potential at present day (i.e. $\alpha = 27°$). $\odot$ indicates the position of the Sun, and the blue star indicates Pal 5's projected position in the plane of the Galaxy (it is located 16.4 kpc above the plane). In this projection, the direction of motion is clockwise for the Sun and Pal 5 (see arrows).

are consistent with recent measurements of these quantities ($v_{\mathrm{circ},\odot} \approx 220$ km s^{-1}, Bovy et al. 2012, see Table 3.1 and Figure 3.1) and that the enclosed mass profile at larger radii is consistent with constraints from halo tracers (Xue et al. 2008; Deason et al. 2012; Küpper et al. 2015).

3.2.1 Orbit integration and mock stream generation

We use a C-implementation of the Dormand-Prince 8th-order Runge-Kutta scheme (Prince & Dormand 1981; Hairer et al. 1993) to integrate orbits in the above potential (wrapped

in `Python` and released with gala: Price-Whelan et al. 2017). We use a time-step of $\Delta t = 0.5$ Myr, which conserves (Jacobi) energy with $|\Delta E_J / E_{J,0}| \leq 10^{-11}$ over our longest integration periods.

We use astropy (Astropy Collaboration et al. 2013) and gala (Price-Whelan et al. 2017) to transform these coordinates to a Galactocentric frame assuming the Sun is at Galactocentric position $(x, y, z) = (-8.0, 0, 0)$ kpc (Schönrich 2012) with velocity $(v_x, v_y, v_z) = (-11.1, 244, 7.25)$ km s^{-1} (Schönrich et al. 2010; Schönrich 2012).

To generate mock streams, we use the "particle spray" method (Fardal et al. 2015a) implemented in gala (Price-Whelan et al. 2017): star particles are created near the Lagrange points of a progenitor system on a given orbit with dispersions in position and velocity set by the mass and orbit of the progenitor (see Section 2.4 in Fardal et al. 2015a). We we fix the Galactic potential parameters and the 6D phase space coordinates of the Pal 5 cluster (see Table 3.1). In this work, we do not include the gravitational influence of the progenitor system on particles after release; this will affect the detailed density distribution and length of the simulated stream (Gibbons et al. 2014) but we do not expect it to affect qualitative comparisons of the stream morphology nor the energy and angular momentum of the stream particles for the mass ratio regime ($M_{\rm progenitor}/M_{\rm host} \approx 10^{-5}$) that Pal 5 probes at pericenter (Choi et al. 2007). We set the initial cluster mass to $m = 50000$ M$_\odot$ and release two particles (one at each Lagrange point) every time step. Due to Pal 5's low present day mass its most recent mass loss might be dominated by disk shocks, however we expect the overall signatures of the stream to be similar using the approximation here (Pearson et al. 2015; Bovy 2014). We generate mock stellar streams following the prescription described above: we first integrate the progenitor orbit backwards in the time-dependent Milky Way model from Pal 5's present day position for 8000 timesteps (4 Gyr), then begin the stream-generating procedure, integrating the orbit and all stream particles forward to present-day.

For reference, Pal 5 completes a full orbit in the Galaxy in ≈300 Myr and a bar pattern speed of 60 km s^{-1} kpc^{-1} corresponds to the bar completing a full revolution in ≈100 Myr.

3.2.2 Isotropic Gaussian ball of particles

To isolate and illustrate this gap formation mechanism, we generate isotropic Gaussian-distributed balls of test particles around the Pal 5 progenitor orbit and follow the orbits of these particles. We integrate the 6D position of the Pal 5 cluster backwards in time from its present-day position for 4000 Myr (from $t = 0$ to $t = -4000$ Myr). From the endpoint of the backwards integration, we generate initial conditions sampled from an isotropic Gaussian in position, with dispersion $\sigma_x = \left(\frac{m_{\rm Pal5}}{M(<r)}\right)^{1/3} r$ where $M(< r)$ is the enclosed Milky Way mass and r the instantaneous orbital radius. We assume $m_{\rm Pal5} = 50000$ M$_\odot$, $r \approx 7 - 8$ kpc, which yields $M(< r) \approx 1.5 \times 10^{11}$ M$_\odot$ and $\sigma_x \approx 50$ pc. Additionally we sample from an isotropic Gaussian in velocity, with dispersion $\sigma_v = 1$ km s^{-1}, comparable to the velocity dispersion of the cluster. These dispersions will cause the ball particles to shear and will therefore approach the bar with slightly different phase angles each time they individually reach pericenter.

From the endpoint of the backwards integration, we first evolve the particles forward in a static bar potential from $t = -4000$ Myr to $t = -1000$ Myr. We then turn on the bar with a pattern speed $\Omega_b = 60$ km s^{-1} kpc^{-1}, evolve the particles and bar to $t_{\rm stop} = -700$ Myr where we again freeze the bar, and then continue integrating the orbits of the particles until present-day. While starting and stopping the bar is unphysical, we do this to isolate one pericentric passage and ensure that the bar does not further perturb the stream.

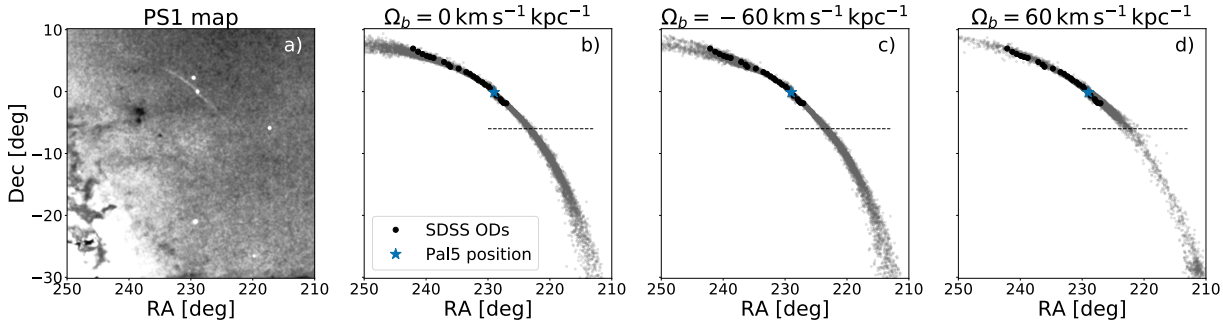

Figure 3.2: **The truncation in the leading arm of Pal 5 can be reproduced by introducing a prograde Galactic bar.** a: matched filter density map from PS1 (Bernard et al. 2016) showing the density truncation of Pal 5's leading arm. Following panels: sky projection of mock Pal 5 stream particles (gray) evolved in a potential with a static bar (b), retrograde bar with $\Omega_b = -60$ km s^{-1} kpc^{-1} (c), and a prograde bar with $\Omega_b = 60$ km s^{-1} kpc^{-1} (d). Over-plotted are the SDSS photometric over-density locations (black). The blue star shows Pal 5's present day position (the errors on the position are smaller than data point). See Section 3.2 for a detailed description of the Pal 5 mock stream generation. The dashed line demonstrates where the Pal 5 stream appears to end in the PS1 dataBernard et al. 2016 (a); this observed density decline of the leading arm is qualitatively reproduced with the prograde bar (d). The PS1 footprint extends to $\delta = -30°$, the lower limit of these panels.

3.3 Results

The bar spin in the Milky Way is prograde with respect to the disk and Pal 5's orbit around the Galaxy, and measurements of the bar pattern speed span ≈25–70 km s^{-1} kpc^{-1} (Gerhard 2011). To explore the effect of adding a bar to the Galactic potential, we investigate three different scenarios:

1. Non-rotating, static bar, $\Omega_b = 0$ km s^{-1} kpc^{-1}.

2. Retrograde bar, $\Omega_b = -60$ km s^{-1} kpc^{-1}.

3. Prograde bar, $\Omega_b = 20$ to 80 km s^{-1} kpc^{-1}, with 1 km s^{-1} kpc^{-1} increments.

As expected based on the study by Hattori et al. (2016), including a static bar (Figure 3.2, second panel) or a retrograde bar (Figure 3.2, third panel) does not much change the prop-

erties of the Pal 5 model stream (see also Erkal et al. 2017). For both of these cases, the stream curvature is qualitatively reproduced and the leading and trailing arm both extend ≈15° in sky projection. See Section 3.2 for a detailed description of the Pal 5 mock stream generation.

In contrast, the mock streams generated in a Galactic potential with a prograde bar generically lead to apparent gaps (caused by an under density) along both the leading and trailing arm. From the grid of pattern speeds, we select streams that qualitatively match the curvature of the trailing arm in sky position and the radial velocity gradient along the stream (Odenkirchen et al. 2009; Kuzma et al. 2015), as well as displaying abrupt density drops in the leading arm. As an example, we present the mock stream generated with a bar pattern speed $\Omega_b = 60$ km s^{-1} kpc^{-1} (Figure 3.2, panel d), for which the dense portion of the trailing arm extends ≈15°, while the leading arm has a drastic density drop at the location of the Pan-STARRS leading arm truncation, $(\alpha, \delta) \approx (222, -6)^\circ$ (dashed line), at ≈8° from the cluster center.

3.3.1 Observational signatures

Our models suggest that the cutoff of the leading arm in the PS1 map of Pal 5 could be an apparent gap and not a complete truncation: more stream stars could be located farther south, as suggested by the over-density of stars near $(\alpha, \delta) \approx (212, -29)^\circ$ seen in the right panel of Figure 3.2. Here we explore the observable phase-space morphology of these stars.

Figure 3.3 (panel a) shows a simulated stellar number-count map of our example model, assuming each particle represents a single star (Figure 3.2, d) and adopting a uniform background of stars with mean density 0.058 stars arcmin^{-2}, Balbinot & Gieles (2017). The figure emphasizes that the leading arm in this case could reappear near the edge of the PS1

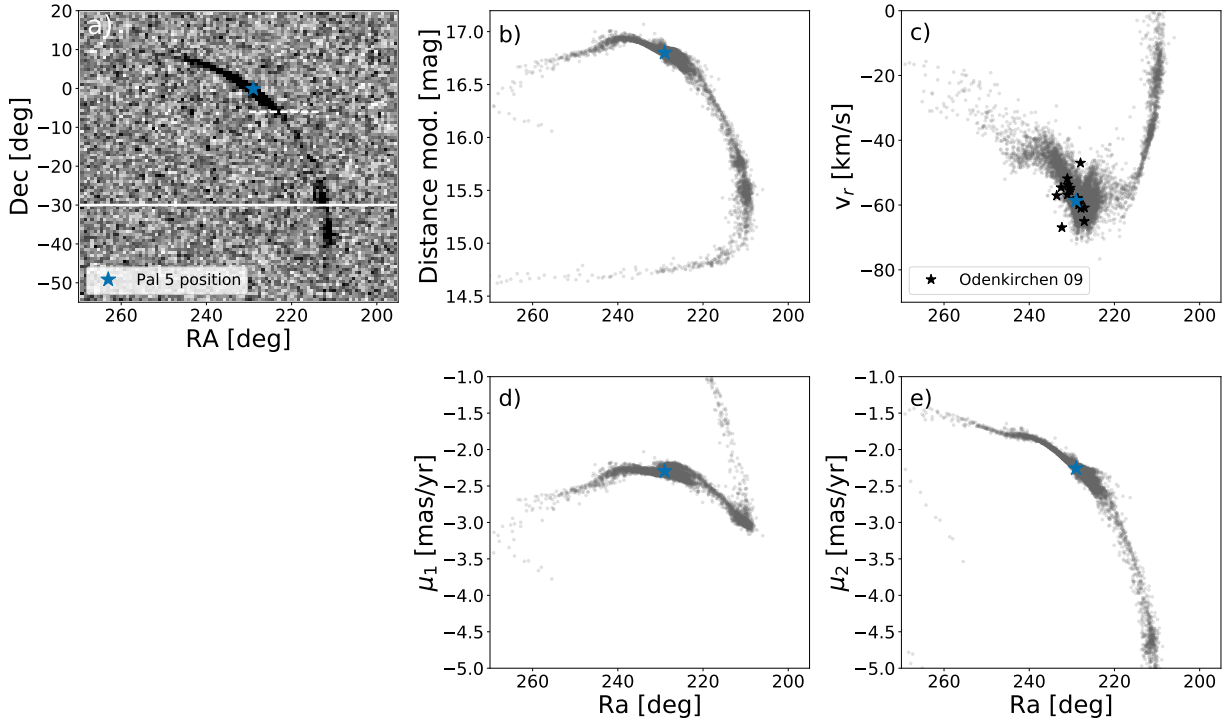

Figure 3.3: **Observables of the Pal 5 stream evolved in a potential with a prograde Galactic bar - note the reappearance of the stream particles south of the truncation.** a: simulated stellar number-count map of the model stream evolved in a potential with $\Omega_b = 60$ km s^{-1} kpc^{-1} using a uniform background of stars with mean density 0.058 stars arcmin^{-2}, (Balbinot & Gieles 2017). See Section 3.2 for a detailed description of the Pal 5 mock stream generation. The blue star shows Pal 5's present day position (the errors on the position are smaller than data point). b, c, d, e: observables of our Pal 5 mock stream evolved in a potential with $\Omega_b = 60$ km s^{-1} kpc^{-1}. The black stars (panel c) are radial velocity measurements (Odenkirchen et al. 2009) (the uncertainties are smaller than the data points: Pearson et al. 2015). We expect that Pal 5's leading arm should reappear south of the reported Pan-STARRS truncation (dashed line, panel a). The solid line shows the lower limit of the PS1 footprint.

footprint (at $\delta = -30°$). There are several uncertainties in this statement since the particle spray method used does not predict the density along the stream and the particle-to-star conversion was arbitrarily chosen. Nevertheless, the model suggest that the dense clumps of particles around $(\alpha, \delta) \approx (212, -30)°$ to $(212, -40)°$ should have surface densities similar to the other dense portions of the stream,and therefore could be detected with extended imaging of this region.

The re-appearance of the stream beyond the PanSTARRS truncation is a common prediction from these model streams (specifically for those with ($\Omega_b = 30, 41, 52, 62, 72, 79$ km s^{-1} kpc^{-1}) so long as the stream has been disrupting for several Gigayears (which is expected: Küpper et al. 2015). The exact location of gaps and further debris depends on the motion of Pal 5, the pattern speed of the bar, and the given potential. We ran the same analysis as presented above using a bar mass of $M_{\rm bar} = 5 \times 10^9$ M$_\odot$, which similarly yielded apparent gaps but of different sizes due to the smaller force field of the bar (see Section 3.3.2). Note the caveat that we do not update the scale length of our bar model based on the pattern speed. Hence, the corotation radius, defined as where the circular velocity is equal to the bar pattern speed, is not in agreement with observational constraints for the corotation radius in the Milky Way for all values of pattern speeds presented here (Englmaier & Gerhard 1999). However, $\Omega_b = 60$ km s^{-1} kpc^{-1} is consistent with current observational constraints of the velocity distribution from the local solar neighborhood, which has a corotation radius of ≈ 4 kpc (Dehnen 2000). A more detailed bar model (and Pal 5 model) would be necessary if we were to use the truncation to constrain the specific parameters of the bar model.

We encourage observers to look for the rest of Pal 5's leading arm stars. These extensions of the stream would have unique observable kinematic properties, as is shown in the other panels in Figure 3.3. First note that the distance modulus of these clumps is over 1 magnitude brighter, so a matched-filtering procedure using an isochrone at the cluster's distance may not

find these stars. Also note the discrepant velocity structure between the near-cluster stream stars and these clumps. With data from the second data release of the *Gaia* mission (Gaia Collaboration et al. 2016), proper motions for red-giant stars (known to exist in the stream (Kuzma et al. 2015) at these distance moduli will have uncertainties around 200 μas yr^{-1} (estimated using PyGaia); using proper motions in combination with photometric matched-filtering should greatly enhance the contrast of the stream in this region and help test for the existence of this other associated debris.

Interestingly, our mock stream generated in the potential with $\Omega_b = 60$ km s^{-1} kpc^{-1}, shows an apparent truncation of the trailing arm as well $(\alpha, \delta) \approx (242, 8)^\circ$, which is also seen in the PS1 data.

3.3.2 "Gap" evolution

The presence of a rotating, triaxial Galactic bar in the Milky Way potential model can create gaps and under-densities in simulated mock streams that are not observed when the bar orientation is fixed. The bar must therefore be asymmetrically perturbing or torquing particle orbits (see also Hattori et al. (2016) for an example with a stream orbiting in the Galactic plane). We expect the most important perturbations to occur at orbital phases where a pericentric passage coincides with a crossing of the Galactic plane when the stream particles are typically closest to the bar. We also expect the magnitude of the perturbation to depend on the phase of the bar relative to a given particle's orbit. Those with pericenters ahead of the bar along their orbits will be pulled back by the bar, while those behind will be pulled ahead. The result of an encounter is differences in net torques at adjacent points in the stream, which induce net differences in energy. Over time, a gap in space will grow due to the energy differences between adjacent stream members, in the same way a tidal stream spreads due to the range in energies of stream stars (Johnston 1998; Helmi & White 1999;

Johnston et al. 2001).

While the energy and angular momentum of each particle is not conserved in the time dependent barred potential, the Jacobi Energy ($E_J = E - \boldsymbol{\Omega} \cdot \boldsymbol{L}$) is conserved for each particle (Binney & Tremaine 2008). We can therefore calculate the offset in energy for each particle experiencing a bar encounter from the change in their z angular momentum:

$$\Delta E_J = \Delta E - \boldsymbol{\Omega} \cdot \Delta \boldsymbol{L} = 0 \tag{3.7}$$

$$\Delta E = -\Omega_b \, \Delta L_z \quad . \tag{3.8}$$

The change in the particle's z angular momentum can be expressed as the integral of the torque over a given interaction with the bar that begins and ends at (t_-, t_+) or a sum over k torques computed over the above interval at K times with fixed timestep Δt:

$$\Delta L_z = \int_{t_-}^{t_+} \tau_z \, dt \approx \Delta t \sum_{k}^{K} \tau_{z,k} \quad , \tag{3.9}$$

The particles that experience a net positive or negative torque will be offset from the rest of the particles in energy and will therefore have different orbital times. This small difference in azimuthal orbital periods, ΔT_Ψ, will then cause an angular separation for each particle, w, that grows by an amount per orbital period:

$$\Delta w \approx 2\pi \, \frac{\Delta T_\Psi}{T_\Psi} \quad . \tag{3.10}$$

In general, the orbital period depends strongly on E and only weakly on L_z (see Hendel & Johnston 2015, Figure 2), therefore we assume that the azimuthal orbital period is similar

for a particle on a circular orbit with the same energy as a particle on an eccentric orbit. We can represent the flat part of the rotation curve (see Figure 3.1) as a logarithmic potential with circular velocity ($v_c \approx 200$ km s^{-1}) and can therefore express $\frac{\Delta T_\Psi}{T_\Psi} = \frac{\Delta E}{v_c^2}$. We can then express the angular offset per angular orbital period for one particle experiencing a net torque as:

$$\Delta w = 2\pi \frac{\Delta E}{v_c^2} = 2\pi \frac{-\Omega_b \, \Delta L_z}{v_c^2} \quad . \tag{3.11}$$

As some particles are positively torqued and some are negatively torqued in a given bar encounter, we can express the apparent gap growth, Λ, per orbital time based on the this torque difference, ξ:

$$\Lambda \approx 2\pi \frac{\Omega_b}{v_c^2} \left(\Delta L_{z,\mathrm{pos}} - \Delta L_{z,\mathrm{neg}}\right) = 2\pi \frac{\Omega_b}{v_c^2} \, \xi \quad . \tag{3.12}$$

3.3.3 "Gap" forming mechanism

To isolate and illustrate this gap formation mechanism, we generate isotropic Gaussian-distributed balls of test particles around the Pal 5 progenitor orbit and follow the orbits of these particles. The advantage of using a ball of particles instead of the "particle spray" technique is that all particles begin to phase mix at a single time instead of being released at uniform time steps and this allows clear examination of the interaction sequence. We focus here on one particular orbital pericenter, at $t \approx -790$ Myr. See Section 3.2 for a description of the evolution of these balls more generally.

Figure 3.4 summarizes the results of this one encounter. Note that, the angular momenta of both the bar and the orbit are negative, so pulling back or forward along the orbit actually corresponds to a positive and negative torque respectively. The leftmost column shows the star particles initially identified as "leading" particles (lower energy relative to the progenitor

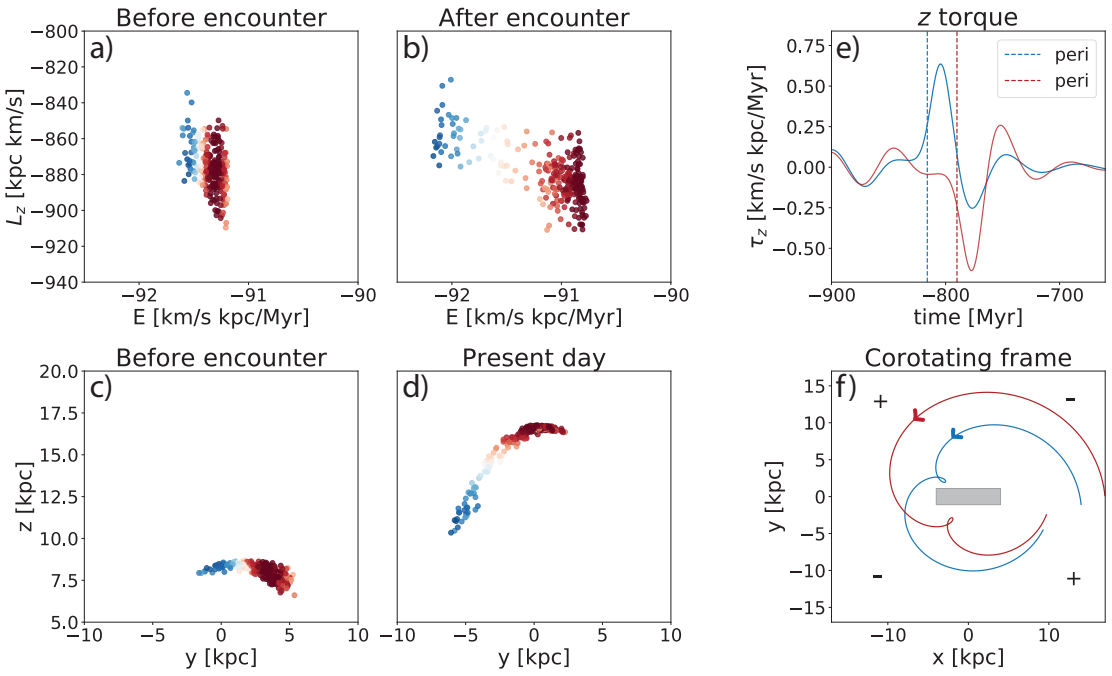

Figure 3.4: **Gap formation and evolution in Pal 5 like stellar stream due to spinning Galactic bar**. Panel a, b, c, d: time evolution of energy E vs. z-component of angular momentum L_z (a, b) and physical positions (c, d) of a ball of particles generated to roughly represent the leading arm of Pal 5 in a barred potential with $\Omega_b = 60$ km s^{-1} kpc^{-1}. Panel e: particles that receive the largest net positive torque (blue) and largest net negative torque (red) near their orbital pericenter (dashed vertical lines). Panel f: Orbits of the same two particles near pericenter (t $= -900$ Myr to t $= -700$ Myr) in the corotating frame with the Galactic bar aligned with the horizontal axis (see gray rectangle). The arrows show the direction of the orbits and "+"/"-" indicate the sign of the bar's torque in the corotating frame (see also Hattori et al. 2016, Figure 1). The blue particle experiences a positive torque as it reaches pericenter (see "loop") while the red particle, which reaches pericenter slightly later, receives a negative torque from the bar. This leads to a difference in the particles' net torque (i.e. z angular momentum) and therefore an offset of the blue and red points in energy and physical space (middle column).

at $t = -4000$ Myr) in the z component of the angular momentum (L_z) vs energy (E) space (top panel) and in projected cartesian, Galactocentric coordinates (bottom panel), at t = −850 Myr prior to the pericenter encounter with the bar. The middle column shows the same particles after the encounter with the bar at t = −700 Myr (top). The particles are color coded based on their total shift in angular momentum. It is clear that there have been changes in angular momenta and therefore the spread in energy increases dramatically after the bar encounter.

Comparing the left column panels to the middle column panels, it is evident that the negatively and positively torqued particles move away from each other in energy space (top) and over time also in physical space leading to the formation of apparent gaps as the particles phase-mix.

Figure 3.4 (e, f) shows the two particles that experience the largest net positive and negative torque in this pericenter encounter (top), and their position with respect to the bar in the corotating bar frame where the orbit directions are counter clockwise (see arrows bottom, f). The two particles see the bar in a different orientation as they reach pericenter (see "loops", bottom panel). The overall effect is to decrease/increase the magnitude of their angular momenta (as seen in the evolution of L_z from left to middle panel) which corresponds to a positive and negative torque respectively (see +/- in panel f).

From the example shown in the upper right panel of Figure 3.4, we find that $\Delta L_{z,pos} = 8.4$ km s^{-1} kpc and $\Delta L_{z,neg} = -10.6$ km s^{-1} kpc. Hence the torque difference, $\xi = 19.0$ km s^{-1} kpc. Given the assumptions stated in the previous section, we can express the gap growth per orbital time from Equation 3.12 as:

$$\Lambda = 10.3^\circ \times \frac{\Omega_b}{60 \text{ km s}^{-1} \text{ kpc}^{-1}} \times \frac{(200 \text{ km s}^{-1})^2}{v_c^2} \times \frac{\xi}{19.0 \text{ km s}^{-1} \text{ kpc}} \quad . \tag{3.13}$$

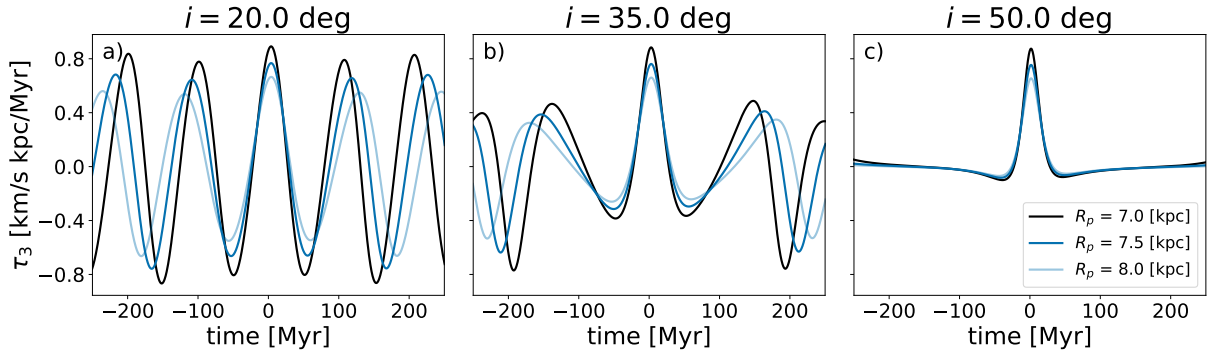

Figure 3.5: **Variations in the torque from the Galactic bar due to stream inclination and pericentric distance**. Particles with three different pericentric distances (black: $R_p = 7.0$ kpc, dark blue: $R_p = 7.5$ kpc, light blue: $R_p = 8.0$ kpc), experience a pericenter and bar passage at the midplane (see peaks in τ_3 shown along the y-axis). Small R_p yields a larger magnitude in the z-direction of the torque. Small orbital inclinations (a), induce periodic bar encounters, while large inclinations (c) are dominated by one bar encounter event, when the particle passes the midplane.

Recall that we here used the most net negatively and net positively torqued particles (Figure 3.4 top, right), and that the actual size of the apparent gap will grow to roughly half of this (see Figure 3.4 panel b) within an orbital time which corresponds to ≈5.15 degrees in this specific example.

A prograde bar can lead to differences in net torques because of the difference in position of the stars with respect to the bar at their orbital pericenter. Stars will not experience this interaction with the bar in a potential with a static bar. With a retrograde bar, the effect is not as important because the interaction time is greatly reduced.

3.4 Discussion

3.4.1 Repeated encounters

Hattori et al. (2016) showed that the long-term influence of a time-dependent bar can affect

the length of streams orbiting in the plane of the galaxy through repeated, resonant torques from the bar; if the stars repeatedly approach the bar with the same or similar phase with respect to the bar, they experience the so-called "shepherding" effect from the encounters. Our analysis differs from the resonant picture as Pal 5 is not orbiting in the plane of the Galaxy. Because of the high inclination of the Pal 5 orbit, different particles can be affected at each approach towards pericenter so that repeated, resonant encounters do not occur. Gaps form and grow because of these individual encounters.

In Figure 3.5, we explore the effect of varying the inclination with respect to the bar plane, $i = (20, 35, 50)^\circ$, for a single particle orbiting the Galaxy with three different pericentric distances, $R_p = (7, 7.5, 8)$ kpc. In each case, a pericenter and bar passage occurs at $t = 0$ at the midplane (where the torque from the bar is maximum). When the inclination is small (a), the particle repeatedly experiences the bar sweeping past it (i.e. a torque in the z-direction). At larger inclinations (b, c), the bar is most important as a particle passes the midplane and can lead to net torques even from single encounters. As expected, a smaller pericentric distance will yield a larger magnitude of the torque (lines ordered by brightness). Additionally, the net torque (and the size of the apparent gap) will depend on the interaction time which is set by the details of the specific orbit.

At high inclinations, the location along the stream where the net torque perturbs particles will change over each orbit. This will lead to more stochastic perturbations and gap formation that can drastically alter or "wash out" the appearance of under-densities from previous encounters. Additionally, since the gap growth depends on the difference in net torque that particles receive after a bar encounter, smaller gaps could form with varying inclination and encounter timescale (in contrast with the idea that the bar can only create relatively large-scale stream asymmetries: Erkal et al. 2017). Although note that these could be of shallow depth (see Erkal et al. (2016) section 4.1).

3.4.2 Consequence for subhalo search

According to the Λ-Cold Dark Matter (ΛCDM) cosmological model, our galaxy is expected to be filled with thousands of dark matter subhalos (Diemand et al. 2008), in contrast with the number of Galactic satellites (≈100s) observed around the Milky Way (Klypin et al. 1999). Recently, alternative dark matter theories have been proposed that suppress small-scale clustering to make the predicted number of subhalos smaller (e.g., "fuzzy" dark matter Hui et al. 2016). Baryonic cosmological simulations also seems to suppress small-scale structure (D'Onghia et al. 2010; Garrison-Kimmel et al. 2017), although it is debated to what degree this affects subhalo destruction (Errani et al. 2017).

One way to test these theories is to search for recent interactions between subhalos and cold stellar streams that leave density perturbations in the form of apparent gaps. Several groups have shown that interactions with subhalos, in abundances similar to those expected from CDM simulations, can induce observable density variations along the Pal 5 stream (Yoon et al. 2011; Carlberg et al. 2012; Erkal et al. 2017; Bovy et al. 2017).

Our work demonstrates an alternative explanation for density variations in stellar streams: interactions with the Galactic bar (Price-Whelan et al. 2016b; Erkal et al. 2017). The effects are most apparent for streams orbiting prograde with respect to the Galactic bar and may only mimic subhalo interactions when the orbital inclinations are large. We therefore conclude that distant cold streams and streams on retrograde orbits with respect to the disk (such as GD1) will be least affected by a bar encounter and therefore most suitable for potential indirect dark matter subhalo detections. A similar conclusion was made by Amorisco et al. (2016), who showed that giant molecular clouds will also affect streams on prograde orbits near the stellar disk.

We confirm that including the bar when modeling streams in the inner Milky Way is critical (Hattori et al. 2016; Price-Whelan et al. 2016b). In future work, we investigate whether all detected under densities in the leading and trailing arms of Pal 5 (Erkal et al. 2017; Thomas et al. 2016) can be solely attributed to the bar, by doing a rigorous comparison of bar gap signatures to other gap signatures (Bovy et al. 2017; Erkal et al. 2016; Amorisco et al. 2016; Sanders et al. 2016; Sandford et al. 2017; Erkal et al. 2017) in an Nbody simulation of the Pal 5 stream.

Acknowledgments

We are pleased to acknowledge Anthony Brown and the Gaia Project Scientist Support Team and the Gaia Data Processing and Analysis Consortium (DPAC) for making the PyGaia package open-source. We thank the Flatiron Institute Center for Computational Astrophysics for providing the space to carry out this project. SP thanks Julio Chanamé and Edouard Bernard for insightful discussions. KVJ and SP acknowledge support from NSF grant AST-1614743.

Chapter 4

Local Volume TiNy Titans: gaseous dwarf-dwarf interactions in the Local Universe

4.1 Introduction

In the current ΛCDM paradigm interactions and mergers between galaxies in the Universe are thought to play an important role in their evolution. Interactions between massive galaxies have been studied extensively both observationally and theoretically. Through these studies, we know that the interactions induce morphological changes (e.g. Toomre & Toomre 1972, De Propris et al. 2007, Ellison et al. 2010, Casteels et al. 2014), can trigger starbursts (e.g. Hernquist 1989, Scudder et al. 2012, Patton et al. 2013, Davies et al. 2016), gas inflows and also AGN activity (e.g. Sanders et al. 1988, Ellison et al. 2011, Silverman et al. 2011, Satyapal et al. 2014). Recently, Sengupta et al. (2015a) studied the tidal forces acting on

This section contains text from an article published in the Monthly Notices of the Royal Astronomical Society (Pearson et al. 2016).

the gas in prograde, low-velocity flyby interactions, which showed that large fractions of the gas can be displaced beyond the optical disks of massive spirals. However, very little is known observationally and theoretically about interactions between the most prevalent type of galaxies at all redshifts, dwarf galaxies (Binggeli & Jerjen 1998; Karachentsev et al. 2013). Dwarf galaxies differ from their more massive counterparts, as their dark matter to baryonic matter fraction tends to be larger, they are much fainter (10-10^5 times fainter than Milky Way (MW) type galaxies) and they are inefficient at forming stars from their large gas reservoirs (e.g. Blanton et al. 2001, Robertson & Kravtsov 2008). It is therefore unclear whether the same processes observed in massive galaxies (e.g. their merger sequence and their displacement of gas with interaction) scale down to the dwarf regime. Since dwarf galaxies dominate the galaxy population of the Universe at all times, the interactions and mergers between them occur more frequently in a given volume than for massive galaxies (Fakhouri et al. 2010, Deason et al. 2014) and they play a crucial role in the hierarchical build up of dark matter and stellar halos. Thus, studying their mutual interaction does not only shed light on the merger sequence of dwarfs, but their interactions also play a key role in how more massive galaxies are fed by accretion, as dwarf galaxies are often captured as pairs or groups (e.g. Wetzel et al. 2015). Pre-processing of gas by tidal interactions prior to infall can drastically increase the efficiency of gas lost to the halos of the more massive galaxies (see e.g. Besla et al. 2010, Salem et al. 2015), hence understanding the baryon cycle in dwarf galaxy interactions provides insight into how the baryon cycle of more massive galaxies is acquired.

Recently, Stierwalt et al. (2015) carried out a systematic study of 104 dwarf galaxy pairs in a wide range of interaction stages and environments, selected from the Sloan Digital Sky Survey (the TiNY Titans Survey). The pairs in their sample all have projected separations $<$ 50 kpc, velocity separations $<$ 300 km s^{-1} and pair member masses between $7 < \log(M_*/M_\odot)$

< 9.7. Interestingly, they find that the star formation rates of the dwarf galaxy pairs averaged over all pairs are enhanced with decreasing pair separation, which is also found for more massive galaxies (e.g. Patton et al. 2013). However, when they investigated the gas fractions of their dwarf pairs using single-dish Arecibo Telescope and Green Bank Telescope data, only pairs within 200 kpc of a massive host galaxy showed signs of gas depletion, whereas the dwarf pairs farther than 200 kpc from a massive host had large atomic gas fractions ($f_{\rm gas} > 0.6$, where $f_{\rm gas} = 1.4M_{\rm HI}/(1.4M_{\rm HI} + M_*)$).

Similarly, Bradford et al. (2015) investigated the baryon content of low mass galaxies using single-dish Arecibo, Green Bank and remeasured ALFALFA data. They found that non-isolated low mass galaxies (in the vicinity of a massive host) had a higher scatter towards lower atomic gas fractions, when compared to isolated galaxies of similar masses (see their Figure 4). Additionally, only non-isolated galaxies were gas-depleted as defined by a -1 dex deviation from the gas mass vs stellar mass fit to all data (Bradford et al. 2015, Figure 5). Lastly, they found that no isolated low mass galaxies had gas fractions lower than $f_{\rm gas} < 0.3$, which sets an upper limit on the amount of gas that can be consumed by star formation or removed by outflows or tides.

The studies by Stierwalt et al. (2015) and Bradford et al. (2015) (see also Geha et al. 2006, Geha et al. 2012) all indicate that environment plays a key role in quenching dwarf galaxies and dwarf galaxy pairs, and that dwarfs and dwarf pairs in an isolated environment have high atomic gas fractions. Recently, Davies et al. (2016) showed that the fraction of passive, non star forming galaxies is higher at all stellar masses for interacting pairs and groups of galaxies, than for galaxies in the field, which introduces an interesting question about the role of galaxy interactions in quenching at the low mass end.

However, a key issue is that the gas fractions estimated from single-dish data could also

Although their median atomic gas fractions were very similar for non-isolated and isolated low mass galaxies ($f_{\rm gas} = 0.81 \pm 0.13$ and $f_{\rm gas} = 0.82 \pm 0.16$, respectively).

include gas that sits in the outskirts of the galaxies, which can have been removed by tidal forces, ram pressure stripping or blown out from star formation. To understand whether this gas is unbound and enriches the intergalactic medium (or circumgalactic medium of a host galaxy), if it falls back and refuels the star formation in the dwarfs or if it resides within the dwarfs themselves, we must resolve the diffuse component of the atomic gas. As the tidal structures can reach HI column densities as low as N(HI) $\sim 10^{18}$ cm^{-2} (e.g. for the LMC: Putman et al. 2003), mapping these structures at large distances, beyond the Local Volume, is difficult with existing instruments.

The Magellanic System (MS) is currently the best template for an ongoing nearby dwarf-dwarf interaction. Evidence for this interaction is most convincingly seen in the extended HI distribution; this includes a bridge of gas connecting the two galaxies and two streams of gas that span $> 100^{o}$ of sky (Putman et al. 2003). Besla et al. (2012) showed the importance of tidally pre-processing the gas prior to infall in shaping the tail of the MS. This scenario was supported by Salem et al. (2015) as they showed that ram pressure stripping is not sufficient to explain the amount of gas in the MS. Furthermore, Salem et al. (2015) showed that the truncation in the LMC's HI disk due to its motion through the Milky Way halo, can be used to constrain the Milky Way's halo density. However, having more examples than the MS is crucial for establishing the stage at which ram pressure stripping becomes important for removing gas and the role of minor mergers of groups in feeding the circum galactic medium (CGM) of galaxies like the Milky Way.

Examples of Local Volume dwarf samples include Odewahn (1994) and Wilcots & Prescott (2004). While Odewahn (1994) found that nearly all Magellanic Irregulars have nearby companions, Wilcots & Prescott (2004) showed that many of these companions might be chance projections. Additionally, the Wilcots & Prescott (2004) study of 13 Magellanic Irregulars found that the asymmetric morphology in the HI profiles of Magellanic Irregulars with

gaseous companions did not seem to differ much from Magellanic Irregulars without gaseous companions. In this paper, we are selecting examples from the literature that are likely to be interacting, and therefore expect to find significant differences between our pairs and isolated analogs. In particular, we investigate the tidal and environmental effects on the diffuse gas in 10 Local Volume dwarf galaxy pairs with low relative velocities within 30 Mpc of the Milky Way.

This paper is a part of a larger body of work (the TiNy Titans Survey (TNT)) and represents the Local Volume TNT sample (LV-TNT). Here we quantify the HI morphologies, HI surface density profiles and the fraction of neutral gas that resides outside vs inside the dwarf galaxies to understand the gas removal process and baryon cycle in these systems. The 10 pairs represent a diverse sample of dwarf galaxy interactions, as they are located at different distances from massive galaxies and are captured in various interaction stages. The diversity of the sample enables us to ask: what is more important - environment or dwarf-dwarf interactions in removing gas to large radii? How much material can be removed in this way and does this material remain bound to the pairs?

The paper is structured as follows: In Section 4.2 we describe the selection process leading to our sample, and present the properties of 10 dwarf galaxy pairs. In Section 4.3, we show the results of our analyses of the diffuse gas from the 10 dwarf pairs. We discuss the results of our study in Section 4.4, and we conclude in Section 4.5.

4.2 Dwarf pair selection and sample

In this Section, we present the sample of 10 Local Volume dwarf galaxy pairs (see Figure 4.1). We describe the sample selection in Section 4.2.1, we describe how properties of the dwarf galaxies were estimated in Section 4.2.2 and we discuss each dwarf pair in detail in

Appendix 4.A.

4.2.1 Sample Selection

Our goal is to investigate the gas distributions around dwarf galaxy pairs. Therefore, we are only interested in Local Volume, interacting dwarf galaxies where the HI structure can be resolved to sufficiently explore the gas beyond the optical extents of the dwarfs. To enforce these criteria, we require that the projected separation, $R_{\rm sep}$, between each pair is < 100 kpc (in practice, only one of our targets has a $R_{\rm sep} > 50$ kpc (see Figure 4.2)), the velocity separation, $v_{\rm sep}$, is < 300 km s^{-1} and that all pairs are within 30 Mpc of the Milky Way. The limits on $R_{\rm sep}$ and $v_{\rm sep}$ are similar to those in the TiNY Titans sample (Stierwalt et al. 2015) and to those known to identify interactions between more massive galaxies (e.g. Patton et al. 2013). We set an upper stellar mass limit for each dwarf galaxy in our sample at $M_* < 10^{10}$ M$_\odot$, and we require that the dwarf galaxy pairs must have HI maps with an outer column density limit of N(HI) $< 7 \times 10^{19}$ atoms cm^{-2}.

After applying these cuts to pairs found through an extensive literature search, we have 10 Local Volume dwarf galaxy pairs, which we present in Section 4.2 and list in Tables 4.1, 4.2 and 4.4. We preferentially selected pairs where evidence of interaction has been presented in the literature, and are therefore biased to systems that are connected by bridges and show signs of interaction through tidal features. This sample can be expanded in the future with further HI maps of existing and newly identified pairs. As the number of dwarf pairs in the Local Volume is observationally and theoretically uncertain, assessing the completeness of our sample is difficult. However, we stress that the goal of this study is not to present a comprehensive census of dwarf pairs in the Local Volume, rather we chose 10 targets that range in projected separation, velocity, mass ratio and environment to probe potential signatures of dwarf-dwarf interactions or environmental effects.

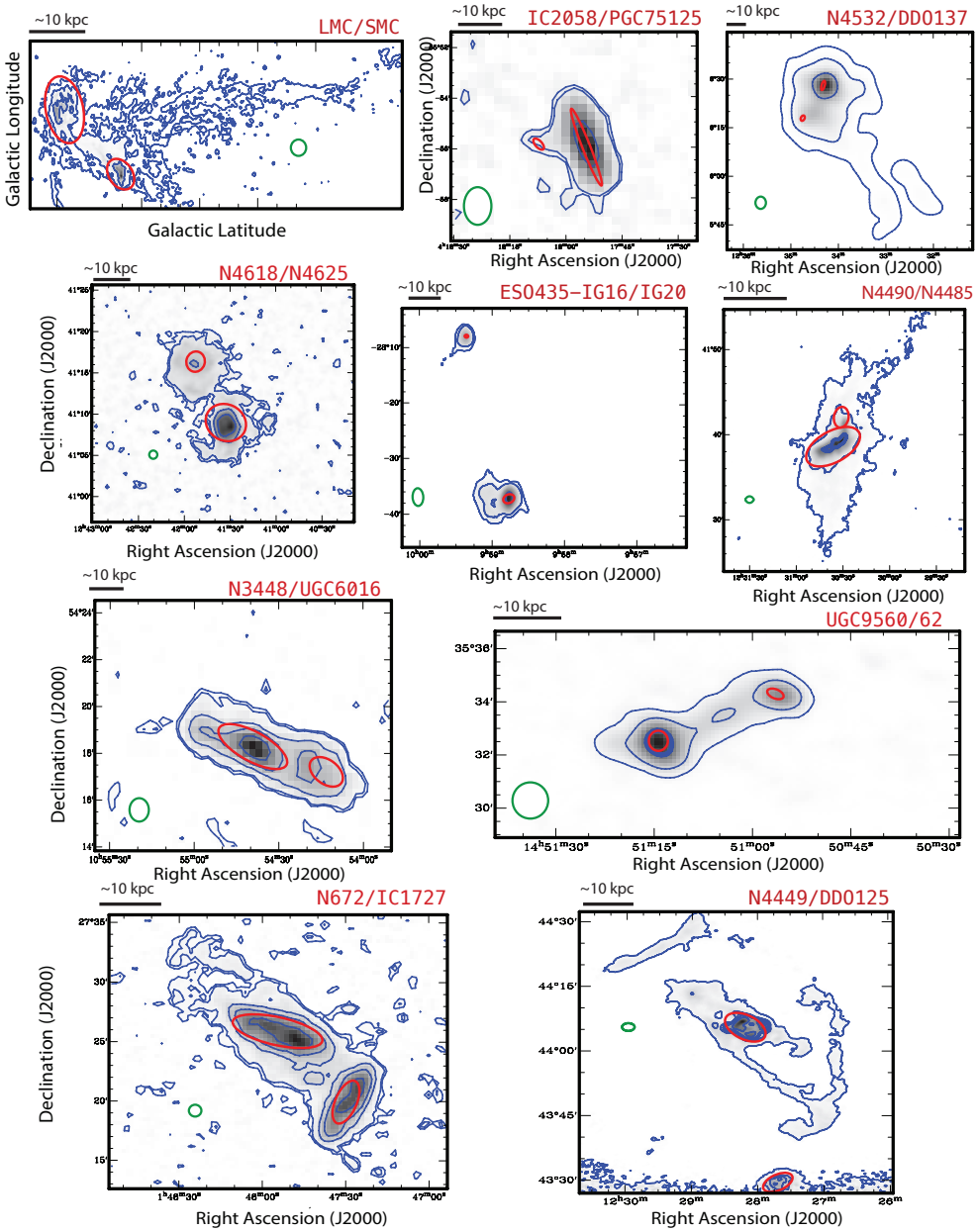

Figure 4.1: HI contours (blue) of all LV-TNT pairs in order of decreasing tidal index, with the 2MASS ellipses in (red) in addition to the beam sizes (green). All N(HI) are listed in units of $\times$ 10^{20} atoms cm^{-2}. **1st row:** N(HI)$_{\rm LMC}$ = 0.1, 1.0, 10.0. N(HI)$_{\rm IC\ 2058}$ = 0.7, 1.0, 10. N(HI)$_{\rm N4532}$ = 0.01, 0.1, 1.0. **2nd row:** N(HI)$_{\rm N618}$ = 0.7, 1.2, 5.0, 1.0, 2.0. N(HI)$_{\rm ESO}$ = 0.1, 0.7, 5.0. N(HI)$_{\rm N4490}$ = 0.7, 7.0, 70.0. **3rd row:** N(HI)$_{\rm N3448}$ = 0.7, 1.2, 5.0, 1.0, 2.0. N(HI)$_{\rm U9560}$ = 0.7, 3.0, 10.0. **4th row:** N(HI)$_{\rm N672}$ = 0.7, 1.2, 5.0, 1.0, 2.0. N(HI)$_{\rm N4449}$ = 0.45, 1.0, 10.0. See Putman et al. (2003) for Galactic coordinates of the LMC/SMC and see Figure 4.3 for deeper data of N4449 (here we show less deep data to include DDO125). For details on the HI observations and column densities: see Table 4.4.

The resolved HI maps for each of our targets are shown in Figure 4.1, and the details of the observations are listed in Table 4.4. The mass ratios, relative line of sight velocities and pair separations of all pairs are shown in Figure 4.2. These are all within the velocity separation used in the Stierwalt et al. (2015) sample, however we include one pair that is at a projected separation of $\sim$ 100 kpc, and four pairs that have stellar mass ratios $10 < (M_1/M_2)^* < 20$ (the Stierwalt et al. (2015) limit is $R_{\rm sep} < 50$ kpc and $(M_1/M_2)^* < 10$).

4.2.2 Properties

Our main goals in this paper are to quantify the relative roles of environment and dwarf-dwarf interactions in removing gas to large radii (e.g. tidally or through ram pressure stripping), to understand how much material can be removed through these processes and determine whether this material remains bound to the pairs. We will do this through a systematic comparison of the HI content of 10 dwarf galaxy pairs utilizing the following terms:

- **Stellar extent of galaxies**: as we are interested in disentangling the atomic gas in the outskirts of the dwarf galaxies from the gas residing within the galaxies, we use the 2MASS Extended Source Catalog to define the stellar extent of each galaxy. The extent is derived from the K_s-band scale length of each galaxy and is $\sim 4 \times$ the K_s-band scale length. An elliptical fit is made by extrapolating the radial surface brightness from the standard isophote. These fits are all illustrated as red ellipses on the HI profiles of the dwarf galaxies in Figure 4.1. This extent is used as the inner stellar component of each dwarf, and permits a uniform definition of the sizes of the main body of each target dwarf galaxy.

See http://www.ipac.caltech.edu/2mass/releases/allsky/doc/sec4_5e.html for details.

For the 2 of our 20 galaxies that did not have 2MASS K_s-band info (DDO137 and UGC 6016), we estimated the extent of the galaxies based on their r-band images. As the r-band traces younger stars, this might introduce a bias towards slightly larger radii.

- **Distances**: for each pair in our sample we use distances to the primary (most massive) dwarf from recent literature as listed in Table 4.1. For three systems where there were no individual distance estimates (the ESO435-IG16 pair, the NGC 3448 pair and the UGC 9562 pair), we used the kinematic flow distance as listed in NED, which were corrected per Mould et al. (2000), assuming $H_0 = 73$ km/s/Mpc. In our tables we show how various parameters scale with distance. For the LMC and SMC, precise distance measurements exist for both galaxies, hence we use these individually for the two dwarfs.

- **Stellar masses**: to determine the stellar masses of the dwarf galaxies, we used the K_s-band magnitudes from the 2MASS Extended Source Catalog of each galaxy and the conversion from light to mass defined in Bell et al. (2003) as:

$$(M/L)_{\odot} = 0.95 \pm 0.03 \tag{4.1}$$

  Both this and the definition of the stellar extent is biased towards older stars, but provide uniform values for our entire sample.

- **Tidal indices, Θ**: our target pairs are located in very different environments (some are close to a more massive tertiary galaxy, and some pairs do not have a more massive galaxy in their vicinity). In order to determine what environment our dwarf pairs reside in, we calculated the tidal index, Θ, used to quantify environment in the ANGST studies by Weisz et al. (2011) and defined in Karachentsev & Makarov (1998) as:

$$\Theta = \log_{10}\left(\frac{M_*[\times 10^{11}\mathrm{M}_{\odot}]}{D^3_{\mathrm{project}}[\mathrm{Mpc}]}\right) \tag{4.2}$$

where M_* is the stellar mass of the nearest massive galaxy and $D_{\rm project}$ is the projected distance from the dwarf pair to the nearest massive galaxy. The nearest massive galaxy is referred to as the host galaxy. Here, $D_{\rm project}$ is converted from an angular separation to a projected physical separation of the primary (most massive) dwarf in the dwarf pair to the host galaxy at the distance of the pair. We list all projected distances to the hosts in Table 4.3. Thus, a higher Θ indicates a stronger influence from a nearby neighbor. We do not use velocity separations of the pair and host when calculating the tidal index.

In this work, we search for a nearby massive galaxy within the NASA Extragalactic Database (NED) and define a massive galaxy as any galaxy with $M_* > 10^{10}$ $M_\odot$, and we require that the velocity separation between the massive galaxy and the pair is $v_{\rm sep} < 500$ km s^{-1}. If our pairs do not have a massive galaxy within $D_{\rm project} < 1500$ kpc with $v_{\rm sep} < 500$ km s^{-1}, we classify the dwarf pair as being isolated and do not calculate the tidal index (see Table 4.3 for details on the host galaxies). Geha et al. (2012) showed that dwarf galaxies in the field (D > 1.5 Mpc from a massive host) are not quenched, hence we apply this criteria for isolation. Similarly, studies for massive galaxy pairs (e.g. Patton et al. 2013) and for dwarf galaxy pairs (Stierwalt et al. 2015) also use this isolation criterion in addition to a velocity cut of $v_{\rm sep,host} < 1000$ km s^{-1}. As our sample is local, we use a stricter limit on $v_{\rm sep,host}$ and our high tidal index pairs all have $v_{\rm sep,host} < 300$ km/s to their hosts (see Table 4.3).

- **Ram pressure stripping**: hallmarks of ram pressure stripping are asymmetric extended structures (such as one sided trailing tails) and asymmetrically truncated disks (which is also seen for more massive galaxies as they fall into clusters, Chung et al. 2007). To assess whether the dwarfs in our sample are experiencing ram pressure, we

investigate if the HI surface density profiles in the inferred direction of motion deviate from the other directions (e.g. if the disks appear truncated). To quantify whether ram pressure can explain the features we see in the HI maps, we investigate the surface density profiles (see below) and use the simplified version of the Gunn & Gott (1972) criterion as used by Vollmer et al. (2008) to investigate the halo densities necessary to explain any truncations:

$$\rho_{\rm IGM} \sim \frac{v_{\rm rot}^2 \Sigma_{\rm gas}}{v_{\rm gal}^2 R} {\rm cm}^{-3} \tag{4.3}$$

where $v_{\rm rot}$ is the rotational velocity of the galaxy, $v_{\rm gal}$ is the motion of the galaxy through the halo of the host, $\Sigma_{\rm gas}$ is the column density of the gas at the truncation radius, and R is the truncation radius.

- **Surface density profiles**: in order to investigate the variations in the HI distributions of pairs in various environments, we compute the radial surface density distributions of the neutral gas for all dwarfs using the *MIRIAD* ellint task. The task integrates the HI surface density maps in elliptical annulus, and we compute the average surface density in each annulus. To estimate how asymmetric the HI distributions are, we use various regions of the HI maps and integrate these separately (see Section 4.3).

- **Dark matter masses from abundance matching**: as we are interested in whether the pairs are bound to each other and whether the gas in the outskirts of the galaxies is bound to the pairs, we need an estimate of the total dark matter masses of our galaxies. For this purpose, we use the relation for abundance matching from Moster et al. (2013) using their Equation 2 and best fit values listed in their Table 1 at $z = 0$. We assume a WMAP7 ΛCDM cosmology with (Ω_m, Ω_Λ, Ω_b, h, n, σ_s) = (0.272, 0.728, 0.046, 0.704, 0.967, 0.810). Abundance matching assumes that the galaxy in question

is isolated, which our galaxies are not. Furthermore, abundance matching is poorly calibrated for low mass galaxies (see e.g. Garrison-Kimmel et al. 2014). However, these estimates of the dark matter masses are only to be used as an approximation to the potential tidal fields of both the massive host and dwarf galaxies.

- **Escape velocities**: from the abundance matching we obtain an estimate of the total halo masses of our systems. That enables us to calculate the escape velocities from both the pairs (which can help quantify whether the gas in the outskirts of the pairs is bound) and from the primary, most massive dwarf (which enables us to estimate if the galaxies in the pair are bound to each other). We therefore adopt an NFW profile to the galaxies:

$$\Phi_{\rm NFW}(R) = -\frac{GM_{200}ln(1+\frac{R}{Rs})}{Rf(c)} \tag{4.4}$$

which enables us to calculate the escape velocity at a specific distance from the primary dwarf:

$$v_{\rm escape} = \sqrt{2 \times \Phi_{\rm NFW(R)}} \tag{4.5}$$

Here $R_s = \frac{R_{200}}{c}$ is the scale length of the halo, where R_{200} is defined as the radius at which the density is 200 times the critical density of the Universe, M_{200} is calculated based on Eq. 2 in Moster et al. (2013) using the cosmological parameters listed above and defines the mass within R_{200}, $f(c) = ln(1+c) - c/(c+1)$ and the halo concentration, c, is defined from Eq. 4 in Neto et al. (2007).

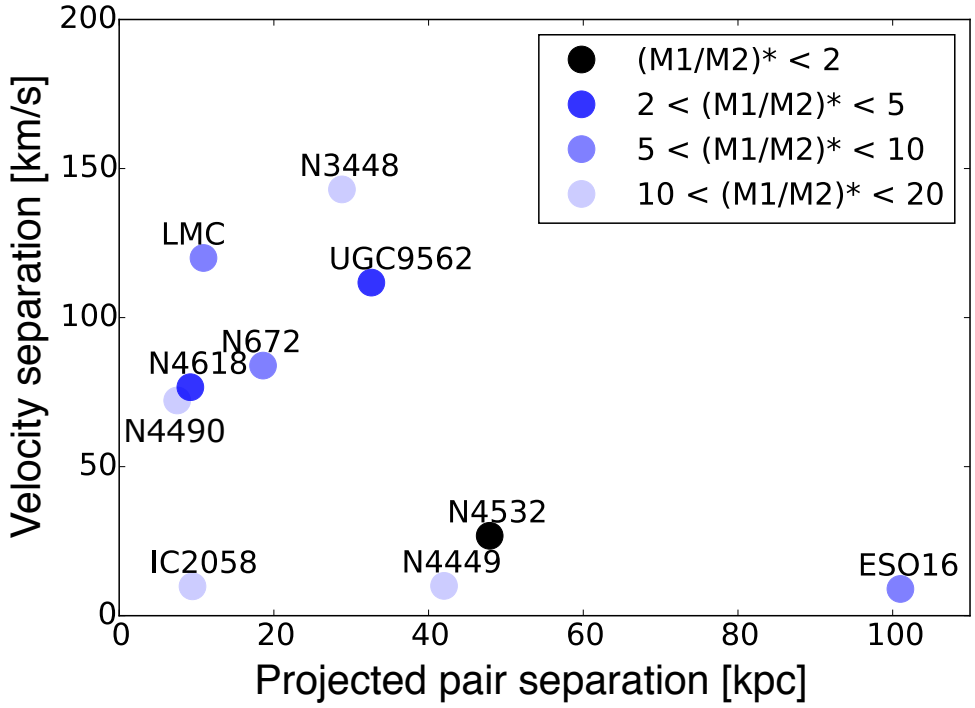

Figure 4.2: Projected radial and line of sight velocity separations for the 10 dwarf pairs colour coded by stellar mass ratios between the two dwarfs. Each data point is named by the primary (most massive) galaxy. All dwarf pairs are separated by less than 200 km s^{-1} in their line of sight velocities and their radial separations are all smaller than 101 kpc.

- **HI bridges**: bridges that connect two galaxies are strong indicators of an ongoing tidal interaction (e.g. Toomre & Toomre 1972, Combes 1978, Hibbard & Mihos 1995, Barnes & Hernquist 1998, Gao et al. 2003, Besla et al. 2010, Besla et al. 2012). In this work, we define a bridge as being continuous in HI column density and having a velocity gradient that smoothly connects one galaxy to the next (e.g. as seen in the Magellanic System, Putman et al. 2003).

4.3 Results

In this section we describe the results of our analyses of the diffuse gas in our LV-TNT sample. First we examine the observational differences between the neutral gas distributions of the dwarf galaxy pairs evolving in isolation and in the vicinity of massive hosts (see Section 5.2). In Section 4.3.2 we examine the global trends of gas removal for our entire sample.

4.3.1 Distribution of Neutral Gas as a Function of Environment

To understand how dwarf-dwarf interactions are affected by their environment, we first examine the influence of dwarf-dwarf encounters on the extended gas structure in Section 4.3.1.1 using isolated dwarf pairs. Subsequently, we search for observational evidence of environmental processing (ram pressure stripping) in the extended gas structure of the non-isolated dwarf pairs in Section 4.3.1.2 and 4.3.1.3. We investigate how these non-isolated dwarf pairs differ from dwarf pairs evolving in isolation, and we break down this analysis in terms of tidal indices. The tidal index is an estimate of the tidal influence of a massive host galaxy on the dwarf galaxy pairs. Here, we define isolated pairs as having $\Theta < 0$, intermediate tidal index pairs as having $0 < \Theta < 1.5$ and high tidal index pairs as having $\Theta > 1.5$ (see Table 4.3 for details on each massive host galaxy). We checked that the only pair potentially affected by the distance errors, which could move it to a lower tidal index group, was the NGC 4532 pair (see Appendix 4.A.3).

4.3.1.1 Dwarf pairs evolving in isolation

By investigating the dwarf pairs evolving in isolation, far from a massive host, we can understand how the interaction between the dwarfs affects the gas distributions. In Figure 4.3 (top row) we show the four pairs in our sample with $\Theta < 0$: NGC 3448 & UGC 6016,

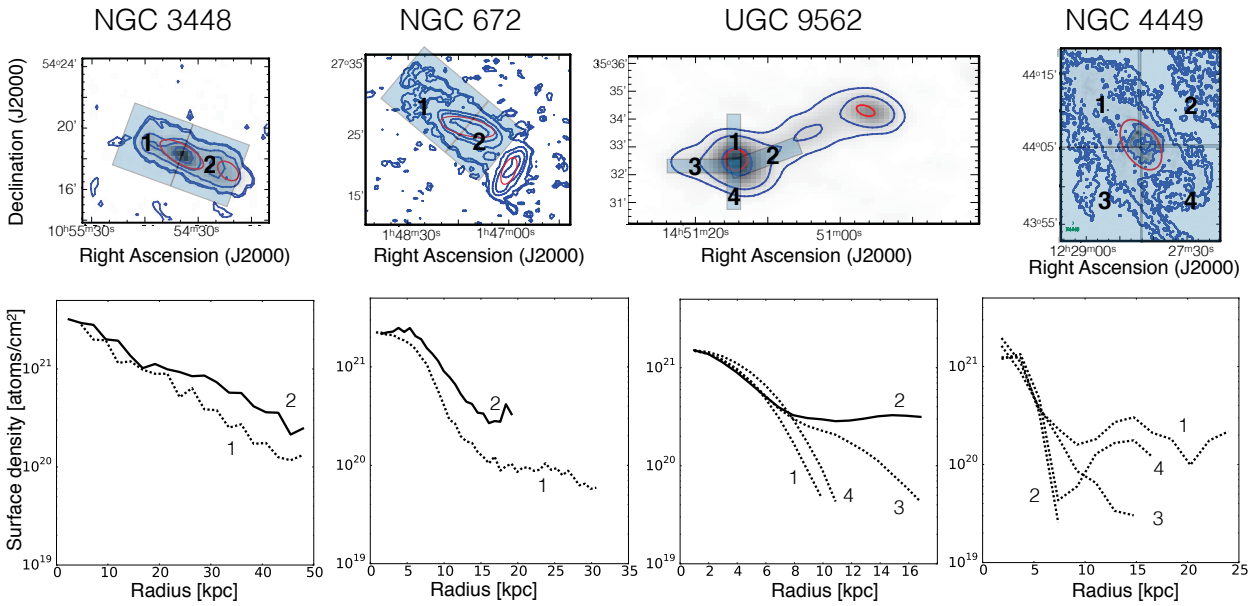

Figure 4.3: **Top row:** HI contours (blue) of the dwarf pairs in our sample that are isolated with $\Theta < 0$. The 2MASS extents of all dwarfs are shown in red ellipses. Here we used deeper data from Hunter et al. (1998), zoomed in on N4449. The numerated boxes indicate regions of the primary dwarf for which we compute HI surface density profiles (see below). **Bottom row:** HI surface density profiles vs radial distance from 2MASS ellipse centre in two or four different directions (see numerated boxes) for each primary dwarf galaxy in each pair. We use two lines if the inclination of the primary dwarfs are high. Solid lines indicate the direction of the bridge connecting the primary to the smaller companion. All profiles show a flattening towards the smaller companion (due to the higher densities in the bridges), however their HI distributions do not show indications of material stripped by ram pressure (no rapid drops to lower column densities in profiles and no asymmetric trailing features). Since there is no bridge connecting NGC 4449 and DDO125, no solid line is shown on the plot.

NGC 672 & IC 1727, UGC9560 & UGC 9562 and NGC 4449 & DDO 125 (from left to right).

All isolated pairs, except for the NGC 4449 pair, show gaseous bridges connecting the two dwarfs indicating a mutual tidal interaction (e.g. Toomre & Toomre 1972, Combes 1978, Hibbard & Mihos 1995, Barnes & Hernquist 1998, Gao et al. 2003, Besla et al. 2010, Besla et al. 2012). Interestingly, NGC 4449 and its companion DDO 125 have the largest separation of the isolated pairs, which could explain why a bridge is not present at this interaction stage. The bridges in the three other pairs are all continuous in HI column density and have smooth velocity gradients across the bridges. The surface density profiles of the first three primary isolated dwarfs (Figure 4.3: lower row) flatten out towards the smaller companion (where dense bridge material is present). The existence of bridges in these isolated pairs implies that material is being removed from the lower mass companion due to the presence of the nearby dwarf (i.e. gas is being pre-processed) and that this process takes place without the aid of other environmental factors (such as a nearby massive host galaxy). While the NGC 4449 pair does not have a bridge, the HI map shows signs of interaction through its gaseous arm surrounding its stellar component (see Appendix 4.A.10 for more details).

Thus, based on our limited sample dwarf-dwarf interactions alone do not seem to create asymmetric extended tails or obvious truncation of the gaseous disks, but tidal pre-processing appears to be taking place.

4.3.1.2 Intermediate tidal index pairs

The dwarfs evolving in the vicinity of massive host galaxies can give insight to how the environmental effects will influence the dwarf pair interactions. We therefore search for evidence of asymmetries indicating ram pressure stripping (such as truncated HI disks and one sided trailing tails) in the non-isolated pairs.

In Figure 4.4 we show the HI maps of the 3 pairs in our sample with $0 < \Theta < 1.5$: NGC

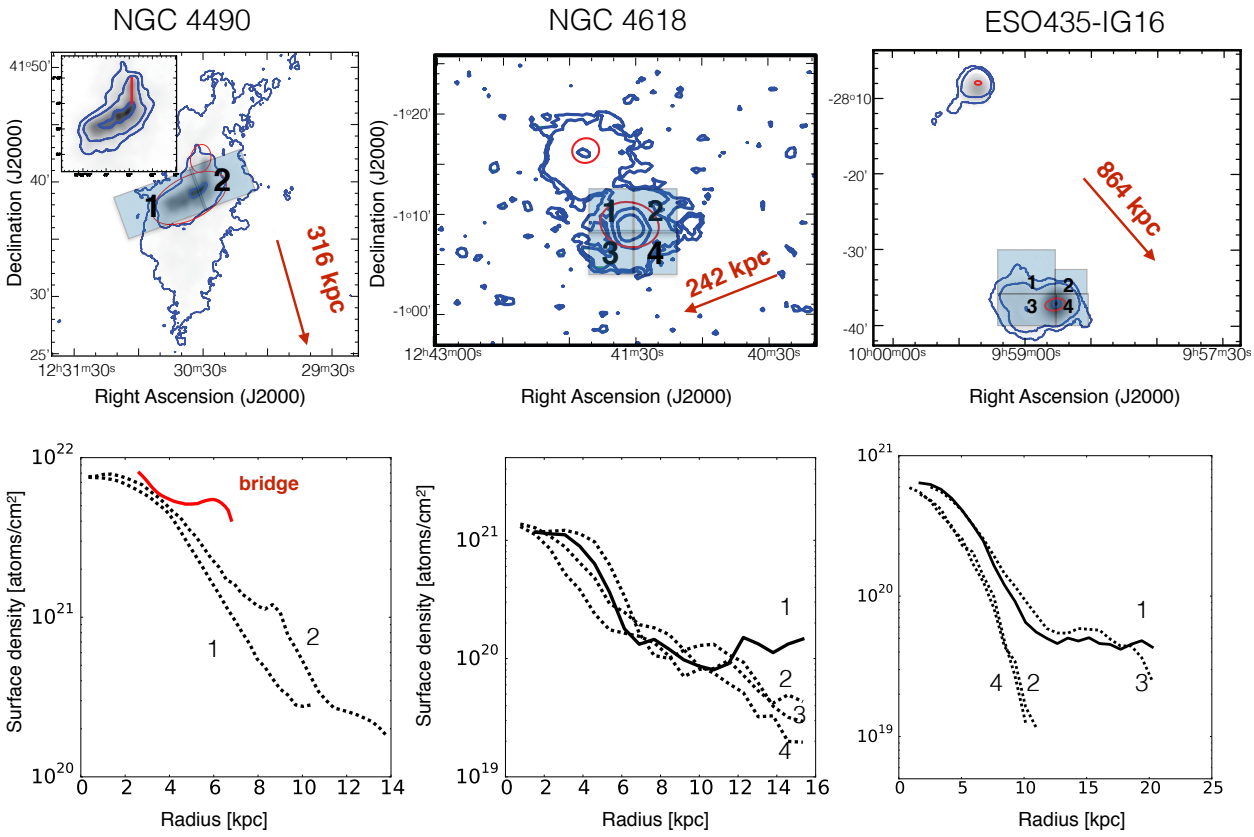

Figure 4.4: **Top row:** HI contours (blue) of the dwarf pairs in our sample that have $0 < \Theta < 1.5$. The 2MASS extents of the dwarfs are shown in red ellipses and the location of the massive host is illustrated by red arrows along with the projected distance to the host in kpc. The numerated boxes indicate regions of the primary dwarf for which we compute HI surface density profiles (see below). **Bottom row:** HI surface density profiles vs radial distance from the 2MASS ellipse centre in different directions (see numerated boxes) for each primary (most massive) dwarf galaxy in each pair. Solid lines indicate the direction of the bridge connecting the primary to the smaller companion. Due to the high inclination of the NGC 4490 system (left), we plotted the surface density using only two regions, and plot the density in the bridge separately (see zoomed box and red solid line). The surface density profiles show a flattening towards the smaller companion, however their HI distributions do not show indications of material stripped by ram pressure (no rapid drops to lower column densities in the HI profiles in the direction of the massive hosts, as compared to towards the other directions and no asymmetric trailing features in the envelopes nor surface density profiles).

4490 & NGC 4485, NGC 4618 & NGC 4625 and ESO435-IG16 & ESO435-IG20. The red arrows indicate the direction of the nearest massive host, which the pairs could in principle be moving towards. The HI distributions of NGC 4490 & NGC 4485 and NGC 4618 & NGC 4625 are both symmetric, with no hint of an extended one-sided tail or a truncation in any direction. NGC 4618 & NGC 4625 have overlapping HI disks, which is also seen in the flattening of the surface brightness profile of NGC 4618 in this direction (Figure 4.4: bottom, right panel, region 1). However, it is unclear from the velocity gradient in the WHISP maps, whether the gas connecting the two galaxies is a bridge or just a projection effect of overlapping HI profiles, as there is only a vague indication of a smooth gradient (van der Hulst et al. 2001).

For NGC 4490 & NGC 4485 a very extended, low density envelope surrounds the pair. Given the symmetric nature of the envelope it is unlikely that it is present due to ram pressure stripping. The dense bridge connecting the two dwarfs indicates an ongoing tidal interaction, which could explain the extended envelope (see red, solid line Figure 4.4). We do not see envelopes in the other isolated and intermediate tidal index pairs, but those have larger pair separations. Thus, it is not surprising to find the strongest tidal signatures for the NGC 4490 pair, as the dwarfs in this pair are located very close to each other.

In contrast to the other pairs, the ESO435-IG16 pair does not have a bridge connecting the two galaxies, however there is extended material from the primary in the direction of the secondary and from the secondary in the direction of the primary, which suggests a tidal interaction between the two galaxies. The ESO435-IG16 pair is a widely separated system ($\sim$ 100 kpc), so it is possible that a dense bridge existed at some point, but now has too low of a column density (since stretched over such a large distance). The surface density profiles in region 2 and 4 of ESO435-IG16 deviate from the other two directions (they drop to lower column densities at smaller radii), which could indicate a truncation in this direction (this

is the same direction as the galaxy NGC 3056, which is $\sim$ 220 kpc away). However, as the pair is located $> 2 \times R_{200}$ (the radius at which the density of the host is 200 $\times$ the critical density of the Universe) of NGC 3056, it is unlikely that ESO435-IG16 is truncated due to ram pressure stripping (see Section 4.4.2 for an analysis of this).

Hence, the three pairs with $0 < \Theta < 1.5$, do not appear to be affected by the closest massive host galaxy and resemble the pairs evolving in isolation, i.e. that significant gas evolution is seen in the formation of bridges and extended envelopes, but there are no large scale asymmetries.

4.3.1.3 High tidal index dwarf pairs

The dwarf galaxy pairs that have tidal indices, $\Theta > 1.5$, indicating that they are not isolated from the influence of a massive neighbor are LMC & SMC, IC 2058 & PGC 75125, NGC4352 & DDO137 (see Figure 4.5). These are the most likely pairs to be affected by ram pressure stripping and tides from the hosts in our sample.

In Figure 4.5 we show the HI maps of the three pairs with $\Theta > 1.5$ (see Table 4.3 for details on each massive host galaxy). These pairs are all within R_{200} of their hosts. The red arrows illustrate the inferred direction of motion of the dwarf pairs (in the case of the LMC we know this from HST proper motion observations (Kallivayalil et al. 2009), and for the other two pairs, we assume that the dwarfs are moving towards their host galaxy).

From Figure 4.5 (top row) it is evident that the morphologies of the HI distributions all show asymmetries and have material stripped preferentially in the opposite direction of the inferred direction of motion. The LMC and NGC 4352 systems in particular have diffuse tails that extend in the opposite direction of their direction of motion (inferred direction for the NGC 4532 pair). For the LMC pair the diffuse tail is detectable at column densities $> 7 \times 10^{19}$ atoms cm^{-2}, where the diffuse tail is only detected at column densities $< 7 \times 10^{18}$

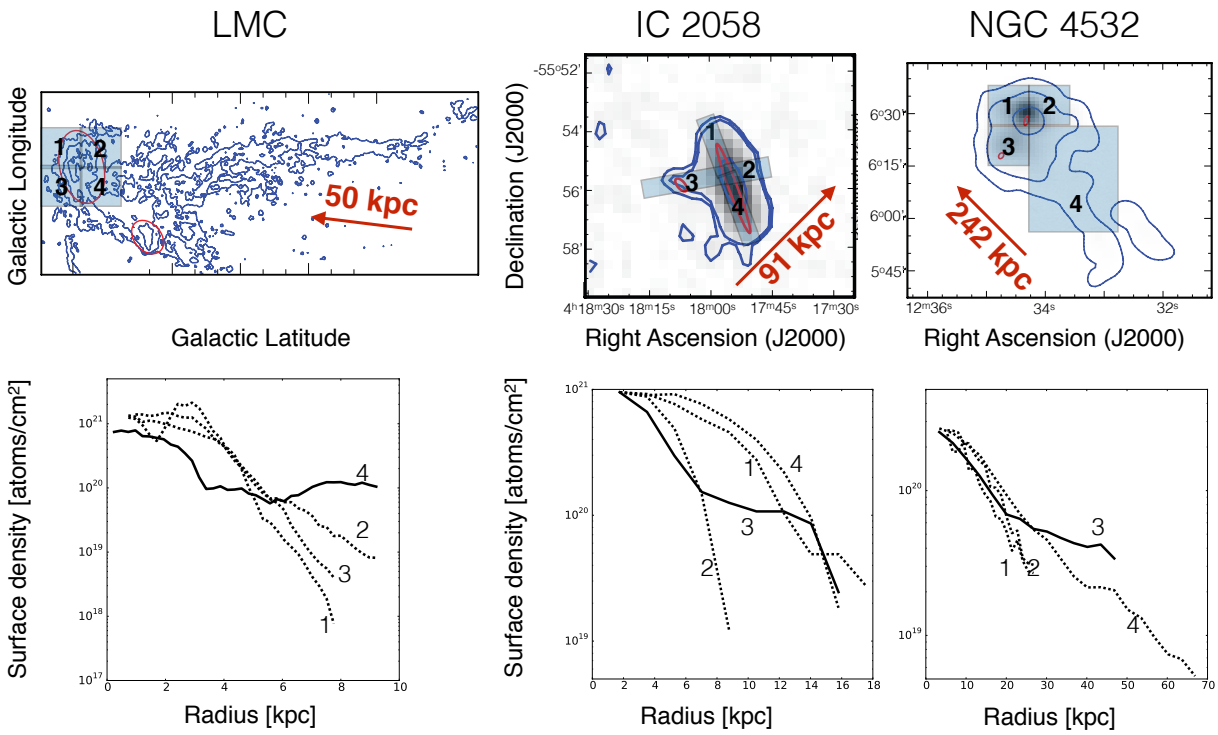

Figure 4.5: **Top row:** HI contours (blue) of the four dwarf pairs in our sample that have $\Theta > 1.5$ indicated by the name of the primary dwarf. The 2MASS extents of all dwarfs are shown in red ellipses, and the assumed direction of motion (true for the LMC/SMC motion) through the halo of the massive host is illustrated by red arrows along with the projected distance to the host in kpc. The numerated boxes indicate regions of the primary dwarf for which we compute HI surface density profiles (see below). **Bottom row:** HI surface density profiles of the primary dwarfs (the most massive dwarf in pair) vs radial distance from the 2MASS ellipse centre in four different directions (see numerated boxes) for each primary dwarf galaxy in each pair. Solid lines indicate the direction of the bridge connecting the primary to the smaller companion. All profiles except for NGC 4449 show a flattening towards the smaller companion (due to the higher densities in the bridges), all profiles show rapid drops in column density in the direction towards the massive host galaxy and all profiles are extended in the opposite direction of the host (due to trailing tails, except for IC 2058 for which the companion is located in this direction making it difficult to disentangle the effect of the companion vs trailing material).

atoms cm^{-2} for the NGC 4532 pair. If the dwarf galaxy pairs are in fact moving through the halo material of the more massive host galaxies (as we know is the case for the LMC & SMC) this extended material has the shape that we would expect from ram pressure stripping (trailing material), which is also observed for the HI distributions of massive spiral galaxies as they fall into clusters (e.g. Chung et al. 2007). For the LMC & SMC, Putman et al. (1998) found a low surface density leading neutral gas component to the Magellanic Stream indicating that the tidal forces along with ram pressure stripping is shaping the MS. Whether leading tidal streams are also present in our other high tidal index pairs is not clear from the level of sensitivity of these HI maps.

In Figure 4.5 (bottom row) we demonstrate how the average HI surface density profiles of the primary dwarf galaxies vary in different directions (see numerated regions centred on the 2MASS ellipses of each primary dwarf galaxy). Interestingly, the surface density profiles all flatten out in the direction towards the smaller companion dwarf where a bridge is present (solid lines). This was also seen for the isolated and intermediate tidal index pairs.

The HI surface density profiles all show a feature similar to a truncation in the inferred direction of motion. This could indicate that ram pressure stripping of the dwarf pairs by halo material from the host might be occurring. While the HI distributions could be extended and asymmetric due to mutual interactions between the pairs alone, truncated HI disks are difficult to explain without ongoing ram pressure stripping, and we explore the possibility of ram pressure stripping in Section 4.4.2. Interestingly, no features of truncated disks were found in the isolated or intermediate tidal index pairs.

Lastly, the surface densities in the direction opposite of the inferred direction of motion are extended (we see trailing material). In IC 2058 this is difficult to assess due to the coincident location of the secondary dwarf galaxy and the high inclination of IC 2058.

Thus, there are asymmetries in the HI distributions surrounding the dwarf pairs in our

sample that are near massive host galaxies. Mutual tidal interaction between the dwarfs might have removed the majority of the HI gas and formed bridges in all examples, but the deviation (drop to lower column densities at smaller radii) in the HI surface density profiles in the direction of the host galaxy and the lack of detectable leading streams, indicate that ram-pressure stripping could play an important role in shaping the systems, which was not the case for the isolated and intermediate tidal index dwarf pairs.

4.3.2 Global Trends: HI Extent and Gas Mass

To better understand the global gas removal processes and to quantify the features we found in the previous sections, we here investigate the amount of gas outside each pair, and its extent compared to non-paired analogs.

4.3.2.1 Quantifying the amount of gas outside the dwarf pairs

In Figure 4.6 we show the amount of gas residing outside the 2MASS ellipses of our dwarf galaxies in each pair compared to the total amount of gas in the dwarf pair system (the data points are named by the primary dwarf in each pair, but represent the amount of gas outside both pair members). In addition to making a uniform definition of the inner vs outer part of the galaxy for all dwarfs (the 2MASS ellipses), we also define a uniform column density cut to each data set (N(HI) = 7×10^{19} atoms cm^{-2}) to enable a systematic comparison between all pairs.

We find that the two highest tidal index pairs (LMC & SMC and IC 2058 & PGC 75125), which have twice the tidal index value of the other dense environment dwarf pairs and are the two closest to their hosts, have low neutral gas mass fraction of outer vs total gas. The other dwarf galaxy pair that showed signs of ram pressure (the NGC 4532 pair) has a large amount of gas in its outskirts compared to the total system, which is also the case for the

more isolated galaxies. The NGC 4532 pair is farther away from its host than LMC/SMC and its host galaxy is less massive than the Milky Way, as such, it is possible that most of the gas removed from the LMC and IC 2058 pairs is in an ionized state, whereas the gas associated with NGC 4532 is neutral. Interestingly, if we were to add the amount of ionized gas found in the MS (Fox et al. 2014) to the total amount of gas in the MS (ignoring the uniform cut in column density for the ionized gas), the outer/total gas of the LMC would be ~ 0.76 (see star in Figure 4.6), which is very similar to the NGC 4532 pair (which has outer/total = 0.74). This supports the idea that the HI in the NGC 4532 tail has not yet been ionized (see HST-COS result presented in Appendix 4.A.3).

While the majority of the isolated and intermediate tidal index pairs have gas mass fractions of their outer vs total neutral gas $> 50\%$, the NGC 4490 & NGC 4485 pair has a low amount of outer to total gas despite the large diffuse envelope surrounding the pair. Due to the small separation between the two dwarf galaxies, it is important to note that the bridge material connecting them is included within the 2MASS ellipses of the dwarfs leading to a higher amount of inner neutral gas in our estimates. As mentioned earlier the envelope is of low column density and the amount of mass in it is not substantial compared the amount of neutral gas residing in the dwarf galaxies ($\sim 30\%$ of the neutral gas is in the envelope). This could indicate that the tidal interaction between the two galaxies did not actually remove a substantial amount of gas, that the gas has been tidally removed but has started to fall back in, or that a substantial amount of the removed gas has been ionized. To differentiate between these processes, detailed modeling of the dynamics and gas physics is necessary (Pearson et al., in prep).

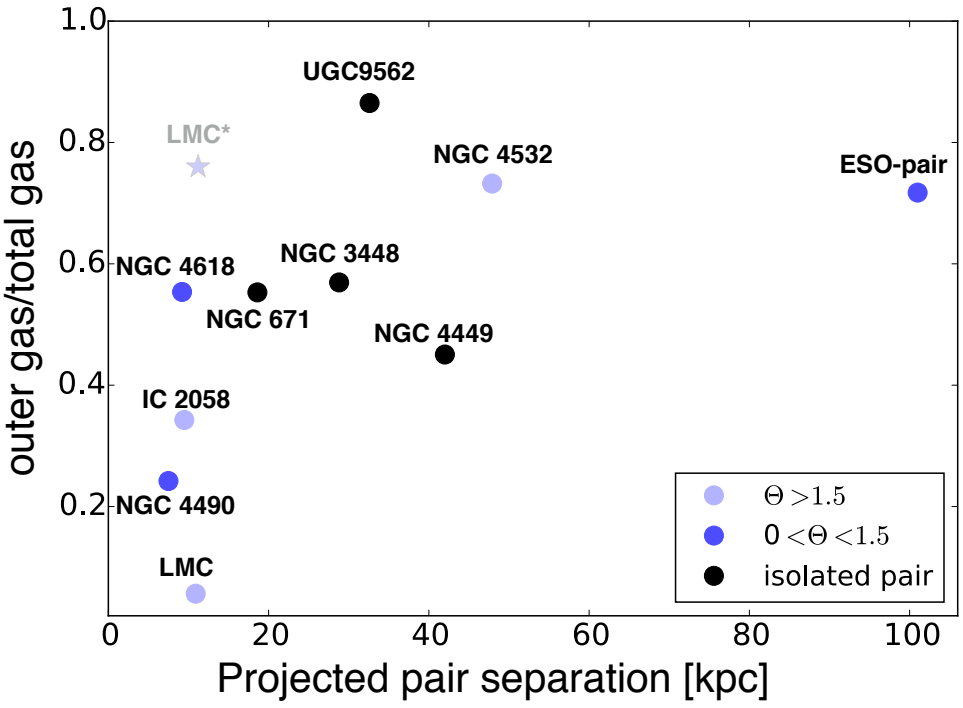

Figure 4.6: Fraction of neutral gas outside the 2MASS extents of all dwarf pairs to their total HI mass for each pair system, colour coded by their environment (tidal index, Θ). The data points are labeled based on the name of the primary dwarf in the pairs. A uniform column density cut of N(HI) = 7×10^{19} atoms cm^{-2} was made on all maps to ensure a systematic comparison. The two pairs close to a massive host (light blue) have a small fraction of gas residing outside their stellar disks. The star indicates the fraction of HI and ionized gas (Fox et al. 2014) outside the 2MASS extent of the LMC/SMC pair to the total HI gas in the pair and the ionized gas outside the pair.

4.3.2.2 The extent of the neutral gas compared to non-paired analogs

As a control sample, we use the late type dwarf irregulars from the Swaters et al. (2002) sample (hereafter S02). This sample consists of 73 galaxies that were selected from the Uppsala General Catalogue of Galaxies, requiring absolute magnitudes fainter than $M_B = 17$, which had HI flux densities larger than 200 mJy and galactic latitudes $> 10^o$. These 73 galaxies were not selected based on any environmental criteria, hence some of them could be close to massive host galaxies. Additionally, a small fraction of the dwarfs in the S02 sample are in dwarf pairs (e.g. IC 1727 and NGC 4449 which are also in our sample). To understand how the HI extents of our dwarf irregulars are affected by their mutual interaction, we investigate how they compare globally to the S02 sample.

Figure 4.7 shows the DHI extent (defined as the diameter at which N(HI) = 1.2 $\times 10^{20}$ atoms cm^{-2}) of our galaxies vs their stellar extents (defined as the extent from the 2MASS extended source catalog). These values are also listed in Table 4.2. Primary dwarf galaxies are marked by circles and secondary dwarf galaxies are marked by stars. The secondary dwarfs, DOO 125 and PGC 75125 were not included in this plot as DDO 125 is at the edge of the HI map and PGC 75125 is much smaller than the beam size (see Figure 4.1), which in both cases makes an assessment of the surface density profiles difficult. We note that due to the presence of the dense bridges, azimuthally smoothing of surface density profiles would lead to an overestimation of the DHI extent. Hence, here we use the DHI from the surface density profiles yielding the maximum extent DHI that is not in the direction of the bridge. If no apparent bridge is present, we use the azimuthally smoothed surface density profiles (i.e. for NGC 4449 and the ESO pair). For highly inclined systems (NGC 3448, UGC 6016, NGC 672, IC 1727 and IC 2058), we use the major axes for which bridge material is not present.

Of the 73 dwarf irregular galaxies in the S02 sample, 22 of them have stellar extents defined in the 2MASS extended source catalog, which enables us to compare them to our data. Of these 22 galaxies, two of them are in our dwarf pair sample (IC 1727 and NGC 4449). The dashed line in Figure 4.7 is the HI diameter vs the 2MASS stellar extent fit for the 20 non-paired dwarf galaxies in the S02 sample that have defined 2MASS stellar extents. The log(2MASS extent) and the log(DHI extent) in the 20 non-paired dwarf galaxies range from 1.5 - 2.7 [arcsec] and 2.1 - 3.1 [arcsec] respectively. Instead of extrapolating the fit from the 20 non-paired dwarf galaxies to LMC/SMC angular scales of $\sim$ 30000 arcsec, we plot the LMC/SMC 2MASS vs HI extents scaled to a distance of 11 Mpc. The errors on the HI extents are not published for the S02 sample nor for the 2MASS extents for the dwarfs. Our HI extent estimates only differ from those in the S02 sample by having non-uniform beam sizes (see Table 4.4), while the S02 beam sizes are all 60". Our HI extents could therefore be over-estimated from the emission not filling the entire beam, and we include this potential overestimate as errorbars on Figure 4.7. We do not include the equivalent for the S02 sample, but this would also cause the dashed line to have an uncertainty downward. Only three of our pairs have beam sizes larger than S02.

We find that the majority of our paired dwarf galaxies fall above the S02 fit (see Figure 4.7) and thus have more extended dense HI disks compared to their stellar extents than their non-paired counterparts. This is true even without having accounted for the HI bridge, which would only increase the DHI value. While extended HI disks are common for dwarf irregular galaxies (seen in large scatter found by S02), the fact that the majority of our dwarf galaxies systematically fall above the fit, suggests that tidal interactions between dwarfs moves gas to the outskirts of the galaxies. Hence, even the high column density neutral gas in these systems is "loosened up" (pre-processed) from tidal interactions, which might affect the efficiency of gas lost to the CGM of more massive galaxies if captured (see e.g. Besla et al.

2012, Salem et al. 2015).

Interestingly, the LMC and SMC fall below the S02 fit, indicating that their gas disks have been truncated and that gas has been pushed to the central regions. As the LMC and SMC pair is the one closest to a massive galaxy in our sample, this provides interesting insight to the importance of pre-processing and how dwarf galaxy pairs eventually feed the massive galaxies they are falling into. Additionally, UGC 9560 (the star with the smallest 2MASS extent) falls slightly below the fit, however the beam is larger than the inferred DHI, which could be affecting our accuracy in determining the HI extent. Higher resolution data would help resolve this.

None of the S02 dwarf irregulars show extended, one sided, trailing features to a depth of $\sim 7 \times 10^{19}$ atoms cm^{-2} (which are seen in the LMC/SMC and NGC 4532/DDO137 pairs), even though the S02 sample was not selected based on any environmental criteria. This further strengthens the argument that pre-processing via dwarf-dwarf tidal interactions are key in removal of gas to the outskirts, and that environmental processes can subsequently shape this extended material, causing truncations and dominant trailing streams.

4.4 Discussion

In the previous section, we found that gas was moved to the outskirts of dwarf galaxies in tidal interactions (see Figure 4.6 and 4.7) and through environmental effects (as seen in the extended tails present in the high tidal index pairs presented in Figure 4.5). Motivated by these results, we explore in Section 4.4.1 whether this gas is unbound and fully removed from our dwarf pairs. Since ram pressure appears to play an important role in moving gas to the trailing tails in our high tidal index pairs, we investigate the host halo densities needed to produce these ram pressure signatures in Section 4.4.2. Independent of the environment,

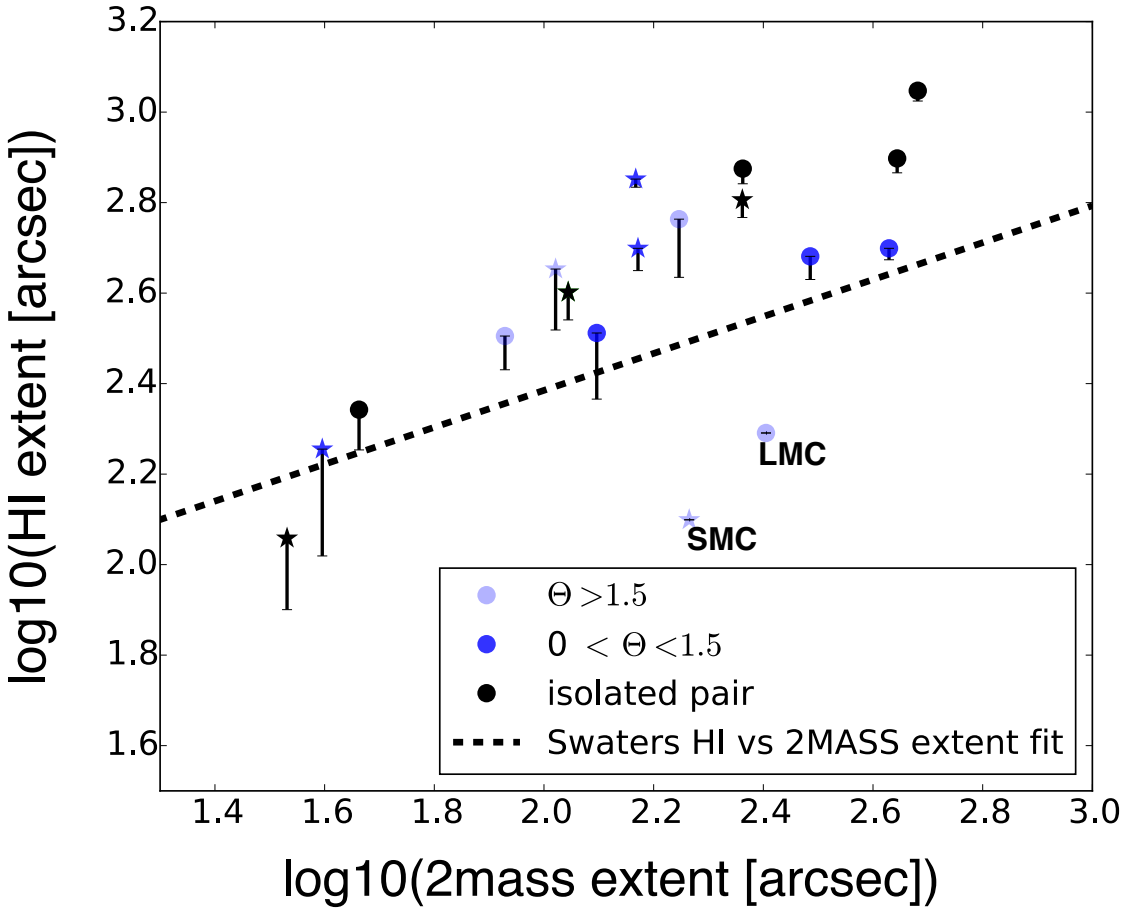

Figure 4.7: The HI extent of all the dwarf galaxies at N(HI) = 1.2×10^{20} atoms cm^{-2} plotted vs the 2MASS extent of all the dwarf galaxies in our sample colour coded by environment (tidal index, Θ). The circles represent the primary dwarf galaxies and the stars represent the secondary dwarf galaxies. The dashed line shows the HI diameter vs the 2MASS stellar extent fit for the 20 non-paired dwarf galaxies in the Swaters et al. (2002) sample that have defined 2MASS stellar extents. To avoid extrapolating the Swaters et al. (2002) fit, the LMC/SMC have been scaled to a distance of 11 Mpc. The error bars indicate the range of HI extents possible due to potential beam dilution. We find that most of our dwarfs fall above the fit indicating that the high column density gas is tidally extended.

the majority of the dwarf pairs have dense bridges connecting the individual galaxies. In Section 4.4.3 we therefore discuss the properties and formation mechanisms of these bridges. In Section 4.4.4 we explore the star formation rates in our sample, as outflows from star formation is a different channel of moving gas to the outskirts of galaxies.

4.4.1 Is the Gas Unbound in the Interactions?

The mechanisms responsible for the morphological transitions of galaxies (e.g. the formation of dwarfs spheroidal galaxies) is still an open question. Grcevich & Putman (2009) found evidence that ram pressure stripping is responsible for the transition of Local Group dwarf galaxies from gas rich to gas poor systems. Others argue that dwarf spheroidals can be produced in mergers between disky dwarf galaxies (e.g. Ebrová & Łokas 2015, Kazantzidis et al. 2011). Additionally, it has been suggested that the origin of a large amount of metals in the IGM (Danforth & Shull 2008) could be due to outflows from the shallower potential wells of dwarf galaxies (e.g. Schwartz & Martin 2004, Martin 2005, Tolstoy et al. 2009). It is uncertain whether mutual tidal interactions between dwarfs can serve as a mechanism for gas removal (although the existence of actively star-forming dwarfs in the field (Geha et al. 2012) suggests this is unlikely to remove all gas from the dwarfs). Removing gas through dwarf-dwarf interactions would be a different channel of transforming from gas rich dwarf irregulars to gas poor systems (e.g. dwarf spheroidals) and simultaneously feed the IGM with baryons. For more massive galaxies, Barnes (2016) recently showed that the extended tails formed in tidal interactions remain bound to the merging galaxies. Using numerical simulations, Bekki (2008) showed that dwarf-dwarf merging can trigger central starbursts and transform the merging dwarfs into blue compact dwarfs (BCDs). While the starburst will consume some of the gas, the newly formed BCDs were surrounded by massive extended HI envelopes, indicating that a substantial amount of HI mass remains bound and is not lost

to the IGM in dwarf interactions.

To explore the question of whether dwarf-dwarf interactions prior to final coalescence can facilitate the morphological transformation of gas rich irregular galaxies to gas poor dwarf spheroidals and whether their interactions feed baryons to the IGM, we utilize available velocity maps to assess whether the extended gas distributions surrounding our dwarf pairs are in fact bound to the primary dwarf galaxy. In particular, we adopted an NFW profile (see Eq. 4.4) for the primary dwarf in each pair and calculated the escape velocity (see Eq. 4.5) at the radius of the extent of the HI profile (hence this is limited to the sensitivity of the data). We subsequently compared the escape velocity from each primary at this radius to the average velocity maps of each galaxy after subtracting the systemic velocities of the galaxy of interest (see values in Table 4.5).

For all pairs, except for the LMC and NGC 4532 pairs, we found that the escape velocity from the primary was larger than the gas velocity at the edge of the HI distribution (see Figure 4.8). The LMC and NGC 4532 pairs are the only two systems with extended tails in the vicinity of a massive host. The escape velocities at the edges of each HI profile for all other pairs ranged from 204-249 km s^{-1}, where the velocity of the gas after subtracting the systemic velocities ranged from: 20-150 km s^{-1} (see Figure 4.8). Most pairs have gas velocities which are 100 km s^{-1} lower than the escape velocity. Hence, from this simple estimate the gas appears to remain bound to the dwarfs despite their tidal interactions, indicating that the gas in the outskirts will eventually fall back to the pairs and continue to fuel star formation.

For the LMC/SMC pair, which has a long trailing stream, we estimated the escape velocity in the stream at a distance of 150 kpc from the LMC, though it has been found

We here assume that the measured radial velocity of the gas is representative of the actual velocity the gas.

The mass of the secondary dwarf was not included in this calculation, but including it would only enhance the escape velocity further, which would lead to the same conclusion: that the gas is bound to the pairs.

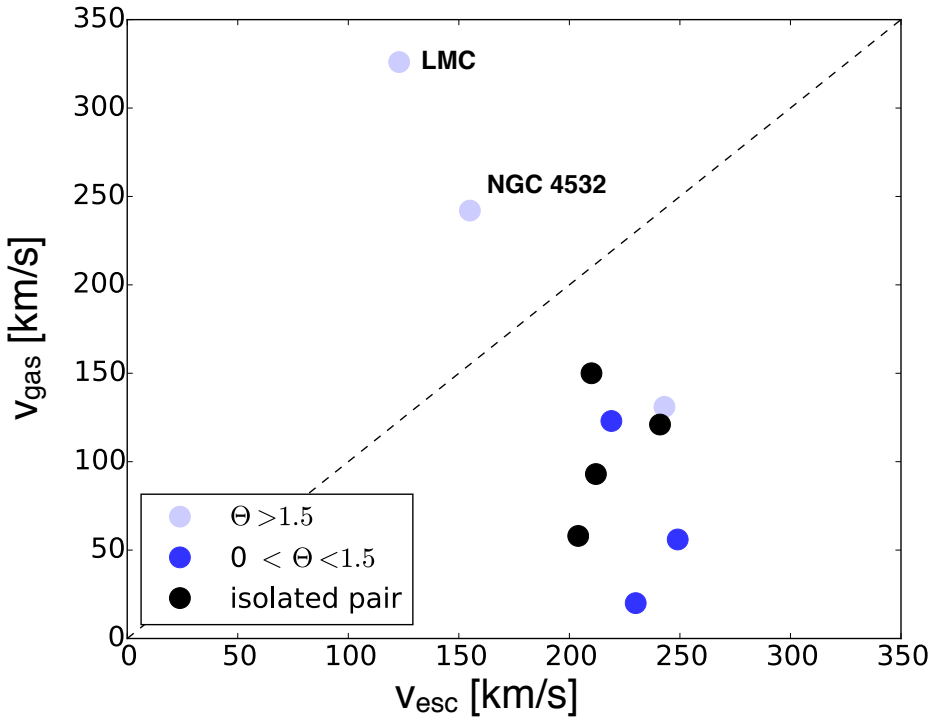

Figure 4.8: The gas velocity at the edges of the HI envelopes/profiles (estimated from velocity channel maps after subtracting the systemic velocity of the galaxy of interest) vs the escape velocity (see Eq. 4.5) of the gas at this distance, calculated by adopting an NFW profile (see Eq. 4.4) for the primary dwarf in each pair. For all pairs except for the LMC pair and NGC 4532 pair, the extended gas remains bound to the dwarfs.

to extend to larger distances (e.g., Nidever et al. 2010). The velocity of the gas in the stream at this distance is 326 km s^{-1} after subtracting the systemic (GSR) velocity of the LMC (Nidever et al. 2010). Similarly, the escape velocity from the LMC at this distance is $v_{\rm esc}$ = 123 km s^{-1}. The velocity limit of 123 km/s encompasses most of the HI mass (see Putman et al. 2012, Figure 2), but the extended ionized component of the stream extends well beyond this and is most likely unbound. For comparison, the escape velocity from the MW (assuming a total mass of 2 $\times 10^{12}$ and adopting an NFW profile) at a distance of 100 kpc is $v_{\rm esc} \sim$ 432 km s^{-1}, hence the strength of the MW potential is much stronger than the strength of the LMC potential at the edges of the trailing stream.

Similarly, the NGC 4532/DDO137 pair has a long trailing tail stretching 500 kpc away from the pair (Koopmann et al. 2008). The majority of the mass of the system is within 150 kpc, so in consistency with the LMC calculation above we estimate the escape velocity at 150 kpc from NGC 4532. We found that $v_{\rm esc}$ = 155 km s^{-1}. The velocity of the gas in the stream at this distance after subtracting the systemic velocity of NGC 4532 is 242 km s^{-1}. Hence, the material at this distance and out to the edge of the stream (at $\sim$ 500 kpc) is not bound to NGC 4532. To compare this to the tidal field from the host, NGC 4570, we computed the escape velocity from NGC 4570 (where we estimate the mass from abundance matching, and adopt an NFW profile) at a distance of 392 kpc from the host (as the pair is already 242 kpc away and the stream material is 150 kpc further). We found that $v_{\rm esc} \sim$ 340 km s^{-1}. Hence, the strength of the host potential is much stronger than the strength of the NGC 4532 potential in the trailing stream, as the case for the LMC pair.

Although, this is a simple way of estimating the relative tidal influences on the trailing streams, we can conclude that the trailing streams for the LMC and NGC 4532 are likely unbound from the dwarfs and are most likely bound to their massive host galaxies. This provides an interesting insight into how gas is truly removed from these systems, as the gas

in all isolated and intermediate tidal index pairs appears to remain bound in the mutual interaction between the dwarfs in the pairs. Dwarf-dwarf interactions seem to be an efficient way to "park" HI gas at large distances, providing a continuous source of fuel for star formation. However, it requires external environmental forces to ultimately cut off this gas supply channel and quench low mass galaxies (supporting the findings of Stierwalt et al. 2015), and the tidal interactions alone will not transform gas rich dwarf irregulars into gas poor systems, nor feed the IGM with significant baryons. In the future, it will be interesting to take deeper HI observations of IC 2058 and other dwarf pairs as a further test.

4.4.2 Exploring the Effects of the CGM of the Host Galaxies

Since we think ram pressure could be important for the gas removal process (see Section 4.3.1.3 and 4.4.1), we explore the influence from ram pressure further in this section. In particular, we make order of magnitude estimates of the required CGM densities of the host galaxies for ram pressure to explain the asymmetries in the HI profiles other than the bridges.

The COS-Halos Survey (Tumlinson et al. 2013, Werk et al. 2014) found that more massive galaxies ($\log M_*/M_\odot < 11.5$) have halo gas within 160 kpc, which was the limiting distance from their central galaxies. Similarly, Bordoloi et al. (2014a) found that a substantial amount of carbon is located > 100 kpc away from galaxies of masses $9.5 < \log M_*/M_\odot < 10$, and Liang & Chen (2014) found CIV enriched halos out to ~ 160 kpc for galaxies of similar masses. Whether or not this CGM extends further from the centres of these galaxies is yet to be determined, however, theoretical work predicts that the CGM extends out to virial radius of galaxies (e.g. Joung et al. 2012, Hummels et al. 2013, Fumagalli et al. 2014).

One way to quantify the importance of ram pressure stripping is to use the Gunn & Gott (1972) relation. Salem et al. (2015) demonstrated that they could probe the density of the halo material of the Milky Way using the Gunn & Gott (1972) relation and by assuming

that the one-sided truncation of the LMC HI disk was due to ram pressure by the Milky Way's halo. They found that the Milky Way halo density is 1.1 $\pm$ 0.44 $\times$ 10^{-4} cm^{-3} at the pericenter passage of the LMC (R = 48.2 $\pm$ 5 kpc). Interestingly, the high sensitivity data of the SMC shows large variations in column densities in the four different regions (see Figure 4.9), and we can examine the ram pressure effect on the SMC from this. In region 3 the surface density profile deviates from the other directions at a column density of $\sim 10^{19}$ atoms cm^{-2} at a radius of R = 4.2 kpc (see Figure 4.9). If we define R = 4.2 kpc as the truncation radius of the SMC based on the deviation in column densities at this radius, we can do an estimate of the halo density needed to produce this truncation radius using Eq. 4.3. Using the 3D velocity of the SMC (Kallivayalil et al. 2013), we obtain a halo density of the MW of $\sim$ 6 $\times 10^{-5}$ cm^{-3} (see Table 4.6) at the distance of the SMC (61 kpc). This is somewhat lower than the Salem et al. (2015), but reasonable for the Milky Way halo, especially given the potential partial shielding by the LMC.

To estimate the required host halo densities to produce truncation features in all $\Theta > 0$ primaries, we use the same procedure as for the SMC outlined above. We list the values used for our simplified Gunn & Gott relation in Table 4.6. For the HI surface density profiles that do not show rapid drops in column densities in the inferred direction of motion, we use the extent of the data as the truncation radius.

We first used the relative velocities of the pair to the hosts to get an upper limit on the CGM densities (as we here ignore any tangential motion and therefore underestimate the velocities). Note that we use the 3D velocities of the LMC and SMC (Kallivayalil et al. 2013), which are higher than the line of sight Δv for these galaxies (Δv_{LMC} = 278 km s^{-1} and Δv_{SMC} = 158 km s^{-1}). Using line of sight Δv for the LMC and SMC instead of the 3D velocities would yield slightly higher CGM densities, as the required CGM density scales inversely with velocity.

Secondly, to estimate a lower limit on the CGM densities we assumed that the largest velocity they could move through the halos of the host galaxies would be the escape velocity from their host (although they could in principle be moving faster). For all $\Theta > 0$ pairs except for NGC 4490 this velocity was higher than the relative velocity of the pair and hosts. The values used and the results of the calculations of upper and lower limit on the CGM densities required for the halos are listed in Table 4.6.

Using the relative velocity of the host and pair for all $\Theta > 0$ primary dwarfs, we find that the $\rho_{\rm CGM}$ of their hosts need to be 3×10^{-4} - 2×10^{-5} cm^{-3} at their current locations to explain the deviations in their profiles from a truncation due to ram-pressure. Using the escape velocity from the host, we find that the $\rho_{\rm CGM}$ of the hosts need to be 3.5×10^{-5} - 5.3×10^{-6} cm^{-3} (here we leave out NGC 4490 as its $v_{\rm esc} < v_{\rm sep}$, see Table 4.6 for CGM densities required for this system). While the halo density result is reasonable for the LMC & SMC, it seems unlikely that the other pairs (see separate discussion of IC 2058 below) are moving through densities of 10^{-4} - 10^{-5} cm^{-3}, since these dwarfs are > 200 kpc from their hosts in projection. From theoretical predictions, the halo densities of MW type galaxies are $< 10^{-5}$ cm^{-3} at radii > 200 kpc (e.g. Sommer-Larsen 2006), which is also supported observationally through studies of the Milky Way's hot halo gas (e.g. Miller & Bregman 2013) and by the COS-Halos Survey results finding declining metal surface density profiles with radius within 160 kpc of L^* galaxies (Werk et al. 2013, Werk et al. 2014). Hence, ram pressure does not appear to be sufficient to truncate and remove gas from these systems (unless they are in fact moving at much larger velocities than assumed here).

An exception is IC 2058. If it is moving at its escape velocity through the halo material of its host, the required halo density is $\sim 5 \times 10^{-6}$ cm^{-3}, which might be plausible at the projected distance of 91 kpc from its quite massive host, NGC 1553. The high inclination

Note that we get lower values for $\rho_{\rm CGM}$ than Salem et al. (2015), due to the simplified version of the Gunn & Gott criterion used here.

of the system makes it difficult to assess whether the HI profile is indeed truncated. With higher resolution data we will be able to examine this and with deeper data we can see if trailing material is present in the opposite direction of its host.

For the NGC 4532 pair, it is possible that even though ram pressure is not the main driver of gas loss, it is shaping the gas distribution. Ram pressure is also not thought to be the main gas loss mechanism for the Magellanic System (Besla et al. 2012) and may be less significant than expected even for low mass dwarf systems (Emerick et al. 2016). Ram pressure by the CGM of the host may be shaping the NGC 4532/DDO137 tail after the dwarf-dwarf interaction "loosened up" (pre-processed) the gas. The densities this system is moving through could also be somewhat higher than expected at this radius due to the environment at the outskirts of the Virgo Cluster.

Another possibility is that tides from the hosts are removing gas from the dwarfs and truncating the HI profiles at their tidal radii. To investigate this, we estimate the tidal radius, r_t, of our high tidal index dwarfs using equation 8.91 from Binney & Tremaine (2008):

$$r_t = \left(\frac{m}{3M}\right)^{1/3} r_p \tag{4.6}$$

where m is the dark halo mass of the primary dwarf (see Table 4.5) , the pericenter distance, r_p, is estimated as the current projected distance from the dwarf to the host (see Table 4.3) and M is the dark halo mass and stellar mass of the host enclosed within r_p calculated using an NFW profile. We find that for all high tidal index dwarfs $r_t > 5.5 \times R_{\rm trunc}$ (see Table 4.6). Hence, tides from the hosts likely do not have a substantial effect on removing gas from the dwarfs. The fact that we do not see a leading stream for NGC 4532 further disfavors the idea that its trailing tail is formed due to tides from its host. However, once the gas has left the dwarfs through other mechanisms, tides from the host can be stronger than the tides

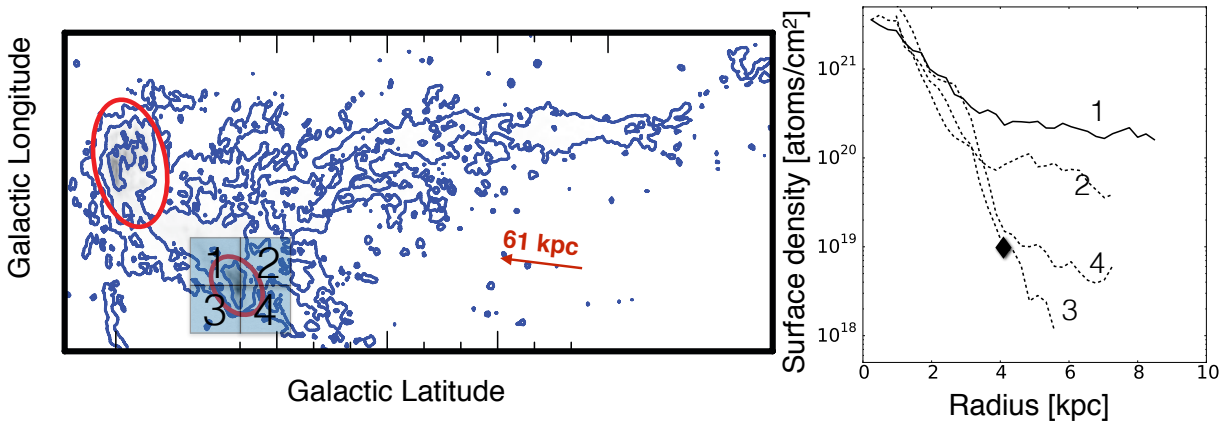

Figure 4.9: **Left**: HI map of the Magellanic System (see Putman et al. (2003) for Galactic coordinates of the data) with four regions (see numerated boxes) centred on the 2MASS ellipse of the SMC. The outer column density shown in the map is N(HI) = 1.0 × 10^{19} atoms cm^{-2}. **Right:** Surface density profiles of the SMC HI distribution in four different directions (see numerated regions on map). The black diamond shows the radial extent at which the SMC disk is truncated ($R_{\rm trunc}$ = 4.1 kpc). The surface densities vary by several orders of magnitude in column density in the four directions due to: the presence of a dense bridge connecting the LMC and SMC (solid line, region 1), the Magellanic Stream (2), the material lagging behind the SMC disk (4) and the general direction of motion towards the MW, where the profile is truncated (3). The sensitivity of the data is limited to a column density of N(HI) = 2.0 × 10^{18} atoms cm^{-2}.

from the dwarfs themselves and gas might be lost to the hosts (as we found in Section 4.4.1).

Hence for all pairs, the process of moving gas to large radii, the formation of bridges and asymmetries are most likely due to a mutual interaction between the two dwarfs in the pair. Additionally, ram pressure from the MW appears to be truncating the HI profiles of the LMC and SMC, and for both the LMC and NGC 4532 pair, ram pressure from the massive hosts appear to be shaping their tails. Therefore, our results indicate that the CGM of this system likely extends out to distances > 200 kpc, as models predict (e.g. Joung et al. 2012, Hummels et al. 2013, Fumagalli et al. 2014). This will be observationally probed with the future CGM^2 project (Werk et al., in prep.) as they plan to map the CGM of L^* galaxies out to 3 × $R_{\rm vir}$.

4.4.3 The Dense Bridges

Based on our definition of bridges as being continuous in HI column density and having a velocity gradient that smoothly connects one galaxy to the next, seven of our ten dwarf pairs have "true" bridges connecting the galaxies (see Figure 4.1 and Table 4.4). For the ones that do not have bridges, pair separations are large (> 40 kpc). Thus HI bridges appear ubiquitous in dwarf pairs, regardless of environment and thus serve as the clearest hallmark of interaction. The column density in these bridges all have N(HI) $\gtrsim 10^{20}$ atoms cm^{-2}, except for the bridge connecting NGC 4532 and DDO137, which has N(HI) $\sim 8 \times 10^{19}$ atoms cm^{-2} (and is probed by a larger beam). These column densities are often several orders of magnitude higher than the column density at the same radial distance from the centre of the primary in the directions that are not pointing towards the companion dwarf (see solid lines in Figures 4.3, 4.4 and 4.5).

Since our sample was selected specifically with the purpose of including interacting dwarf galaxy systems, it is not surprising that many of our pairs have bridges connecting the two dwarfs. However, the high HI column densities in the bridges not only hints at a recent close encounter between the pairs (e.g. Toomre & Toomre 1972, Combes 1978, Hibbard & Mihos 1995, Barnes & Hernquist 1998, Gao et al. 2003, Besla et al. 2010, Besla et al. 2012)), but it also introduces a compelling case for why star formation should occur in the bridges connecting interacting galaxies and not in the trailing tails. Besla et al. (2012) showed that a high density bridge between the LMC and SMC can easily be reproduced from simulations of their mutual interaction. Interestingly, there is evidence for star formation in the Magellanic Bridge (e.g. Irwin et al. 1985, Demers & Battinelli 1998, Harris 2007) while no star formation has been observed in the Magellanic Stream.

From pure tidal theory, it is not expected that the density in the bridges should be

higher than in the tails. However, the higher column densities in the bridges than in the tails can be explained from hydrodynamics (see e.g. hydro simulations in Besla et al. 2010 and observational evidence of dense HI bridges in Gao et al. 2003), since ram-pressure acts most efficiently on low column density gas (i.e. produces low column density tails). In addition, the high density in the bridges could be explained from overlapping gas from both galaxies which could be occurring in a close encounter (this is likely the formation mechanism of the Magellanic bridge; Besla et al. 2012).

Several other studies have found evidence for star formation in HI bridges connecting more massive interacting galaxies (e.g. de Mello et al. 2008, Condon et al. 2002), and evidence for star formation in bridges of pre-merger dwarf galaxies (including the NGC 4490/85 bridge) have been found in the UV (Smith et al. 2010). Studying the bridges of dwarf pairs in the optical, UV and higher resolution HI could reveal higher column density cores that have formed in gaseous tidal features, which could provide insight to a different mechanism for star formation than in disks (e.g. Werk et al. 2010).

4.4.4 Star Formation in the Dwarfs

Gas outflows from galaxies owing to supernova feedback is a different gas removal process that could move gas out to large distances (e.g. Hopkins et al. 2014, Arraki et al. 2014, Pontzen & Governato 2012, Tolstoy et al. 2009, Clemens & Alexander 2002). Furthermore, it has been proposed that mergers between gas rich dwarfs can trigger starbursts and potentially transform the dwarfs into gas poor systems (e.g. Bekki 2008). Hence, it is important to assess the impact of star formation as we are investigating extended gas around dwarfs and their mutual interactions.

Stierwalt et al. (2015) showed that the dwarf galaxy pairs in their sample had enhanced star formation rates when at smaller pair separations. Furthermore, they showed that the

dwarf galaxies that were star bursting (Hα equivalent width: EQW $>$ 100 Å) did not appear to be gas depleted. This agrees with the findings of Bradford et al. (2015) that the smallest gas fractions of dwarfs in isolation are $f_{\rm gas} \sim 0.3$, indicating that star formation and stellar feedback from e.g. supernovae does not remove all gas from these systems. Interestingly, the dwarf galaxies in the Stierwalt et al. (2015) sample that were gas depleted (hence within 200 kpc of a massive host) did not show an enhancement in SF with interaction stage (Stierwalt et al., in prep.). This indicates that once the gas is ultimately removed by the environment, interactions between dwarf galaxies do not enhance the star formation.

Motivated by gas outflows owing to supernova feedback and by the results in Stierwalt et al. (2015), we investigate whether our paired dwarfs are outliers in terms of their SFs when compared to a larger sample of non-paired dwarfs. In particular, we compare the SFRs derived from Hα luminosities of our dwarfs (see Table 4.2) to the SFRs in Lee et al. (2009) (hereafter L09). The L09 sample consists of 300 dwarf galaxies (both pairs and single dwarfs) within 11 Mpc of the MW in a B-band luminosity range of -11 $< M_B <$ -20. Starburst galaxies are 6% of this sample. Our SFRs were inferred from the Hα luminosities based on the following relation:

$$\mathrm{SFR}[\mathrm{M}_{\odot}\mathrm{yr}^{-1}] = 7.9 \times 10^{-42} L(H\alpha)(\mathrm{erg/s}) \tag{4.7}$$

In Figure 4.10 we show the SFRs of our dwarf galaxies (black points) over plotted on the L09 sample (grey points). Nine of our individual dwarf galaxies are overlapping with the L09 sample. L09 used a different relation to calculate the SFRs than Equation 4.7, however we re-calculated all SFRs in their sample using Equation 4.7. It is evident that our dwarfs are all within the scatter of the L09 sample, although a fit through our sample would yield

a systematically higher SFR for a given M_B, than the L09 fit (dotted line). It is important to note that in the specific B-band range of our sample, the majority of the L09 data points also fall above their fit, which is based on a range of B-band absolute magnitudes from -11 < M_B < -20. Seeing an enhancement in the star formation rates will depend on the interaction history of the pairs, hence they could have had a burst of star formation previously. The fact that our pairs do not appear to have an overall enhancement in SF when compared to the other L09 data in that M_B band range, supports the idea that the extended gas is due to tidal pre-processing of the gas and not due to outflows from star formation.

To investigate whether it is reasonable that our dwarf pairs do not appear to have an overall enhanced SF, we can compare the results to similar studies of more massive galaxies. Recently, Knapen & Cisternas (2015) found that while the majority of interacting (massive) galaxies do not have enhanced SFRs, those that do have extremely high SFRs when compared to their non-paired counterparts (see also Knapen et al. 2015). Patton et al. (2013) found that the strongest enhancements for massive galaxies were seen at small separations: < 20 kpc, which is in agreement with the results of Scudder et al. (2012) and Davies et al. (2016), who also find that galaxy interactions trigger enhanced star formation.

Whether dwarf galaxies are also more extremely elevated in their SFRs at separations < 20 kpc is unclear, as Stierwalt et al. (2015) did not look into pair separation bins smaller than 50 kpc. There are four dwarf pairs in our sample that have pair separations < 20 kpc for which we have SFRs (the LMC pair, the NGC 4618 pair, the NGC 4490 pair and the NGC 672 pair, Table 4.1). While their Hα derived SFRs are within the scatter of the L09 sample (see Figure 4.10), the Hα equivalent widths (EQWs) of NGC 4490/85 (our closest pair) are both > 65 Å (Kennicutt et al. 2008), which could indicate that they have triggered star bursts (indeed L09 found that NGC 4449 and NGC 4485 are starbursts as their EQWs exceeded the logarithmic mean of their dwarf sample by 2σ). However, there are no signs

that the four pairs with the smallest pair separations in our sample have systematically elevated SFRs compared to the other dwarf pairs. Hence, so far our findings do not agree with the results for more massive galaxies, but given the small sample size the SFRs of our dwarfs could be consistent with the type of enhancement seen for massive galaxies (e.g. Patton et al. 2013).

4.5 Conclusion

In this paper we have investigated HI synthesis maps of a local sample of interacting dwarf galaxy pairs (the LV-TNT sample) and have considered the importance of environment and dwarf-dwarf interactions in removing and shaping the gas. We note that our sample consists of only 10 pairs and that our conclusions can be strengthened with future HI observations of interacting dwarf pairs.

Our results and conclusions are summarized as follows:

1. Dwarf galaxy pairs residing in the proximity of a massive host galaxy ($\Theta > 1.5$) are affected morphologically by their environment, when compared to dwarf galaxy pairs interacting in isolation. Their surface density profiles are highly asymmetric indicating both tidal interactions with each other (bridges) and interactions with the halos of the massive hosts (extended tails in the directions of their host). In contrast, dwarf galaxy pairs with $\Theta < 1.5$ primarily have variations in their surface density profiles in the direction towards their companion, where dense bridges are present.

2. The majority of dwarf galaxy pairs have a large amount of gas in their outskirts ($> 50\%$ of their total gas mass is beyond their 2MASS stellar extents) and they appear to have extended dense gas envelopes when compared to non-paired dwarf irregulars. This

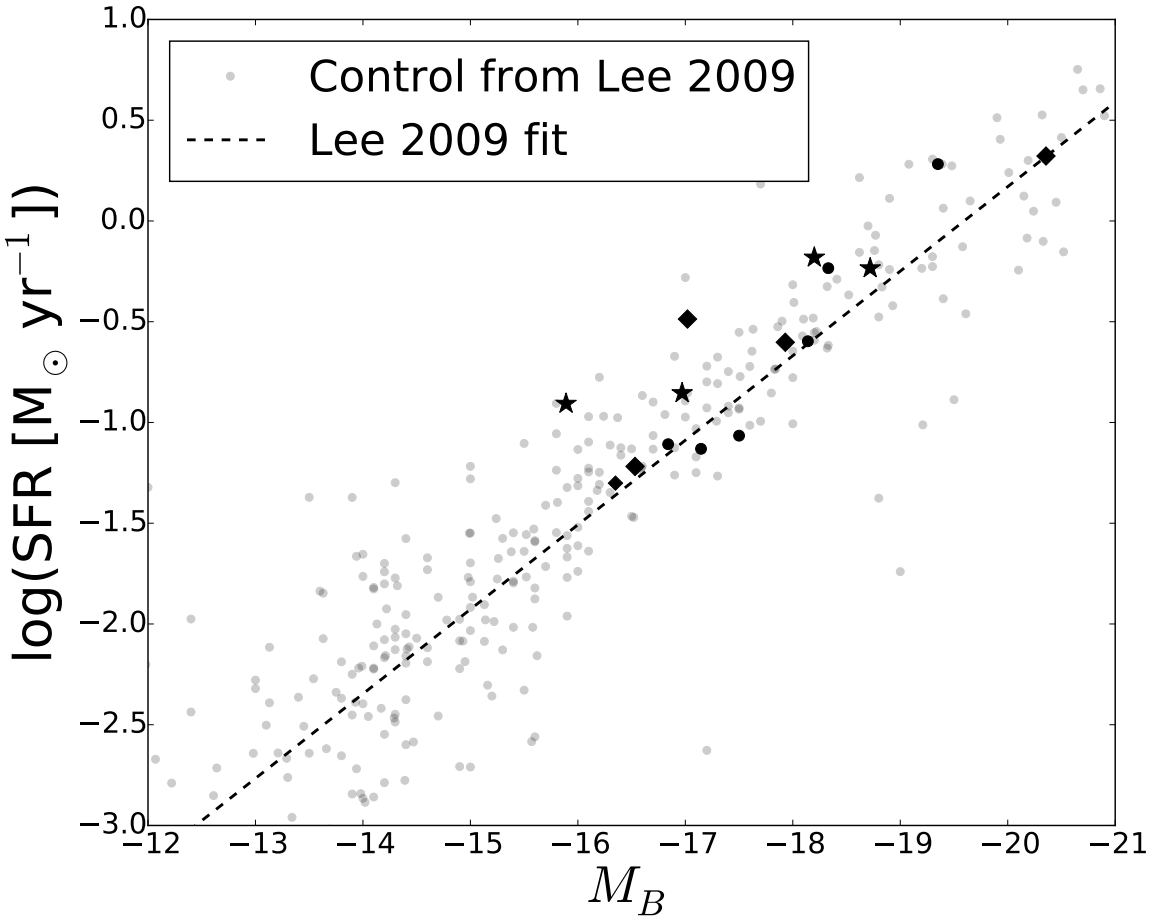

Figure 4.10: Hα inferred star formation rates vs B-band magnitude for 300 dwarf galaxies from the Lee et al. (2009) sample (grey) plotted along with our sample of dwarf galaxies (black stars: EW $>$ 70 Å, black diamonds: no EW available, black circles: EW $<$ 70 Å). The dotted line represents the fit to the 300 dwarfs in the Lee et al. (2009) sample.

implies that dwarf-dwarf interactions move gas to the outskirts of these galaxies.

3. The gas remains bound to the systems from tidal interactions between the dwarfs alone. As such, this gas will be reaccreted by the system, providing fuel for future star formation.

4. Two of the three $\Theta > 1.5$ pairs (in the vicinity of a massive host galaxy) have long, trailing tails. We find that the gas in these tails is unbound and likely lost from the pairs to the massive host halos. This combined with point 3. above indicates that the environment is what ultimately quenches low mass galaxies, by preventing the gas from returning to these systems. This supports the conclusions from Stierwalt et al. (2015) and Bradford et al. (2015).

5. For the pairs in the vicinity of a massive host, ram pressure stripping alone is found to be insufficient to remove gas from the pairs. Pre-processing via dwarf-dwarf interactions is key to enabling this gas supply channel to the CGM if they eventually fall into the halos of more massive galaxies. For the LMC and NGC 4532 pairs, ram pressure stripping appears to be shaping the gas once it leaves the pairs.

6. Seven of our ten dwarf pairs have dense bridges connecting them. The bridge column densities are higher than in other regions in the outskirts of the systems, potentially explaining why SF can be ongoing in the bridge and not in the other extended structures (e.g. as observed in the LMC/SMC and NGC4490/85 bridges). Such high column

density tidal structures require close passages between the two pairs to form.

7. The star formation rates of our sample are within the scatter of the Lee et al. (2009) sample of nearby dwarf irregular galaxies, hence our dwarf pairs do not have substantially elevated star formation rates. This supports that the extended structures we find are from tidal interactions and not from outflows.

This study highlights dwarf-dwarf interactions as an important part of the baryon cycle of low mass galaxies, enabling the "parking" of gas at large distances to serve as a continual gas supply channel until accretion by a more massive host prevents this gas from being reaccreted by the pair.

Acknowledgements

We thank Fiona Audcent-Ross, Marcel Clemens, Thijs van der Hulst, Diedre Hunter, Rebecca Koopmann, Janice Lee, Moire Prescott, Eric Wilcots and Dennis Zaritsky for sharing their data of the dwarfs in this sample. We also thank Jessica Werk, Gerhardt Meurer, Lauranne Lanz, Joshua Peek and Kathryn V. Johnston for useful discussions. MEP acknowledges support for program 13383 from NASA through a grant from the Space Telescope Science Institute, which is operated by the Association of Universities for Research in Astronomy, Inc., under NASA contract NAS5-26555. XF is supported by an NSF Astronomy and Astrophysics Postdoctoral Fellowship under award AST-1501342. We have made use of the WSRT on the Web Archive. The Westerbork Synthesis Radio Telescope is operated by the Netherlands Institute for Radio Astronomy ASTRON, with support of NWO. This paper includes archived data obtained through the Australia Telescope Online

Archive (http://atoa.atnf.csiro.au). The Australia Telescope Compact Array (/ Parkes radio telescope / Mopra radio telescope / Long Baseline Array) is part of the Australia Telescope National Facility which is funded by the Australian Government for operation as a National Facility managed by CSIRO.

4.A Dwarf Galaxy Pairs in our Sample

In this appendix, we describe each dwarf galaxy pair in our sample. The pairs are listed in order of decreasing tidal index, Θ. See Table 4.1 and 4.2 for details on the physical properties of each pair, and Table 4.4 and Figure 4.1 for details on all HI observations.

Using Eq. 4.4, Eq. 4.5 and the line of sight velocity separation of each pair listed in Table 4.1, we find that each secondary dwarf is bound to its primary dwarf (i.e. $v_{\rm sep} < v_{\rm escape}$).

4.A.1 LMC, SMC

As described in Section 5.1, the evidence for an ongoing interaction between the LMC and SMC is the extended HI distribution surrounding the pair (e.g. Putman et al. 2003 which is the data set used in this study). The Magellanic Clouds are currently $\sim$ 23 kpc apart (11 kpc projected) and 50 kpc from the Milky Way disk. Their currently measured stellar mass ratio is ($M_{*\rm LMC}/M_{*\rm SMC}$) $\sim$ 10 (van der Marel et al. 2002, Stanimirović et al. 2004). As of yet, stellar components to the gaseous streams have not been found, and therefore the interaction is revealed only by the gaseous extensions (although Belokurov & Koposov (2016) recently found an over density of Blue Horizontal Branch stars approximately aligned with the proper motions of the clouds). The Magellanic System has an HI mass $> 10^9$ $M_\odot$ and an extended ionized gas mass of the same magnitude (Putman et al. 2003; Fox et al. 2014).

The origin of the extended gaseous features has remained ambiguous since their discovery (Mathewson et al. 1974). Many models have invoked primarily tidal or ram pressure forces from the Milky Way halo to create the gaseous features (Gardiner & Noguchi 1996, Connors et al. 2006a, Mastropietro et al. 2005, Diaz & Bekki 2011); others create the gas streams primarily through the interaction of the Clouds themselves (Besla et al. 2010, Besla et al. 2012), while including the tidal influence of the MW. The Clouds possess a well studied bridge that has a smooth velocity gradient of 50 km s^{-1} (Nidever et al. 2010), which is evidence for a mutual interaction between the two dwarfs. The bridge is known to be an ongoing site of star formation (SF) (e.g. Irwin et al. 1985, Demers & Battinelli 1998, Harris 2007).

The Magellanic Clouds are important members of our Local Volume sample, as they are in a high tidal index environment ($\Theta = 3.7$) owing to their proximity to the MW.

4.A.2 IC 2058, PGC 75125

IC 2058 and its companion PGC 75125 are located 18.1 Mpc (Nasonova et al. 2011) from the Milky Way, but only 91 kpc in projection from the more massive galaxy: NGC 1553. The pair's close proximity to a more massive galaxy, results in a high tidal index of $\Theta = 3.2$. Observations of this system were done in 2006 and 2007 with the Australian Compact Telescope Array (ATCA) and are presented for the first time in this work (see Figure 4.1 and Table 4.4). Kilborn et al. (2005) studied the system using single dish observations from the Parkes Telescope and concluded that it is a part of the NGC 1566 group (the projected distance to NGC 1566 is 350 kpc). The two dwarf galaxies, IC 2058 and PGC 75125, are separated from each other by only 9.5 kpc in projection, and a small HI bridge is connecting them (see Figure 4.1). The bridge connecting the two galaxies is a strong indicator of an

The data were uniformly weighed with a spectral resolution of 20 km s^{-1} and pixel size of 19″/pixel.

ongoing tidal interaction (e.g. Toomre & Toomre 1972). Additionally, the line of sight velocity separation of the two dwarfs is only $\sim$ 10 km s^{-1}, and their stellar mass ratio is quite high ($\sim$ 11, similar to the Magellanic Clouds). Hence, it is likely that the two galaxies are in fact interacting.

Hα imaging of the system (available on NED) suggests a potential ram pressure stripping of the smaller companion, as both edges of the disk seem to be warped in the same direction away from the larger galaxy. However, due to the small angular size of PGC 75125, this can not be confirmed with the HI map.

4.A.3 NGC 4532, DDO 137

NGC 4532 and DDO 137 are defined as Magellanic class dwarf galaxies and are interacting, as evident from their large common HI envelope and HI tail that extends for 200-500 kpc (Koopmann et al. 2008; Hoffman et al. 1992). These galaxies have elevated star formation rates and a disturbed central kinematic structure (Koopmann & Kenney 2004; Hoffman et al. 1999). The two galaxies are separated in projection by 48 kpc, their velocity separation is only $v_{\rm sep} \sim 27$ km s^{-1}, and they have a similar stellar mass: $(M_{*\rm NGC\ 4532}/M_{*\rm DDO137}) = 1.4$. The system is located in the outskirts of the Virgo Cluster 13.8 Mpc from the MW (Tully et al. 2009), and it is located $\sim$ 240 kpc away from NGC 4570 in projection, which has $M_* > 4 \times 10^{10}$ M$_\odot$. This results in a tidal index of $\Theta = 1.5$, which places the pair in our high tidal index group (see Table 4.3). However, if the NGC 4532 pair is farther from the MW than 13.8 Mpc (as suggested by e.g. Willick et al. 1997), the pair would be in the intermediate tidal index group (see Table 4.3) and could be less affected by its host than assumed throughout the rest of the paper.

The large trailing tail (see Figure 4.1) could be an indication of ram pressure stripping by the more massive NGC 4570. Due to the fortunate alignment of a bright background quasar

with the NGC 4532/DDO137 tail, the Hubble Space Telescope Cosmic Origin Spectrograph (HST-COS) was used to probe the metallicity and ionization conditions of the tail (HST Proposal ID: 13383). However, little or no absorption was detected at the velocity of the system despite going through the HI tail. This little or non-detection could indicate that there is no ionized gas present in the trailing tail of the system. In contrast, we know that the Magellanic Stream has a large amount of ionized gas (see Fox et al. 2014). The fact that NGC 4532/DDO 137 is located much farther from its host than the Magellanic System is from the MW, might explain why its tail is not ionized (see Section 4.4.2 for more details).

4.A.4 NGC 4618, NGC 4625

The NGC 4618 and NGC 4625 dwarf galaxy pair is an example of two Magellanic spirals that have adjoining HI distributions (see Figure 4.1). The pair is located 7.9 Mpc from the MW and are only separated by 9.2 kpc in projection and have a $v_{\rm sep} = 77$ km s^{-1}. They reside in the vicinity of the more massive galaxy, Messier 94, which is ~ 240 kpc away from the pair, yielding a tidal index of $\Theta = 1.4$ (i.e. much lower than the MW's influence on the Magellanic System (MS)). The morphology of the HI distribution around NGC 4618 reveals a ring-structure ($\sim$10% of total HI mass), which could indicate recent tidal interactions. However, Kaczmarek & Wilcots (2012) argued that it is not clear that this is due to close proximity of NGC 4625. In fact, they conclude that the two Magellanic spirals are not interacting. This was also argued by Bush & Wilcots (2004), who pointed out that the degree of asymmetry in both galaxies is indistinguishable from the expected asymmetry in lopsided galaxies. From the maps presented in van der Hulst et al. (2001) the HI column density appears continuous between the two galaxies. However, Kaczmarek & Wilcots (2012) pointed out that the interface where the two disks overlap are separated by 50 km s^{-1} in velocity (i.e. a non-smooth velocity gradient), and that it therefore unlikely that this is a

true gas bridge (see their Figure 13).

However, due to the disturbed velocity field of NGC 4618 (see Bush & Wilcots 2004) and the fact that the two galaxies are in close proximity of one another in both velocity and position space, with overlapping HI disks, we include them in our sample. We note that the kinematics and HI distribution of NGC 4625 are surprisingly regular, and we consider this system as a potential non-interacting dwarf pair in the rest of the paper.

4.A.5 NGC 4490, NGC 4485

The NGC 4490 and NGC 4485 pair is an example of a well studied, nearby Magellanic System analog. The two dwarfs are surrounded by one of the most extended known HI envelopes ($\sim$ 50 kpc), and they are connected by a dense HI bridge, which is continuous in its HI column density and has a smooth velocity gradient (Huchtmeier et al. 1980, Clemens et al. 1998, and see Figure 4.4). The dwarfs are separated by only $\sim$ 7.5 kpc, and their $v_{\rm sep}$ = 72 km s^{-1}. Their interaction is also evident from the disturbed stellar morphology of NGC 4490 (warped disk), and from the fact that NGC 4485 is experiencing a starburst (Lee et al. 2009). While Clemens et al. 1998 argue that the envelope is formed from outflows, Elmegreen et al. (1998a) argued that both NGC 4490 and NGC 4485 have stellar tidal tails associated with their disks, which strengthens the argument for a tidal origin of the HI envelope.

The closest massive galaxy to the dwarf system is NGC 4369 ($M_* = 2.6 \times 10^{10}$ $M_\odot$), which is located $\sim$ 310 kpc from the pair in projection (although $v_{\rm sep} > 400$ km s^{-1} for the pair and host). It has been discussed whether the extended envelope is of tidal origin or due to ram pressure. However, as NGC 4369 is $\sim$ 10 times less massive than the Milky Way and as the dwarf pair system is quite far from the more massive galaxy, a ram pressure stripping scenario seems unlikely (see Section 4.4.2). The pair is therefore a nice analog to the Magellanic System prior to infall, as it has an extended, more symmetric HI distribution

surrounding the pair.

In this paper we adopt the distance of. 7.14 Mpc to the pair (Theureau et al. 2007), while e.g. Karachentsev et al. (2013) found a distance of 5.8 Mpc to the pair. Adopting a different distance would yield slightly different stellar masses, physical pair separations and inferred physical extents of the galaxies which will not affect our conclusions of this paper (see how these parameters scale with distance in Table 4.1 and 4.2). Using the distance found in Karachentsev et al. (2013), the estimated projected distance to the host would be 256 kpc. However this would not change the tidal index group that we use for this pair throughout the paper (see Table 4.3).

4.A.6 ESO 435-IG16, ESO 435-IG20

Observations of ESO 435-IG16 & ESO 435-IG20 were taken with ATCA in 2002 (Kim et al. 2015). The two dwarfs are located 11.6 Mpc from the Milky Way and are at a large separation from each other ($\sim$ 100 kpc). Despite the separation, evidence of an interaction or ongoing gas removal between the two galaxies is seen in the eastern extension of ESO 435-IG16 and in the tail of ESO 435-IG20 (see Figure 4.1). Their stellar mass ratios are 1:10, and they are only separated by 9 km s^{-1} in line of sight velocities. The pair is located $\sim$ 860 kpc from a more massive host (NGC 2997), which is $\sim$ 2 times farther than the R_{200} of the host. The pair is also located $\sim$ 220 kpc in projection from another dwarf (NGC 3056) which is on the West (right) side of the pair. Interestingly, the HI distributions seem more extended to the opposite direction of the location of NGC 3056, however it is unlikely that dense halo material of this dwarf extends out to 220 kpc (Bordoloi et al. 2014a), which is beyond R_{200} of NGC 3056. HIPASS observations of the system (which reach a column density of N(HI) $\sim 10^{18}$ cm^{-2}), show that the two dwarfs are covered by a large envelope of neutral gas surrounding both galaxies (Kim et al. 2015).

4.A.7 NGC 3448, UGC6016

The NGC3448 and UGC6016 pair is a part of the M81 group of galaxies and is located 24.7 Mpc from the MW. The closest galaxy more massive than 5 $\times 10^9$ $M_\odot$ is located within a projected distance of $\sim$ 1050 kpc from the pair (NGC 3310), yielding a tidal index of $\Theta < 0$. Hence, we classify this pair as being isolated. Both a leading and trailing stellar tail of NGC 3448 have been observed with multiple telescopes (first published in the ARP catalog 1966). The two dwarf galaxies are separated by $\sim$ 30 kpc and are rotating with opposite spin. Their line of sight velocities are separated by 143 km s^{-1}. Models of their interactions indicate that this is a retrograde encounter (hence the rotation of UGC6016 is opposite to that of the orbit of the encounter between the two galaxies). Toomre & Toomre (1972) showed that a retrograde encounter between galaxies will not lead to a dramatic distortion in the kinematics (see also D'Onghia et al. 2009). This explains the relatively undisturbed, regular stellar dynamics of UGC 6016 as discussed by Noreau & Kronberg (1986). Noreau & Kronberg (1986) showed that the perturbed HI morphology of NGC 3448, could be satisfactorily reproduced through a tidal interaction scenario between the two galaxies. Bertola et al. (1984) studied this system in detail using optical, UV and radio observations. They also conclude that a tidal interaction can explain the morphology of the gas distribution surrounding the pair, which is overlapping (the peak of the HI emission is centred on NGC 3448, and the other peak appears to be offset from the optical centre of UGC 6016) with a smooth velocity gradient between the pairs.

4.A.8 UGC 9562, UGC 9560

Compelling evidence that the dwarf galaxies UGC 9562 and UGC 9560 are interacting was presented by Balkowski et al. (1978) and Cox et al. (2001), who showed that there is a

gaseous bridge connecting the two galaxies ($M_{HI} = 2.8 \times 10^8$ $M_\odot$). The bridge is continuous in HI column density between the two pairs, and the velocity gradient is smooth (see Cox et al. 2001 for velocity map and higher resolution HI data). The system is located 25.5 Mpc from the Milky Way and the two pairs are at a projected separation of $\sim$ 33 kpc and a line of sight velocity separation of 112 km s^{-1}. In addition to the gaseous bridge connecting the two dwarfs, Cox et al. (2001) found evidence of a polar ring around UGC 9562 with Hα line emission, which could be a remnant of a recent interaction. The two galaxies are located more than 1.5 Mpc from any massive galaxy, hence they are evolving in isolation.

4.A.9 NGC 0672, IC 1727

NGC 672 and IC 1727 are two dwarf spiral galaxies, that are connected through a massive HI bridge (see Figure 4.1). The bridge is continuous in HI column density, and the velocity gradient in the bridge connecting the two galaxies is smooth (see WHISP velocity maps: van der Hulst et al. 2001). They are located 7.9 Mpc from the MW and their optical centres are separated only by 19 kpc. The galaxy pair is evolving in isolation, as the nearest, more massive galaxy is $>$ 1.5 Mpc away. Combes et al. (1980) argued that a gravitational interactions between the two galaxies is taking place, based on the offset in HI centres compared to the galaxies optical centres, and from the bridge of gas connecting them. Subsequently, Ramirez-Ballinas & Hidalgo-Gámez (2014) found that the interstellar medium of IC 1727 is very perturbed, which could be a sign of recent interaction. Furthermore, the WHISP map (van der Hulst et al. 2001) and the more recent HALOGAS map (Heald et al. 2011) of the system shows a tidal arm trailing behind NGC 672, which also suggests an ongoing tidal interaction.

4.A.10 NGC 4449, DDO 125 (and halostream)

NGC 4449 is unusual since it has two counter rotating gas systems (Hunter et al. 1998) and has a large tidal or spiral feature surrounding its optical disk. DDO 125 is located $\sim$ 40 kpc from the centre of NGC 4449 with a velocity separation of only 10 km s^{-1}. The two galaxies are both located approximately 4 Mpc from the Milky Way, and there is no bridge connecting the two galaxies, though an extension in HI is seen in the direction of DDO 125 from the NGC 4449 HI distribution. DDO 125 does not seem tidally disturbed in HI nor in its stellar component, however its $M_{\rm HI}/L_B$ is low, indicating that it could have lost a substantial amount of gas in an encounter with NGC 4449.

Karachentsev et al. (2007) noticed an elongated stream candidate near NGC 4449, and recently Martínez-Delgado et al. (2012a) presented deep, wide-field optical imaging of the faint stellar stream (NGC 4449B) 10 kpc southeast of NGC 4449, which has a stellar mass of only $\sim$5 $\times$ 10^7 M$_\odot$. Additionally, Rich et al. (2012) pointed out the "s"-shape of the stream, which is characteristic of an ongoing tidal disruption. This stellar stream provides an alternative explanation for the complex HI structure of NGC 4449 (which includes rings, shells and a counter-rotating core). The present day mass ratios of NGC 4449 to DDO125 and NGC 4449 to NGC 4449B are 15 and 80, respectively. There is no massive host galaxy in the vicinity of the pair, which is therefore evolving in isolation.

Table 4.1: Local interacting dwarf galaxies

Primary name	Secondary name	Distance [Mpc]	Pair sep., Δd[j] [kpc] $\times(D/D_{\rm Table1})$	Vel. sep., Δv[k] [km s^{-1}]	Prim. *-mass $\times10^9$[M$_\odot$] $\times(D/D_{\rm Table1})^2$	Sec. *-mass $\times10^9$[M$_\odot$] $\times(D/D_{\rm Table1})^2$
LMC	SMC	0.05[a]/0.061[b]	11	120	2.3	0.23
IC 2058	PGC 75125	18.1[c]	9.5	10	2.7	0.24
NGC 4532	DDO 137	13.8[d]	48	27	6.2	3.0
NGC 4618	NGC 4625	7.9[e]	9.2	77	4.3	1.3
NGC 4490	NGC 4485	7.14[f]	7.5	72	7.2	0.82
ESO435-IG16	ESO435-IG20	11.6[g]	101	9.0	2.3	0.28
NGC 3448	UGC 6016	24.7[g]	29	143	3.6[l]	0.081[l]
UGC 9562	UGC 9560	25.5[g]	33	112	2.0	1.0
NGC 672	IC 1727	7.9[h]	19	84	5.0	0.96
NGC 4449	DDO 125	3.82[i]	40	10	3.7	0.24

a: Pietrzyński et al. (2013), b: Cioni et al. (2000), c:, Nasonova et al. (2011), d: Tully et al. (2009)
e: Karachentsev et al. (2013), f: Theureau et al. (2007), g: NED kinematic flow distance (Virgo + GA + Shapley) assuming $H_0 = 73$ km/s/Mpc, corrected by Mould et al. (2000). h: Sohn & Davidge (1996), i: Annibali et al. (2008)
j: Based on angular separation from centre to centre and converted to physical distance based on distance to pair.
k: From NED redshift: Δv = c $\times|z1 - z2|/(1 + (z1 + z2)/2)$.
l: Lanz et al. (2013)

Table 4.2: Properties of dwarf pairs in our sample

Host dist.	Dwarf Pair	r_{ext}[**] [arcsec]	r_{ext}[***] [kpc] $\times(D/D_{\rm Table1})$	DHI_{ext}[j] [arcsec]	DHI_{ext} [kpc] $\times(D/D_{\rm Table1})$	SFR prim. [M$_\odot$yr^{-1}] $\times(D/D_{\rm Table1})^2$	SFR sec. [M$_\odot$yr^{-1}] $\times(D/D_{\rm Table1})^2$
0-500	LMC/SMC	27996/16634	6.8/5.0	42988.0/22721	10/6.7	0.25[a]	0.05[b]
	IC 2058/PGC 75125	96.7/16	8.5/1.4	320/-	28/-	-	-
	NGC4532/DDO137	88/52*	5.9/3.5	580/550	39/ 37	0.71[d]	-
	NGC4618/25	153/74	5.3/2.8	480/500	18/19	0.29[f]	0.037[f]
	NGC4490/85	213/74	7.4/2.6	500/710	17/25	2.6[e]	0.17[e]
	ESO435-IG16/IG20	62/19	3.5/1.1	325/180	18/10	-	0.012[c]
1000 - 1200	NGC3448/UGC6016	115/55*	14/6.6	750/396	90/47	0.60[g]	0.75[j]
>1500	UGC 9562/60	23/17	2.8/2.1	220/114	27/14	0.085[h]	0.40[h]
	NGC672/IC1727	220/115	8.4/4.4	790/640	30/25	0.24[i]	0.11[i]
	NGC4449/DDO125	240/133.5	4.4/2.5	1114/-	20/-	0.59[e]	-

* Indicates that 2MASS observations of the galaxy were not available, in which case the r-band extent was used.
** All r_{ext} are determined from the 2MASS scale lengths (see Section 4.2.2).
*** Same as r_{ext}, but converted to kpc based on distance to dwarf pair.
SFRs are derived from Hα fluxes: a: Whitney et al. (2008), b: Wilke et al. (2004), c: Gil de Paz et al. (2003)
d: Koopmann & Kenney (2004), e: Clemens & Alexander (2002), f: Epinat et al. (2008), g: Lanz et al. (2013), h: Cox et al. (2001)
i: Karachentsev et al. (2004)
j: Defined as the diameter at which N(HI) = 1.2 $\times10^{20}$ atoms cm^{-2}.

Table 4.3: Properties of the host galaxies

	Dwarf Pair	Host name	Proj. dist. host[a] [kpc]	Host stellar mass $\times 10^{10}[M_\odot]$	Host dark halo mass[b] $\times 10^{11}[M_\odot]$	Θ[c]	Vel. sep., Δv[d] [km s^{-1}]
High tidal index	LMC, SMC	MW	55	6.4	34	3.7	278
	IC 2058, PGC 75125	NGC 1553	91	11.2	107	3.2	298
	NGC 4532, DDO 137	NGC 4570	242	4.8	25	1.5	224
Intermediate tidal index	NGC 4618/25	Messier 94	242	3.4	20	1.4	236
	NGC 4490/85	NGC 4369	316	2.6	6.9	0.91	479
	ESO435-IG16/IG20	NGC 2997	864	8.6	60	0.1	118
Isolated	NGC 3448, UGC6016	NGC 3310	1056	2.6	6.9	-0.65	355
	UGC 9562/60	none	> 1500				
	NGC 672, IC 1727	none	> 1500				
	NGC 4449, DDO 125	none	> 1500				

[a] The projected distances to the hosts are calculated based on the angular separation between the primary dwarf and the host galaxy at the distance of the primary (see Table 4.1), after applying the velocity cuts ($v_{sep} < 500$ km s^{-1} and $D_{project} < 1.5$ Mpc (except for the LMC/SMC where we used the average distance to the MW from the two galaxies).
[b] The dark matter halo masses are estimated using the Moster et al. (2013) abundance matching Eq. 2.
[c] Θ is the tidal index as defined in Equation 4.2. The pairs are sorted in order of decreasing Θ.
[d] Velocity separation of primary and host: $\Delta v = c \times |z1 - z2|/(1 + (z1 + z2)/2)$.

Table 4.4: HI properties of dwarf pairs in our sample

Dwarf Pair	Beam size [arcsec]	Beam size [kpc] $\times(D/D_{\rm Table1})$	HI inner $\times 10^9[M_\odot]$ $\times(D/D_{\rm Table1})^2$	HI total $\times 10^9[M_\odot]$ $\times(D/D_{\rm Table1})^2$	HI total uni[i] $\times 10^9[M_\odot]$ $\times(D/D_{\rm Table1})^2$	NHI outer [10^{19} atom/cm^2]	Telescope	Bridge present
LMC/SMC	930	0.25	0.27/0.26	0.90	0.57	0.2	HIPASS[b]	yes
IC 2058/PGC 75125	60	5.3	0.39/0.037	0.69	0.64	4.5	ATCA[c]	yes
NGC 4532/DDO 137	200	13.4	0.28/0.068	3.5	1.3	0.1	ARECIBO[a]	yes
NGC4618/25	60	2.3	0.47/0.079	1.4	1.4	7.0	WSRT[e]	not clear
NGC 4490/85	30	1.0	2.4/0.23	3.7	3.5	1.0	VLA[d]	yes
ESO435-IG16/IG20	130.4	7.3	0.14/0.055	0.8	0.69	1.0	ATCA[e]	no
NGC 3448/UGC6016	60	7.2	2.6/0.63	7.5	7.5	7.0	WSRT[f]	yes
UGC 9562/60	52.4 x 48.8	6.5 x 6.0	0.2/0.07	2.0	2.0	7.0	VLA[g]	yes
NGC 672/IC 1727	60	2.3	1.1/0.42	3.4	3.4	7.0	WSRT[e]	yes
NGC 4449/DDO 125	62 x 54	1.1 x 1.0	0.39/0.11	1.1	0.91	0.2	VLA[h]	no

Data from: a: Koopmann et al. 2008, b: Putman et al. 2003, c: ATCA archives, d: Clemens et al. 1998, e: van der Hulst et al. 2001 f: Kim et al. 2015, g: Cox et al. 2001, h: Hunter et al. 1998.
i: The total HI mass in the dwarf system after applying the uniform cut of N(HI) = 7×10^{19} atoms cm^{-2}.

Table 4.5: Escape velocities as the edges of the HI profiles

Primary dwarf name	Systemic velocity [km s^{-1}]	HI extent distance [kpc]$\times(D/D_{\rm Table1})$	Dark mass of primary $[\times 10^{11} M_\odot]$	Gas velocity at extent[a] [km s^{-1}]	Escape velocity [km s^{-1}]
LMC	84	150	1.5	326	123
IC 2058	1369	9	1.6	131	243
NGC 4532	2012	150	2.4	242	155
NGC 4618	533	14	2.0	56	249
ESO435-IG16	990	11	1.5	20	230
NGC 4490	575	49	2.6	123	219
NGC 3448	1350	30	1.8	150	210
UGC 9562	1292	20	1.4	58	204
NGC 672	429	20	2.1	121	241
NGC 4449	207	30	1.8	93	212

a: After subtracting systemic velocity of galaxy

Table 4.6: Gunn & Gott calculations

Dwarf galaxy name	$R_{\rm trunc}{}^a$ [kpc] $\times(D/D_{\rm Table1})$	$v_{\rm rot}$ [km s^{-1}]	$v_{\rm sep}$, Δv^i [km s^{-1}]	$v_{\rm esc}$ [km s^{-1}]	ρ ($v_{\rm sep}$) $\times10^{-5}$ [cm^{-3}]	ρ ($v_{\rm esc}$) $\times10^{-5}$[cm^{-3}]	$r_t{}^j$ [kpc] $\times(D/D_{\rm Table1})$
LMC	5.2	92^b	321	606	5.1	1.4	31
SMC	4.2	60^c	217	587	5.9	0.81	26
IC 2058	9.0	110^d	298	857	4.2	0.53	50
NGC 4532	22.0	110^e	224	382	7.8	2.7	132
NGC 4618	14	73^f	236	347	2.2	1.0	
NGC 4490	12	144^g	479	194	29	180	
ESO435-IG16	11	40^h	118	383	37	3.5	

a: Defined as the radius at which the surface density profile in the direction towards the massive host deviates from the surface density in other directions. If no deviation is present, $R_{\rm trunc}$ is defined as the extent of the data.
b: van der Marel & Kallivayalil (2014), c: Stanimirović et al. 2004, d: our data, e: Rubin et al. (1999), f: Bush & Wilcots (2004)
g: Huchtmeier et al. (1980), h: Kim et al. (2015)
i: From NED redshift of host and primary: $\Delta v = c \times|z1 - z2|/(1 + (z1 + z2)/2)$. For the LMC and SMC we use the 3D velocities (Kallivayalil et al. 2013).
j: Tidal radius of high tidal index dwarfs defined in Equation 4.6.

Chapter 5

Modeling the Baryon Cycle in Low Mass Galaxy Encounters: the case of NGC 4490/85

5.1 Introduction

The impact of mergers on the structure and gas content of massive galaxies has been studied extensively both theoretically (e.g. Toomre & Toomre 1972, Barnes 1988, Springel & White 1999, Dubinski et al. 1999, Barnes 2016) and observationally (e.g. Arp 1966, Sanders et al. 1988, Engel et al. 2010, Bussmann et al. 2012). However, the merger sequence and any consequent morphological transformation of low mass galaxies ($M_* < 10^{10}$ $M_\odot$) through tidal processes is not well constrained. There is reason to believe that the merger sequence of dwarf galaxies could differ substantially from that of massive galaxies. Dwarfs in the field have higher gas fractions (Geha et al. 2012, Bradford et al. 2015), higher dark matter

This section contains text from an article submitted to the Monthly Notices of the Royal Astronomical Society (Pearson et al. 2018, *submitted to MNRAS*).

to baryon ratios (e.g. Tolstoy et al. 2009) and dwarf mergers are more numerous per unit volume than massive galaxy mergers (Fakhouri et al. 2010).

In this work we present the first detailed model of an observed isolated low mass galaxy pair, NGC 4490/4485. We use this model to study in detail the role of tidal encounters with companions in the morphological evolution of low mass galaxies. Detailed dynamically matched models to real systems are needed to age-date the systems, constrain the initial encounter parameters and to understand the timescales involved in the gas cycling due to the interactions. While generic dwarf-dwarf mergers have been modeled in the literature (e.g. Bekki 2008, Kim et al. 2009), only one observed dwarf-dwarf interaction has been modeled in detail, namely the Large and Small Magellanic Clouds (LMC and SMC) (e.g. Gardiner & Noguchi 1996, Bekki & Chiba 2005, Connors et al. 2006a, Besla et al. 2010, Besla et al. 2012, Diaz & Bekki 2011,Guglielmo et al. 2014, Pardy et al. 2018). Without additional models of isolated, interacting dwarf systems, we cannot assess whether the LMC/SMC scenario is typical of dwarf interactions.

Observational studies of dwarf pairs and groups are growing (Tully et al. 2006, Stierwalt et al. 2017) providing insight to the role of dwarf-dwarf interactions in the evolution of low mass galaxies. The TiNy Titans Survey (TNT: Stierwalt et al. 2015) showed that dwarf galaxy pairs in the field ($>$ 1.5 Mpc from a massive galaxy) appear just as gas rich as their non-paired counterparts, despite exhibiting elevated star formation rates relative to unpaired field dwarfs. Recent work by Privon et al. (2017) suggests that dwarf interactions trigger large-scale interstellar medium (ISM) compression, rather than nuclear starbursts often associated with massive mergers. The high gas fractions of dwarfs in the field indicate that dwarfs (with $M_* > 10^7$ $M_\odot$) do not fully exhaust their gas through tidal interactions or internal processes (star formation, feedback etc., e.g. Bradford et al. 2015) even with their shallower potential wells (e.g. Lelli et al. 2014). However, the TNT and Bradford et al.

(2015) works are based on single dish neutral hydrogen observations (HI). Without resolved imaging it is unclear if the gas is still located within the galaxies or is spatially extended.

This motivated the Local Volume TiNy Titans Survey (LV-TNT: Pearson et al. 2016), where we investigated resolved synthesis HI maps and surface density profiles for 10 dwarf galaxy pairs located within 25 Mpc of the Milky Way (MW). We found that tidal interactions between low mass galaxies can "park" gas at large distances and that the gas is only prevented from being re-accreted to the dwarfs if the pairs are in the vicinity of a massive galaxy, as in the case for the Magellanic System. The gas at large distances is not actively participating in the formation of stars, which helps explain why the single dish TNT survey found that dwarf pairs with elevated SFRs could still have high gas fractions. The low mass galaxy pair NGC 4490/4485 is an example of one of the LV-TNT pairs with gas at large distances and will be the focus of this paper. This system is an isolated analog of the Magellanic Clouds that is surrounded by a massive, spatially extended HI complex ($>$ 50 kpc in extent Clemens et al. 1998).

In particular, we present a detailed N-body simulation that simultaneously reproduces the observed present-day morphology and kinematics of NGC 4490/4485 using *Identikit* (Barnes & Hibbard 2009). *Identikit* is a hybrid N-body and test-particle simulation, which enables a rapid exploration of the parameter space of galaxy mergers. The goal of this study is to utilize *Identikit* to test whether interactions between NGC 4490/4485 can naturally explain the origin of the observed extended gas complex surrounding the galaxy pair or whether other mechanisms, such as outflows, are necessary (e.g. as suggested by Clemens et al. 1998). Additionally, we aim to investigate the timescales involved in cycling gas in an isolated dwarf galaxy interaction and consider the affect of the interaction on the dwarfs involved.

If dwarf-dwarf tidal interactions are shown to be capable of "parking" gas at large distances, there will be important implications to our understanding of the baryon cycle of low

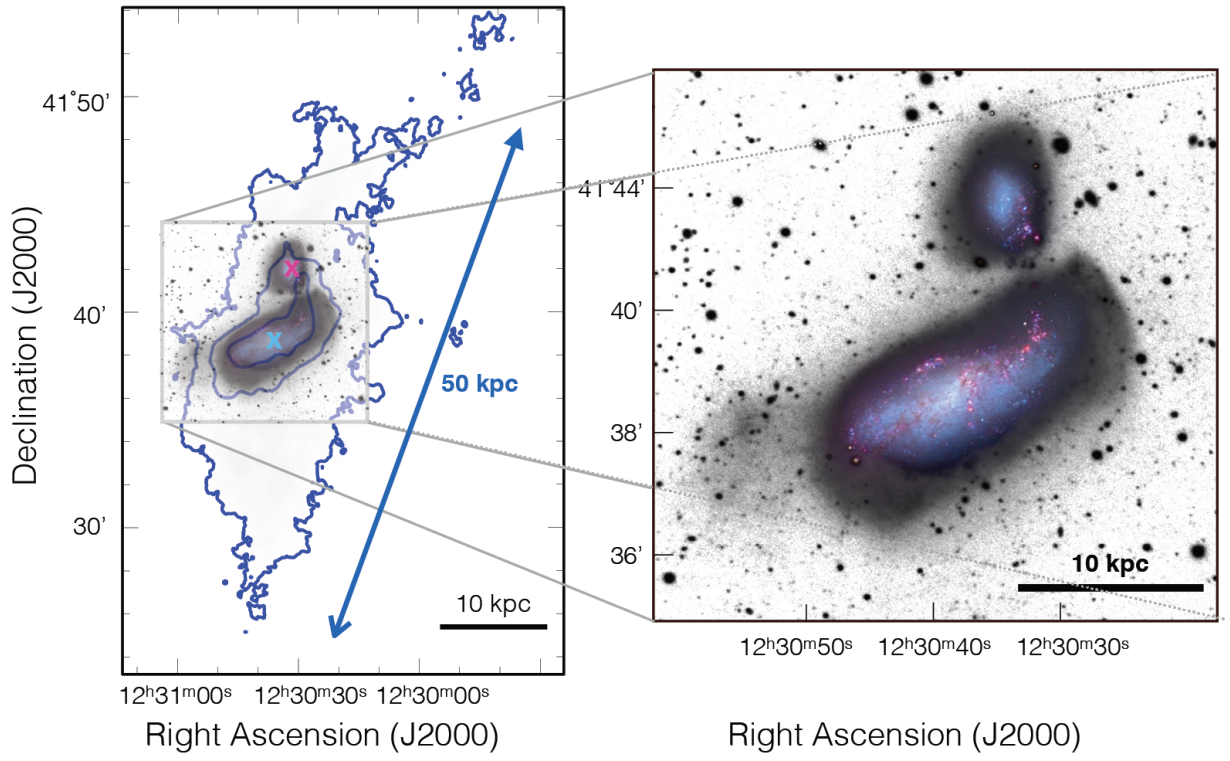

Figure 5.1: **Left:** Neutral hydrogen (HI) envelope surrounding the dwarf galaxy pair NGC 4490 and NGC 4485 (blue: N(HI) = 0.7, 7, 35 $\times 10^{20}$ atoms cm^{-2}). The x's correspond to the optical centers of NGC 4490 (cyan) and NGC 4485 (magenta). The 10 kpc and 50 kpc scale bars are plotted assuming a distance of 7.14 Mpc (Theureau et al. 2007) to the dwarf galaxy pair. The HI is distributed roughly symmetrically around the dwarf pair (outer contour) and an HI bridge extends from the more massive NGC 4490 dwarf towards the smaller companion (inner contour). The gray box shows the optical data. **Right:** Optical deep image of NGC 4490 and NGC 4485 obtained with the BBRO2 0.5-meter telescope (see Section 5.2.2). The surface brightness limit of this image is $\sim$ 29 mag arcsec^{-2}, revealing a very faint plume of stars on the East (left) side of the NGC 4490's main body. A color inset of the disk of the galaxies taken with the same telescope is included for reference.

mass galaxies. Specifically, hierarchical processes can enable a long-lived gas supply channel for future star formation. Additionally, if the gas remains extended for a long period of time following the interaction, this could greatly affect the efficiency at which gas is stripped from these systems if they fall into a gas rich environment, such as a galaxy cluster or the CGM of a massive galaxy. We follow up the best dynamical match with self-consistent N-body simulations that test the match. We do not include hydrodynamics in this study, as we present here a first step towards addressing the plausibility that tidal interactions between a low mass galaxy encounter can generate tidal debris to large distances. Hydrodynamics should not strongly affect the large scale tidal features (Barnes & Hernquist 1996).

We will utilize these simulations to explicitly define the NGC 4490/4485 system's current dynamical state, encounter history and future fate. We further compare the resulting N-body simulation to new optical data of the system from the f/8.1 Ritchey-Chretien 0.5-meter telescope of the Black Bird Observatory 2 (BBRO2) to investigate the consequences of dwarf-dwarf tidal interactions to the internal stellar morphology of the galaxies.

The paper is organized as follows: in Section 5.2 we present the dwarf pair, NGC 4490/4485. In Section 5.3 we describe our dwarf models and the matching process using *Identikit* (Barnes & Hibbard 2009). In Section 5.4 we show the results of our dynamical match to the NGC 4490/4485 pair. We discuss the fate of the HI envelope in Section 5.5. In Section 5.6 we compare our results to the Magellanic System and we discuss the implications of tidal pre-processing and the inflow of gas to the merger remnant. We conclude in Section 5.7.

Table 5.1: Properties of NGC 4490/4485 and the LMC/SMC

Dwarf pair	Distance [Mpc] $\equiv D^*$	Stellar mass $\times 10^9$ $M_\odot \times (D/D^*)^2$	HI mass[1] $\times 10^9$ $M_\odot \times (D/D^*)^2$	HI mass outside[2] $\times 10^9$ $M_\odot \times (D/D^*)^2$	Proj. sep. [kpc]$\times (D/D^*)$	Vel. sep. [km s^{-1}]	Massive galaxy	Av. dist. to host [kpc]$\times (D/D^*)$
NGC 4490/4485	7.14[3]	7.2/0.82	2.4/0.23	1.07	7.5	30[4]	NGC 4369	310
LMC/SMC	0.055[5]	2.7[6]/0.3[7]	0.27/0.26	0.37	11	116[8]	Milky Way	55

5.2 The NGC 4490/4485 pair

The low mass galaxy pair NGC 4490/4485 (presented in Figure 5.1 and with optical centers marked by cyan and magenta "x"s, respectively) is a slightly more massive analog of the LMC/SMC, with a stellar mass ratio of $\sim$ 8:1 (Clemens et al. 1998) and isolated from any massive galaxy. The NGC 4490/4485 galaxies are separated by only 7.5 kpc in projection (the projected separation of the LMC/SMC is 11 kpc). See Table 5.1 for a comparison of the two dwarf pairs. NGC 4490/4485 resides 7.14 Mpc from the Milky Way (Theureau et al. 2007). The nearest massive galaxy (defined as $M_* > 10^{10}$ $M_\odot$ as in Geha et al. 2012) is NGC 4369 which has a stellar mass of $M_* = 2.6 \times 10^{10}$ $M_\odot$. The projected separation between the pair and NGC 4369 is $d_{\rm proj} > 300$ kpc and the velocity separation to the pair is $v_{\rm sep} > 400$ km s^{-1} (Pearson et al. 2016). Cosmologically, dwarf galaxy pairs do not remain bound to each other for long when in proximity to a massive galaxy (González & Padilla 2016). The relatively isolated environment of the NGC 4490/4485 system thus allows us to examine the evolution of a low mass galaxy pair, independent of environmental factors, for the first time.

5.2.1 Archival HI data

The system is clearly detected in HI and an HI envelope, first discovered by Huchtmeier et al. (1980), symmetrically surrounds the NGC 4490/4485 pair and extends $\sim$50 kpc in projection.

The HI data presented in this paper are originally from Clemens et al. (1998) and were obtained with the VLA in C-configuration and D-configuration. The velocity of the pair's HI ranges from -123 km s^{-1} to 83 km s^{-1} centered at a systemic heliocentric radial velocity of v_{sys} = 575 km s^{-1}, and the data have a velocity width per channel of 20.7 km s^{-1}. The envelope is detected to column densities of N(HI)$\sim 3 \times 10^{19}$ atoms cm^{-2}, which is close to the sensitivity limit of the data (N(HI) $\sim 10^{19}$ atoms cm^{-2}: Clemens et al. 1998). The total gas mass of the system is $M_{\rm HI} \sim 3.7 \times 10^9$ M$_\odot$, where $\sim$ 30% of the gas ($\sim 1.07 \times 10^9$ M$_\odot$, see Table 5.1) resides beyond the stellar extents of the two galaxies (defined as beyond the 2MASS extents of each disk; Pearson et al. 2016). Based on the relatively isolated environment of the pair, Pearson et al. (2016) found it unlikely that ram pressure is playing a significant role in the origin of the extended envelope surrounding the pair.

There is a dense bridge (N(HI)$> 3.5 \times 10^{21}$ atoms cm^{-2}) of gas connecting the pair (see Figure 5.1, left: inner HI contour) which suggests a tidal encounter between the galaxies (Toomre & Toomre 1972). The bridge material peaks at $v \sim -123$ to -82 km s^{-1} with respect to the systemic velocity. GALEX UV data of the system (Smith et al. 2010) show that stars are forming in the NGC 4490/4485 bridge. This suggests that the high gas density in the bridge is not due to a chance projection of overlapping gas.

Interestingly, Lee et al. (2009) found that NGC 4485 is likely undergoing a starburst, as its Hα equivalent width is EW = 76 ± 13, which exceeds the logarithmic mean by 2σ limit when compared to the $\sim$ 300 dwarfs in the 11HUGS Dwarf Galaxy Survey (Lee et al. 2009). NGC 4485's star formation rate inferred from the far ultraviolet (FUV) non-ionizing continuum is SFR(FUV) = 0.22 M$_\odot$ yr^{-1} (assuming a distance of 7.14 Mpc; see Lee et al. 2009 table 1). This is consistent with findings of the TNT survey that the secondary (smaller) galaxy in a dwarf galaxy pair is more likely to be starbursting, and with theoretical expectations of stronger tides acting on the secondary.

Using HI data presented in Viallefond et al. (1980), Elmegreen et al. (1998a) computed a rotation curve for NGC 4490 and found that it peaks at a radius of 6 kpc from the center with $v_{rot}/\sin(i) \sim 80$ km s^{-1}, where i is the inclination of the primary in the sky plane, which is $\sim 60°$. A peak rotational velocity of $v_{\rm rot,peak} = 80$ km s^{-1}, is similar to that of the LMC ($v_{\rm rot,peak} \sim 90$ km s^{-1}: van der Marel & Kallivayalil 2014). These findings are consistent with the Clemens et al. (1998) HI data (see their figure 2).

Kinematic constraints are important in breaking model degeneracies that arise when matching only the morphology of galaxy mergers (e.g. Barnes & Hibbard 2009). In this work, we assume that the optical centers are approximately the dynamical centers of the two galaxies. Exploring the HI data cube, we find that the gas associated with the optical center of NGC 4485 is at $v \sim -20$ km s^{-1} with respect to the systemic velocity. The optical center of NGC 4485 is located to the left of the bridge material (see magenta x vs blue inner HI counter in Figure 5.1, left). Hence, the position of NGC 4485 is offset from the bridge in position and kinematics, and has lower column densities. Clemens et al. (1998) found the gas associated with the optical center of NGC 4490 to be at +10 km s^{-1} with respect to the systemic velocity. As the velocity channel widths are 20.7 km s^{-1}, we use a velocity center between 0 km s^{-1} and 20 km s^{-1} with respect to the centered HI cube as our constraint for the line-of-sight velocity.

5.2.2 Deep optical imaging

Optical data provides further support of a tidal encounter between NGC 4490/4485 (Elmegreen et al. 1998a, figure 3). In Figure 5.1 , right, we present new optical data of the NGC 4485/4490 system obtained with the f/8.1 Ritchey-Chretien 0.5-meter telescope of the Black Bird Observatory 2 (BBRO2) in Alder Springs (California) during different dark-sky nights between April 8th-22th, 2012. A 16 mega-pixel Apogee Imaging Systems U16M CCD camera

was used, with 31.3 × 31.3 arcmin field of view and a 0.46 arcsec pixel scale. We acquired a total of 22.66 hours of imaging data in 46 half-hour sub-exposures, using a non-infrared clear luminance Astrodon E-series filter (e.g. see Figure 1 in Martínez-Delgado et al. 2015a). Each sub-exposure was reduced following standard procedures for dark-substraction, bias-correction and flat-fielding (Martínez-Delgado et al. 2009). The surface brightness limit of this image is $\sim$ 29 mag arcsec^{-2}. We see evidence of a tidal encounter through a faint stellar extension to the left of the NGC 4490 galaxy's main body (Figure 5.1, right), which interestingly was also identified in Elmegreen et al. (1998a) in the B band at a surface brightness of 23.5 mag arcsec^{-2} and in SDSS gri imaging[9] (Baillard et al. 2011) which has a typical surface brightness limit of 24.5 mag/arcsec^2. In Elmegreen et al. (1998a) and SDSS the extension is detected as a narrower tail-like feature extending from the northern part of the NGC 4490 main body. We confirm the existence of this structure and our deeper data reveal this structure to be spanning larger distances ($\sim$ 8 kpc) in a more plume-like feature extending from the plane of the NGC 4490 disk.

To summarize, the existence of a bridge connecting the two galaxies and a starburst in the secondary is suggestive of strong tidal interactions between the two galaxies that may have resulted in the observed extended gaseous envelope. The NGC 4490/4485 pair is therefore an excellent candidate for testing a dynamically-driven formation scenario for an extended HI envelope through a dwarf-dwarf encounter. Despite such tidal encounters, the primary NGC 4490 still possesses a disk with a well-defined rotation curve. We seek to reproduce these properties using a tidal interaction model.

[9] http://ned.ipac.caltech.edu/img/2011A+A...532A..74B/gri/PGC_041333:I:gri:bbl2011.jpg

5.3 Dynamical Simulations

When modeling the mergers of galaxies, several degrees of freedom exist and searching the full parameter space of a galaxy merger can therefore be time consuming. As discussed in detail in Barnes & Hibbard (2009), to model the dynamical interaction of two disk galaxies, the mass ratio (μ), disk orientations (i_1, ω_1) and (i_2, ω_2) following the definition in Toomre & Toomre (1972), the eccentricity of the orbit (e) and the pericentric separation (r_{peri}) need to be specified. Hence, seven parameters are needed to model the dynamical interaction, without accounting for the internal structure of the galaxies. An additional nine parameters are needed to compare the models to observations: the length scale (L), the velocity scale (V), the center of mass position on the plane of the sky (X_m, Y_m), the center of mass velocity (V_c), the viewing angles ($\theta_x, \theta_y, \theta_z$) and the time of viewing (t). Without varying the internal structure of the galaxies involved (e.g. dark matter to baryon fractions, scale lengths etc.) 16 free parameters are present.

In this work, we use *Identikit* (Barnes & Hibbard 2009 and *Zeno* (Barnes 2011) to explore the parameter space of the NGC 4490/4485 interaction. Our procedure is summarized as follows:

1. We build a library of encounters using hybrid test-particle disks embedded in live N-body dark matter halos with a fixed orbital eccentricity, and vary the mass ratios and pericentric separations of the two galaxies.

2. We load the test-particle simulations and projections of the data into the *Identikit* visualization interface and vary the disk orientations, viewing angles, time of viewing, scaling and center of mass position of the galaxies in order to identify the best match to the HI kinematic and morphological data of the NGC 4490/4485 system.

3. Based on our best match obtained with the test-particle simulations, we run a small set of N-body simulations of galaxy encounters with self-gravitating disks embedded in live dark matter halos. For these we fix the eccentricity, mass ratios, disk inclinations and scalings, but allow for the time and viewing angles to be varied along with a small set of pericentric separations.

Identikit was initially tested by Barnes & Hibbard (2009) on 36 artificially constructed mergers of massive galaxies. They demonstrated that, in cases where the merging system displayed prominent tidal features, the viewing directions, spin orientations and time since pericenter were well recovered, while the pericenter separation showed the largest scatter. Additionally, the velocity scalings showed a $\sim 10\%$ bias for dynamically cold massive galaxy disks, as the test-particles in *Identikit* have zero velocity dispersion.

Re-simulating the galaxy interactions with a self-gravitating disk is an important test to verify the overall morphology. The global morphology and kinematics (the focus of this paper) should not be strongly modified by self-gravity in contrast to self-gravitating features such as spiral arms (Privon et al. 2013). See Barnes & Hibbard (2009) for a detailed description on the *Identikit* methodology and visualization techniques.

In the following, we describe the details of the galaxy mass models (Section 5.3.1), the library of *Identikit* test-particle simulations and the matching procedure (Section 5.3.2) as well as the self-gravitating N-body follow-up simulations (Section 5.3.3).

5.3.1 Galaxy Models

Using *Zeno* (e.g. Barnes & Hibbard 2009, Barnes 2011), we set up two galaxy mass models mimicking the primary (more massive) dwarf (NGC 4490) and secondary (less massive) dwarf (NGC 4485), respectively. We construct galaxy mass models with the same parameters as presented in Barnes & Hibbard (2009) but we omit the bulge, such that our galaxy models

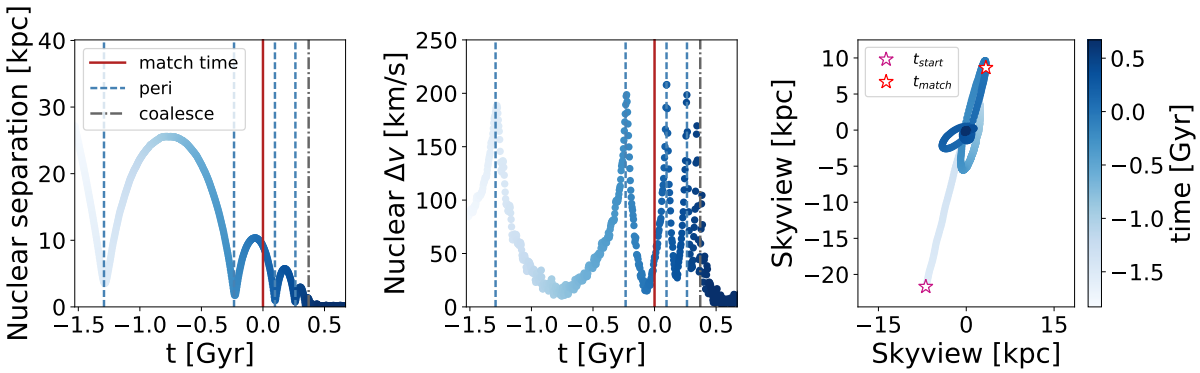

Figure 5.2: **Left:** Nuclear separation of the two galaxies as a function of time demonstrating the secondary's (NGC 4485 analog) orbital decay. The initial orbit is a parabolic ($e = 1$) orbit with a mass ratio of 8:1 between the galaxies and a first pericentric separation of 3.5 kpc. The physical scaling is based on the best match (see Table 5.2) and assuming a distance of 7.14 Mpc (Theureau et al. 2007) to the system. The color gradient encodes the evolution in time relative to the start of the simulation (white: simulation start time). The dashed blue lines show the time of each pericentric passage while the red solid line shows the time of the best match to the system ($t = 0$ Gyr). The match is located near the second apocenter and we predict the pair will coalesce $\sim$ 370 Myr after the time of match (gray vertical line). At the time of match the 3D nuclear separation is $\sim$ 9.3 kpc. **Middle:** Nuclear velocity separation of the two galaxies as a function of time since the start of the simulation. At the time of match the velocity separation (Δv) is ($\sim$ 43 km s^{-1}). **Right:** Orbit of the secondary about the primary, projected onto the plane of the sky for our best-fit viewing directions. The magenta star indicates the initial position of the secondary galaxy in the simulation, and the red star indicates the position of the secondary at the time of match. The orbit is centered on the position of the primary. As this is a high mass ratio merger (8:1) the center of the primary galaxy only moves slightly in response to the secondary's orbital evolution. The fact that we observe the system today (and that the two galaxies have not yet fully merged) indicates that they formed very far apart and that it is unlikely for the pair to have survived as a binary for a Hubble time.

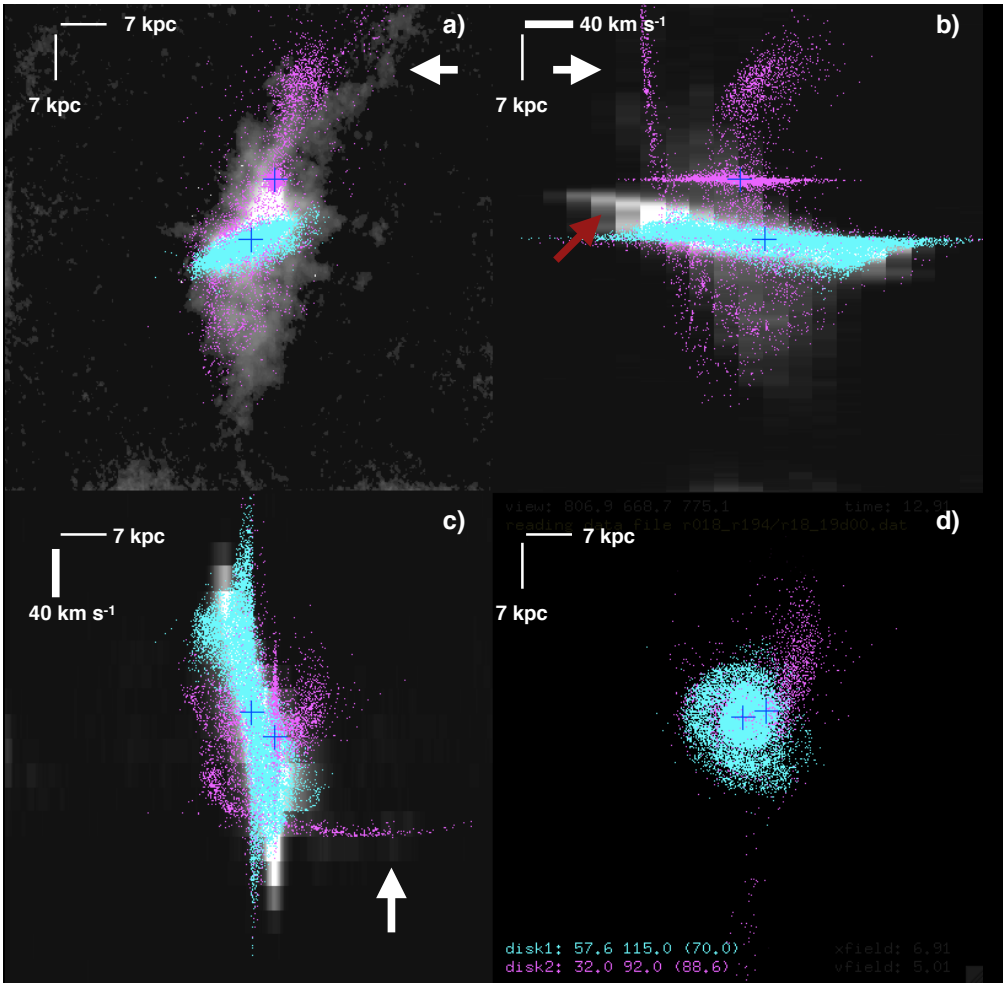

Figure 5.3: Visualization of a self-consistent N-body simulation for NGC 4490 (cyan) and NGC 4485 (magenta), matched to the observed system based on *Identikit* test-particle simulations. The match quantitatively reproduces the kinematics and morphology for galaxy values that mimic the system. (a) sky view of the system (RA-Dec), (b) line-of-sight velocity vs position diagram (vel-Dec), (c) position vs line-of-sight velocity diagram (RA-vel), and (d)"top-down" (RA vs line-of-sight distance) view of the simulation. Assuming a distance of 7.14 Mpc to the system (Theureau et al. 2007) the sky view covers 69.2 kpc × 69.2 kpc. The HI data from Clemens et al. (1998) is shown in grayscale, with the lighter pixels corresponding to higher peak values along a vector through the data cube. The velocity range is -123 km s^{-1} to 83 km s^{-1} with a velocity width per channel of 20.7 km s^{-1}, and the velocity increases from left to right in panel b and from bottom to top in panel c. The cyan and magenta points show collisionless baryonic particles from the self-gravitating primary and secondary representing the galaxies NGC 4490 and NGC 4485, respectively. The blue crosses represent the nuclei of each N-body realization. The match shown here occurs between the second and third pericentric passage, which is ∼1.29 Gyr after the first pericentric passage and ∼230 Myr after the second passage. The white arrows point to the end of the secondary's tidal tail produced in the first pericentric passage and the red arrow points to the HI emission in the bridge.

are more dwarf-like. See Barnes & Hibbard (2009) Appendix B for a detailed description of the galaxy construction in *Zeno*. The galaxy models were set up in approximate initial dynamical equilibrium (Barnes 2012). Each galaxy consists of an NFW dark matter halo (Navarro et al. 1996), which tapers at large radii (b_{halo}) following Springel & White (1999):

$$\rho_{halo}(r) = \frac{m_{halo}(a_{halo})}{4\pi(\ln(2)-1/2)}\frac{1}{r(r+a_{halo})^2}, r \leq b_{halo} \tag{5.1}$$

$$= \rho^*_{halo}\left(\frac{b_{halo}}{r}\right)^{\beta} e^{-r/a_{halo}}, r > b_{halo}$$

where $m_{halo}(a_{halo})$ is the halo mass within the scale radius of the halo (a_{halo}) and ρ^*_{halo} and β are fixed by requiring that both $\rho_{halo}(r)$ and $d\rho_{halo}/dr$ are continuous at $r = b_{halo}$.

The disk follows an exponential radial profile (Freeman 1970) and a sech^2 vertical profile (van der Kruit & Searle 1981):

$$\rho_{disk}(q,\phi,z) = \frac{m_{disk}}{4\pi r_s^2 z_{disk}} e^{-q/r_s}\text{sech}^2(z/z_{disk}), \tag{5.2}$$

where $(q = \sqrt{x^2+y^2}, \phi, z)$ are cylindrical coordinates, r_s is the disk scale radius, z_{disk} is the disk scale height and m_{disk} is the mass of the disk. For the secondary galaxy, we setup mass models with 1/4th, 1/6th and 1/8th of the mass of the primary galaxy. The scale length of the smaller galaxy is scaled accordingly to maintain constant mass surface density.

In both galaxies, 20% of the mass is made up by baryons and 80% of the mass is dark matter (see Section 5.4.1.4 for the affect of variations on these values). The ratio of the disk scale radius, r_s, to dark matter halo scale radius, a_{halo}, is $r_s/a_{halo} = 1/3$ in both the primary (more massive) and secondary (less massive) galaxy model. The galaxy encounters are run in simulation units and then the scale factors are fit during the matching process. All model parameters are listed in Table 5.2.

We ran isolated realizations of both galaxy mass models to check their long-term stability. Initially both galaxies are unstable to bar formation due to omission of the bulge. A bar forms after 2 rotation periods at 3 disk scale lengths ($t_{\rm sim} = 2$, see Table 5.2 for the scale from simulation to physical units in our match)[10].

5.3.2 *Identikit* test-particle simulations and matching

To explore the parameter space of the NGC 4490/4485 encounter, we build a library of dwarf encounters with various mass ratios ($\mu = 4:1, 6:1, 8:1$) and initial pericentric separations ranging from $r_{peri} = [0.75 - 5.25] \times r_{s,prim}$ in increments of 0.75 $\times r_{s,prim}$, where $r_{s,prim}$ is the disk scale length of the primary galaxy. We limit our investigation to $e = 1$ orbits as e < 1 orbits imply a previous encounter (see Barnes & Hibbard 2009). The eccentricity will evolve over the course of the encounter owing to dynamical friction.

We create two self-consistent galaxy halos (see previous section) and specify the eccentricity of the orbit and the pericentric separation. We place the galaxies' initial positions such that their dark matter halos are not overlapping and the velocities are set based on an initial idealized point-source Keplerian orbit. The galaxies are evolved in time using a standard treecode (Barnes & Hut 1986, Barnes 2011) and initially follow a Keplerian orbit, however the orbit rapidly decays due to the dynamical friction from the live N-body dark matter halos. The initial pericentric pass of the idealized point-source Keplerian orbit is slightly smaller (see Section 5.4) than the initial pericentric pass including the extended live N-body dark matter halos. Throughout the paper we quote the non-idealized pericentric separations.

[10]Note, we ran the galaxies in isolation and re-ran a simulation of the encounter using disks in which the bars had formed and settled prior to the encounter. This did not change the overall results of our preferred match. However, the specific location of induced spiral arms might be affected slightly by the bar's phase at the time of match (see also Barnes 2004, Privon et al. 2013 for a discussion on bar misalignments in the Mice: NGC 4676A/B).

Both dark matter halos are populated with a spherical distribution of massive particles that has the same cumulative radial mass distribution as for the initial stellar disks. These spheres are populated with multiple disks of test particles on circular orbits. This is similar to populating each galaxy with all possible disk configurations, although the test-particles do not have mass and are therefore not self-gravitating (see Barnes & Hibbard 2009 for a detailed description).

After completing a library of test-particles simulations, we load them into the *Identikit* visualization software along with the HI data (see Section 5.4.1.2) and decide which disk to display. Subsequently, we require the simulated galaxies' positions (X_m, Y_m) and velocities (V_c) to agree with the observed galaxy positions and velocities. In real time, we then vary the disk orientations (i_{prim}, ω_{prim}, i_{sec}, ω_{sec}), the viewing angles ($\theta_x, \theta_y, \theta_z$) and the scaling ($L, V$) of the system, while stepping through time (t), mass ratio (μ) and pericentric separations (r_p) until we obtain a good match to the data (see Barnes & Hibbard 2009, Privon et al. 2013 for a detailed description of the matching procedure).

The key features we aim to reproduce are: 1) the position of the two galaxies; 2) the tidal debris populating the symmetric envelope (north and south) morphologically and kinematically; 3) the optical centers of NGC 4490/4485 in position (see x's in Figure 5.1, left) and velocity space; 4) that the orbit of the secondary passes through the dense bridge material (see Figure 5.1, left, inner blue contour) both in the morphological and kinematic panels of the *Identikit* visualization interface in order to have a plausible formation scenario for the dense bridge (e.g. ram-pressure from passing through the NGC 4490 disk: Clemens et al. 2000). We also test matches in which the orbit does not pass through the dense bridge material in the data (see *Appendix*), as the bridge could in principle be purely tidal (Toomre & Toomre 1972).

Using the test-particle simulations visualized in the *Identikit* interface, we scale the sys-

tem so that it matches the observed extent on the sky. The scale lengths of the galaxies might be affected by the tidal interaction, so the scale length inferred for the progenitor galaxy does not necessarily have to be the present-day scale factor. However, once we find a good match we use the scale lengths as a sanity check such that we obtain a physical size scale mimicking these types of galaxies. In particular, we require that the scale length of the primary disk, $r_{s,prim}$, is at least 0.7 kpc. None of our matches had scale lengths larger than that of the LMC disk scale length in the Besla et al. (2012) models (1.7 kpc), hence we did not set a strict upper limit for the scale length when exploring our matches. Once we obtain a physical scaling, we search for test-particle simulation matches that approximately reproduce the physical separation of the galaxies at present day (i.e. $\sim 7 \pm 2$ kpc in projection). In addition to the physical size scale, we ensure that the extent of kinematic data mimics that of our primary galaxy as we match our simulation output to the HI data in the *Identikit* visualization interface. As a sanity check, we also compute the rotational velocity curve for our primary galaxy and check whether it is consistent with the observed HI rotational velocity curve from Elmegreen et al. (1998a), peaking at $v_{\rm rot,peak} \sim 80$ km s^{-1}.

5.3.3 Self-consistent N-body simulations

After obtaining a dynamical match to the system using the test-particle simulations (see Section 5.3.2, 5.4.1), we run a self-consistent collisionless N-body simulation including self-gravity of the disks. We compare this simulation to the test-particle simulation to check whether a more realistic disk treatment changes our match to the tidal features. Using the N-body follow-up with self-gravitating disks, we investigate if the match is affected by the slightly different dynamical friction that arises due to the higher local density in the self-consistent stellar disks. We do not include hydrodynamics in our simulations and the baryonic mass is therefore assumed to be a combination of stars and gas throughout this

paper. These simulations will be followed up with full hydrodynamics in future studies. The goal of this study is to assess the plausibility that tides can create tidal structures similar in extent and kinematics as the observed HI envelope.

The self-gravitating N-body model presented in this paper utilizes the mass models in Section 5.3.1 and encounter parameters based on the best match using the test-particle simulations, introduced in Section 5.4.1. To test the sensitivity of our best-match to encounter parameters in the full N-body simulation, we also run three different initial pericentric separations, r_p, centered on the value obtained for the best match in the test-particle simulations.

We load the output of the self-gravitating encounter into the *Identikit* visualization software with the same viewing angles, $(\theta_x, \theta_y, \theta_z)$, and scalings ($L$, V) as obtained for our best match in our test-particle simulations. Subsequently, to investigate potential differences between the test-particle match and the N-body follow-up, we test the viewing angles, scaling of the system and pericentric separation at different points in time in the simulation to assess the quality of the match to the observational data.

5.4 Results

In this section we detail the best-match parameters (see Section 5.3.2) obtained using the *Identikit* test-particle simulations and visualization interface and we present and analyze the N-body follow-up with self-gravitating disks (Section 5.4.1). Additionally, we describe the formation mechanism of the extended tidal envelope (Section 5.4.2) and the morphological consequences of the interaction on the primary galaxy (Section 5.4.3). We reiterate that the goal of our study is not to reproduce every detail of the NGC 4490/4485 system, but to explore whether there is a plausible dynamical solution for which the kinematics and morphology of its baryonic distribution can be quantitatively matched through a tidal en-

counter between the two galaxies. This is the first time *Identikit* has been used to simulate a dwarf-dwarf merger.

5.4.1 The dynamical match to NGC 4490/4485

Our best test-particle simulation match to the data of NGC 4490/4485 has a galaxy mass ratio of $\mu = 8:1$, and a first pericentric separation of $r_{peri} = 4.2 \times r_{s,prim}$ (3.5 kpc).

Subsequent to obtaining the best test-particle simulation match, we run three N-body follow-up simulations with self-gravitating disks and pericentric separations close to the value for the best test-particle match ($r_{peri} = 3.4, 4.2, 5.0 \times r_{s,prim}$). When we load these into the *Identikit* visualization interface, we find that for the three N-body follow-ups, the best agreement with the data was still for the $r_{peri} = 4.2 \times r_{s,prim}$ case, with minor variation from the test-particle match by a few degrees in the viewing angles of the system. We therefore present and analyse only the N-body follow-up with $r_{peri} = 4.2 \times r_{s,prim}$ throughout this section. In Table 5.2 we present the specific scalings and galaxy properties obtained in our match. The t_{start}-column describes the initial conditions with the scaling values from the best-match applied. The t_{match} column describes the properties at the time of match (i.e. present day, $t = 0$ Gyr).

For our best N-body match, the two galaxies are separated by 28 kpc at the beginning of the simulation (t_{start} = -1.528 Gyr) and initially follow a Keplerian ($e = 1$) orbit (see Figure 5.2). The idealized Keplerian orbit has an initial pericentric separation of $r_{p,1} = 2.5$ kpc, however the first pericentric passage using the extended galaxies from the N-body and test-particle simulations deviates slightly from the idealized Keplerian orbit, resulting in a pericentric approach of $r_{p,1} = 3.5$ kpc (see Figure 5.2).

The first pericentric passage occurs ~ 0.2 Gyr after the start of the simulation and the orbit decays due to dynamical friction between the galaxies. The time of match ($t = 0$

Table 5.2: Self-consistent N-body run of best match

Identikit **match scalings**	simulation units (sim)	physical
Velocity	1	82.5 km s^{-1}
Time	1	118.7 Myr
Length	1	10.02 kpc
Mass	1	1.58 $\times 10^{10}$ $M_\odot$

	Primary Galaxy	**Secondary Galaxy**
Simulation properties		
Grav. soft. (sim)/physical	(0.00375)/0.0375 kpc	
Particle no. dark matter	65536	32768
Particle no. baryonic	65536	32768
Particle mass dark matter	244,141 $M_\odot$	61,035 $M_\odot$
Particle mass baryons	61,033 $M_\odot$	15,259 $M_\odot$
Dynamical properties		
$\mathbf{t}_{start}$ (initial conditions)		
$m_{\rm halo}$ (sim)/physical	(1)/1.6 $\times 10^{10}$ $M_\odot$	(0.125)/2 $\times 10^9$ $M_\odot$
$m_{\rm disk,baryons}$(sim)/physical	(0.25)/4 $\times 10^9$ $M_\odot$	(0.03125)/0.5 $\times 10^9$ $M_\odot$
$f_{\rm baryon}$	0.25	0.25
$r_{p,1}$ (idealized Keplerian orbit)	(0.25)/2.5 kpc	
$r_{p,1}$ (simulation orbit)	(0.35)/3.5 kpc	
$r_{\rm disk}$ (sim)/physical	(1/12)/0.835 kpc	(1/33.941)/0.295 kpc
$z_{\rm disk}$ (sim)/physical	(0.0125)/ 0.125 kpc	(0.00442)/0.044 kpc
$a_{\rm halo}$ (sim)/physical	(0.25)/2.505 kpc	(0.0884)/0.886 kpc
$b_{\rm halo}$ (sim)/physical	(0.975)/ 9.77 kpc	(0.3448)/ 3.45 kpc
$c_{\rm halo}$	3.9	3.9
(i, ω)-disks	(58 $\pm 5°$,115 $\pm 20°$)	(32 $\pm 10°$,92 $\pm 15°$)
Δv_{3D}	$\sim$ 85 km s^{-1}	
Δpos_{3D}	$\sim$ 28 kpc	
$\mathbf{t}_{match}$ (present day)		
$M_{\rm disk,baryons}(< 7 \times r_s)$	3.76 $\times 10^9$ $M_\odot$	0.33 $\times 10^9$ $M_\odot$
$\Delta v_{\rm 3D}$	43 km s^{-1}	
$\Delta pos_{\rm 3D}$	9.3 kpc	
$\Delta pos_{\rm projected}$	6.5 kpc	
Viewing angles	(87$\pm 3°$, 309$\pm 3°$, 55$\pm 3°$)	
Galaxy inclination sky view	70.0 $\pm 15°$	88 $\pm 10°$

Gyr) occurs between the second and third pericentric passage, close to apocenter, and is 1.29 Gyr after the first pericentric passage between the two galaxies. The viewing angle that affords the best match is aligned with the orbital plane. Hence from our perspective, the tidal tails are aligned along our line-of-sight (see Figure 5.3). In the following we discuss the orbital solution of the match (Section 5.4.1.1), the morphology of the match (Section 5.4.1.2), the kinematics of the match (Section 5.4.1.3) and the initial properties of the primary and secondary galaxy (Section 5.4.1.4) in detail.

5.4.1.1 The orbit

The secondary galaxy has a prograde spin with respect to the orbital angular momentum vector enabling substantial mass loss such that the envelope is mainly produced from material from the secondary galaxy (see magenta particles in Figure 5.3). In Figure 5.2 we show the evolution of the primary and secondary galaxies' nuclear separation (left), velocity separation (middle) and the secondary's orbital evolution around the primary galaxy (right) for the N-body simulation of the match shown in Figure 5.3. The color bar illustrates the time evolution with respect to present day, which is the time of the best match in the simulation ($t = 0$ Gyr). The physical scaling is based on the best match (see Table 5.2) and assuming a distance of 7.14 Mpc (Theureau et al. 2007) to the system. At the time of match (red solid line), two close encounters have occurred ($r_{p,1} = 3.5$ kpc, $r_{p,2} = 1.7$ kpc) and the primary galaxy's tidal field strips material from the secondary at each close encounter.

The fact that the match (red solid line) occurs close to apocenter, where the two galaxies are farthest apart, is not surprising as this is the point in their orbit at which they spend the most time (i.e. move at the lowest velocity, see Figure 5.2 middle panel). In Figure 5.2, left, we show that the galaxies are separated by $d_{3D} = 9.3$ kpc ($d_{\rm proj} = 6.5$ kpc) at the time of match and that the relative velocity between the two nuclei is 43 km s^{-1} (Figure 5.2, middle)

in good agreement with observations (see Table 5.1).

The time between the first and second pass is ∼1.1 Gyr, and following the simulation after the time of match reveals the prediction that the dwarfs coalesce ∼ 1.7 Gyr after the first pericentric passage (370 Myr after the time of match: Figure 5.2, left, gray vertical line). Thus, capturing the two galaxies separately as an interacting pair is not a short-lived stage (see also Besla et al. 2016).

Given the decay time of ∼ 1.7 Gyr, which is quite rapid compared to a Hubble time, our best match orbit indicates that the two galaxies likely formed very far apart and have had a long infall time as we still observe the two galaxies separately today. This provides dynamical insight to the survivability of these types of of low mass galaxy pairs and groups (e.g. Stierwalt et al. 2017). Our study suggests that close pairs viewed today are likely to have begun their encounter on high eccentricity orbits to prevent rapid merging and are unlikely to have survived as bound systems for a Hubble time.

The third panel of Figure 5.2 shows the evolution of the secondary's orbit around the primary in the plane of the sky. The orbit is centered on the primary galaxy, the initial position of the secondary is marked by the magenta star and the red star indicates the position of the secondary at the time of match. From our viewing perspective the secondary galaxy is initially on a high inclination orbit with respect to the disk plane of the more massive galaxy, spanning ∼ 30 kpc in the Declination direction and only ∼ 15 kpc in the Right Ascension direction.

We stress that when exploring the *Identikit* library, we found that the extended morphology of the envelope could generically be reproduced by this broad type of orbital configuration. However reproducing the details of the match and its kinematics required narrowing down the free parameters of the disks (see Section 5.4.1.3).

5.4.1.2 The morphology of the preferred match

Figure 5.3, panel **a)** shows the morphology of the observed (grey scale) and simulated data (colored points) in RA-Dec. The magenta particles (secondary galaxy, NGC 4485 analog) in Figure 5.3, panel **a)** populate both the north and the south of the data morphologically. The magenta particles are partially made up of a long tidal tail stripped from the secondary on its first pericentric passage which wraps around the primary galaxy as a roughly symmetric 50 kpc envelope when viewed from our perspective. Hence, the viewing angle places the tail stripped in the first pass mostly along the line-of-sight, populating both the northern and southern envelope, which explains why the tidal tails do not look like long thin features (e.g. as the case for the Antennae galaxies: Toomre & Toomre 1972). The fact that the match occurs between the second and third pericentric passage, allows for the tidal tail from the secondary galaxy's first pericentric pass to grow and populate the full extent of the $\sim$ 50 kpc HI envelope. Additional material stripped at the second pericentric passage (see material north of the magenta main body, Figure 5.3 panel **a**) also contributes to the HI envelope.

5.4.1.3 The kinematics of the preferred match

Figure 5.3, panel **b)** shows line-of-sight velocity vs. position (vel-Dec) with increasing velocity from left to right. Panel **c)** shows the position vs velocity (RA-vel), where the velocity is increasing from bottom to top. The data and magenta particles in the tail feature in the lower right part of panel **c)** is marked by a white arrow in each of panels **a**, **b**, and **c**, although the contrast in Figure 5.3 does not highlight the observational data clearly in this region. This feature is the end of the tail produced in the first pericentric passage, which wraps around the system when viewed from our perspective (see Section 5.4.1.2). This structure populates both the north and the south of the envelope morphologically and kinematically.

To reproduce this "end-of-the-tail" feature, a specific configuration was required: viewing angles $\theta_x = 87°$, $\theta_y = 309°$, $\theta_z = 55°$ and secondary disk orientation: $i_{sec} = 32°$, $\omega_{sec} = 92°$. We explored the acceptable range in the viewing angles by varying them in the N-body follow-up until the simulated particles no longer provided a good match to the system. Via this approach we found that the approximate uncertainty on each viewing angle is $\pm 3°$. We carried out the same test for the disk orientation using the test-particle simulation (we cannot vary the disk inclinations in the N-body follow-up, as they are modeled self-consistently) and found that the approximate uncertainty was $i_{sec} = 32 \pm 10°$ and $\omega_{sec} = 92 \pm 15°$.

To match the morphological and kinematic gradient along the primary's body while matching the extended tidal debris required a specific disk orientation ($i_{prim} = 58°$, $\omega_{prim} = 115°$) for the primary. We explored the acceptable range in the primary disk orientation by varying i_{prim}, ω_{prim} in the test-particle simulation until it no longer provided a good match to the system. Via this approach we found that the approximate uncertainty on the primary disk orientation is $i_{prim} = 58 \pm 5°$ and $\omega_{prim} = 115 \pm 20°$.

Observational data marked by the red arrow in Figure 5.3, panel **b** are unpopulated by magenta or cyan particles. This observational feature corresponds to the higher column density bridge material at $v \sim -123$ to -82 km s^{-1} (see Section 5.2.1). We see the secondary move through the disk of the primary during the most recent passage, but this feature likely is not reproduced due to the lack of hydrodynamics in our simulations (see Section 5.3.2 and Section 5.6.3).

We use the optical centers as additional constraints on the model. The secondary galaxy (magenta particles) is therefore located at $v \sim -20$ km s^{-1} and the primary galaxy is centered at $v \sim 0$ km s^{-1} (see Section 5.2.1). We reproduce both the kinematic position of the primary and secondary in panel **b** and **c**.

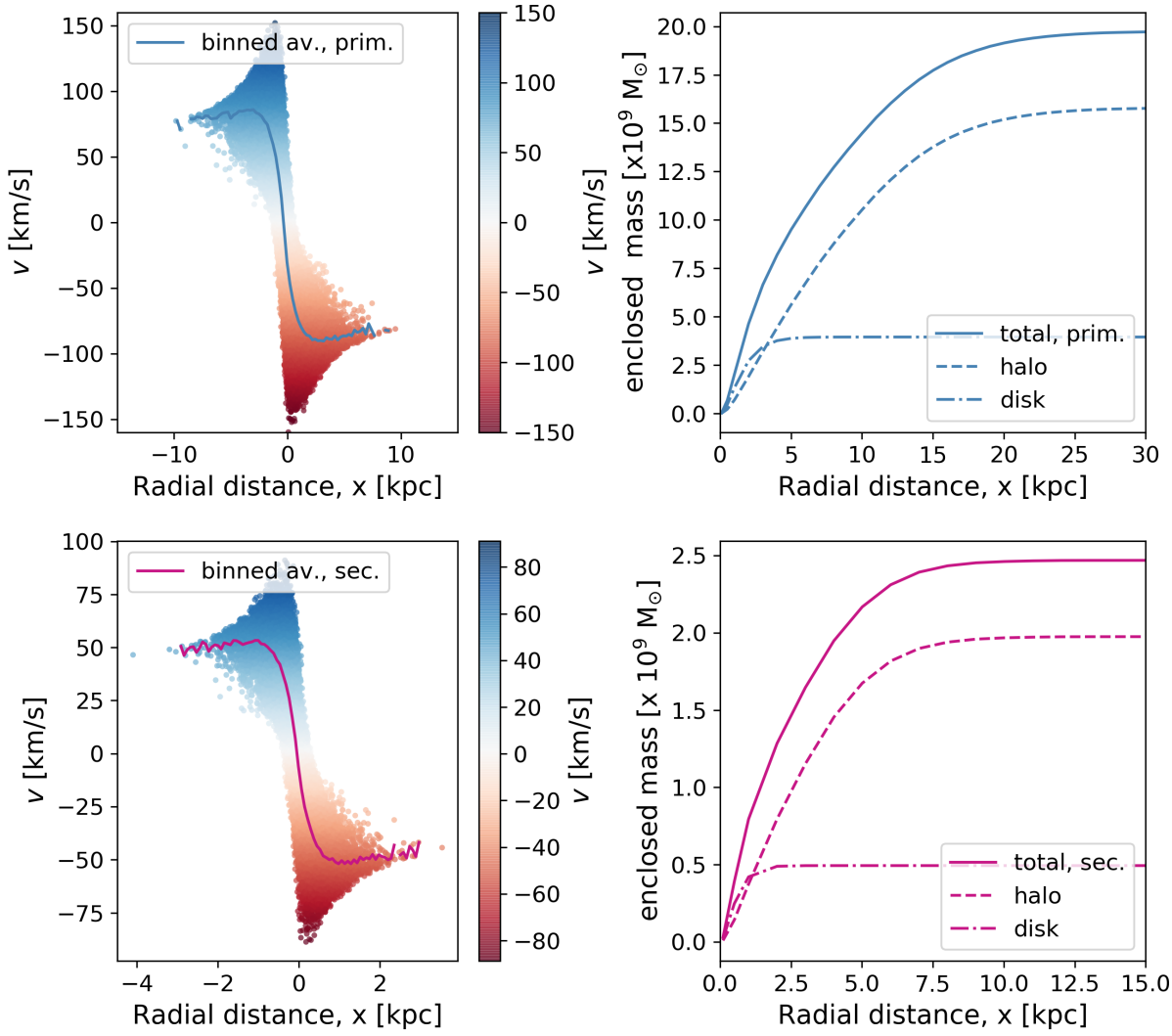

Figure 5.4: **Left:** Velocities of our simulated primary (top) and secondary (bottom) galaxies as a function of radial distance from their centers at the beginning of our simulation (t_{start}). The size and velocity scale is derived from our mass models, using the best match parameters (see Table 5.2). The color coding shows the velocities in the edge on projection of the two galaxies.The blue (primary) and magenta (secondary) lines show the averaged v, binned in 100 bins. Our primary galaxy model has a peak velocity of $v_{\rm peak} \sim 80$ km s^{-1} which then flattens after 4 kpc. This is roughly consistent with the observations of NGC 4490: at present day NCC 4490's peak rotational velocity is $v_{\rm rot,peak} \sim 80$ km s^{-1} (Elmegreen et al. 1998a) whereafter the rotation curve drops and does not follow a flat curve. The secondary's rotation curve is similar to that of the SMC (Stanimirović et al. 2004) peaking at $v_{\rm rot,peak} \sim 50$ km s^{-1} and does not have an observationally derived curve. **Right**: Spherically averaged enclosed baryonic and dark mass profiles of the primary (top) and secondary (bottom) galaxy at t_{start} scaled based on our best match parameters (see Table 5.2).

5.4.1.4 Initial properties of the primary and secondary

Throughout the paper we have used mass models mimicking those of massive galaxies (see Section 5.3.1, Barnes & Hibbard 2009). In Figure 5.4, left we show the disk rotation curve and the mass profiles of our primary and secondary galaxy models at the beginning of our simulation t_{start} scaled based on the best match parameters (see Table 5.2). For the primary galaxy, our rotation curve peaks at $v_{\rm rot,peak} \sim 80$ km s^{-1}, which is the same value as obtained for the observational HI rotation curve (Elmegreen et al. 1998a). We used the kinematic extent of the data as part of the *Identikit* matching procedure (see Figure 5.3 panel b, c), so it is encouraging that our initial conditions based on our preferred match are consistent with the observed present day rotation curve for NGC 4490. Our primary galaxy's rotation curve peaks at slightly smaller radius than what Elmegreen et al. (1998a) found (6 kpc), which could be addressed with a different mass model. There is no observational rotation curve available for the secondary galaxy, and we expect hydrodynamical effects to have distorted the present day HI within NGC 4485 as it has recently passed through NGC 4490 (see discussion in 5.6.3). Our secondary's simulated rotation curve peaks at $v_{\rm rot,peak} \sim 50$ km s^{-1} in the beginning of the simulation, which is similar to that of the SMC ($v_{\rm rot,peak} \sim 60$ km s^{-1} at 3 kpc: Stanimirović et al. 2004) if it is modeled.

Based on our match the implied total initial baryon mass of the primary and secondary in the simulation are $m_{\rm disk,prim} = 4 \times 10^9$ M$_\odot$ and $m_{\rm disk,sec} = 0.5 \times 10^9$ M$_\odot$, respectively (see Table 5.2 and Figure 5.4, right). This initial baryonic mass is a factor of ~ 2.6 lower compared to the total baryon mass in the data (see stellar masses, HI masses and envelope HI mass in Table 5.1). Obtaining a better match to the NGC 4490/4485 system would require carefully altering the mass models by making the halos less concentrated and then adding mass back in baryons, which is beyond the scope of this paper. We stress that where

we can compare to data (i.e. the NGC 4490 rotation curve), our simulated galaxy mass profiles are consistent with observations (see rotation curves Figure 5.4, and morphological and kinematic match in Figure 5.3).

Compared to what we would expect from abundance matching (e.g. Moster et al. 2013) the halo masses for our two galaxies are quite low: $m_{\rm halo,prim} = 1.6 \times 10^{10}$ M$_\odot$ and $m_{\rm halo,sec} = 2 \times 10^9$ M$_\odot$, respectively (Table 5.2 and total enclosed mass in Figure 5.4, right). The observed stellar mass ratio is 8:1, but in our simulation both the stellar mass ratio and halo mass ratios are 8:1. If the two galaxies were isolated, from abundance matching (using Eq. 2 in Moster et al. 2013) we obtain a halo mass of $m_{\rm halo} = 2.6 \times 10^{11}$ M$_\odot$ for NGC 4490 and $m_{\rm halo} = 9.1 \times 10^{10}$ M$_\odot$ for NGC 4485 (see Table 5.1). This corresponds to a halo mass ratio of $\sim 2.85:1$ although there is a large scatter in the Moster et al. (2013) abundance matching relation at small stellar masses. The dark matter halo mass at large radii is therefore not well constrained by our simulation match, and it is possible that more dark matter mass is present at larger radii than in our galaxy mass models presented here (Figure 5.4, right).

As a sanity check of the robustness of our retrieved encounter geometry, we explored mass models with galaxies more consistent with expectations from ΛCDM with less baryons as compared to dark matter (∼3% baryons as opposed to 20%), and larger halo concentrations ($c_{halo} = 12$ instead of $c_{halo} = 3.9$). We found that using the same viewing angles, disk angles, time of match and initial pericentric separations the match did not significantly change although this resulting match favored more massive halos (by a factor of 3.5). Hence the encounter geometry seems robust to the specific choice of mass model. In Section 5.5.2 we discuss the consequences of our lower dark halo mass models when we explore the fate and return timescales of the envelope.

See the *Appendix* for a discussion of alternative matches which reproduce the character of the system, but do not provide as satisfactory matches.

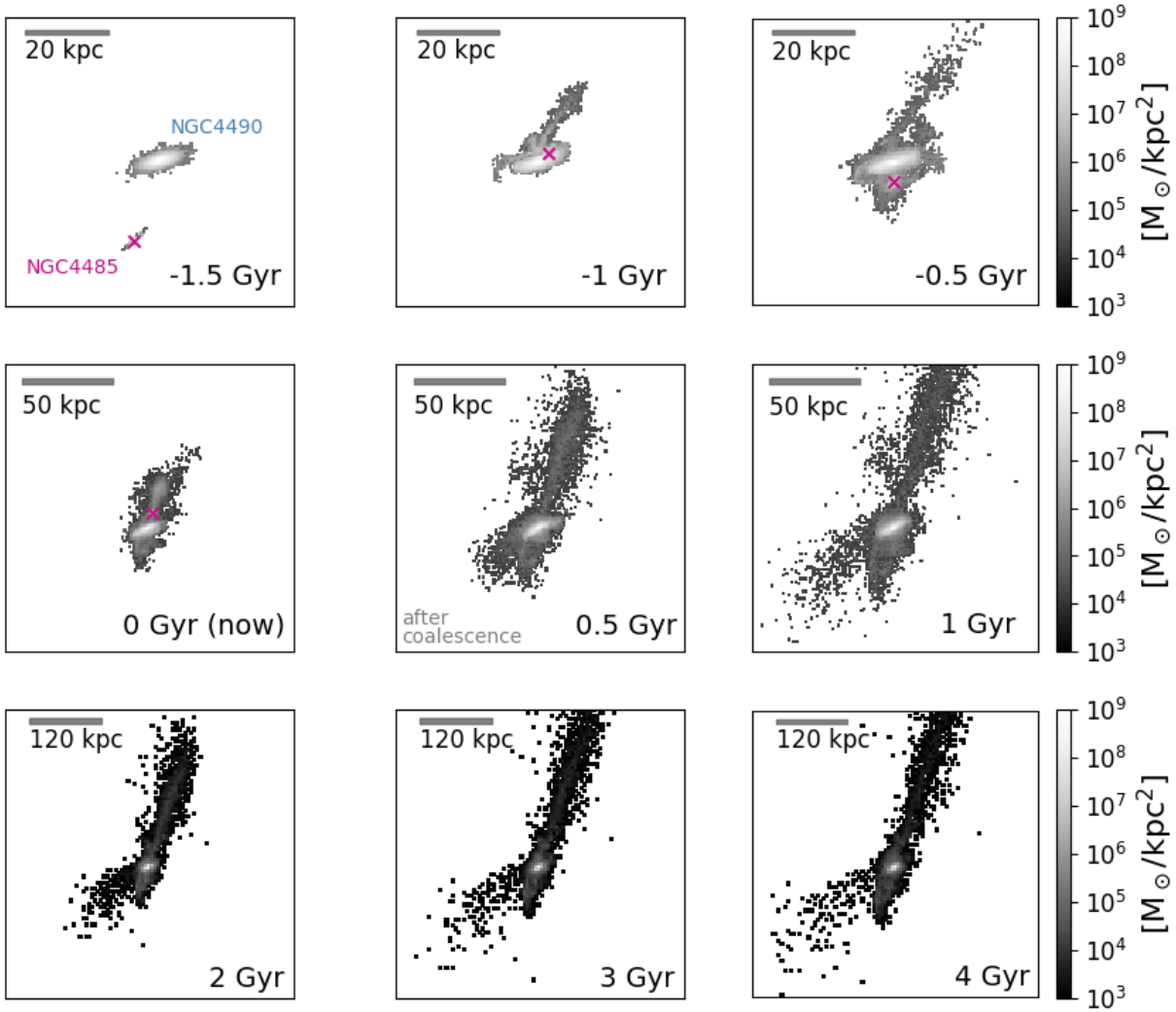

Figure 5.5: Snapshots of the evolution of the collisionless baryonic material from the N-body simulation of the bast match to NGC 4490/4485 as a function of time. The time is indicated relative to the time of match (present day, $t = 0$ Gyr). The magenta x's indicate the center of the secondary galaxy (NGC 4485) prior to its disruption. The panels are centered on the primary galaxy. The pair coalesces between $t = 0$ and $t = 0.5$ Gyr, after which the debris continues to grow in size and persists for several Gyr. The color bar denotes the density of the material, which is small in the large envelope compared to the densities in the main bodies at the time of match. The densities are converted to physical units based on the particle masses and the bin sizes in each row, and we saturate the density at 10^9 $M_\odot$ kpc^{-2}to better illustrate the faint features. The scale bars and densities are plotted assuming a distance of 7.14 Mpc (Theureau et al. 2007). Note the difference in the spatial scaling between the three rows.

5.4.2 The Formation of the Extended HI Envelope

The match presented in the previous subsection demonstrates that the extended ~ 50 kpc HI envelope can be reproduced through a dynamically-driven dwarf-dwarf tidal encounter formation scenario. Additionally our results show that a mutual interaction between two dwarf galaxies can move baryons to very large distances through tides alone, without the presence of outflows, tidal stripping through the Lagrange points due to a host galaxy's tides (e.g. a Milky Way) or ram-pressure effects. In this section we investigate the formation of the extended envelope and the mass and tail evolution of the tidal debris (see Sections 5.4.2.1 and 5.4.2.2). Throughout the rest of the paper we alternate between showing the system in the plane of the sky and in a "top-down" view (RA vs line-of-sight distance as in Figure 5.3, panel **d**). This enables us to highlight various features of the extended tidal debris.

Figure 5.5 illustrates the evolution of the baryonic density distribution of the NGC 4490/4485 system throughout their encounter, projected along our line-of-sight. Initially the two galaxies are separated by $d_{3D} = 28$ kpc. The first pericentric passage occurs at $t = -1.29$ Gyr (between the -1.5 and -1.0 Gyr panels). In the first three panels we see the formation of the envelope and the subsequent panels show its predicted evolution. From our viewing perspective the debris stripped from the secondary in the first pericentric passage wraps around the primary's disk.

The middle, left panel of Figure 5.5 shows the system at the time of match, where a large 50 kpc (projected) envelope surrounds the two dwarf galaxies which are separated by $d_{3D} = 9.3$ kpc corresponding to a projected separation of $d_{\rm proj} = 6.5$ kpc. The surface density of material in the large envelope is a factor of 10^4 lower than the densities in the main bodies, and the tidal debris in the north and south of the envelope is of similar surface density, which is consistent with the Clemens et al. (1998) observations.

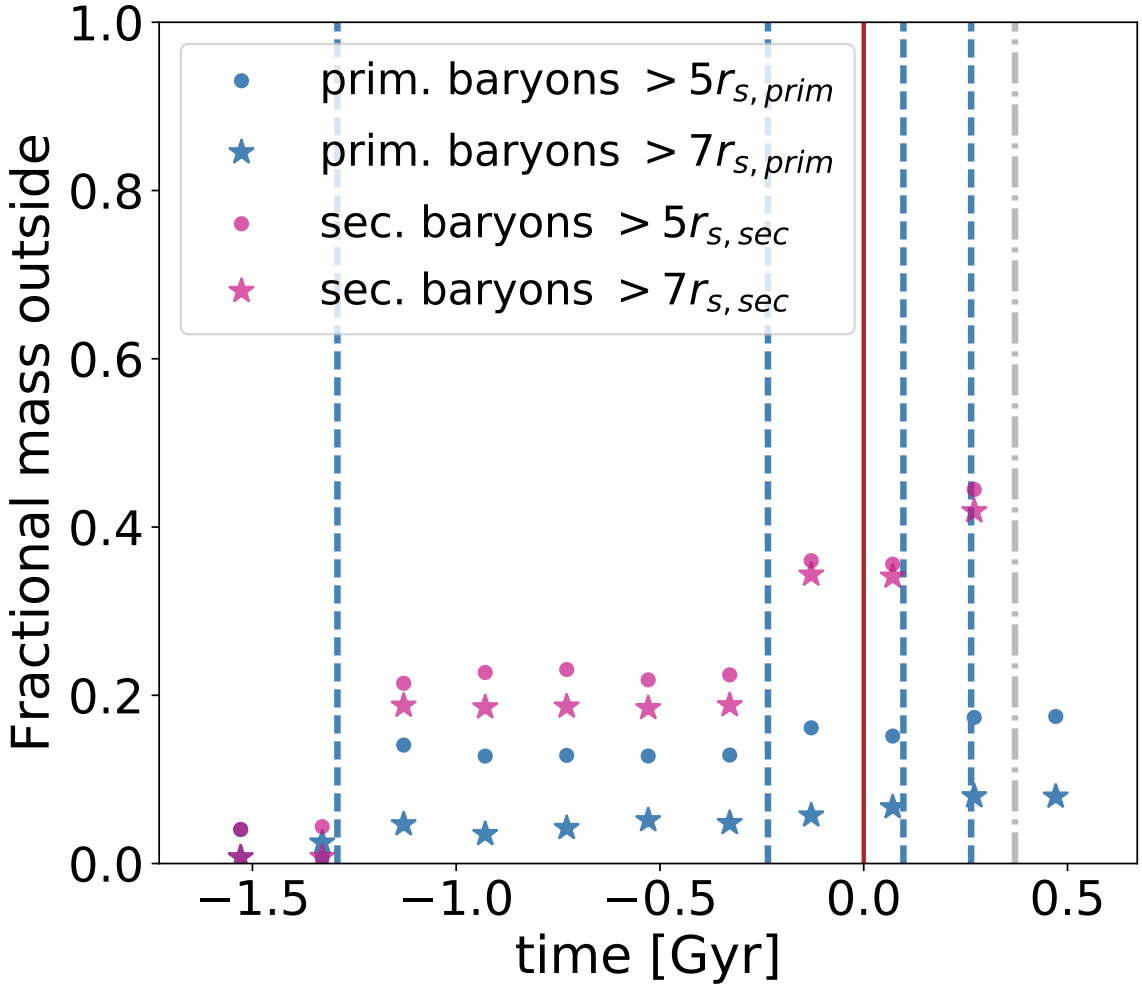

Figure 5.6: The fraction of baryonic mass residing outside 5 (circle markers) and 7 (star markers) disk scale radii divided by the total initial baryonic mass of each galaxy is plotted as a function of time, in 200 Myr increments. Blue points indicate results for the primary and magenta points for the secondary. We do not account for mass transfer between the two galaxies in this figure. The vertical blue dashed lines correspond to pericentric passages, the red solid line indicates the time of match (present day) and the gray dash dotted vertical line demonstrates when the two galaxies coalesce, after which we do not track the mass outside the secondary. At the beginning of the simulation all baryonic material resides within $7r_s$ of each galaxy respectively (see star markers). After each pericentric passage both galaxies get more extended and the secondary loses a substantial fraction of its mass. Given the eccentricity of the orbit, tidal stripping does not proceed smoothly over the course of the encounter. After coalescence the fractional masses outside the main bodies remain constant until re-accretion of material (see Figure 5.11).

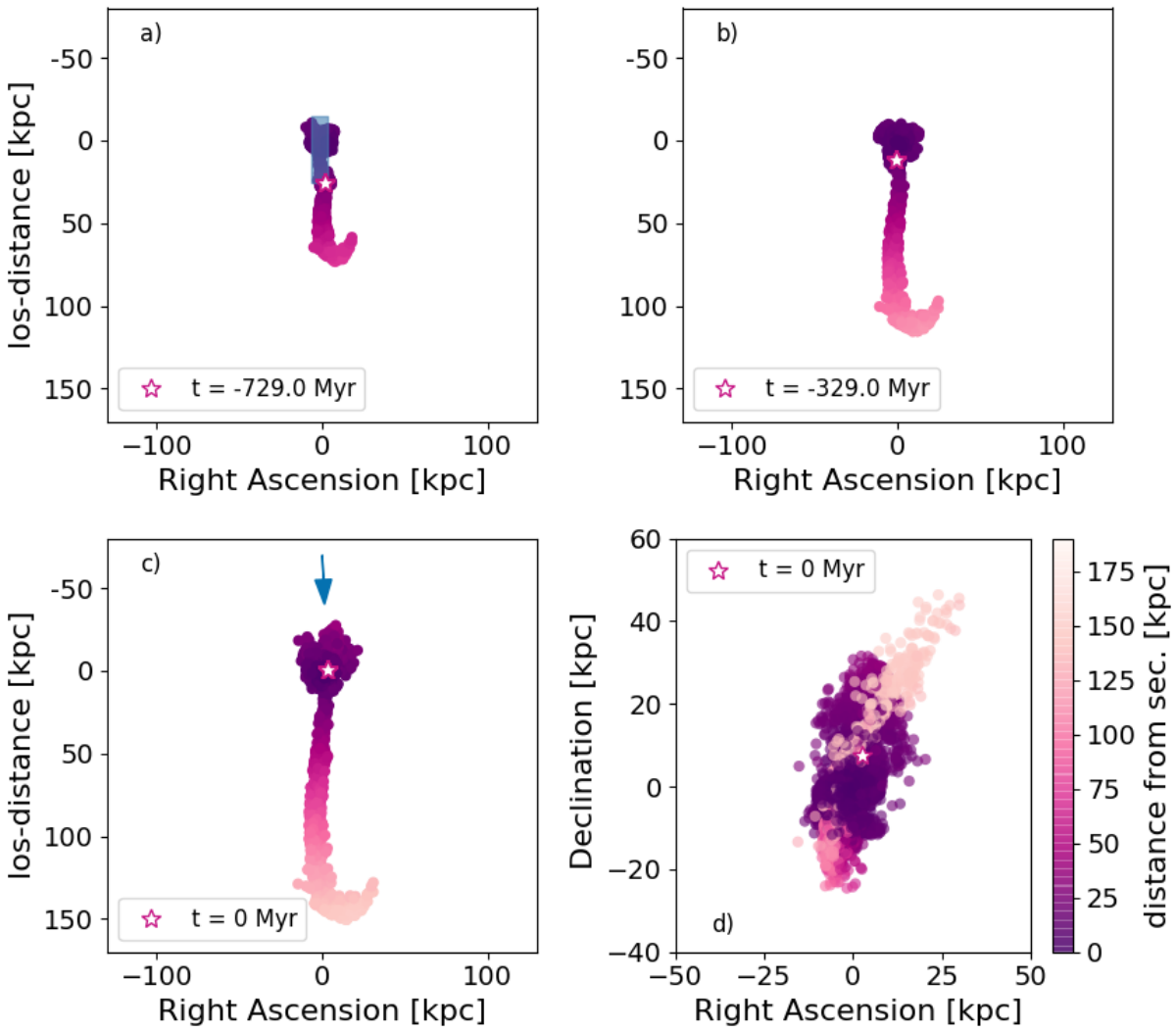

Figure 5.7: **Panel a through c:** "top-down" view (RA vs line-of-sight distance) of the evolution of the secondary dwarf's (NGC 4485) baryonic material beyond 7 disk scale radii at three different time steps. Panel **a)** is roughly the time of first apocenter, Panel **b)** is close to the time of second pericentric passage, Panel **c)** and **d)** is at the time of match. Each plot is centered on the position of the primary dwarf (NGC 4490) (x,y = 0,0). The star indicates the position of the secondary at each snapshot. The blue box in panel **a)** indicates the physical extent of the secondary's orbit. The blue arrow in panel **c)** indicates the skyview angle for an observer at the location of the Earth. The color demonstrates the 3D distance to each particle from the center of the secondary. **Panel d**: A rotation of panel **c)** to skyview showing all the secondary's particles beyond 7 disk scale radii at the time of match ($t = 0$ Myr). The tail lost at the first pericentric passage continues to grow beyond the size scale of the orbit. Due to our viewing angle of the system, we see the tail as a 50 kpc symmetric envelope surrounding the dwarf galaxy pair.

Figure 5.5 additionally shows that the debris continues to grow in size throughout the encounter and the bulk of the material does not immediately return to the system. In particular, the debris field will persist and should be observable long after the system coalesces (at ∼370 Myr). In the last snapshot we see that the final system will look like a companionless galaxy surrounded by a system of gaseous streams, although the exact properties of the merger remnant will depend on dissipational effects which are not included in this analysis.

5.4.2.1 Evolution of the Baryonic Disk Mass Distribution

To quantify how much baryonic material is pulled out in tidal structures during this encounter, in Figure 5.6 we show the fraction of the baryonic particles removed from the primary and secondary by their mutual tidal forces as a function of time. The two galaxies are investigated separately, and we do not account for transfer of mass between the two galaxies in this plot. Instead, at each time step we evaluate the amount of mass beyond the listed radius (5 or 7 × the scale radius) of each galaxy separately.

Initially (at $t = -1.53$ Gyr), all baryons reside within $7r_s$, where r_s is the disk scale length of each galaxy, listed in Table 5.2. After each pericentric passage both galaxies become more extended and/or have baryons pulled out in tidal features. Fractionally, the secondary loses much more material than the primary at each pericentric passage in the simulation (see Figure 5.6, magenta vs cyan points). This is due to the high mass ratio between the two galaxies and the fact that the secondary is spinning prograde with respect to its orbit around the primary (e.g. Toomre & Toomre 1972, D'Onghia et al. 2010, Sengupta et al. 2015a). While some of the secondary's particles do end up within 7 disk scale radii of the primary ($< 5\%$ of the secondary's particles after both the first and second pericentric pass), the point here is to track which galaxy loses the most mass fractionally in the encounter.

The mass loss occurs at pericenter, with little evolution in the mass profile between

pericenters. At the time of match (Figure 5.6, red vertical line) $\sim 34\%$ of the baryons from the secondary galaxy reside outside $7r_{s,sec}$, and only $\sim 6\%$ of the primary's baryons are beyond $7r_{s,prim}$. Interestingly, the difference between the amount of material within $5r_s$ and $7r_s$ at a given time step is larger for the primary galaxy than for the secondary after the first pericentric pass (the blue circles vs. stars are more separated than the magenta circles vs. stars). This indicates that the primary is being morphologically affected by the secondary, despite the high mass ratio of $\mu = 8:1$ (see Section 5.4.3 for a discussion of this).

Observationally, the amount of HI gas outside the stellar disks of NGC 4490/4485 is M_{HI}(outside)$= 1.07 \times 10^9$ $M_\odot$ (as defined in Pearson et al. 2016, table 2, 3 and shown as red ellipses in their figure 1). This estimate was done defining the size of the stellar disks of NGC 4490/4485 as 4 times the K_s-band scale length from the 2MASS catalog. This corresponds to $r_{\rm ext,prim} = 7.4$ kpc and $r_{\rm ext,sec} = 2.6$ kpc for NGC 4490/4485 respectively, which is slightly larger than but comparable to 7 disk scale lengths used for our analysis in this paper ($7r_{s,prim} = 5.8$ kpc and $7r_{s,sec} = 2.1$ kpc). In our simulation at the time of match the amount of baryons beyond 7 disk scale radii of the primary and secondary galaxies correspond to 6.9×10^8 $M_\odot$ and 2.3×10^8 $M_\odot$, respectively (see Table 5.2). Hence in our match, a total baryon mass of $\sim 0.9 \times 10^8$ $M_\odot$ resides outside the galaxies at the time of match, which is similar to the observed value for M_{HI} outside the 2MASS extents of the galaxies.

While it is encouraging that this number is the right order of magnitude, we do not distinguish between stars and gas in our baryon mass budget. In this section we are comparing to HI observations, but stars should similarly be tidally removed in the interaction. As mentioned in Section 5.4.1.4, varying the mass models (e.g. the disk extent, halo concentration, halo mass) could change the amount of mass lost from the baryonic disks during the encounter. In this work we have matched the simulations to HI data, and typically gas disks

are more extended than stellar disks (Swaters et al. 2002) which could ensure that the tidal debris would be primarily made of gas, rather than stars. This is the explanation commonly invoked to explain the lack of stars in the Magellanic Stream (Besla et al. 2012).

5.4.2.2 Visualizing the Tidal Tail Debris

To explore in detail how the tidally removed material evolves relative to the galaxies, in Figure 5.7 we investigate the "top-down" view (RA vs line-of-sight distance) of the simulation (see blue arrow in panel **c** for the observers line-of-sight view, which would recover the perspective plotted in Figure 5.5). In particular, we show the morphological evolution of the particles beyond 7 disk scale radii of the secondary dwarf (see magenta stars in Figure 5.6) at three different times (Figure 5.7, panel **a** through **c**). To ensure that the tidal features have had time to grow, the first time step is near the first apocenter (see Figure 5.2, left). The color scale indicates the 3D distance of each particle from the center of the secondary galaxy at each time step. In this projection, the orbit of the secondary around the primary is confined within the blue box in the first panel and is shown here for scale. The magenta star indicates the position of the secondary in each panel, and the first three panels are centered on the position of the primary dwarf.

Figure 5.7 shows that the tidal tail produced in the first passage grows > 100 kpc beyond the physical scale of the orbit. As expected, the tail does not stay in the plane of the orbit due to the offset between the orbital plane and the inclination of the secondary dwarf. Panel **c)** shows the time of match "top-down" view and the blue arrow indicates our viewing perespective of the system. At the time of match the tail initially raised at the first pericentric passage has grown to be $\sim$175 kpc in size. Interestingly, the ongoing Arp 299 galaxy merger (Hibbard & Yun 1999) has one of the longest HI tails observed ($\sim$180 kpc in projection) and is a factor of 10 more massive than the NGC 4490/4485 system. The fact that the dwarf

encounter between NGC 4490/4485 produces a tail of similar length further emphasizes that low mass dwarf-dwarf encounters can have dramatic effects, although the true 3D length of Arp 299 might be even longer than 180 kpc due to projection effects and the sensitivity of the observations. When we rotate the system into the plane of the sky (Figure 5.7, panel **d**), the long tail wraps around the primary galaxy as a roughly symmetric ∼50 kpc envelope when viewed from the Earth (as described in Section 5.4.1.2).

5.4.3 Consequences for the primary galaxy

In this section we investigate the effect of the repeated interactions with the secondary on the primary dwarf in our simulation. In Figure 5.6, we found that the primary gets more extended and that a small fraction of its baryons reside beyond $7r_{s,prim}$. Additionally, we presented diffuse starlight extending towards the left of the primary's main body in optical observations in Figure 5.1 (right) but we did not include this feature as one of the *Identikit* matching parameters. Can this structure be caused by perturbations of the primary's stellar disk from interactions with the secondary?

In Figure 5.3, panel **a)** there is an off-centered extension of the primary disk body to the left (cyan particles). This is a common feature of each simulation where the secondary has a close encounter with the primary. Figure 5.3, panel **d)** shows the "top-down" (RA vs line-of-sight distance) view of the simulation, where a spiral feature is evident in the primary (cyan) galaxy. In order to investigate how this structure compares to the diffuse extension of NGC 4490 seen in the optical data (Figure 5.1, right), we explore the structure of the primary galaxy at the time of match in Figure 5.8. In panels **a** and **b** we plot the face-on and plane-of-the-sky density projections of the baryons in the primary dwarf.

The gray box is overlayed to highlight the location of the diffuse starlight in the optical observations (Figure 5.8, panel **c**, black arrow). The primary dwarf indeed appears to be

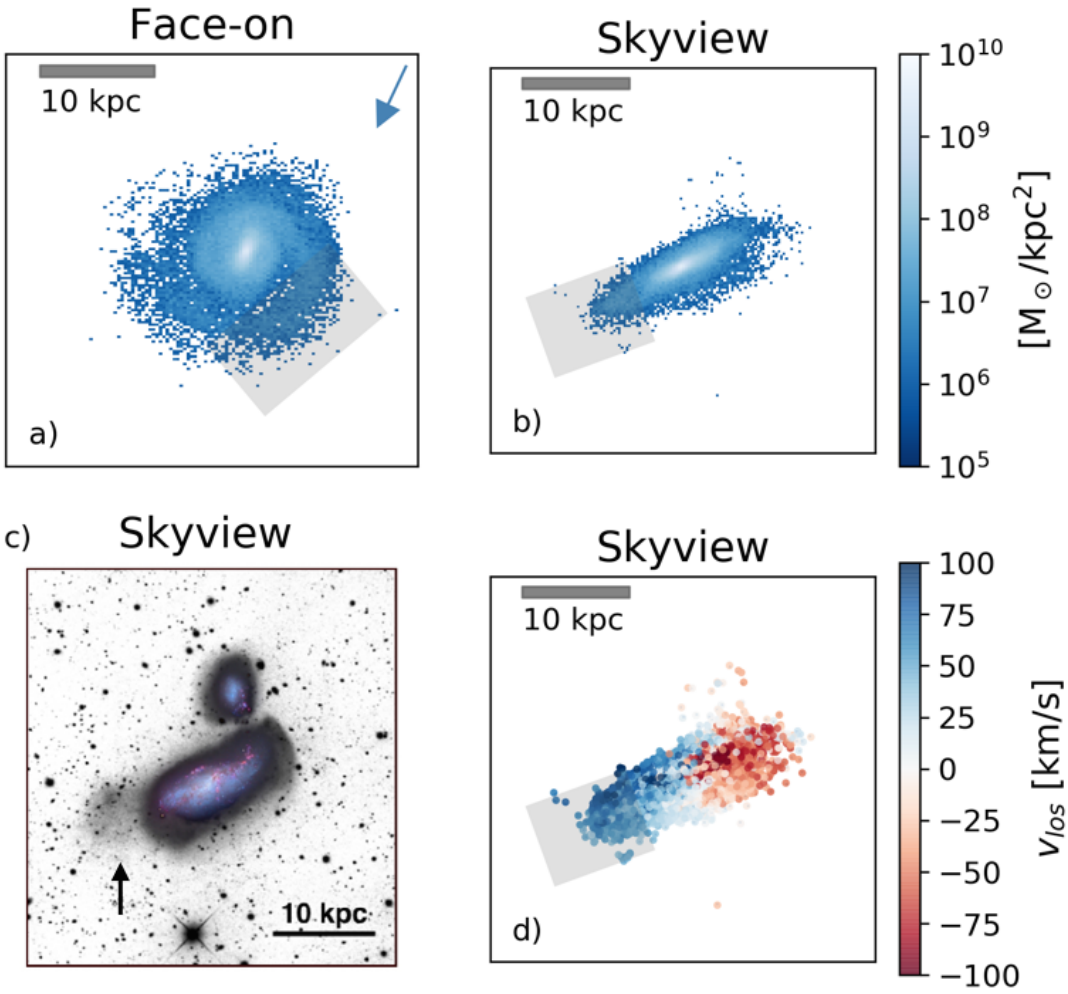

Figure 5.8: Projections of the primary's baryonic particles at the time of match. **Panel a)** Face-on projection of the density distribution in the primary dwarf (NGC 4490) at the time of match. The blue arrow indicates our viewing direction of the system. The gray box highlights the particles in the one armed spiral (panel **a**) associated with the extension of diffuse star light seen in the optical data (black arrow, panel **c**). These particles are located in a one armed spiral induced by the most recent pericentric passage with the secondary (NGC 4485) where the impact parameter was $r_{p,2} = 1.7$ kpc. **Panel b)** Skyview projection of the density distribution in the primary (NGC 4490) at the time of match. **Panel c)** Optical data of the dwarf pair (see Figure 5.1). **Panel d)** Skyview of all primary baryonic particles at the time of match. The color bar shows the line-of-sight velocity (v_{los}) of the particles ranging from -100 to 100 km s^{-1}. The particles associated with the extended diffuse starlight (see black arrow, panel **c**) are highlighted in the gray boxes and are blue-shifted. The recent encounter with the secondary dwarf appears to have induced a one-arm spiral mimicking the optical extension of the main body when viewed from our perspective.

extended in the direction of the diffuse starlight from our viewing direction (panel **b**), and when viewing the primary's baryonic disk face on, we see that the extension is due to the presence of a one-armed spiral extending from the main body (panel **a**). The feature is moving towards us at the time of match (panel **d**).

This asymmetric one-armed spiral is formed during the second pericentric passage and persists for ∼300 Myr (see also Lang et al. 2014, Besla et al. 2016) after which it is destroyed due to the third pericentric close passage ($r_{p,3} = 0.95$ kpc, see Figure 5.2).

The one-armed spiral appears to be a generic outcome of a collision (low impact parameter encounter) between a low mass perturber and a barred galaxy (see Athanassoula 1996, Pardy et al. 2016, Berentzen et al. 2003, Bekki 2009, Besla et al. 2012, Besla et al. 2016). The exact location of the one-armed spiral feature is sensitive to the specific bar phase at the time of encounter, hence the details of the observed one-armed spiral might differ from the simulation result presented here. Our simulation of the NGC 4490/4485 provides further evidence that these types of dynamical encounters could explain the classical morphological signpost of Magellanic Irregulars (de Vaucouleurs & Freeman 1972).

At the time of match, the extension of the primary has a surface density of $\sim 10^7$ $M_\odot$ kpc^{-2}. While the exact surface density is dependent on our mass model for the primary galaxy, this value is at least a factor of 100 higher than the surface density in the envelope surrounding the pair (see Figure 5.5, middle left), which can explain why we have not yet found a stellar envelope associated with the 50 kpc HI envelope. Additionally, the stellar disk scale length might be smaller than the HI disk scale length (Swaters et al. 2002), which could also limit the amount of stars in the envelope.

5.5 The fate of the envelope

Throughout the paper, we have focused on the dynamical match to the system and what happens up until the time of match. In this section we discuss the future evolution of the system and the fate of the extended baryonic envelope.

5.5.1 Energetic and Morphological Evolution of the Envelope

Based on the morphological evolution of the system seen in Figure 5.5 it is clear that the large scale structure of the system persists and continues to evolve long after the time of match (t = 0 Gyr) and long after coalescence of the two dwarf galaxies (t = 0.37 Gyr). But will all of the envelope be re-accreted or is some unbound? And how long will it take the bound portion to re-accrete? With a dynamical match to the system, we can begin to address these otherwise observationally challenging questions.

In Figure 5.9 we plot the 3D velocity, $v_{\rm 3D}$, of each secondary baryonic particle in the simulation (32768 particles) as a function of their total energy, $E_{\rm tot}$, at the time of match. The color bar shows the 3D distance of each particle from the center of the secondary dwarf. The total energy is calculated as:

$$E_{\rm tot} = \frac{1}{2}(v_{\rm 3D} - v_{\rm prim})^2 + \phi, \tag{5.3}$$

where v_{prim} is the magnitude of the center of mass velocity of the primary at the time of match and ϕ is the potential energy of each particle based on their location, stored as an output for each particle in each snapshot of the simulation. If the particles have a negative total energy they are bound to the center of mass of the combined system of the primary and the secondary galaxy.

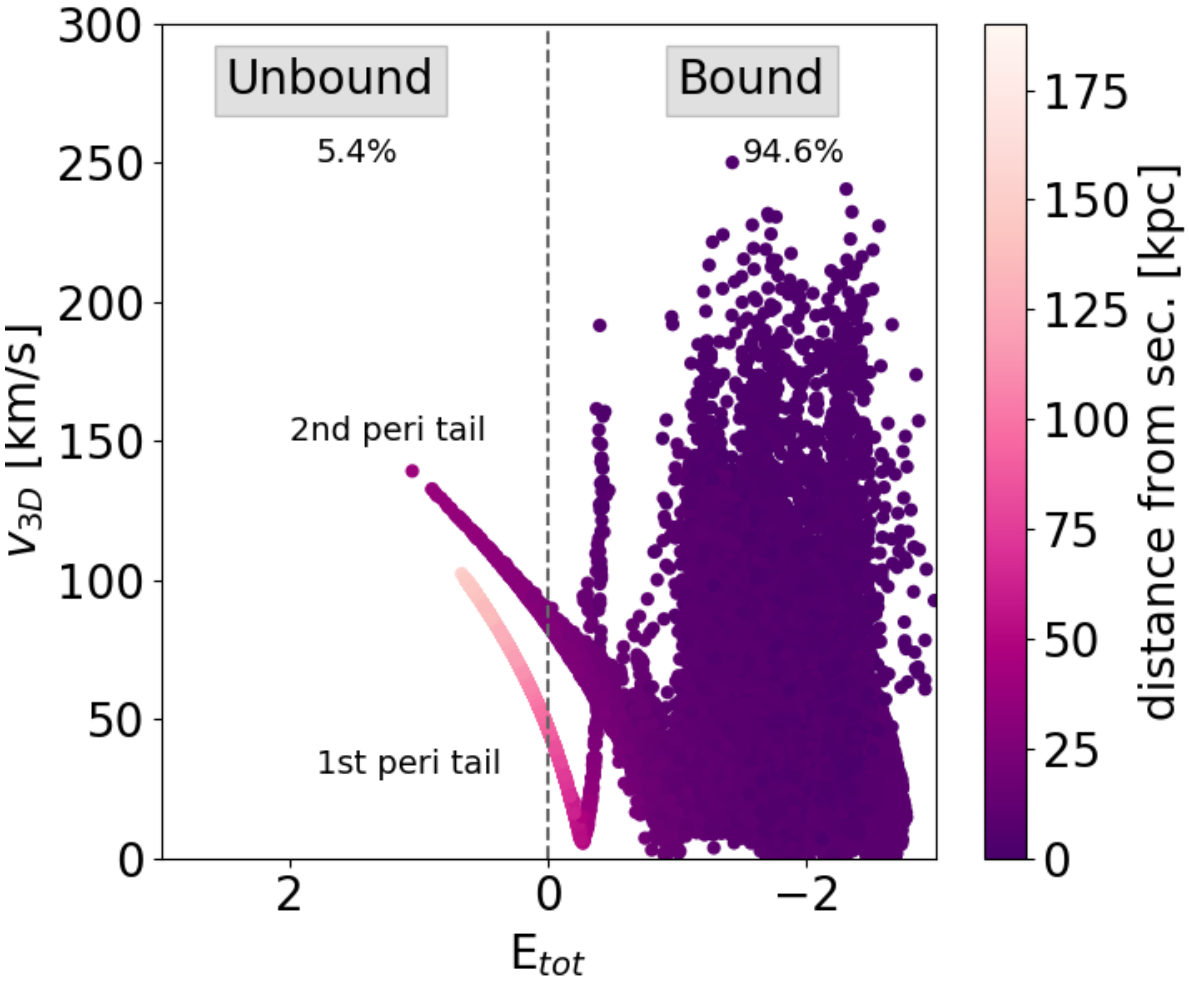

Figure 5.9: The magnitude of the 3D velocity vector as a function of total energy for all the secondary dwarf's baryonic particles at the time of match. The color bar indicates the 3D distance from each particle to the center of the secondary at the time of match (same color bar as in Figure 5.7). Of the 32768 baryonic particles in the secondary dwarf galaxy, 1775 are unbound (5.4%). The two distinct kinematic features are produced in the first and secondary pericentric passage, respectively, where the second pericentric tail particles are closer to the secondary at the time of match. Note how the tail produced in the first pass has a velocity reversal where $v_{3D} = 0$ km s^{-1} close to $E_{tot} = 0$. This indicates that some material in the tidal tail from the first pericentric passage is moving away from the galaxies while some material has reached its turnaround point ($v_{3D} = 0$ km s^{-1} relative to the center) and has started to fall back.

The tidal features produced in the first two pericentric passages separate as two distinct kinematic features. The part of the tail produced in the first pericentric encounter ($t = -1.29$ Gyr, see Figure 5.2, left) is located farthest away ($d_{3D} \sim 175$ kpc), while the tidal debris stripped in the more recent second pericentric passage ($t = -0.23$ Gyr, see Figure 5.2, left) has only reached $d_{3D} \sim 34$ kpc at the time of match.

At the time of match only 5.4% of the total baryonic mass of the secondary is unbound and is removed at either the first or second pericentric passage. From Figure 5.6 we know that $\sim 34\%$ of the secondary particles reside beyond 7 disk scale radii at the time of match and that the rest of the material is within the main body at small distances (see dark purple points). If we only include the particles beyond 7 disk scale radii of the secondary ($7 \times r_{s,sec}$ = 2.1 kpc) at the time of match in our calculation, 18.9% of those secondary particles are unbound.

Figure 5.9 shows that the tail from the first pericentric passage exhibits a velocity reversal (where part of the bound tidal tail has $v_{3D} = 0$ km s^{-1}), indicating that some material in the tidal tail from the first pericentric passage is moving away from the galaxies while some material has reached its turnaround point ($v_{3D} = 0$ km s^{-1}) and has started to fall back.

Motivated by this velocity reversal, we investigate the future evolution of the secondary's debris beyond 7 disk scale radii at the time of match. In Figure 5.10, we show 4 "top-down" (RA vs los-distance) simulation snapshots tracking the future fate of the tidally stripped material at the time of match.

The unbound particles (18.9%) are marked as "+" symbols. We do not include these particles in our analysis of material "moving away" and "falling back" to the merger remnant as we know this material is already lost to the surroundings. It is important to note that the timescales involved will be affected by our assumed galaxy mass model (see Section 5.5.2).

In Figure 5.10, we do not explicitly track material tidally removed from within 7 disk

scale lengths in future passages, as we are only tracking the present day envelope. We expect that the later tidal tails are generally much less extended and should re-accrete more rapidly. The blue arrow indicates our viewing direction towards the system at the time of match. The color bar denotes the 3D velocity (y-axis from Figure 5.9). We fix the maximum value of the color bar to $v_{3D} = 70$ km s^{-1} such that the color bar is not dominated by the high velocity particles within the secondary's disk (see y-axis from Figure 5.9). This enables us to better illustrate the velocity gradient along the tail stripped at the first pass (some material is starting to fall back, white particles: $v_{3D} = 0$ km s^{-1}). The black bars in Figure 5.10 indicate where $E_{\rm kin} = v_{3D} = 0$ for the tail produced in the first pericentric passage. All tidal material in the tail closer to the center of mass than this limiting distance (black bars) is falling back and returning to the primary.

Panel **a)** of Figure 5.10 represents the current state of the system (the time of match). At this point in time the secondary has undergone two pericentric passages, creating two kinematically distinct tidal tails (see Figure 5.9). In this projection of the simulation ("top-down"), the particles stripped in the second pericentric passage, are moving mostly in the negative z(positive declination)-direction. Therefore, we do not plot the velocity reversal black bars for the tail produced in the secondary pass, however we do account for these particles in our mass budget of material moving away vs returning to the system.

Panel **b)** represents the system 1 Gyr into the future. The debris from the second pericentric passage tail is growing in length (to more negative z-values in this projection) and some of the material starts to fall back towards the center of mass. The secondary has made a third passage (see Figure 5.2), generating more tidal debris (towards more negative RA values). Recall that we are only tracking debris which was already beyond 7 disk scale radii at the time of match (in principle more debris from within 7 disk scale radii will also be tidally moved in this third pass). At this point in time 68.1% of the bound present day

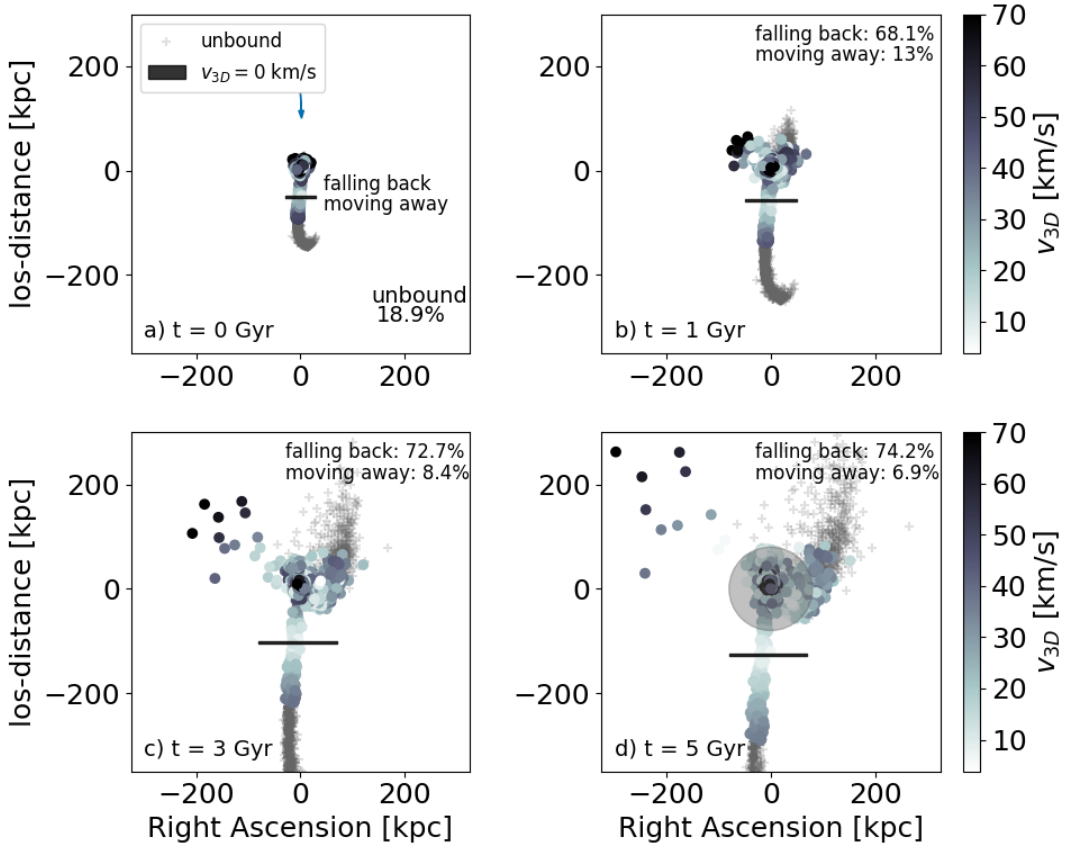

Figure 5.10: The "top-down" (RA vs los-distance) morphological evolution in time (panel **a** through **d**) of the secondary dwarf galaxy's particles that were beyond 7 disk scale radii at the time of match. The color bar denotes the 3D velocity (y-axis from Figure 5.9). We fix the maximum value of the color bar to $v_{3D} = 70$ km s^{-1}. The gray "+"s show the 18.9% of particles beyond 7 disk scale radii at the time of match that are unbound and which will continue to move away from the system. This number will remain the same between all panels, and we do not include these particles in our analysis of material "moving away" and "falling back" to the merger remnant. The blue arrow in panel **a** indicates our viewing perspective of the system. The black bars demonstrate the turnaround-radius (apocenter/zero-point-velocity) at which the particles in the tidal tail from the first pericentric passage shift from moving outwards to start falling back towards the center of mass (white particles have $v_{3D} = 0$ km s^{-1}). As time passes, more and more particles start to fall back towards the center of mass (see percentages) and the $v_{3D} = 0$ km s^{-1} turnaround points move further out along the tidal tails to larger distances. The gray circle in panel **d** illustrates an 80 kpc sphere, which encloses the particles that have fallen back from the tidal tails and orbit the center of mass. After 5 Gyr (panel **d**) much of the debris remains in the two tails produced during first and second pericentric passages, demonstrating that the large scale structure persist for several Gyr after the dwarfs coalesce.

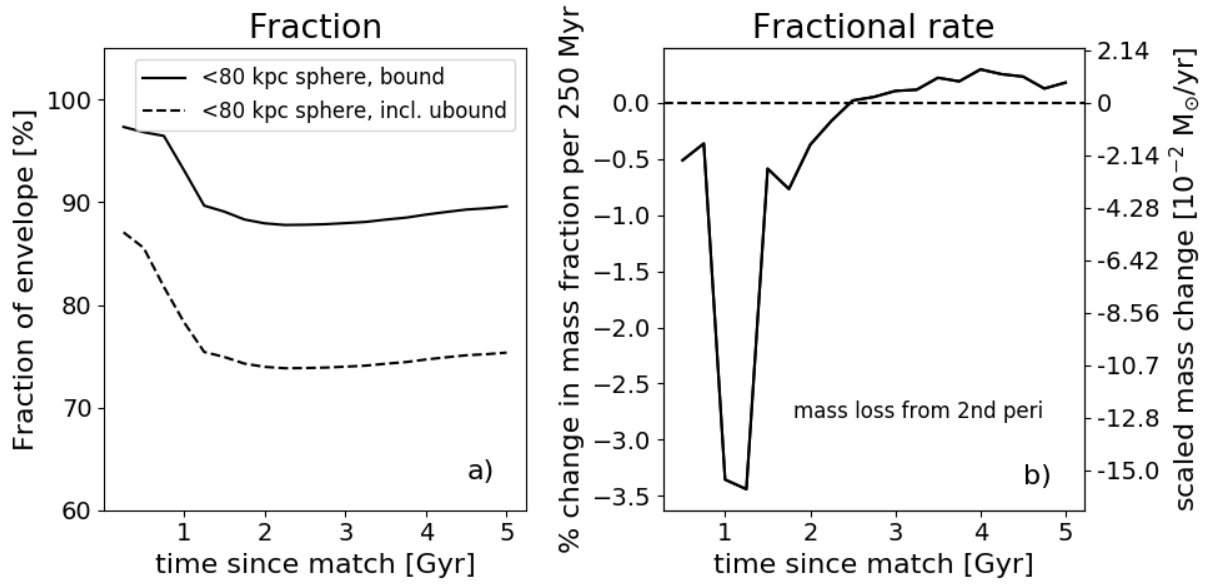

Figure 5.11: **Panel a)** Fraction of the total baryonic envelope that resides within a sphere of 80 kpc in radius centered on the primary (NGC 4490) (illustrated in Figure 5.10 panel **d**) as a function of time after match (in the future). The solid line shows the fraction using only the bound particles in the envelope at the time of match. The dashed line shows the same calculation, but now including the unbound particles (see "+" markers in Figure 5.10). **Panel b)** Fractional rate of mass moving in/out of the 80 kpc sphere for the bound particles as a function of time after match. Left y-axis demonstrates the percentage of all the bound particles in the simulation that are moving out of/into the 80 kpc sphere. The right y-axis shows this same rate converted to $M_\odot$/Myr and scaled based on the mass in the present day observed envelope (M_{HI}(outside)= 1.07×10^9 $M_\odot$). The dashed horizontal line shows where no mass accretion nor mass loss occurs. The large drop in the fractional rate occurs as the material from the secondary pericentric pass moves out of the 80 kpc sphere. From both panels it is evident that mass continues to be lost for several Gyr after the time of match, but that after > 2 Gyr the re-accretion of debris from both the first and second pericentric dominates over the fraction of mass flowing out of the 80 kpc sphere.

envelope is returning to the merger remnant, 13% is moving away from the remnant (some of this might be unbound in the third pass) while 18.9% of the particles which were already unbound at the time of match are still moving away (gray "+" markers).

In Panel **c)** it is evident that the location of the velocity reversal (black bar) has moved even farther out along the first tidally produced tail (to more negative los-distance values). This is due to the fact that the particles along the tail lose kinetic energy as time passes and start falling back towards the center of mass (see percentages). At this point in time 72.7% of the present day bound envelope is returning to the merger remnant, and only 8.4% of the particles are moving away along with the 18.9% unbound particles from the time of match.

Panel **d)** represents the system 5 Gyr into the future and we have overlayed an 80 kpc sphere, which roughly represents the turnaround radius for debris that has returned from the tails and has started to orbit the center of mass of the merger remnant. This limiting radius of 80 kpc sphere was determined by investigating particle motion of the returned debris at $t = 5$ Gyr. We seek to track the motion of particles across this radius to infer the rate at which the present day tidal debris will return to the system. In this work, we are investigating a collisionless N-body simulation (i.e. without hydrodynamical effects), but we would not expect the gas in the remnant to extend beyond the collisionless particles (i.e. beyond 80 kpc), as the gas should dissipate energy likely resulting in a more compact configuration than we see here. See Section 5.6.3 for a discussion of hydrodynamical effects.

Interestingly, after 5 Gyr (panel **d**) much of the debris remains in the tails produced during the various pericentric passages, demonstrating that the large scale structure may persist for several Gyr after the dwarfs coalesce. For a discussion on return of tidal material in a $\mu = 1:1$ mass ratio galaxy merger, see Hibbard & Mihos (1995).

5.5.2 Rate of return of the envelope

It is very difficult to assess the inflow rates of baryons to galaxies observationally and only few examples exist (e.g. Zheng et al. 2017). However, when simulating a dynamical encounter, we can estimate the inflow rate of baryons to the merger remnant (see also Hibbard & Mihos 1995). We use the 80 kpc radius radius sphere described in Section 5.5.1 and shown in Figure 5.10 panel **d**, to track the future evolution of all material in the present day envelope. We define the envelope to be all material beyond $7 \times r_{s,sec}$ (2.1 kpc) at the time of match. We can thus track the inflow of material from the outer HI envelope in time.

In Figure 5.11 we track the tidal debris that is in the envelope at the time of match. In particular, we investigate fractionally how much of this material is residing within vs outside the 80 kpc sphere as a function of time (Figure 5.11, panel **a**). Here, we distinguish between the bound (solid line) and total (bound+unbound; dashed line) debris. As the unbound material will not return to the system, it will not affect the mass inflow to the system (or rate of return).

Up until $\sim$ 2 Gyr after the time of match, the 80 kpc sphere loses more mass than it gains, hence the bulk of the tidal material is still moving away from the system, which is consistent with the fact that the second pericentric tail is leaving the system during this time (see Figure 5.10). As time progresses more material from the outer envelope returns to reside within the 80 kpc sphere. After 2.5 Gyr we see a net inflow of the outer envelope to the 80 kpc sphere, hence more material is flowing into than out of the sphere. This implies that the material within this radius (i.e. the bulk of the envelope) will return to the merged system. The total bound mass in the simulated envelope shown in Figure 5.11, panel **a**, corresponds to $\sim 1.4 \times 10^8$ $M_\odot$ and after 5 Gyr $\sim$ 10% of the envelope has yet to be re-accreted.

This behavior is more clearly seen in Figure 5.11, panel **b**, where we plot the fractional

rate of return of bound material within the 80 kpc sphere. The second pericentric passage causes a net outflow of material, but after 3 Gyr there is a net inflow. Scaling the fractional values using the total mass of the observed envelope implies a net inflow rate of 0.01 $M_\odot$ yr^{-1} at 80 kpc (see right y-axis).

We have utilized light dark matter halos in this study. Barnes (2016) showed that the ratio of the escape velocity (v_e) from a galaxy and its circular disk velocity (v_c) at the half mass radius ($\mathcal{E} = \frac{v_e^2}{v_c^2}$) can greatly affect the radii to which tidal material reach after tidal removal and its re-accretion rate. If $\mathcal{E}$ is higher the galaxies reabsorb their tails faster. Using more massive halos, as expected from abundance matching, would result in the debris reaching smaller radii before velocity reversal and that the acceleration is higher as the debris falls back due to the deeper potential well. The results presented in this section should therefore be interpreted as lower limits on the inflow rate of the outer envelope. Given that the bulk of the envelope remains within 80 kpc of the system even in our low mass halo models, we conclude that the observed envelope will provide a long lived gas supply channel to the merged remnant.

5.6 Discussion

In this section we compare our results to previous simulations of the Magellanic System (Section 5.6.1), and we discuss the implications of our work in the context of tidal pre-processing and ongoing dwarf galaxy surveys (Section 5.6.2). Finally, we discuss baryon cycles in dwarf galaxies in the context of gas inflows and dissipational effects (Section 5.6.3).

5.6.1 Comparison to the LMC & SMC system

Besla et al. (2012) showed that the mutual interaction between the Magellanic Clouds (MCs) can reproduce both the large-scale gaseous distribution (bridge, leading and trailing arm) of the Magellanic System along with internal properties of the clouds, irrespective of tides from the Milky Way. Our match to the NGC 4490/4485 system is similar to the LMC/SMC models as both solutions suggest that a substantial amount of baryons are moved to large distances from the secondary galaxy (i.e. NGC 4485 and the SMC) in a prograde encounter.

Additionally, the NGC 4490/4485 system might provide clues to what the LMC/SMC would have evolved into if they had not been in the vicinity of the Milky Way (see Besla et al. 2016). Because the LMC/SMC are passing close by the Milky Way, the SMC might be unbound from the LMC (González & Padilla 2016), which has been suggested based on proper motion measurements of the clouds (Kallivayalil et al. 2006, Vieira et al. 2010 Kallivayalil et al. 2013, Zivick et al. 2018, Niederhofer et al. 2018). In the Besla et al. (2016) simulation (LMC/SMC evolving without the Milky Way), the Magellanic Clouds' present day 3D separation is 26 kpc ($t \sim 6.3$ Gyr in their figure 5), and the most recent orbit has a timescale of $\sim$ 800 Myr. For comparison the 3D separation between NGC 4490/4485 in our best match is only 9.3 kpc at present day and the orbital timescale of the last orbit is only $\sim$330 Myr (see Figure 5.2, left). This is similar to what the LMC/SMC orbit would yield after one more pericentric passage close to the next apocenter (Besla et al. 2016, figure 5), suggesting that the NGC 4490/4485 pair is a more evolved version of the Magellanic Clouds, had they never fallen in to the Milky Way. Both our orbit and the Besla et al. (2016) orbit have high eccentricities at the time of their best match ($e = 0.83$ and $e = 0.66$, respectively), but the two orbits are not exactly analogous. Our models thus expand the range of plausible orbital parameters for dwarf-dwarf binary galaxy encounters. Both the LMC/SMC and NGC

4490/4485 solutions predict that in isolation, both systems would rapidly merge without the intervention of a massive third body.

A recent example of a dwarf pair that also mimics the LMC/SMC system was reported by Paudel & Sengupta (2017). The pair (UGC 4703/4703B) is very gas rich, shows signs of interaction (e.g. HI bridge, SF in bridge, extended gas) and the individual galaxies reside 81 and 104 kpc from their MW-type host, respectively. This pair provides an interesting example in addition to NGC 4490/4485 for understanding the effect of a mutual dwarf-dwarf tidal interaction, prior to infall to a massive host (i.e. pre-processing). In future work, we plan to assess the statistics of orbital configurations for dwarf encounters to advanced our understanding of the dwarf-dwarf merger sequence. See also Besla et al. 2018, *in prep.* for a theoretical comparison between the frequency of dwarf-dwarf encounters in *Illustris* and SDSS at low redshift.

5.6.2 Tidal pre-processing

The fact that baryons can remain extended for several Gyr after coalescence of interacting dwarf galaxies is important for understanding how tidal pre-processing between dwarfs can affect gas removal from low mass galaxies (quenching) after infall to more massive/gas rich environments. Ram-pressure and tides from a nearby massive galaxy seem to be inefficient at stripping gas that is tightly bound to the dwarfs (e.g. Emerick et al. 2016, Fillingham et al. 2016). If the gas is much more extended, removing it from the dwarfs through e.g. tides from a host galaxy or ram-pressure stripping by a hot halo of a host galaxy will be more efficient (e.g. Emerick et al. 2016, Salem et al. 2015) and extended gas structures caused by dwarf-dwarf interactions could help this process (Pearson et al. 2016).

This picture appears consistent with the ΛCDM theory as Wetzel et al. (2015) have shown that 30-60% of dwarf satellites are expected to have been accreted as part of a low mass

group. Furthermore, Marasco et al. (2016) found that quenched dwarf satellites of MW type hosts at $z = 0$ preferentially experienced a satellite-satellite encounter prior to accretion.

From the TiNy Titans Survey, we know that dwarf galaxy pairs are just as gas rich as non-paired dwarfs if they reside far from a massive host galaxy (Stierwalt et al. 2015), but that much of this gas can be located in extended tidal features (Pearson et al. 2016). The work presented in this paper demonstrates that in encounters where gas is moved to large radii, gas may remain extended for several Gyr. These long timescales indicate that we should expect to find gas in large extended structures surrounding the dwarfs when surveying dwarf galaxy pairs (e.g. Stierwalt et al. 2015), dwarf groups (e.g. Stierwalt et al. 2017) and dwarfs with merger driven starbursts (e.g. Lelli et al. 2012). Interestingly, there is a pair of dwarf galaxies (NGC 4618 & NGC 4625: Pearson et al. 2016) with stellar masses of $M_* = 4.3 \times 10^9$ $M_\odot$ and $M_* = 1.3 \times 10^9$ $M_\odot$, respectively in the vicinity of NGC 4490/4485. NGC 4618/25 pair has a velocity separation of only $\Delta v = 20$ km s^{-1},[11] with respect to the NGC 4490/4485 pair, and they are at a projected separation of $d_{\rm proj} \sim 267$ kpc, assuming a distance of 7.14 Mpc (as for NGC 4490/4485). The NGC 4618/25 pair is at a larger separation than reported for the seven newly discovered dwarf groups in Stierwalt et al. (2017) (their projected separations are < 80 kpc), and it is unlikely the NGC 4618/25 pair has had a dynamical influence on the NGC 4490/4485 pair due to the large projected separation. Besla et al. 2018, *in prep.* shows that cosmologically it should be rare to find groups of dwarfs at low redshift ($0.013 < z < 0.0252$) with stellar masses of the members larger than $M_* > 2 \times 10^8$ $M_\odot$, although they use a more conservative search criterion of $15 < d_{\rm proj} < 150$ kpc and $\Delta v < 150$ km s^{-1}.

The COS-Dwarfs Survey (Bordoloi et al. 2014a) find substantial amounts of ionized gas at large distances (~ 110 kpc) surrounding 43 dwarf galaxies at low redshift ($z < 0.1$) and they suggest a wind-driven origin of the gas. While it remains unclear whether the tidally

[11] From NED redshifts: $\Delta v = c \times |z1 - z2|/(1 + (z1 + z2)/2)$.

removed gas in our dwarf-dwarf encounter will be and/or remain ionized as a result of the interaction (see Weilbacher et al. (2017) for an example and discussion of ionized gas in a massive galaxy merger), our work presents another contributing factor to gas at large distances as we find baryons orbiting the dwarf merger remnant long after coalescence (see Figure 5.5 and 5.10).

5.6.3 The Baryon Cycle and Unmodeled Hydrodynamic Effects

The current star formation rate of NGC 4490 inferred from the FUV non-ionizing continuum is $\mathrm{SFR_{N4490}(FUV)} = 1.9\ \mathrm{M_\odot\ \ yr^{-1}}$ (Lee et al. 2009, scaled to a distance of 7.14 Mpc here). We showed that ∼90% of the gas envelope is within a sphere of 80 kpc after 5 Gyr and that the material beyond the 80 kpc sphere (the outer envelope) is flowing into the region at a roughly constant rate of $\sim 10^{-2}\ \mathrm{M_\odot\ yr^{-1}}$ after 3 Gyr, representing a lower bound on the inflow rate. We expect all of the bound material (within and beyond the 80 kpc sphere) to accrete back on to the merger remnant at some point, potentially refueling star formation. However, to quantify the exact properties of the accretion rate of material onto the merger remnant itself, we need hydrodynamical simulations.

In this work, we have narrowed down the parameter space of the tidal interaction between the two dwarf galaxies NGC 4490 and NGC 4485. Our work is based on collisionless N-body simulations and we do not expect our global match to be much affected by dissipational effects as the large scale features (e.g. the symmetric HI envelope) and orbital decay are not strongly affected by the inclusion of gas (Barnes & Hernquist 1996). However, to properly study the structure of the remnant and where the accreted gas goes, hydrodynamical effects will be important to include in future simulations.

Additionally, we need hydrodynamical simulations to investigate the HI bridge connecting NGC 4490/4485 (see Figure 5.1, left). Based on our collisionless particle simulation presented

in Figure 5.3, we do not see evidence of a tidal bridge at the location of the dense bridge material (see red arrow in Figure 5.3), which indicates that this is a hydrodynamical feature. In our match, the orbit of the secondary passes through the dense gas bridge observed in HI during the first two pericentric passages in Figure 5.3, panel **a** and in the first pericentric passage in Figure 5.3, panel **b**, **c**, hence a hydrodynamical origin of the bridge seems plausible.

5.7 Conclusion

In this paper, we have computed the first dynamical match to an observed isolated galaxy encounter at the low mass, dwarf scale using *Identikit* with N-body follow-up. The system NGC 4490/4485 is an analog of the Magellanic System, surrounded by a massive HI envelope but located in isolation from any massive galaxy. Our results and conclusions are summarized as follows:

1. We are able to find a kinematic and morphological match to the gas distribution of the dwarf pair NGC 4490/4485 through solely the tidal forces from the primary (NGC 4490) stripping material from the secondary (NGC 4485). The match to the pair required a solution in which the secondary dwarf galaxy's (NGC 4485's) spin is prograde to the orbit and has a high inclination orbit with respect to the more massive dwarf (NGC 4490).

2. In this match the $\sim$50 kpc (projected) envelope consists of a large tail from NGC 4485, lost during the first pericentric encounter between the two galaxies ($\sim$ 1.4 Gyr ago). Due to our viewing perspective we see the tail as an envelope wrapping around the entire system. This demonstrates that through tidal interactions between two low mass galaxies, gas can be moved to large distances, without the need for stellar feedback or perturbations from a massive host.

3. We predict that NGC 4490 & 4485 will fully merge in 370 Myr, but that the gaseous envelope will remain extended well after coalescence.

4. During the encounter a one-armed spiral is induced in primary dwarf (NGC 4490) which is also seen in the new optical data of the system presented in this paper. This demonstrates that a high mass ratio, small impact parameter collision between two low mass galaxies can explain the classical morphological signpost of Magellanic Irregulars (de Vaucouleurs & Freeman 1972).

5. The fact that the extended tidal features evolve and persist for several Gyr after coalescence, supports the idea that dwarf-dwarf interactions play an important role aiding gas removal and quenching of low mass galaxies. Subsequent ram-pressure stripping and even weak tidal forces will be much more efficient to remove gas from such extended structures formed by pre-processing.

6. We studied the current dynamical state of the HI envelope around the NGC 4490/4485 system and concluded that baryons are "parked" and eventually re-accreted by the merger remnant over long timescales (> 5 Gyr). The material in the extended tidal features will return to the system, crossing an 80 kpc radius at a rate of 0.01 $M_{\odot}$ yr^{-1} within 2.5 Gyr. The bulk of the HI envelope will be re-accreted to the merged remnant, providing a long-lived supply channel of gas. If dwarfs in the field with large gas reservoirs (e.g. Meurer et al. 1996, Werk et al. 2010, Kreckel et al. 2011) have had a previous merger, the long accretion time can help explain the limited star formation in their gaseous outskirts.

7. This work provides a novel isolated analog to simulations of the LMC/SMC. We illustrate that, generically, a significant fraction of the gas can be moved to large distances in prograde dwarf-dwarf interactions, without the aid of a massive host (see also Besla et al. 2012, D'Onghia et al. 2010). Additionally, we find that the NGC 4490/4485 orbit appears to be an evolved version of what the LMC/SMC might have looked like had they not been accreted by the Milky Way.

Acknowledgments

We thank Sabrina Steirwalt, Kelsey E. Johnson, Sandra E. Liss, Joshua Barnes, Kelly Blumenthal and Andrew Emerick for insightful discussions. We thank Marcel Clemens for sharing his data of NGC 4490 & NGC 4485. The Zeno software package was used in this research. The Numpy software package (Walt et al. 2011) and Matplotlib graphics package (Hunter et al. 2007) were used in this research. This research has made use of the NASA/IPAC Extragalactic Database (NED) which is operated by the Jet Propulsion Laboratory, California Institute of Technology, under contract with the National Aeronautics and Space Administration. This material is based upon work supported by the National Science Foundation under Grant No. NSF grant 1714979 and NSF grant 1715944. We also acknowledge support from NASA for program 13383 from the Space Telescope Science Institute, which is operated by the Association of Universities for Research in Astronomy, Inc., under NASA contract NAS5-26555. KVJ's contributions were supported by NSF grant AST-1614743. G.C.P. acknowledges support from the University of Florida. DMD acknowledges support by Sonderforschungsbereich (SFB) 881 "The Milky Way System" of the German Research Foundation (DFG), particularly through sub-project A2.

5.A Appendix

Throughout the paper, we have presented a kinematic and morphological match to the low mass, isolated galaxy encounter NGC 4490/4485, which reproduces key features of the HI and optical data. In this appendix we discuss some of the alternative configurations which could reproduce some, but not as many of the features of the encounter.

- **Number of pericentric passes**

  A natural starting point when searching for a match is ensuring that the positions of the galaxies end up at the correct locations in morphology and velocity space. A natural next step is to explore how many pericentric passages are needed. The match presented in the paper occurs between the second and third pericentric pass close to apocenter. When exploring other matches, we found that any scenario in which only one pericentric passage had occurred did not provide a good match, as the tail from the first passage had not grown to be large enough to populate the envelope if the sizes of the galaxies (and separations) had to match the data. This was the case even in the most prograde scenario with substantial mass loss from the galaxies.

  When moving to a third pericentric pass, we could reproduce the overall morphology and kinematics of the encounter, often with a slightly larger length scaling (to fit the extent of NGC 4490 HI disk), however the tidal tail from the secondary galaxy produced in the first passage grew to be much too long and extended beyond the extent of the HI envelope in the wrong direction.

- **Wider passes**

  We also explored the initial separation. A closer initial pass will lead to a more dramatic

mass loss (depending on the disk angles). The match presented in this paper has an idealized pericentric separation at first pass of $4.2 \times r_{disk,prim}$. We explored wider pericentric separations for the encounter, but we were not able to populate the south of the HI emission kinematically (see Figure 5.3, panel **b**). In the wider passes the angle of the tail produced in the first pass became too wide and did not populate the south of the envelope with the tail "wrapping around" from the first pass. We tested that moving to a later interaction stage and a different viewing angle did not resolve this problem.

The widest pass we explored was a pass with an initial pericentric separation ($r_{peri} \sim 20\ r_{disk,prim}$). Between the third and fourth pass, we could get a match similar to the one presented in this paper. However, some debris from the first pass was present and predicted emission where none was observed. Hence, we did not obtain a better match by adding another pass.

- **Populating north and south from the secondary and primary, respectively**
  We explored encounters in which the north of the envelope morphologically and kinematically was solely populated by debris coming off of the secondary galaxy in the second pericentric pass, and in which the south was populated by debris from the primary galaxy kinematically and morphologically. Given the known high stellar mass ratio between the two galaxies, we were not able to populate the HI envelope symmetrically morphologically (the south was unpopulated) nor populate the kinematic features with this approach. In particular the emission located where the white arrows point to in Figure 5.3 was left unpopulated. The observed baryonic mass ratio of the pair is $\mu \sim 8:1$, however it is possible that the dark matter halo mass ratio is lower (see Section 5.4.1.4). Going to more equal mass ratios would probably violate the

observed stellar mass ratio.

- **Populating the "bridge region"**

  As discussed in Section 5.6.3, the orbit of the match presented in the paper passes through the dense bridge region in Figure 5.3, panel **b)** (see red arrow) in the first pericentric pass, and the orbit passes through the bright HI emission in the panel **a)** (see also Figure 5.1, left, inner HI contour) in both the first and second pass. The fact that the secondary's orbit passes through the primary's disk and through the bright HI emission associated with the bridge, provides a plausible scenario for forming a gas bridge due to ram-pressure effects (e.g. Besla et al. 2012).

  As a bridge could be a transient phenomenon, we also explored matches for which the orbit passed through the bright HI emission of panel **b)** in Figure 5.3 (red arrow) in the second pass instead of the first. Using this constraint, we could find a match for which the overall properties were similar (scaling, separations, morphology) to our presented match. However, we could not reproduce the kinematics of the tail from the first pericentric pass in this scenario (see white arrows in Figure 5.3, panel **b/c**) and the southern part of the emission was not as populated (Figure 5.3, panel **a**) as the tail from the first pass did not wrap around the system which is the case in our presented match. Hence, we discarded this match in favor of the match presented in the paper.

While there is some room for changing the exact parameters of the encounter (see Section 5.4.1), the match presented in the paper was the most satisfactory in terms of populating the northern and southern parts of the HI data morphologically and kinematically, reproducing the present day positions (i.e. separation) of the galaxies morphologically and kinematically, matching the observed velocity scale of the data, and having an orbit that passes through the dense bridge material in Figure 5.3, panel **a, b, c**. Hence, we have presented a plausible

scenario for the encounter geometry of the NGC 4490/85 system, yet further explorations of the eccentricity of the orbit, specific mass models of the galaxies and adding dissipational effects might change the specifics of the match. However, we do not expect the overall encounter geometry, which was common between all matches discussed above, to change (prograde orbit enabling substantial mass loss from the secondary galaxy and high inclination orbit such we see the tail in projection from our viewing direction).

Chapter 6

Conclusion

The chapters in this Dissertation are united by a common theme: hidden dynamical tracers from gravitational interactions providing us with information of events transpiring billions of years ago in our own and external galaxies. Using numerical methods and the dynamical intuition assembled over the last centuries, we have developed new techniques which could draw us closer to the true nature and behavior of dark matter, and we have shown how interactions between low mass galaxies have dramatic effects on their subsequent evolution. Below we summarize our results and put them into context of current and future work.

6.1 Stellar Stream Morphology as a Potential Probe

In Chapter 2 using "streak-line" methods with direct N-body follow-up, we demonstrated how the long, thin and curved morphology of the Pal 5 stellar stream orbiting the Milky Way could not be reproduced in the moderately triaxial dark matter potential. However, in this triaxial potential key observational properties of the Sgr stream had successfully been reproduced (Law & Majewski 2010). Simulating Pal 5's evolution in both a logarithmic and a triaxial dark matter halo yielded outcomes which were distinguishable through the

morphology of the stream alone. The Pal 5 stream appears to "fan" out in the triaxial potential, behavior which has not been seen for streams before (see also Fardal et al. 2015a). The distinction between potentials through the morphology of streams alone is exciting, as it in principle allows us to probe dark matter halos around the outskirts of our own and potentially other galaxies where detailed velocity information is difficult to obtain. We found that the Lyapunov time for orbits leading to "stream-fanning" were tens of Hubble times, hence the nature of "stream-fanning" could not simply be explained by strong chaos.

Since this work I have been involved in follow-up collaborative projects where we demonstrated that "stream-fanning" could be caused by mild chaotic orbits within triaxial potentials (Price-Whelan et al. 2016a). In particular we found that chaos in stellar streams manifested itself on much shorter timescales than predicted by classical chaos indicators such as Lyapunov times and diffusion timescales of the fundamental frequencies. Over only tens of orbits, excursions in the fundamental frequencies (which are constant for regular orbits) spread more than the initial spread in frequencies for the progenitor which lead to "stream-fanning". We therefore conclude that the long, thin streams that we do observe, must be on regular orbits in their host potential, providing a simple technique for probing orbit distributions in galaxies. Additionally, this work provides direct a method for probing observational signatures of chaos in galaxies through "fanned" streams (see also Price-Whelan et al. 2016b, Sesar et al. 2016). We are currently investigating what determines this spread in the fundamental frequencies, what sets the timescale for "stream-fanning" to occur and how important the effect of mild chaos should be for streams in a Milky Way type galaxy (see Yavetz et al., *in prep.*).

Placing our work in broader context, the findings that Pal 5 could be well reproduced within a logarithmic representation of the dark matter halo potential of the Milky Way, demonstrates that there is no need to introduce triaxiality in the inner parts of the halo

(within Pal 5's orbit: $r_{\rm apo} \sim 18$ kpc). This could indicate that our halo indeed is transitioning from a more spherical shape to a triaxial shape in its outskirts (see e.g. Vera-Ciro & Helmi 2013), which could be due to the condensations of baryons in the inner parts of the halo (e.g. Wetzel et al. 2016) or the effect of an accreting and evolving dark matter halo (e.g. Vera-Ciro et al. 2011). This could also imply that the ongoing interaction between the Magellanic Clouds and the MW (Gómez et al. 2015) has not yet affected the potential of the Milky Way within Pal 5's orbit. This seems plausible if the LMC and SMC are currently on their "first infall" to the Milky Way (as suggested by Besla et al. 2007). Additionally, our work makes it evident that unveiling the dark matter distribution within our Galaxy from streams, will require simulating the evolution of multiple streams, as different streams are successfully reproduced using different dark matter halo parameters (Pearson et al. 2015). Several groups have since advanced the field and combined the information of simulating multiple streams at once (e.g. Bonaca et al. 2016, Bovy et al. 2017, Bonaca & Hogg 2018).

6.2 Galactic Bar Parameters from Stellar Streams

In Chapter 3 we provide evidence that the Galactic bar can punch holes in stellar streams and that a recently discovered Pan-STARRS (PS1: Bernard et al. 2016) truncation of the leading stellar arm of Pal 5, can be explained by previous interactions with the Galactic bar. The interaction between the Galactic bar with the Pal 5 stream is similar to that of a "quasi resonant" interaction (see Chapter 1) as the bar will "sweep by" certain Pal 5 stream members during Pal 5's pericentric passages. In this analogy, the Pal 5 stream is the "victim" and the interaction occurs at each pericentric passage granted the stream has grown to be long enough such that the "edge of the bar" is close to part of the stream as the stream passes pericenter. Because Pal 5's orbital inclination changes slightly with each

pericentric pass, the magnitude of the effect will thus change in each encounter. The gaps induced by the bar can be understood simply due to the energy offset of stream members due to the torque from the bar. As described in Chapter 1 and 3 this leads to an offset in the stars' orbital periods leading to the growth of gaps. Similar as in the case of "quasi resonant stripping" we find that the effect of the bar is suppressed if a stream is orbiting retrograde with respect to the bar.

The gaps induced by the bar are very similar to density distortions induced by dark matter subhalos passing close by a stellar stream. The mass scale at which we should be able to detect subhalo interactions (see Erkal et al. 2016, Bovy et al. 2017) provide very intriguing tests of our current paradigm of ΛCDM as the "cold dark matter" paradigm predicts subhalos on smaller mass scales than e.g "fuzzy dark matter" models (Hui et al. 2016). Thus, we caution that streams which are prograde with respect to the bar spin, could have gaps from the bar (see also similar effects from molecular clouds in the disk: Amorisco et al. 2016). We suggest using streams on retrograde orbits (where the "quasi resonant" effect of the bar is minimal), when attempting to indirectly detect dark matter subhalos and in particular we propose GD1 as a good candidate, thin Milky Way stream as it is orbiting retrograde with respect to the bar. Interestingly, the Gaia DR2 data has recently revealed convincing kinematic and morphologically evidence of gaps in the GD1 stream, which could be consistent with the interaction of a subhalo with the stream (Price-Whelan & Bonaca 2018).

Additionally, we found that the growth and location of the gaps along the stream depend on the magnitude of the torque exerted by the bar, which is set by the bar's mass, its pattern speed and Pal 5's orbital properties, yielding a promising method for constraining bar properties using a stellar stream. We further predicted that the Pal 5 leading arm should reappear at similar surface densities further south.

Following publication, we discovered that there indeed appears to be "clumpy" debris in the PS1 data with a location consistent with Pal 5 debris from model predictions from a rapidly spinning bar ($\Omega = 60$ km s^{-1}kpc^{-1}). Interestingly, Price-Whelan et al. (2016b) demonstrated that a pattern speed of $\Omega = 60$ km s^{-1} kpc^{-1} could also reproduce the short nature of the Ophiuchus stellar stream, as the end of the stream "fans out" due to chaotic motion of the stream members in the presence of a time-dependent triaxial bar (see also Sesar et al. 2016). If we can confirm the "clumpy" debris' association with the leading arm of Palomar 5 (e.g. with Gaia data and radial velocity follow-up observations) this provides a new technique for constraining bar parameters (e.g. the bar's mass and pattern speed) using streams. We could also answer whether all reported gaps in Pal 5 are from previous interactions with the bar.

6.3 Baryon Cycling in Dwarf-Dwarf Interactions

In Chapter 4 we studied neutral hydrogen (HI) maps and surface density profiles for 10 dwarf galaxy pairs within 25 Mpc of the Milky Way to investigate the consequences of their mutual interactions. The pairs were selected based on a literature search of interacting dwarf galaxy pairs and mostly showed clear signs of "quasi resonant" stripping (e.g. due to the presence of tidal tails, bridges and extended gaseous features). In particular, we investigated the pairs' large scale environment, HI morphology (e.g. extended envelopes or bridges), and gas masses inside and outside the main galaxy bodies. We showed that tidal interactions between low mass galaxies can "park" (but not unbind) gas at large distances, and that the gas is most likely only prevented from being re-accreted if the pair is in the vicinity of a massive galaxy (as in the case for the Magellanic System). Additionally we found that pairs close to massive host galaxies are morphologically affected, but that the amount of gas in their outskirts can

not be understood through ram-pressure effects alone: tidal pre-processing appears to be key. The fact that dwarf interactions can move gas to large distances without unbinding it, has direct implications for the baryon cycles of these systems as it could enable a long lived gas supply. Given the relatively small sample size of 10 pairs, in future work we plan to expand the analysis of Pearson et al. (2016) to include more dwarf pairs at various separations and in different environments with newly obtained VLA data. In particular we plan to investigate how much gas mass resides outside the stellar disks of the dwarfs and if the gas distributions are morphologically affected by the environment.

As a follow-up to our observational study of interacting dwarf galaxies, in Chapter 5 we created a detailed model matched to one of the low mass, isolated pairs from Chapter 4 (NGC 4490 & NGC 4485). The NGC 4490 & NGC 4485 pair has a gaseous envelope extending more than 50 kpc in projection and resemble the Magellanic Clouds in that they have a similar stellar mass ratio ($\mu \sim 8:1$), they have a stellar and gaseous bridge connecting them, and they have a large amount of gas in their close vicinity. In the Chapter, we presented the first match to an isolated galaxy interaction on the low mass scale. We found this match by simultaneously reproducing the kinematic and morphological HI data using our simulation of the encounter, building upon many years of intuition on how gravity pulls out tidal features as galaxies interact (e.g. Toomre & Toomre 1972, D'Onghia et al. 2010). We found that the gas surrounding the two dwarfs is shed to large distances mainly from the small galaxy, due to its galactic disk spin being aligned with the orbital spin (i.e. it is close to prograde). With an interacting dwarf galaxy model matched to an observed system, we could investigate the timescales involved in cycling baryons from the large extended gas envelope back into the galactic remnant. We found that the gas will remain extended for several billion years before most of it will return to the merger remnant potentially fueling new star formation. The fact that the gas remains extended for several billion years validates the conclusions from our

observational studies, as the extended gas distribution will allow the large gaseous envelope to be stripped very efficiently if the remnant were to fall into a more massive galaxy later in its lifetime.

As mentioned in Chapter 5, this scenario is exactly what is thought to have been the case for the Magellanic Clouds: the two galaxies likely had a very extended gas envelope prior to falling into the Milky Way, explaining the enormous amount of gas deposited to the Milky Way's halo (Besla et al. 2012, Fox et al. 2014, Salem et al. 2015). Ram-pressure and tides from a nearby massive galaxy seem to be inefficient at stripping gas that is tightly bound to dwarfs (e.g. Emerick et al. 2016, Fillingham et al. 2016), and if their gas is already extended due to their prior interaction (as found in Chapter 4), this can help explain why gas is stripped so efficiently from galaxies residing close to the Milky Way (e.g. Grcevich & Putman 2009). The picture that tidal pre-processing is key to understanding the ultimate quenching of dwarfs is supported by cosmological simulations where e.g. Wetzel et al. (2015) finds that 30-60% of dwarf galaxies appear to fall into more massive systems as pairs and groups (see also Marasco et al. 2016).

Lastly, the fact that the gas remains extended for a long time can explain why we can observe isolated dwarf galaxies without companions far from anything else, with huge gas envelopes but not much star formation (e.g. Meurer et al. 1996, Werk et al. 2010, Kreckel et al. 2011). These systems may have had a merger in the past, with the extended envelope representing some of this reaccreted gas. With a dynamically matched simulation to a dwarf-dwarf interaction in hand, we can investigate hydrodynamical effects in future work. Hydrodynamical simulations of the encounter will enable a detailed investigation of the re-accretion of gas onto the merger remnant (e.g. the velocity and the rate of return) and therefore an assessment of the effect of dwarf-dwarf interactions on subsequent star formation. We also plan to expand the sample of dynamically matched simulations to dwarf-dwarf

interactions in order to get a statistical understanding of the dwarf merger sequence.

Bibliography

Aarseth, S. J. 1999, PASP, 111, 1333

Aarseth, S. J. 2003, Gravitational N-Body Simulations

Allen, A. J. & Richstone, D. O. 1988, ApJ, 325, 583

Amorisco, N. C. 2015, MNRAS, 450, 575

Amorisco, N. C., Gómez, F. A., Vegetti, S., & White, S. D. M. 2016, MNRAS, 463, L17

Annibali, F., Aloisi, A., Mack, J., Tosi, M., van der Marel, R. P., Angeretti, L., Leitherer, C., & Sirianni, M. 2008, AJ, 135, 1900

Arp, H. 1966, ApJS, 14, 1

Arraki, K. S., Klypin, A., More, S., & Trujillo-Gomez, S. 2014, MNRAS, 438, 1466

Astropy Collaboration, Robitaille, T. P., Tollerud, E. J., Greenfield, P., Droettboom, M., Bray, E., Aldcroft, T., Davis, M., Ginsburg, A., Price-Whelan, A. M., Kerzendorf, W. E., Conley, A., Crighton, N., Barbary, K., Muna, D., Ferguson, H., Grollier, F., Parikh, M. M., Nair, P. H., Unther, H. M., Deil, C., Woillez, J., Conseil, S., Kramer, R., Turner, J. E. H., Singer, L., Fox, R., Weaver, B. A., Zabalza, V., Edwards, Z. I., Azalee Bostroem, K., Burke, D. J., Casey, A. R., Crawford, S. M., Dencheva, N., Ely, J., Jenness, T.,

Labrie, K., Lim, P. L., Pierfederici, F., Pontzen, A., Ptak, A., Refsdal, B., Servillat, M., & Streicher, O. 2013, A&A, 558, A33

Athanassoula, E. 1996, in Astronomical Society of the Pacific Conference Series, Vol. 91, IAU Colloq. 157: Barred Galaxies, ed. R. Buta, D. A. Crocker, & B. G. Elmegreen, 309

Baillard, A., Bertin, E., de Lapparent, V., Fouqué, P., Arnouts, S., Mellier, Y., Pelló, R., Leborgne, J.-F., Prugniel, P., Makarov, D., Makarova, L., McCracken, H. J., Bijaoui, A., & Tasca, L. 2011, A&A, 532, A74

Balbinot, E. & Gieles, M. 2017, ArXiv e-prints

Balbinot, E., Santiago, B. X., da Costa, L. N., Makler, M., & Maia, M. A. G. 2011, MNRAS, 416, 393

Balkowski, C., Chamaraux, P., & Weliachew, L. 1978, A&A, 69, 263

Barnes, J. & Hut, P. 1986, Nature, 324, 446

Barnes, J. E. 1988, ApJ, 331, 699

Barnes, J. E. 2004, MNRAS, 350, 798

Barnes, J. E. 2011, ZENO: N-body and SPH Simulation Codes, Astrophysics Source Code Library

Barnes, J. E. 2012, MNRAS, 425, 1104

Barnes, J. E. 2016, MNRAS, 455, 1957

Barnes, J. E. & Hernquist, L. 1996, ApJ, 471, 115

Barnes, J. E. & Hernquist, L. 1998, ApJ, 495, 187

Barnes, J. E. & Hibbard, J. E. 2009, AJ, 137, 3071

Bekki, K. 2008, MNRAS, 388, L10

Bekki, K. 2009, MNRAS, 393, L60

Bekki, K. & Chiba, M. 2005, MNRAS, 356, 680

Bell, E. F., McIntosh, D. H., Katz, N., & Weinberg, M. D. 2003, ApJS, 149, 289

Belokurov, V., Evans, N. W., Irwin, M. J., Lynden-Bell, D., Yanny, B., Vidrih, S., Gilmore, G., Seabroke, G., Zucker, D. B., Wilkinson, M. I., Hewett, P. C., Bramich, D. M., Fellhauer, M., Newberg, H. J., Wyse, R. F. G., Beers, T. C., Bell, E. F., Barentine, J. C., Brinkmann, J., Cole, N., Pan, K., & York, D. G. 2007, ApJ, 658, 337

Belokurov, V. & Koposov, S. E. 2016, MNRAS, 456, 602

Belokurov, V., Koposov, S. E., Evans, N. W., Peñarrubia, J., Irwin, M. J., Smith, M. C., Lewis, G. F., Gieles, M., Wilkinson, M. I., Gilmore, G., Olszewski, E. W., & Niederste-Ostholt, M. 2014, MNRAS, 437, 116

Belokurov, V., Zucker, D. B., Evans, N. W., Gilmore, G., Vidrih, S., Bramich, D. M., Newberg, H. J., Wyse, R. F. G., Irwin, M. J., Fellhauer, M., Hewett, P. C., Walton, N. A., Wilkinson, M. I., Cole, N., Yanny, B., Rockosi, C. M., Beers, T. C., Bell, E. F., Brinkmann, J., Ivezić, Ž., & Lupton, R. 2006, ApJ, 642, L137

Berentzen, I., Athanassoula, E., Heller, C. H., & Fricke, K. J. 2003, MNRAS, 341, 343

Bernard, E. J., Ferguson, A. M. N., Schlafly, E. F., Abbas, M., Bell, E. F., Deacon, N. R., Martin, N. F., Rix, H.-W., Sesar, B., Slater, C. T., Peñarrubia, J., Wyse, R. F. G., Burgett, W. S., Chambers, K. C., Draper, P. W., Hodapp, K. W., Kaiser, N., Kudritzki,

R.-P., Magnier, E. A., Metcalfe, N., Morgan, J. S., Price, P. A., Tonry, J. L., Wainscoat, R. J., & Waters, C. 2014, MNRAS, 443, L84

Bernard, E. J., Ferguson, A. M. N., Schlafly, E. F., Martin, N. F., Rix, H.-W., Bell, E. F., Finkbeiner, D. P., Goldman, B., Martínez-Delgado, D., Sesar, B., Wyse, R. F. G., Burgett, W. S., Chambers, K. C., Draper, P. W., Hodapp, K. W., Kaiser, N., Kudritzki, R.-P., Magnier, E. A., Metcalfe, N., Wainscoat, R. J., & Waters, C. 2016, MNRAS, 463

Bertin, E. & Arnouts, S. 1996, A&AS, 117, 393

Bertola, F., Casini, C., Bettoni, D., Galletta, G., Noreau, L., & Kronberg, P. P. 1984, AJ, 89, 350

Besla, G., Kallivayalil, N., Hernquist, L., Robertson, B., Cox, T. J., van der Marel, R. P., & Alcock, C. 2007, ApJ, 668, 949

Besla, G., Kallivayalil, N., Hernquist, L., van der Marel, R. P., Cox, T. J., & Kereš, D. 2010, ApJ, 721, L97

Besla, G., Kallivayalil, N., Hernquist, L., van der Marel, R. P., Cox, T. J., & Kereš, D. 2012, MNRAS, 421, 2109

Besla, G., Martínez-Delgado, D., van der Marel, R. P., Beletsky, Y., Seibert, M., Schlafly, E. F., Grebel, E. K., & Neyer, F. 2016, ApJ, 825, 20

Binggeli, B. & Jerjen, H. 1998, A&A, 333, 17

Binney, J. & Tremaine, S. 1987, Galactic dynamics

Binney, J. & Tremaine, S. 2008, Galactic Dynamics: Second Edition (Princeton University Press)

Blanton, M. R., Dalcanton, J., Eisenstein, D., Loveday, J., Strauss, M. A., SubbaRao, M., Weinberg, D. H., Anderson, Jr., J. E., Annis, J., Bahcall, N. A., Bernardi, M., Brinkmann, J., Brunner, R. J., Burles, S., Carey, L., Castander, F. J., Connolly, A. J., Csabai, I., Doi, M., Finkbeiner, D., Friedman, S., Frieman, J. A., Fukugita, M., Gunn, J. E., Hennessy, G. S., Hindsley, R. B., Hogg, D. W., Ichikawa, T., Ivezić, Ž., Kent, S., Knapp, G. R., Lamb, D. Q., Leger, R. F., Long, D. C., Lupton, R. H., McKay, T. A., Meiksin, A., Merelli, A., Munn, J. A., Narayanan, V., Newcomb, M., Nichol, R. C., Okamura, S., Owen, R., Pier, J. R., Pope, A., Postman, M., Quinn, T., Rockosi, C. M., Schlegel, D. J., Schneider, D. P., Shimasaku, K., Siegmund, W. A., Smee, S., Snir, Y., Stoughton, C., Stubbs, C., Szalay, A. S., Szokoly, G. P., Thakar, A. R., Tremonti, C., Tucker, D. L., Uomoto, A., Vanden Berk, D., Vogeley, M. S., Waddell, P., Yanny, B., Yasuda, N., & York, D. G. 2001, AJ, 121, 2358

Bonaca, A., Geha, M., & Kallivayalil, N. 2012, ApJ, 760, L6

Bonaca, A., Geha, M., Küpper, A. H. W., Diemand, J., Johnston, K. V., & Hogg, D. W. 2014, ApJ, 795, 94

Bonaca, A. and Geha, M. C. and Hogg, D. W. and Kupper, A. H. W. and Johnston, K. V. and Diemand, J. 2016, American Astronomical Society Meeting Abstracts, 227

Bonaca, A. & Hogg, D. W. 2018, ArXiv e-prints

Bordoloi, R., Tumlinson, J., Werk, J. K., Oppenheimer, B. D., Peeples, M. S., Prochaska, J. X., Tripp, T. M., Katz, N., Davé, R., Fox, A. J., Thom, C., Ford, A. B., Weinberg, D. H., Burchett, J. N., & Kollmeier, J. A. 2014a, ApJ, 796, 136

Bovy, J. 2014, ApJ, 795, 95

Bovy, J. 2015, ApJS, 216, 29

Bovy, J., Allende Prieto, C., Beers, T. C., Bizyaev, D., da Costa, L. N., Cunha, K., Ebelke, G. L., Eisenstein, D. J., Frinchaboy, P. M., García Pérez, A. E., Girardi, L., Hearty, F. R., Hogg, D. W., Holtzman, J., Maia, M. A. G., Majewski, S. R., Malanushenko, E., Malanushenko, V., Mészáros, S., Nidever, D. L., O'Connell, R. W., O'Donnell, C., Oravetz, A., Pan, K., Rocha-Pinto, H. J., Schiavon, R. P., Schneider, D. P., Schultheis, M., Skrutskie, M., Smith, V. V., Weinberg, D. H., Wilson, J. C., & Zasowski, G. 2012, ApJ, 759, 131

Bovy, J., Bahmanyar, A., Fritz, T. K., & Kallivayalil, N. 2016, ArXiv e-prints

Bovy, J., Erkal, D., & Sanders, J. L. 2017, MNRAS, 466, 628

Bradford, J. D., Geha, M. C., & Blanton, M. R. 2015, ApJ, 809, 146

Buck, T., Ness, M. K., Macciò, A. V., Obreja, A., & Dutton, A. A. 2017, ArXiv e-prints

Bullock, J. S. 2002, in The Shapes of Galaxies and their Dark Halos, ed. P. Natarajan, 109–113

Bullock, J. S. & Johnston, K. V. 2005, ApJ, 635, 931

Bush, S. J. & Wilcots, E. M. 2004, AJ, 128, 2789

Bussmann, R. S., Dey, A., Armus, L., Brown, M. J. I., Desai, V., Gonzalez, A. H., Jannuzi, B. T., Melbourne, J., & Soifer, B. T. 2012, ApJ, 744, 150

Carlberg, R. G., Grillmair, C. J., & Hetherington, N. 2012, ApJ, 760, 75

Carlin, J. L., Sand, D. J., Price, P., Willman, B., Karunakaran, A., Spekkens, K., Bell, E. F., Brodie, J. P., Crnojević, D., Forbes, D. A., Hargis, J., Kirby, E., Lupton, R., Peter, A. H. G., Romanowsky, A. J., & Strader, J. 2016, ApJ, 828, L5

Casey, A. R., Da Costa, G., Keller, S. C., & Maunder, E. 2013, ApJ, 764, 39

Casteels, K. R. V., Conselice, C. J., Bamford, S. P., Salvador-Solé, E., Norberg, P. R., Agius, N. K., Baldry, I., Brough, S., Brown, M. J. I., Drinkwater, M. J., Driver, S. P., Graham, A. W., Bland-Hawthorn, J., Hopkins, A. M., Kelvin, L. S., López-Sánchez, A. R., Loveday, J., Robotham, A. S. G., & Vázquez-Mata, J. A. 2014, MNRAS, 445, 1157

Chambers, K. C., Magnier, E. A., Metcalfe, N., Flewelling, H. A., Huber, M. E., Waters, C. Z., Denneau, L., Draper, P. W., Farrow, D., Finkbeiner, D. P., Holmberg, C., Koppenhoefer, J., Price, P. A., Saglia, R. P., Schlafly, E. F., Smartt, S. J., Sweeney, W., Wainscoat, R. J., Burgett, W. S., Grav, T., Heasley, J. N., Hodapp, K. W., Jedicke, R., Kaiser, N., Kudritzki, R.-P., Luppino, G. A., Lupton, R. H., Monet, D. G., Morgan, J. S., Onaka, P. M., Stubbs, C. W., Tonry, J. L., Banados, E., Bell, E. F., Bender, R., Bernard, E. J., Botticella, M. T., Casertano, S., Chastel, S., Chen, W.-P., Chen, X., Cole, S., Deacon, N., Frenk, C., Fitzsimmons, A., Gezari, S., Goessl, C., Goggia, T., Goldman, B., Grebel, E. K., Hambly, N. C., Hasinger, G., Heavens, A. F., Heckman, T. M., Henderson, R., Henning, T., Holman, M., Hopp, U., Ip, W.-H., Isani, S., Keyes, C. D., Koekemoer, A., Kotak, R., Long, K. S., Lucey, J. R., Liu, M., Martin, N. F., McLean, B., Morganson, E., Murphy, D. N. A., Nieto-Santisteban, M. A., Norberg, P., Peacock, J. A., Pier, E. A., Postman, M., Primak, N., Rae, C., Rest, A., Riess, A., Riffeser, A., Rix, H. W., Roser, S., Schilbach, E., Schultz, A. S. B., Scolnic, D., Szalay, A., Seitz, S., Shiao, B., Small, E., Smith, K. W., Soderblom, D., Taylor, A. N., Thakar, A. R., Thiel, J., Thilker, D., Urata, Y., Valenti, J., Walter, F., Watters, S. P., Werner, S., White, R., Wood-Vasey, W. M., & Wyse, R. 2016, ArXiv e-prints

Choi, J.-H., Weinberg, M. D., & Katz, N. 2007, MNRAS, 381, 987

Chung, A., van Gorkom, J. H., Kenney, J. D. P., & Vollmer, B. 2007, ApJ, 659, L115

Cioni, M.-R. L., van der Marel, R. P., Loup, C., & Habing, H. J. 2000, A&A, 359, 601

Clemens, M. S. & Alexander, P. 2002, MNRAS, 333, 39

Clemens, M. S., Alexander, P., & Green, D. A. 1998, MNRAS, 297, 1015

Clemens, M. S., Alexander, P., & Green, D. A. 2000, MNRAS, 312, 236

Combes, F. 1978, A&A, 65, 47

Combes, F., Debbasch, F., Friedli, D., & Pfenniger, D. 1990, A&A, 233, 82

Combes, F., Foy, F. C., Weliachew, L., & Gottesman, S. T. 1980, A&A, 84, 85

Combes, F. & Sanders, R. H. 1981, A&A, 96, 164

Condon, J. J., Helou, G., & Jarrett, T. H. 2002, AJ, 123, 1881

Connors, T. W., Kawata, D., & Gibson, B. K. 2006a, MNRAS, 371, 108

Cox, A. L., Sparke, L. S., Watson, A. M., & van Moorsel, G. 2001, AJ, 121, 692

Danforth, C. W. & Shull, J. M. 2008, ApJ, 679, 194

Davies, L. J. M., Robotham, A. S. G., Driver, S. P., Alpaslan, M., Baldry, I. K., Bland-Hawthorn, J., Brough, S., Brown, M. J. I., Cluver, M. E., Holwerda, B. W., Hopkins, A. M., Lara-López, M. A., Mahajan, S., Moffett, A. J., Owers, M. S., & Phillipps, S. 2016, MNRAS, 455, 4013

de Mello, D. F., Smith, L. J., Sabbi, E., Gallagher, J. S., Mountain, M., & Harbeck, D. R. 2008, AJ, 135, 548

De Propris, R., Conselice, C. J., Liske, J., Driver, S. P., Patton, D. R., Graham, A. W., & Allen, P. D. 2007, ApJ, 666, 212

de Vaucouleurs, G. & Freeman, K. C. 1972, Vistas in Astronomy, 14, 163

Deason, A., Wetzel, A., & Garrison-Kimmel, S. 2014, ApJ, 794, 115

Deason, A. J., Belokurov, V., Evans, N. W., & An, J. 2012, MNRAS, 424, L44

Debattista, V. P., Ness, M., Gonzalez, O. A., Freeman, K., Zoccali, M., & Minniti, D. 2017, MNRAS, 469, 1587

Debattista, V. P., Roškar, R., Valluri, M., Quinn, T., Moore, B., & Wadsley, J. 2013, MNRAS, 434, 2971

Debattista, V. P. & Sellwood, J. A. 1998, ApJ, 493, L5

Debattista, V. P. & Sellwood, J. A. 2000, ApJ, 543, 704

Dehnen, W. & Binney, J. 1998, MNRAS, 294, 429

Dehnen, W. 2000, AJ, 119, 800

Dehnen, W., Odenkirchen, M., Grebel, E. K., & Rix, H.-W. 2004, AJ, 127, 2753

Demers, S. & Battinelli, P. 1998, AJ, 115, 154

Diaz, J. & Bekki, K. 2011, MNRAS, 413, 2015

Diemand, J., Kuhlen, M., Madau, P., Zemp, M., Moore, B., Potter, D., & Stadel, J. 2008, Nature, 454, 735

D'Onghia, E., Besla, G., Cox, T. J., & Hernquist, L. 2009, Nature, 460, 605

D'Onghia, E., Vogelsberger, M., Faucher-Giguere, C.-A., & Hernquist, L. 2010, ApJ, 725, 353

Dotter, A., Sarajedini, A., & Anderson, J. 2011, ApJ, 738, 74

Dubinski, J., Mihos, J. C., & Hernquist, L. 1999, ApJ, 526, 607

Dwek, E., Arendt, R. G., Hauser, M. G., Kelsall, T., Lisse, C. M., Moseley, S. H., Silverberg, R. F., Sodroski, T. J., & Weiland, J. L. 1995, ApJ, 445, 716

Ebrová, I. & Łokas, E. L. 2015, ApJ, 813, 10

Ellison, S. L., Patton, D. R., Mendel, J. T., & Scudder, J. M. 2011, MNRAS, 418, 2043

Ellison, S. L., Patton, D. R., Simard, L., McConnachie, A. W., Baldry, I. K., & Mendel, J. T. 2010, MNRAS, 407, 1514

Elmegreen, D. M., Chromey, F. R., Knowles, B. D., & Wittenmyer, R. A. 1998a, AJ, 115, 1433

Emerick, A., Mac Low, M.-M., Grcevich, J., & Gatto, A. 2016, ApJ, 826, 148

Engel, H., Tacconi, L. J., Davies, R. I., Neri, R., Smail, I., Chapman, S. C., Genzel, R., Cox, P., Greve, T. R., Ivison, R. J., Blain, A., Bertoldi, F., & Omont, A. 2010, ApJ, 724, 233

Englmaier, P. & Gerhard, O. 1999, MNRAS, 304, 512

Epinat, B., Amram, P., Marcelin, M., Balkowski, C., Daigle, O., Hernandez, O., Chemin, L., Carignan, C., Gach, J.-L., & Balard, P. 2008, MNRAS, 388, 500

Erkal, D., Belokurov, V., Bovy, J., & Sanders, J. L. 2016, MNRAS, 463, 102

Erkal, D., Koposov, S. E., & Belokurov, V. 2017, MNRAS, 470, 60

Errani, R., Peñarrubia, J., Laporte, C. F. P., & Gómez, F. A. 2017, MNRAS, 465, L59

Fakhouri, O., Ma, C.-P., & Boylan-Kolchin, M. 2010, MNRAS, 406, 2267

Fardal, M. A., Huang, S., & Weinberg, M. D. 2015a, MNRAS, 452, 301

Fellhauer, M., Belokurov, V., Evans, N. W., Wilkinson, M. I., Zucker, D. B., Gilmore, G., Irwin, M. J., Bramich, D. M., Vidrih, S., Wyse, R. F. G., Beers, T. C., & Brinkmann, J. 2006, ApJ, 651, 167

Fillingham, S. P., Cooper, M. C., Pace, A. B., Boylan-Kolchin, M., Bullock, J. S., Garrison-Kimmel, S., & Wheeler, C. 2016, MNRAS, 463, 1916

Fox, A. J., Wakker, B. P., Barger, K. A., Hernandez, A. K., Richter, P., Lehner, N., Bland-Hawthorn, J., Charlton, J. C., Westmeier, T., Thom, C., Tumlinson, J., Misawa, T., Howk, J. C., Haffner, L. M., Ely, J., Rodriguez-Hidalgo, P., & Kumari, N. 2014, ApJ, 787, 147

Freeman, K. C. 1970, ApJ, 160, 811

Fritz, T. K. & Kallivayalil, N. 2015, ApJ, 811, 123

Froeschlé, C., Gonczi, R., & Lega, E. 1997, Planet. Space Sci., 45, 881

Fumagalli, M., Hennawi, J. F., Prochaska, J. X., Kasen, D., Dekel, A., Ceverino, D., & Primack, J. 2014, ApJ, 780, 74

Gaia Collaboration, Prusti, T., de Bruijne, J. H. J., Brown, A. G. A., Vallenari, A., Babusiaux, C., Bailer-Jones, C. A. L., Bastian, U., Biermann, M., Evans, D. W., & et al. 2016, A&A, 595, A1

Gao, L., White, S. D. M., Jenkins, A., Stoehr, F., & Springel, V. 2004, MNRAS, 355, 819

Gao, Y., Zhu, M., & Seaquist, E. R. 2003, AJ, 126, 2171

Gardiner, L. T. & Noguchi, M. 1996, MNRAS, 278, 191

Garrison-Kimmel, S., Boylan-Kolchin, M., Bullock, J. S., & Lee, K. 2014, MNRAS, 438, 2578

Garrison-Kimmel, S., Wetzel, A. R., Bullock, J. S., Hopkins, P. F., Boylan-Kolchin, M., Faucher-Giguere, C.-A., Keres, D., Quataert, E., Sanderson, R. E., Graus, A. S., & Kelley, T. 2017, ArXiv e-prints

Geha, M., Blanton, M. R., Masjedi, M., & West, A. A. 2006, ApJ, 653, 240

Geha, M., Blanton, M. R., Yan, R., & Tinker, J. L. 2012, ApJ, 757, 85

Gerhard, O. 2011, Memorie della Societa Astronomica Italiana Supplementi, 18, 185

Gibbons, S. L. J., Belokurov, V., Erkal, D., & Evans, N. W. 2016, MNRAS, 458, L64

Gibbons, S. L. J., Belokurov, V., & Evans, N. W. 2014, MNRAS, 445, 3788

Gil de Paz, A., Madore, B. F., & Pevunova, O. 2003, ApJS, 147, 29

Gillessen, S., Eisenhauer, F., Trippe, S., Alexander, T., Genzel, R., Martins, F., & Ott, T. 2009, ApJ, 692, 1075

Gómez, F. A., Besla, G., Carpintero, D. D., Villalobos, Á., O'Shea, B. W., & Bell, E. F. 2015, ApJ, 802, 128

González, R. E. & Padilla, N. D. 2016, ApJ, 829, 58

Grcevich, J. & Putman, M. E. 2009, ApJ, 696, 385

Grillmair, C. J. 2009, ApJ, 693, 1118

Grillmair, C. J. & Carlin, J. L. 2016, in Astrophysics and Space Science Library, Vol. 420, Tidal Streams in the Local Group and Beyond, ed. H. J. Newberg & J. L. Carlin, 87

Grillmair, C. J. & Dionatos, O. 2006, ApJ, 643, L17

Grillmair, C. J. & Johnson, R. 2006, ApJ, 639, L17

Guglielmo, M., Lewis, G. F., & Bland-Hawthorn, J. 2014, MNRAS, 444, 1759

Gunn, J. E. & Gott, III, J. R. 1972, ApJ, 176, 1

Hairer, E., Nørsett, S. P., & Wanner, G. 1993, Springer Series in Computational Mathematics, Vol. 8, Solving Ordinary Differential Equations. I. Nonstiff Problems, 2nd edn. (Berlin: Springer-Verlag), xvi+528, a reprinting with corrections appeared in 2000.

Harris, J. 2007, ApJ, 658, 345

Hattori, K., Erkal, D., & Sanders, J. L. 2016, MNRAS, 460, 497

Heald, G., Józsa, G., Serra, P., Zschaechner, L., Rand, R., Fraternali, F., Oosterloo, T., Walterbos, R., Jütte, E., & Gentile, G. 2011, A&A, 526, A118

Heggie, D. & Hut, P. 2003, The Gravitational Million-Body Problem: A Multidisciplinary Approach to Star Cluster Dynamics

Helmi, A. & White, S. D. M. 1999, MNRAS, 307, 495

Hendel, D. & Johnston, K. V. 2015, MNRAS, 454, 2472

Hernquist, L. 1989, Nature, 340, 687

Hernquist, L. 1990, ApJ, 356, 359

Hernquist, L. & Ostriker, J. P. 1992, ApJ, 386, 375

Hibbard, J. E. & Mihos, J. C. 1995, AJ, 110, 140

Hibbard, J. E. & Yun, M. S. 1999, AJ, 118, 162

Hoffman, G. L., Lu, N. Y., Salpeter, E. E., & Connell, B. M. 1999, AJ, 117, 811

Hoffman, G. L., Salpeter, E. E., Lamphier, C., & Roos, T. 1992, ApJ, 388, L5

Hogg, D. W. 2012, ArXiv e-prints

Hogg, D. W., Bovy, J., & Lang, D. 2010, ArXiv e-prints

Hopkins, P. F., Kereš, D., Oñorbe, J., Faucher-Giguère, C.-A., Quataert, E., Murray, N., & Bullock, J. S. 2014, MNRAS, 445, 581

Hubble, E. P. 1929, ApJ, 69

Huchtmeier, W. K., Seiradakis, J. H., & Materne, J. 1980, A&A, 91, 341

Hui, L., Ostriker, J. P., Tremaine, S., & Witten, E. 2016, ArXiv e-prints

Hummels, C. B., Bryan, G. L., Smith, B. D., & Turk, M. J. 2013, MNRAS, 430, 1548

Hunt, J. A. S., Bovy, J., Pérez-Villegas, A., Holtzman, J. A., Sobeck, J., Chojnowski, D., Santana, F. A., Palicio, P. A., Wegg, C., Gerhard, O., Almeida, A., Bizyaev, D., Fernandez-Trincado, J. G., Lane, R. R., Longa-Peña, P., Majewski, S. R., Pan, K., & Roman-Lopes, A. 2018a, MNRAS, 474, 95

Hunt, J. A. S., Bovy, J. et al. 2018b, MNRAS, 477, 3945

Hunter, D. A., Wilcots, E. M., van Woerden, H., Gallagher, J. S., & Kohle, S. 1998, ApJ, 495, L47

Hunter, J. D. 2007, Computing in Science and Engineering, 9, 90

Ibata, R., Lewis, G. F., Irwin, M., Totten, E., & Quinn, T. 2001, ApJ, 551, 294

Ibata, R., Lewis, G. F., Martin, N. F., Bellazzini, M., & Correnti, M. 2013, ApJ, 765, L15

Ibata, R. A., Gilmore, G., & Irwin, M. J. 1994, Nature, 370, 194

Ibata, R. A., Lewis, G. F., & Martin, N. F. 2016, ApJ, 819, 1

Irrgang, A., Przybilla, N., Heber, U., Böck, M., Hanke, M., Nieva, M.-F., & Butler, K. 2014, A&A, 565, A63

Irwin, M. J., Kunkel, W. E., & Demers, S. 1985, Nature, 318, 160

Jing, Y. P. & Suto, Y. 2002, ApJ, 574, 538

Johnston, K. V. 1998, ApJ, 495, 297

Johnston, K. V., Bullock, J. S., Sharma, S., Font, A., Robertson, B. E., & Leitner, S. N. 2008, ApJ, 689, 936

Johnston, K. V., Law, D. R., & Majewski, S. R. 2005, ApJ, 619, 800

Johnston, K. V., Sackett, P. D., & Bullock, J. S. 2001, ApJ, 557, 137

Johnston, K. V., Spergel, D. N., & Hernquist, L. 1995, ApJ, 451, 598

Joung, M. R., Bryan, G. L., & Putman, M. E. 2012, ApJ, 745, 148

Kaczmarek, J. F. & Wilcots, E. M. 2012, AJ, 144, 67

Kallivayalil, N., van der Marel, R. P., & Alcock, C. 2006, ApJ, 652, 1213

Kallivayalil, N., van der Marel, R. P., Anderson, J., Besla, G., & Alcock, C. 2009, in IAU Symposium, Vol. 256, IAU Symposium, ed. J. T. Van Loon & J. M. Oliveira, 93–98

Kallivayalil, N., van der Marel, R. P., Besla, G., Anderson, J., & Alcock, C. 2013, ApJ, 764, 161

Karachentsev, I. D., Karachentseva, V. E., & Huchtmeier, W. K. 2007, Astronomy Letters, 33, 512

Karachentsev, I. D., Karachentseva, V. E., Huchtmeier, W. K., & Makarov, D. I. 2004, AJ, 127, 2031

Karachentsev, I. D. & Makarov, D. I. 1998, A&A, 331, 891

Karachentsev, I. D., Makarov, D. I., & Kaisina, E. I. 2013, AJ, 145, 101

Kazantzidis, S., Λokas, E. L., Mayer, L., Knebe, A., & Klimentowski, J. 2011, ApJ, 740, L24

Kennicutt, Jr., R. C., Lee, J. C., Funes, José G., S. J., Sakai, S., & Akiyama, S. 2008, ApJS, 178, 247

Kilborn, V. A., Koribalski, B. S., Forbes, D. A., Barnes, D. G., & Musgrave, R. C. 2005, MNRAS, 356, 77

Kim, J., Sung, E.-C., Chung, A., & Staveley-Smith, L. 2015, Publication of Korean Astronomical Society, 30, 513

Kim, J.-h., Wise, J. H., & Abel, T. 2009, ApJ, 694, L123

King, I. 1962, AJ, 67, 471

Klypin, A., Kravtsov, A. V., Valenzuela, O., & Prada, F. 1999, ApJ, 522, 82

Knapen, J. H. & Cisternas, M. 2015, ApJ, 807, L16

Knapen, J. H., Cisternas, M., & Querejeta, M. 2015, MNRAS, 454, 1742

Koopmann, R. A., Giovanelli, R., Haynes, M. P., Kent, B. R., Balonek, T. J., Brosch, N., Higdon, J. L., Salzer, J. J., & Spector, O. 2008, ApJ, 682, L85

Koopmann, R. A. & Kenney, J. D. P. 2004, ApJ, 613, 851

Koposov, S. E., Glushkova, E. V., & Zolotukhin, I. Y. 2008, A&A, 486, 771

Koposov, S. E., Rix, H.-W., & Hogg, D. W. 2010, ApJ, 712, 260

Kreckel, K., Peebles, P. J. E., van Gorkom, J. H., van de Weygaert, R., & van der Hulst, J. M. 2011, AJ, 141, 204

Kuijken, K. 1996, in Astronomical Society of the Pacific Conference Series, Vol. 91, IAU Colloq. 157: Barred Galaxies, ed. R. Buta, D. A. Crocker, & B. G. Elmegreen, 504

Küpper, A. H. W., Balbinot, E., Bonaca, A., Johnston, K. V., Hogg, D. W., Kroupa, P., & Santiago, B. X. 2015, ApJ, 803, 80

Küpper, A. H. W., Kroupa, P., Baumgardt, H., & Heggie, D. C. 2010, MNRAS, 401, 105

Küpper, A. H. W., Lane, R. R., & Heggie, D. C. 2012, MNRAS, 420, 2700

Küpper, A. H. W., Maschberger, T., Kroupa, P., & Baumgardt, H. 2011, MNRAS, 417, 2300

Kuzma, P. B., Da Costa, G. S., Keller, S. C., & Maunder, E. 2015, MNRAS, 446, 3297

Lane, R. R., Küpper, A. H. W., & Heggie, D. C. 2012, MNRAS, 423, 2845

Lang, M., Holley-Bockelmann, K., & Sinha, M. 2014, ApJ, 790, L33

Lanz, L., Zezas, A., Brassington, N., Smith, H. A., Ashby, M. L. N., da Cunha, E., Fazio, G. G., Hayward, C. C., Hernquist, L., & Jonsson, P. 2013, ApJ, 768, 90

Laporte, C. F. P., Johnston, K. V., & Tzanidakis, A. 2018, ArXiv e-prints

Law, D. R. & Majewski, S. R. 2010, ApJ, 714, 229

Lee, J. C., Kennicutt, Jr., R. C., Funes, S. J. J. G., Sakai, S., & Akiyama, S. 2009, ApJ, 692, 1305

Lelli, F., Verheijen, M., & Fraternali, F. 2014, A&A, 566, A71

Lelli, F., Verheijen, M., Fraternali, F., & Sancisi, R. 2012, A&A, 537, A72

Liang, C. J. & Chen, H.-W. 2014, MNRAS, 445, 2061

Lux, H., Read, J. I., Lake, G., & Johnston, K. V. 2012, MNRAS, 424, L16

Madau, P. & Dickinson, M. 2014, ARA&A, 52, 415

Majewski, S. R., Skrutskie, M. F., Weinberg, M. D., & Ostheimer, J. C. 2003, ApJ, 599, 1082

Malhan, K., Ibata, R. A., & Martin, N. F. 2018, ArXiv e-prints

Marasco, A., Crain, R. A., Schaye, J., Bahé, Y. M., van der Hulst, T., Theuns, T., & Bower, R. G. 2016, ArXiv e-prints

Martin, C. L. 2005, ApJ, 621, 227

Martínez-Delgado, D., D'Onghia, E., Chonis, T. S., Beaton, R. L., Teuwen, K., GaBany, R. J., Grebel, E. K., & Morales, G. 2015a, AJ, 150, 116

Martínez-Delgado, D., Pohlen, M., Gabany, R. J., Majewski, S. R., Peñarrubia, J., & Palma, C. 2009, ApJ, 692, 955

Martínez-Delgado, D., Romanowsky, A. J., Gabany, R. J., Annibali, F., Arnold, J. A., Fliri, J., Zibetti, S., van der Marel, R. P., Rix, H.-W., Chonis, T. S., Carballo-Bello, J. A.,

Aloisi, A., Macciò, A. V., Gallego-Laborda, J., Brodie, J. P., & Merrifield, M. R. 2012a, ApJ, 748, L24

Mastrobuono-Battisti, A., Di Matteo, P., Montuori, M., & Haywood, M. 2012, A&A, 546, L7

Mastropietro, C., Moore, B., Mayer, L., Wadsley, J., & Stadel, J. 2005, MNRAS, 363, 509

Mateo, M., Mirabal, N., Udalski, A., Szymanski, M., Kaluzny, J., Kubiak, M., Krzeminski, W., & Stanek, K. Z. 1996, ApJ, 458, L13

Mathewson, D. S., Cleary, M. N., & Murray, J. D. 1974, ApJ, 190, 291

McConnachie, A. W., Irwin, M. J., Ibata, R. A., Dubinski, J., Widrow, L. M., Martin, N. F., Côté, P., Dotter, A. L., Navarro, J. F., Ferguson, A. M. N., Puzia, T. H., Lewis, G. F., Babul, A., Barmby, P., Bienaymé, O., Chapman, S. C., Cockcroft, R., Collins, M. L. M., Fardal, M. A., Harris, W. E., Huxor, A., Mackey, A. D., Peñarrubia, J., Rich, R. M., Richer, H. B., Siebert, A., Tanvir, N., Valls-Gabaud, D., & Venn, K. A. 2009, Nature, 461, 66

Meurer, G. R., Carignan, C., Beaulieu, S. F., & Freeman, K. C. 1996, AJ, 111, 1551

Mihos, J. C., McGaugh, S. S., & de Blok, W. J. G. 1997, ApJ, 477, L79

Miller, M. J. & Bregman, J. N. 2013, ApJ, 770, 118

Miyamoto, M. & Nagai, R. 1975, PASJ, 27, 533

Moore, B., Ghigna, S., Governato, F., Lake, G., Quinn, T., Stadel, J., & Tozzi, P. 1999, ApJ, 524, L19

Moster, B. P., Naab, T., & White, S. D. M. 2013, MNRAS, 428, 3121

Mould, J. R., Huchra, J. P., Freedman, W. L., Kennicutt, Jr., R. C., Ferrarese, L., Ford, H. C., Gibson, B. K., Graham, J. A., Hughes, S. M. G., Illingworth, G. D., Kelson, D. D., Macri, L. M., Madore, B. F., Sakai, S., Sebo, K. M., Silbermann, N. A., & Stetson, P. B. 2000, ApJ, 529, 786

Nasonova, O. G., de Freitas Pacheco, J. A., & Karachentsev, I. D. 2011, A&A, 532, A104

Navarro, J. F., Frenk, C. S., & White, S. D. M. 1996, ApJ, 462, 563

Ness, M., Freeman, K., Athanassoula, E., Wylie-De-Boer, E., Bland-Hawthorn, J., Lewis, G. F., Yong, D., Asplund, M., Lane, R. R., Kiss, L. L., & Ibata, R. 2012, ApJ, 756, 22

Ness, M. & Lang, D. 2016, AJ, 152, 14

Neto, A. F., Gao, L., Bett, P., Cole, S., Navarro, J. F., Frenk, C. S., White, S. D. M., Springel, V., & Jenkins, A. 2007, MNRAS, 381, 1450

Newberg, H. J., Willett, B. A., Yanny, B., & Xu, Y. 2010, ApJ, 711, 32

Ngan, W. H. W. & Carlberg, R. G. 2014, ApJ, 788, 181

Nidever, D. L., Majewski, S. R., Butler Burton, W., & Nigra, L. 2010, ApJ, 723, 1618

Niederhofer, F., Cioni, M.-R. L., Rubele, S., Schmidt, T., Bekki, K., de Grijs, R., Emerson, J., Ivanov, V. D., Marconi, M., Oliveira, J. M., Petr-Gotzens, M. G., Ripepi, V., van Loon, J. T., & Zaggia, S. 2018, ArXiv e-prints

Nitadori, K. & Aarseth, S. J. 2012, MNRAS, 424, 545

Noreau, L. & Kronberg, P. P. 1986, AJ, 92, 1048

Odenkirchen, M., Grebel, E. K., Dehnen, W., Rix, H.-W., & Cudworth, K. M. 2002, AJ, 124, 1497

Odenkirchen, M., Grebel, E. K., Dehnen, W., Rix, H.-W., Yanny, B., Newberg, H. J., Rockosi, C. M., Martínez-Delgado, D., Brinkmann, J., & Pier, J. R. 2003, AJ, 126, 2385

Odenkirchen, M., Grebel, E. K., Kayser, A., Rix, H.-W., & Dehnen, W. 2009, AJ, 137, 3378

Odenkirchen, M., Grebel, E. K., Rockosi, C. M., Dehnen, W., Ibata, R., Rix, H.-W., Stolte, A., Wolf, C., Anderson, Jr., J. E., Bahcall, N. A., Brinkmann, J., Csabai, I., Hennessy, G., Hindsley, R. B., Ivezić, Ž., Lupton, R. H., Munn, J. A., Pier, J. R., Stoughton, C., & York, D. G. 2001, ApJ, 548, L165

Odewahn, S. C. 1994, AJ, 107, 1320

O'Neill, J. K. & Dubinski, J. 2003, MNRAS, 346, 251

Pardy, S. A., D'Onghia, E., Athanassoula, E., Wilcots, E. M., & Sheth, K. 2016, ApJ, 827, 149

Pardy, S. A., D'Onghia, E., & Fox, A. J. 2018, ArXiv e-prints

Patton, D. R., Torrey, P., Ellison, S. L., Mendel, J. T., & Scudder, J. M. 2013, MNRAS, 433, L59

Paudel, S. & Sengupta, C. 2017, ArXiv e-prints

Pearson, S., Besla, G., Putman, M. E., Lutz, K. A., Fernández, X., Stierwalt, S., Patton, D. R., Kim, J., Kallivayalil, N., Johnson, K., & Sung, E.-C. 2016, MNRAS, 459, 1827

Pearson, S., Küpper, A. H. W., Johnston, K. V., & Price-Whelan, A. M. 2015, ApJ, 799, 28

Pearson, S., Price-Whelan, A. M., & Johnston, K. V. 2017, Nature Astronomy, 1, 633

Pietrzyński, G., Graczyk, D., Gieren, W., Thompson, I. B., Pilecki, B., Udalski, A., Soszyński, I., Kozłowski, S., Konorski, P., Suchomska, K., Bono, G., Moroni, P. G. P., Villanova, S., Nardetto, N., Bresolin, F., Kudritzki, R. P., Storm, J., Gallenne, A., Smolec, R., Minniti, D., Kubiak, M., Szymański, M. K., Poleski, R., Wyrzykowski, Λ., Ulaczyk, K., Pietrukowicz, P., Górski, M., & Karczmarek, P. 2013, Nature, 495, 76

Plummer, H. C. 1911, MNRAS, 71, 460

Pontzen, A. & Governato, F. 2012, MNRAS, 421, 3464

Portail, M., Gerhard, O., Wegg, C., & Ness, M. 2016, ArXiv e-prints

Portail, M., Gerhard, O., Wegg, C., & Ness, M. 2017, MNRAS, 465, 1621

Portail, M., Wegg, C., Gerhard, O., & Martinez-Valpuesta, I. 2015, MNRAS, 448, 713

Price-Whelan, A., Sipocz, B., & Oh, S. 2017, adrn/gala: v0.1.3

Price-Whelan, A. M. & Bonaca, A. 2018, ArXiv e-prints

Price-Whelan, A. M., Hogg, D. W., Johnston, K. V., & Hendel, D. 2014, ApJ, 794, 4

Price-Whelan, A. M., Johnston, K. V., Valluri, M., Pearson, S., Küpper, A. H. W., & Hogg, D. W. 2016a, MNRAS, 455, 1079

Price-Whelan, A. M., Sesar, B., Johnston, K. V., & Rix, H.-W. 2016b, ApJ, 824, 104

Prince, P. & Dormand, J. 1981, Journal of Computational and Applied Mathematics, 7, 67

Privon, G. C., Barnes, J. E., Evans, A. S., Hibbard, J. E., Yun, M. S., Mazzarella, J. M., Armus, L., & Surace, J. 2013, ApJ, 771, 120

Privon, G. C., Stierwalt, S., Patton, D. R., Besla, G., Pearson, S., Putman, M., Johnson, K. E., Kallivayalil, N., Liss, S., & Titans, T. 2017, ApJ, 846, 74

Putman, M. E., Gibson, B. K., Staveley-Smith, L., Banks, G., Barnes, D. G., Bhatal, R., Disney, M. J., Ekers, R. D., Freeman, K. C., Haynes, R. F., Henning, P., Jerjen, H., Kilborn, V., Koribalski, B., Knezek, P., Malin, D. F., Mould, J. R., Oosterloo, T., Price, R. M., Ryder, S. D., Sadler, E. M., Stewart, I., Stootman, F., Vaile, R. A., Webster, R. L., & Wright, A. E. 1998, Nature, 394, 752

Putman, M. E., Peek, J. E. G., & Joung, M. R. 2012, ARA&A, 50, 491

Putman, M. E., Staveley-Smith, L., Freeman, K. C., Gibson, B. K., & Barnes, D. G. 2003, ApJ, 586, 170

Ramirez-Ballinas, I. & Hidalgo-Gámez, A. M. 2014, MNRAS, 442, 2282

Read, J. I., Wilkinson, M. I., Evans, N. W., Gilmore, G., & Kleyna, J. T. 2006, MNRAS, 366, 429

Reid, M. J., Menten, K. M., Brunthaler, A., Zheng, X. W., Dame, T. M., Xu, Y., Wu, Y., Zhang, B., Sanna, A., Sato, M., Hachisuka, K., Choi, Y. K., Immer, K., Moscadelli, L., Rygl, K. L. J., & Bartkiewicz, A. 2014, ApJ, 783, 130

Rich, R. M., Collins, M. L. M., Black, C. M., Longstaff, F. A., Koch, A., Benson, A., & Reitzel, D. B. 2012, Nature, 482, 192

Robertson, B. E. & Kravtsov, A. V. 2008, ApJ, 680, 1083

Rockosi, C. M., Odenkirchen, M., Grebel, E. K., Dehnen, W., Cudworth, K. M., Gunn, J. E., York, D. G., Brinkmann, J., Hennessy, G. S., & Ivezić, Ž. 2002, AJ, 124, 349

Rubin, V. C., Waterman, A. H., & Kenney, J. D. P. 1999, AJ, 118, 236

Salem, M., Besla, G., Bryan, G., Putman, M., van der Marel, R. P., & Tonnesen, S. 2015, ApJ, 815, 77

Sanders, D. B., Soifer, B. T., Elias, J. H., Madore, B. F., Matthews, K., Neugebauer, G., & Scoville, N. Z. 1988, ApJ, 325, 74

Sanders, J. L. & Binney, J. 2013, MNRAS, 433, 1826

Sanders, J. L. & Binney, J. 2014, MNRAS, 441, 3284

Sanders, J. L., Bovy, J., & Erkal, D. 2016, MNRAS, 457, 3817

Sandford, E., Kuepper, A. H. W., Johnston, K. V., & Diemand, J. 2017, ArXiv e-prints

Satyapal, S., Ellison, S. L., McAlpine, W., Hickox, R. C., Patton, D. R., & Mendel, J. T. 2014, MNRAS, 441, 1297

Schönrich, R. 2012, MNRAS, 427, 274

Schönrich, R., Binney, J., & Dehnen, W. 2010, MNRAS, 403, 1829

Schwartz, C. M. & Martin, C. L. 2004, ApJ, 610, 201

Scudder, J. M., Ellison, S. L., Torrey, P., Patton, D. R., & Mendel, J. T. 2012, MNRAS, 426, 549

Sengupta, C., Scott, T. C., Paudel, S., Saikia, D. J., Dwarakanath, K. S., & Sohn, B. W. 2015a, A&A, 584, A114

Sesar, B., Price-Whelan, A. M., Cohen, J. G., Rix, H.-W., Pearson, S., Johnston, K. V., Bernard, E. J., Ferguson, A. M. N., Martin, N. F., Slater, C. T., Chambers, K. C., Flewelling, H., Wainscoat, R. J., & Waters, C. 2016, ApJ, 816, L4

Shipp, N., Drlica-Wagner, A., Balbinot, E., Ferguson, P., Erkal, D., Li, T. S., Bechtol, K., Belokurov, V., Buncher, B., Carollo, D., Carrasco Kind, M., Kuehn, K., Marshall, J. L., Pace, A. B., Rykoff, E. S., Sevilla-Noarbe, I., Sheldon, E., Strigari, L., Vivas, A. K., Yanny, B., Zenteno, A., Abbott, T. M. C., Abdalla, F. B., Allam, S., Avila, S., Bertin, E., Brooks, D., Burke, D. L., Carretero, J., Castander, F. J., Cawthon, R., Crocce, M., Cunha, C. E., D'Andrea, C. B., da Costa, L. N., Davis, C., De Vicente, J., Desai, S., Diehl, H. T., Doel, P., Evrard, A. E., Flaugher, B., Fosalba, P., Frieman, J., García-Bellido, J., Gaztanaga, E., Gerdes, D. W., Gruen, D., Gruendl, R. A., Gschwend, J., Gutierrez, G., Hoyle, B., James, D. J., Johnson, M. D., Krause, E., Kuropatkin, N., Lahav, O., Lin, H., Maia, M. A. G., March, M., Martini, P., Menanteau, F., Miller, C. J., Miquel, R., Nichol, R. C., Plazas, A. A., Romer, A. K., Sako, M., Sanchez, E., Scarpine, V., Schindler, R., Schubnell, M., Smith, M., Smith, R. C., Sobreira, F., Suchyta, E., Swanson, M. E. C., Tarle, G., Thomas, D., Tucker, D. L., Walker, A. R., Wechsler, R. H., & the DES Collaboration. 2018, ArXiv e-prints

Silverman, J. D., Kampczyk, P., Jahnke, K., Andrae, R., Lilly, S. J., Elvis, M., Civano, F., Mainieri, V., Vignali, C., Zamorani, G., Nair, P., Le Fèvre, O., de Ravel, L., Bardelli, S., Bongiorno, A., Bolzonella, M., Cappi, A., Caputi, K., Carollo, C. M., Contini, T., Coppa, G., Cucciati, O., de la Torre, S., Franzetti, P., Garilli, B., Halliday, C., Hasinger, G., Iovino, A., Knobel, C., Koekemoer, A. M., Kovač, K., Lamareille, F., Le Borgne, J.-F., Le Brun, V., Maier, C., Mignoli, M., Pello, R., Pérez-Montero, E., Ricciardelli, E., Peng, Y., Scodeggio, M., Tanaka, M., Tasca, L., Tresse, L., Vergani, D., Zucca, E., Brusa, M., Cappelluti, N., Comastri, A., Finoguenov, A., Fu, H., Gilli, R., Hao, H., Ho, L. C., & Salvato, M. 2011, ApJ, 743, 2

Skokos, C. 2010, in Lecture Notes in Physics, Berlin Springer Verlag, Vol. 790, Lecture Notes

in Physics, Berlin Springer Verlag, ed. J. Souchay & R. Dvorak, 63–135

Smith, B. J., Giroux, M. L., Struck, C., Hancock, M., & Hurlock, S. 2010, ArXiv e-prints

Sofue, Y. 2013, PASJ, 65, 118

Sohn, Y.-J. & Davidge, T. J. 1996, AJ, 112, 2559

Sommer-Larsen, J. 2006, ApJ, 644, L1

Springel, V. & White, S. D. M. 1999, MNRAS, 307, 162

Springel, V., White, S. D. M., Jenkins, A., Frenk, C. S., Yoshida, N., Gao, L., Navarro, J., Thacker, R., Croton, D., Helly, J., Peacock, J. A., Cole, S., Thomas, P., Couchman, H., Evrard, A., Colberg, J., & Pearce, F. 2005, Nature, 435, 629

Stanimirović, S., Staveley-Smith, L., & Jones, P. A. 2004, ApJ, 604, 176

Stierwalt, S., Besla, G., Patton, D., Johnson, K., Kallivayalil, N., Putman, M., Privon, G., & Ross, G. 2015, ApJ, 805, 2

Stierwalt, S., Liss, S. E., Johnson, K. E., Patton, D. R., Privon, G. C., Besla, G., Kallivayalil, N., & Putman, M. 2017, Nature Astronomy, 1, 0025

Swaters, R. A., van Albada, T. S., van der Hulst, J. M., & Sancisi, R. 2002, A&A, 390, 829

Theureau, G., Hanski, M. O., Coudreau, N., Hallet, N., & Martin, J.-M. 2007, A&A, 465, 71

Thomas, G. F., Ibata, R., Famaey, B., Martin, N. F., & Lewis, G. F. 2016, MNRAS, 460, 2711

Tolstoy, E., Hill, V., & Tosi, M. 2009, ARA&A, 47, 371

Toomre, A. & Toomre, J. 1972, ApJ, 178, 623

Tully, R. B., Rizzi, L., Dolphin, A. E., Karachentsev, I. D., Karachentseva, V. E., Makarov, D. I., Makarova, L., Sakai, S., & Shaya, E. J. 2006, AJ, 132, 729

Tully, R. B., Rizzi, L., Shaya, E. J., Courtois, H. M., Makarov, D. I., & Jacobs, B. A. 2009, AJ, 138, 323

Tumlinson, J., Thom, C., Werk, J. K., Prochaska, J. X., Tripp, T. M., Katz, N., Davé, R., Oppenheimer, B. D., Meiring, J. D., Ford, A. B., O'Meara, J. M., Peeples, M. S., Sembach, K. R., & Weinberg, D. H. 2013, ApJ, 777, 59

van den Bosch, F. C., Jiang, F., Hearin, A., Campbell, D., Watson, D., & Padmanabhan, N. 2014, MNRAS, 445, 1713

van der Hulst, J. M., van Albada, T. S., & Sancisi, R. 2001, in Astronomical Society of the Pacific Conference Series, Vol. 240, Gas and Galaxy Evolution, ed. J. E. Hibbard, M. Rupen, & J. H. van Gorkom, 451

van der Kruit, P. C. & Searle, L. 1981, A&A, 95, 105

van der Marel, R. P., Alves, D. R., Hardy, E., & Suntzeff, N. B. 2002, AJ, 124, 2639

van der Marel, R. P. & Kallivayalil, N. 2014, ApJ, 781, 121

van Dokkum, P. G., Leja, J., Nelson, E. J., Patel, S., Skelton, R. E., Momcheva, I., Brammer, G., Whitaker, K. E., Lundgren, B., Fumagalli, M., Conroy, C., Förster Schreiber, N., Franx, M., Kriek, M., Labbé, I., Marchesini, D., Rix, H.-W., van der Wel, A., & Wuyts, S. 2013, ApJ, 771, L35

van Dokkum, P. G., Nelson, E. J., Franx, M., Oesch, P., Momcheva, I., Brammer, G., Förster Schreiber, N. M., Skelton, R. E., Whitaker, K. E., van der Wel, A., Bezanson, R., Fumagalli, M., Illingworth, G. D., Kriek, M., Leja, J., & Wuyts, S. 2015, ApJ, 813, 23

van Dokkum, P. G., Whitaker, K. E., Brammer, G., Franx, M., Kriek, M., Labbé, I., Marchesini, D., Quadri, R., Bezanson, R., Illingworth, G. D., Muzzin, A., Rudnick, G., Tal, T., & Wake, D. 2010, ApJ, 709, 1018

Varghese, A., Ibata, R., & Lewis, G. F. 2011, MNRAS, 417, 198

Vera-Ciro, C., Sales, L. V., Helmi, A., Frenk, C. S., Navarro, J. F., Springel, V., Vogelsberger, M., White, S. D. M. 2011, MNRAS, 416, 1377

Vera-Ciro, C. & Helmi, A. 2013, ApJ, 773, L4

Viallefond, F., Allen, R. J., & de Boer, J. A. 1980, A&A, 82, 207

Vieira, K., Girard, T. M., van Altena, W. F., Zacharias, N., Casetti-Dinescu, D. I., Korchagin, V. I., Platais, I., Monet, D. G., López, C. E., Herrera, D., & Castillo, D. J. 2010, AJ, 140, 1934

Vogelsberger, M., Genel, S., Springel, V., Torrey, P., Sijacki, D., Xu, D., Snyder, G., Bird, S., Nelson, D., & Hernquist, L. 2014, Nature, 509, 177

Vollmer, B., Soida, M., Chung, A., van Gorkom, J. H., Otmianowska-Mazur, K., Beck, R., Urbanik, M., & Kenney, J. D. P. 2008, A&A, 483, 89

Walt, S. v. d., Colbert, S. C., & Varoquaux, G. 2011, Computing in Science and Engg., 13, 22

Wang, Y., Zhao, H., Mao, S., & Rich, R. M. 2012, MNRAS, 427, 1429

Wegg, C. & Gerhard, O. 2013, MNRAS, 435, 1874

Wegg, C., Gerhard, O., & Portail, M. 2015, MNRAS, 450, 4050

Weilbacher, P. M., Monreal-Ibero, A., Verhamme, A., Sandin, C., Steinmetz, M., Kollatschny, W., Krajnović, D., Kamann, S., Roth, M. M., Erroz-Ferrer, S., Marino, R. A., Maseda, M. V., Wendt, M., Bacon, R., Dreizler, S., Richard, J., & Wisotzki, L. 2017, ArXiv e-prints

Weisz, D. R., Dolphin, A. E., Dalcanton, J. J., Skillman, E. D., Holtzman, J., Williams, B. F., Gilbert, K. M., Seth, A. C., Cole, A., Gogarten, S. M., Rosema, K., Karachentsev, I. D., McQuinn, K. B. W., & Zaritsky, D. 2011, ApJ, 743, 8

Werk, J. K., Prochaska, J. X., Thom, C., Tumlinson, J., Tripp, T. M., O'Meara, J. M., & Peeples, M. S. 2013, ApJS, 204, 17

Werk, J. K., Prochaska, J. X., Tumlinson, J., Peeples, M. S., Tripp, T. M., Fox, A. J., Lehner, N., Thom, C., O'Meara, J. M., Ford, A. B., Bordoloi, R., Katz, N., Tejos, N., Oppenheimer, B. D., Davé, R., & Weinberg, D. H. 2014, ApJ, 792, 8

Werk, J. K., Putman, M. E., Meurer, G. R., Thilker, D. A., Allen, R. J., Bland-Hawthorn, J., Kravtsov, A., & Freeman, K. 2010, ApJ, 715, 656

Wetzel, A. R., Deason, A. J., & Garrison-Kimmel, S. 2015, ApJ, 807, 49

Wetzel, A. R., Hopkins, P. F., Kim, J.-h., Faucher-Giguère, C.-A., Kereš, D., & Quataert, E. 2016, ApJ, 827, L23

Whitney, B. A., Sewilo, M., Indebetouw, R., Robitaille, T. P., Meixner, M., Gordon, K., Meade, M. R., Babler, B. L., Harris, J., Hora, J. L., Bracker, S., Povich, M. S., Churchwell, E. B., Engelbracht, C. W., For, B.-Q., Block, M., Misselt, K., Vijh, U., Leitherer, C.,

Kawamura, A., Blum, R. D., Cohen, M., Fukui, Y., Mizuno, A., Mizuno, N., Srinivasan, S., Tielens, A. G. G. M., Volk, K., Bernard, J.-P., Boulanger, F., Frogel, J. A., Gallagher, J., Gorjian, V., Kelly, D., Latter, W. B., Madden, S., Kemper, F., Mould, J. R., Nota, A., Oey, M. S., Olsen, K. A., Onishi, T., Paladini, R., Panagia, N., Perez-Gonzalez, P., Reach, W., Shibai, H., Sato, S., Smith, L. J., Staveley-Smith, L., Ueta, T., Van Dyk, S., Werner, M., Wolff, M., & Zaritsky, D. 2008, AJ, 136, 18

Wilcots, E. M. & Prescott, M. K. M. 2004, AJ, 127, 1900

Wilke, K., Klaas, U., Lemke, D., Mattila, K., Stickel, M., & Haas, M. 2004, A&A, 414, 69

Willick, J. A., Courteau, S., Faber, S. M., Burstein, D., Dekel, A., & Strauss, M. A. 1997, ApJS, 109, 333

Xue, X. X., Rix, H. W., Zhao, G., Re Fiorentin, P., Naab, T., Steinmetz, M., van den Bosch, F. C., Beers, T. C., Lee, Y. S., Bell, E. F., Rockosi, C., Yanny, B., Newberg, H., Wilhelm, R., Kang, X., Smith, M. C., & Schneider, D. P. 2008, ApJ, 684, 1143

Yoon, J. H., Johnston, K. V., & Hogg, D. W. 2011, ApJ, 731, 58

York, D. G., Adelman, J., Anderson, Jr., J. E., Anderson, S. F., Annis, J., Bahcall, N. A., Bakken, J. A., Barkhouser, R., Bastian, S., Berman, E., Boroski, W. N., Bracker, S., Briegel, C., Briggs, J. W., Brinkmann, J., Brunner, R., Burles, S., Carey, L., Carr, M. A., Castander, F. J., Chen, B., Colestock, P. L., Connolly, A. J., Crocker, J. H., Csabai, I., Czarapata, P. C., Davis, J. E., Doi, M., Dombeck, T., Eisenstein, D., Ellman, N., Elms, B. R., Evans, M. L., Fan, X., Federwitz, G. R., Fiscelli, L., Friedman, S., Frieman, J. A., Fukugita, M., Gillespie, B., Gunn, J. E., Gurbani, V. K., de Haas, E., Haldeman, M., Harris, F. H., Hayes, J., Heckman, T. M., Hennessy, G. S., Hindsley, R. B., Holm, S., Holmgren, D. J., Huang, C.-h., Hull, C., Husby, D., Ichikawa, S.-I., Ichikawa, T., Ivezić, Ž.,

Kent, S., Kim, R. S. J., Kinney, E., Klaene, M., Kleinman, A. N., Kleinman, S., Knapp, G. R., Korienek, J., Kron, R. G., Kunszt, P. Z., Lamb, D. Q., Lee, B., Leger, R. F., Limmongkol, S., Lindenmeyer, C., Long, D. C., Loomis, C., Loveday, J., Lucinio, R., Lupton, R. H., MacKinnon, B., Mannery, E. J., Mantsch, P. M., Margon, B., McGehee, P., McKay, T. A., Meiksin, A., Merelli, A., Monet, D. G., Munn, J. A., Narayanan, V. K., Nash, T., Neilsen, E., Neswold, R., Newberg, H. J., Nichol, R. C., Nicinski, T., Nonino, M., Okada, N., Okamura, S., Ostriker, J. P., Owen, R., Pauls, A. G., Peoples, J., Peterson, R. L., Petravick, D., Pier, J. R., Pope, A., Pordes, R., Prosapio, A., Rechenmacher, R., Quinn, T. R., Richards, G. T., Richmond, M. W., Rivetta, C. H., Rockosi, C. M., Ruthmansdorfer, K., Sandford, D., Schlegel, D. J., Schneider, D. P., Sekiguchi, M., Sergey, G., Shimasaku, K., Siegmund, W. A., Smee, S., Smith, J. A., Snedden, S., Stone, R., Stoughton, C., Strauss, M. A., Stubbs, C., SubbaRao, M., Szalay, A. S., Szapudi, I., Szokoly, G. P., Thakar, A. R., Tremonti, C., Tucker, D. L., Uomoto, A., Vanden Berk, D., Vogeley, M. S., Waddell, P., Wang, S.-i., Watanabe, M., Weinberg, D. H., Yanny, B., Yasuda, N., & SDSS Collaboration. 2000, AJ, 120, 1579

Zheng, Y., Peek, J. E. G., Werk, J. K., & Putman, M. E. 2017, ApJ, 834, 179

Zivick, P., Kallivayalil, N., van der Marel, R. P., Besla, G., Linden, S. T., Kozłowski, S., Fritz, T. K., Kochanek, C. S., Anderson, J., Sohn, S. T., Geha, M. C., & Alcock, C. R. 2018, ArXiv e-prints